

Vishal Youhanna

Conceptual Design of Martian Aerial Robots

Faculty of Engineering and Applied Sciences

Doctorate Research Programme in Aerospace

PhD
Academic Year: 2021 - 2024

Supervisor: Dmitry Ignatyev
Associate Supervisor: Leonard Felicetti
September 2024



Faculty of Engineering and Applied Sciences
Doctorate Research Programme in Aerospace

PhD

Academic Year 2021 - 2024

Vishal Youhanna

Conceptual Design of Martian Aerial Robots

Supervisor: Dmitry Ignatyev
Associate Supervisor: Leonard Felicetti
September 2024

© Cranfield University 2024. All rights reserved. No part of this publication may be reproduced without the written permission of the copyright owner.

Academic integrity declaration

I declare that:

- the thesis submitted has been written by me alone.
- the thesis submitted has not been previously submitted to this university or any other.
- that all content, including primary and/or secondary data, is true to the best of my knowledge.
- that all quotations and references have been duly acknowledged according to the requirements of academic research.

I understand that to knowingly submit work in violation of the above statement will be considered by examiners as academic misconduct.

Abstract

This thesis addresses the design and optimisation of rotary Vertical Take-Off and Landing (VTOL) aerobots for Mars exploration. Current surface exploration robots, such as rovers and landers, are constrained by their limited mobility in accessing Mars' diverse and rugged terrain. To overcome these challenges, this research investigates the feasibility and performance of aerobots as a complementary solution, building on NASA's Ingenuity Helicopter technology demonstrator.

The research focuses on overcoming the engineering challenges posed by Mars' thin atmosphere, low gravity, and extreme environmental conditions. A structured framework is developed to systematically integrate environmental constraints and mission-specific requirements into the aerobot design process. Central to the study is the adaptation of helicopter momentum theory for Martian conditions, providing a theoretical basis for estimating power consumption and rotorcraft performance during key flight phases, including hover, vertical climb, and forward flight. Following the theoretical groundwork, a parametric analysis evaluates several rotorcraft configurations such as single-rotor, dual, quadcopter, and hexacopter, focusing on power efficiency, lift capacity, and operational feasibility. Among the configurations analysed, hexacopters demonstrate superior stability, redundancy, and power efficiency, making them the most promising design for Martian missions.

The research also develops practical design variants for the proposed aerobots, addressing deployment challenges such as packaging within spacecraft aeroshells through the implementation of foldable rotor systems. These innovations ensure that the aerobots meet the spatial constraints of Mars exploration missions while maximising performance. The findings from this research provide a foundation for future Mars aerobot development, with recommendations for further computational modelling and experimental validation to enhance reliability in mission-critical applications.

Keywords: Mars Exploration, Systematic Drone Framework, Planetary Aerobots, Rotorcraft Preliminary Design, Space UAV

Acknowledgements

In gratitude for the boundless wisdom of the cosmos, which has silently guided me through the vast expanse of this journey, I begin by acknowledging the source of all inspiration and discovery that fuels both the stars above and the curiosity within.

I express my deepest admiration to my supervisor, Dr Dmitry Ignatyev, for his belief in me since our first meeting and his mentorship throughout. His invaluable feedback on the technical aspects of this research and overall support has been key to my progress. I thank my associate supervisor, Dr Leonard Felicetti, for his regular presence, encouragement and suggestions that have enhanced the quality of my academic research. I also express my gratitude to my progress reviewers, Prof James Whidborne and Prof Yifan Zhao, whose early feedback helped guide the direction and focus of my PhD research. Collectively, their guidance has enriched my understanding of the field and shaped my approach to scientific research.

I convey my thanks to Prof Antonios Tsourdos, head of the department, for the opportunity to undertake this research and for ensuring access to the necessary resources. Additionally, I extend my gratefulness to Cranfield University for its support and for providing an environment that fosters both academic excellence and personal growth. The serenity of Cranfield has been a source of calm and focus throughout my studies.

I share my appreciation to the global researchers whose concepts in Martian aerobot design have benefitted the planetary research community, and NASA and the Ingenuity Helicopter team for inspiring this project and laying the groundwork for future Mars exploration.

Lastly, and most importantly, a heartfelt gratitude to my family and well-wishers for their unconditional support, patience, and belief in me throughout this journey. Their encouragement and love have been my greatest source of strength.

Foreword

Cranfield University offers the possibility to choose between two doctoral thesis formats: the classic, monograph and the collection of papers (or paper-format). In this thesis, the latter approach is followed.

In accordance with Cranfield University Senate Handbook - Research Students' Handbook[1], the thesis is organised as follows:

1. Introduction: Here the context and a short background on the work area are given, followed by the project's aims and objectives, a list of published, submitted, or completed works and how they link together.

2. Papers: a series, usually three to five, of self-contained chapters (e.g. a global literature review is not required).

3. Conclusion/s and Suggestions for Future Work.

[1] Senate Handbook: Research Students' Handbook: https://www.cranfield.ac.uk/-/media/files/corporate_documents/research-students-handbook.ashx [Retrieved on 06/09/2024]

Table of Contents

Academic integrity declaration i
Abstract ii
Acknowledgements iii
Foreword iv
Table of Contents v
List of Figures ix
List of Tables xvi
List of Equations xvii
List of Abbreviations xx
List of Definitions of Key Terms xxii
1 Introduction 25
1.1 Background and motivation 25
1.2 Research Gap, Aim and Objectives 28
1.2.1 Research Gap 28
1.2.2 Aim 29
1.2.3 Objectives 29
1.3 Contribution to Knowledge 29
1.4 Thesis Structure 31
1.4.1 Chapter 1: Introduction 33
1.4.2 Chapter 2: Mars Planetary Insights and Design Framework for Future In-Situ Aerial Robotic Missions 34
1.4.3 Chapter 3: Systematic Methodology for the Preliminary Design of Future Rotary VTOL Martian Aerobots 34
1.4.4 Chapter 4: Parametric Analysis of Multirotor Aerobot Configurations for Mars 35
1.4.5 Chapter 5: Conclusion and Future Work 35
1.5 Key Assumptions for Problem Definitions 36
1.6 List of Research Outputs 38
1.6.1 Journal Papers – Peer Reviewed 38
1.6.2 Conference Papers – Peer Reviewed 38
References 40
2 Mars Planetary Insights and Design Framework for Future In-Situ Aerial Robotic Missions 41
2.1 Introduction 42
2.2 Comprehending Planetary Exploration Development 44
2.2.1 Earth's Two Neighbours – First to Most Explored 45
2.2.2 Standing on the Shoulders of the Giants – Mars Exploration History 48
2.3 Comprehending Mars Exploration Science Goals and Requirements 52
2.4 Martian Aerobot Science Missions Subject to Areography 54

2.4.1 Mars Topography Influencing Aerobot Mechanical Design 54
2.4.2 Mars Climatology Influencing Aerobots Performance 63
2.5 Design, Development and Delivery Considerations for Martian Aerobots 79
2.5.1 Ingenuity into the Design and Development Considerations 81
2.5.2 Interplanetary Delivery Considerations 86
2.6 Mars Aerobot Design Thinking Matrix 92
2.6.1 The Rationale for Aerobots Inclusion 92
2.6.2 Orders of Martian Aerobot Preliminary Design 94
2.7 Conclusion 104
References 106
3 Systematic Methodology for the Preliminary Design of Future Rotary VTOL Martian Aerobots 120
3.1 Introduction 121
3.1.1 Martian Flight Conditions 121
3.1.2 Literature 122
3.1.3 Proposed Research 125
3.2 Framework for Preliminary Martian Rotary VTOL Aerobot Design Methodology 127
3.3 Mission Statement and Requirements 129
3.3.1 Mission Aim Identification 129
3.3.2 Mission Location Requirement and Justification 130
3.3.3 Top-Level Mission Profile Definition 132
3.3.4 Flight Operations and Profile Definition 133
3.3.5 Aerobot's Performance Criteria Establishment 135
3.4 Specification of Key Parameters 137
3.4.1 Approaches to Local Air Density Determination 137
3.4.2 Aerobot's Size Constraints Definition 141
3.4.3 Rotor Speed Limits Determination 141
3.5 Methodology for Estimating Required Flight Power of Rotorcraft Configurations 142
3.5.1 Single Rotor Conventional Rotorcraft 143
3.5.2 Coaxial Rotorcraft 145
3.5.3 Isolated Rotors (Non-Overlapping Rotors e.g., Rotorcraft with Side-by-Side Rotors) 147
3.5.4 Rotorcraft with Partial Overlapping Rotors (e.g., Tandem Rotorcraft) 148
3.6 Methodology for the Initial Sizing of Battery-Electric Aerobot 150
3.7 Establishing Rotorcraft Configuration Cases for Parametric Analysis 152
3.7.1 Tandem Rotorcraft Configuration Cases Formation 154
3.7.2 Parameters and Variables Finalisation 157
3.8 Results and Analysis 159
3.8.1 Hover and Vertical Climb Analysis 160

3.8.2 Forward Flight Analysis 166
3.8.3 Battery Mass Fraction (*BMF*) Analysis 172
3.9 Practical Application of the Analysis and Discussions 174
3.9.1 Efficient Rotor Configuration Shortlisting 174
3.9.2 Initial Sizing Application and Battery Considerations 177
3.9.3 Discussion 180
3.10 Conclusion 182
References 184
4 Parametric Analysis of Multirotor Aerobot Configurations for Mars 189
4.1 Introduction 190
4.1.1 Planet Mars 190
4.1.2 Literature 191
4.1.3 Proposed Study 192
4.2 Power Requirement Analysis Methodology For Rotorcraft 193
4.2.1 Rotorcraft Types 193
4.2.2 Conventional Rotorcraft 194
4.2.3 Coaxial Rotorcraft 196
4.2.4 Isolated Rotors: rotorcraft having non-overlapping rotors 197
4.2.5 Rotorcraft with Partial Overlapping Rotors (e.g., Tandem Rotorcraft) 198
4.3 Initial Sizing Methods for Battery-Electric Aircraft 200
4.4 Initial Sizing Methods and Analysis for Estimating Rotor Blade Mass 202
4.4.1 Existing Rotor Blade Mass Scaling Methods 203
4.4.2 Proposed Rotor Blade Mass Scaling Model – 3D MSH Scale 204
4.5 Definition of Rotorcraft Configurations 223
4.5.1 Tandem Rotorcraft Cases 223
4.5.2 Quadcopter and Hexacopter Cases 225
4.6 Definition of Parameters for Performance Analysis 228
4.7 Results and Analysis 231
4.7.1 Hover and Vertical Climb Analysis 231
4.7.2 Forward Flight Analysis 234
4.7.3 BMF Comparative Analysis of Rotor Configurations 237
4.7.4 Power Efficient Rotor Configuration 239
4.7.5 Implementing Initial Sizing on Selected Configuration 241
4.8 Discussion and Conclusion 245
4.8.1 Discussion 245
4.8.2 Conclusion 246
References 247
5 Conclusion 251
5.1.1 Potential Impact 252
5.2 Future Work Recommendations 253
Global References/Bibliography 256
Appendices 276

Appendix A Appendix A. Ethical approval letter 276

List of Figures

Fig. 1.1 Six whys and rationale for the PhD Thesis theme ‘Conceptual Design of Martian Aerial Robots 33

Fig. 2.1Colour picture of the surface of Venus from the Venera 13 Lander. Image credit: NASA/NSSDC (ID -VG00261,262) 46

Fig. 2.2. Schiaparelli's 1877 surface map of Mars. (Image Source [17]) 49

Fig. 2.3 (left) before and (right) after one month of the global storm in 2001 captured by NASA's Mars Global Surveyor orbiter. Image credit: NASA/JPL/MSSS (ID- PIA03170)..... 50

Fig. 2.4 First Colour Image from Viking Lander 1 of the Mars ground. Image credit: NASA/JPL (ID- PIA00563)..... 51

Fig. 2.5 Topographic Map of Mars - M 25M RKN, by USGS 2003 based on data from the Mars Orbiter Laser Altimeter (MOLA) an instrument on NASA’s Mars Global Surveyor (MGS) [36] 56

Fig. 2.6 Mars Cartographic Chart [42] 57

Fig. 2.7 Slice runs showing a slope of 0.036° from the north pole (left) to the south pole (right) at 0° Longitude. Image credit: NASA/MOLA Science Team 57

Fig. 2.8 A non-exhaustive chart list diagram of the 2nd, 4th and 5th orders of relief of Mars, based on [37]. Some features listed have picture examples shown in Fig. 2.9..... 58

Fig. 2.9 Distinct topographic features and terrains of Mars with a potential for future science missions by aerial robots. Mars Reconnaissance Orbiter images are publicly accessible on the HiRISE web catalogue [44]. a) Victoria Crater at Meridiani Planum with scalloped shaped rim and floored with dunes (TRA_000873_1780). b) Non-circular 3 km impact crater on Tithonium Chasma’s inclined wall (ESP_044998_1745). c) False coloured 3D rendered view of Olympus Mons, Arsia Mons, Pavonis Mons & Ascræus Mons. (generated in JMars5 (GIS) [45]) d) False coloured 3D rendered view of Elysium Rise showing Hecates Tholus (front), Elysium Mons & Albor Tholus. (generated in JMars) e) A pit crater about 50m across formed over an underground lava tube (ESP_065887_1660). f) Delta structure showing distributary network including lobes, inverted channels, & meander cutoffs in Eberswalde Crater (PSP_001336_1560). g) Cerberus Fossae East of the Head of Athabasca Valles (ESP_016216_1900). h) Gully-like landslides, including alcoves and channels, on the interior wall of Valles Marineris (ESP_022632_1670). i) Chaotic terrain of Aram Chaos showing rough floor topography with large, slumped blocks & fractures (PSP_008311_1835). j) Mesas, buttes & yardangs surrounded by sand dunes in Meridiani Planum (ESP_034129_1820). k) Inverted Crater and dunes in Arabia Terra (ESP_016459_1830). l) Alpine glaciers, common at middle latitudes (ESP_019213_2210). m) Dunes in the North covered primarily with ice, during springtime get topped with dark sand streaks due to geyser-like

eruptions of carbon dioxide (ESP_017043_2640). n) Swiss cheese terrain formed by circular & blob-shaped depressions at the South Pole due to the gradual ongoing sublimation of the CO2 ice layer (PSP_005095_0935). o) Brain terrain is icy lobate features, in the image layering a small hill (ESP_033165_2195). Images Credit: NASA/JPL-Caltech/UArizona (image id number next to each image caption)).... 59

Fig. 2.10 NASA's Goddard Mars Model-3 (GMM-3) free-air gravity anomaly map. (mGal=0.00001 m/s²). Image: NASA/GSFC [49] 63

Fig. 2.11 Mars positions in the solar orbit. Illustration not to Scale. 64

Fig. 2.12 The graphs show global environmental parameters on Mars at the altitude of 10 m above the local surface of Mars at Longitude 0° Local time 11:00 on Sol 514.6 (Ls 270) during the Northern Hemisphere Winter Solstice. The parameters a) Air Density b) Air Viscosity c) Horizontal Wind Speed d) Temperature are based on the climatology average solar scenario generated in MCD_v6.1 [58]. 70

Fig. 2.13 The colours in the map refer to the annual dose equivalent in milli sievert (mSv) estimated utilising NASA's Mars Odyssey orbiter data. The range is generally from 100 Sv (colour-coded dark blue) to 200 Sv (colour-coded dark red) [82]. Original Image Credit: NASA/JPL/JSC. Modification: Altered equivalent units.... 76

Fig. 2.14 Mars Helicopter Technology Demonstrator Subsystem Classification. Modified Image from source [92] 85

Fig. 2.15 The top images depict Mars's past mission aeroshells during the testing phase: a) Mars Science Laboratory aeroshell (2011, size 4.5 m). b) Mars Viking 1 aeroshell (1975, size 3.5 m). c) Mars Exploration Rover 2 aeroshell (2003, size 2.65 m). Images Credit: NASA. The bottom images are CAD model illustrations showing different aircrafts folded and packed inside the respective aeroshell shown at the top a.i) Winged VTOL concept CAD model 4.5 m aeroshell [100]. b.i) Folded hexacopter concepts folded inside a petal lander comprising thrusters which are packed inside the Viking aeroshell (3.5 m) [98]. c.i) Coaxial rotorcraft with 3 and 4 blades variants packed inside 2.65 aeroshells [98] 89

Fig. 2.16 The image at the left shows the reusable SpaceX Starship, currently in development, standing at the launch pad. The rendered images at the right illustrate the concept of a Starship spacecraft (stage 2) separating from a Super Heavy Rocket (Stage 1) in the near-Earth orbit and travelling to Mars, where it enters the atmosphere and lands on the ground with its payload door open. Images Credit: SpaceX.... 90

Fig. 2.17 Estimated increases in Earth launch, Mars entry, and lander mass as a function of Mars aerial robot mass. Graph recreated from source [91]. 91

Fig. 2.18 The Mars Aerobot Design Thinking Matrix Flow Chart 95

Fig. 2.19 NASA's Mars Electric Reusable Flyer concept proposed a rover-dependant tail-sitter rotorcraft deployed by the rover with a robotic arm to explore caves and canyons. After each mission, it returns to the rover for recharging. Still images from the NASA Langley Research Center's YouTube post [110] 97

Fig. 2.20 Mini-Sniffer III. The image on the right shows the crew wearing self-contained suits and oxygen tanks because the engine was fueled with toxic hydrazine fuel. Image Credit: NASA. 99

Fig. 2.21 Categories Chart of Aerobot Types for Mars proposed in the literature 103

Fig. 3.1 Flow chart of the framework for the preliminary Martian aerobot design methodology 128

Fig. 3.2 a) Map showing SW Melas basin (red spot) in Valles Marineris. Cropped Topographic Map of Mars (M 25M RKN) by USGS 2003 based on data from the Mars Orbiter Laser Altimeter, an instrument on NASA's Mars Global Surveyor. b) Close-up of SW Melas Basin perches on the southwestern rim of Melas Chasma, with two ROI (red dots). The white outline (not to scale) is the 9.7 x 8.7 km landing ellipse centred at - 9.81° N, - 76.46° E, elevation - 1.92km [22]. Image created using JMars 5 (GIS) [28]. 132

Fig. 3.3 Mission Profile Map showing Valles Marineris created in JMars5 (GIS) [28]. The green and red dots on each mission profile line depict the start and finish, respectively. 133

Fig. 3.4 Flight specifications and profile of an aerobot for the proposed Mars mission 134

Fig. 3.5 The graphs show air density over the altitude above the local surface of SW Melas Chasma (Latitude -9.81N. Longitude 283.5E.) at a local time of 11.0h, spread over the full range of Martian Solar Longitude. a) altitude range of 0 m to 1000 m. b) at altitude 0 m and 1000 m. MCD_v6.1 with climatology average solar scenario [35]. 140

Fig. 3.6 a) Mars Science Laboratory aeroshell during testing (2011, size 4.5 m). Credits: NASA/Kim Shiflett. b) Folding option for coaxial helicopter concept in Pathfinder Aeroshell (size 2.65 m) [5]. c) Winged VTOL concept CAD model called FuMAD, folded and packed in Mars 2020 mission aeroshell (size 4.5) [37] 141

Fig. 3.7 Illustration of existing rotorcraft configurations: (top left) Single Conventional, (top right) Coaxial, (bottom left) Isolated Side-by-Side, and (bottom right) Tandem rotorcraft 143

Fig. 3.8 Schematic illustration of tandem rotors overlapping area showing a generic top view and side view of rotors in the (a) same plane and (b) separate planes. (Not to scale) 149

Fig. 3.9 Schematic diagram illustrating the terms $\boldsymbol{A}$, $\boldsymbol{Dmax}$, $\boldsymbol{h}$, $\boldsymbol{d}$. Left side image shows a fuselage of the rotorcraft within a spacecraft aeroshell highlighting

the size limit A. Right side image shows 3 different sizes of rotor disks at a fixed rotor hub position, demonstrating how changes in rotor diameter affect the degree of rotor overlap. 154

Fig. 3.10 Schematic illustration of three cases of tandem rotor hub positions on the fuselage placed inside the aeroshell. (Not to scale) 155

Fig. 3.11 Schematic illustration of the rotor positioning of tandem rotorcraft cases 1, 2 and 3 in operational mode. (Not to scale) 156

Fig. 3.12 Flight profile for the analysis 157

Fig. 3.13 Power Required (Hover & Vertical Climb) vs Rotor Disk Diameter – 20 kg & 40 kg Martian Conventional Helicopter 161

Fig. 3.14 Power required (Hover) vs Rotor Disk Diameter – Comparison between various 20 kg rotorcraft configurations (Helicopter, Coaxial, Tandem Cases, 2 Isolated Rotors) 163

Fig. 3.15 Power required (Vertical Climb) vs Rotor Disk Diameter – Comparison between various 20 kg rotorcraft configurations (Helicopter, Coaxial, Tandem Cases, 2 Isolated Rotors) 163

Fig. 3.16 Power required (Hover) vs Disk Loading (W/S - on log scale base 2) – Comparison between various 20 kg rotorcraft configurations (Helicopter, Coaxial, Tandem Cases, 2 Isolated Rotors) 165

Fig. 3.17 Power Loading (W/P) (Hover) vs Disk Loading (W/S) (both axes on Log scale base 2) – Comparison between various 20 kg rotorcraft configurations (Helicopter, Coaxial, Tandem Cases, 2 Isolated Rotors) 166

Fig. 3.18 Power Required (Forward Level & Climb Flight) vs Rotor Disk Diameter – 20 kg Martian Conventional Helicopter 167

Fig. 3.19 Power Required (Forward Level) vs Rotor Disk Diameter– Comparison between various 20 kg rotorcraft configurations (Helicopter, Coaxial, Tandem Cases, 2 Isolated Rotors) 168

Fig. 3.20 Power required (Forward Level & Climb Flight at 55.56 m/s) vs Rotor Disk Diameter (Rotor Diameter Limits - 1 to 9 m) – Comparison between various 20 kg rotorcraft configurations (Helicopter, Coaxial, Tandem Cases, 2 Isolated Rotors) 168

Fig. 3.21 Power required (Forward Level Flight) vs Disk Loading (W/S) – Comparison between various 20 kg rotorcraft configurations (Helicopter, Coaxial, Tandem Cases, 2 Isolated Rotors) 170

Fig. 3.22 Power Loading (W/P) (Forward Level Flight) vs Disk Loading (W/S) (both axes on Log scale base 2) – Comparison between various 20 kg rotorcraft configurations (Helicopter, Coaxial, Tandem Cases, 2 Isolated Rotors) 170

Fig. 3.23 21 Power Required (Forward Level) vs Rotor Disk Diameter (1 to 4.5 m)– Comparison between various 20 kg rotorcraft configurations (Helicopter, Coaxial and Tandem Case1) at 0.013 kg/m3 and 0.025 kg/m3 171

Fig. 3.24 BMF Vertical Climb Segment (at 8.33 m/s for 2 minutes) vs Rotor Disk Diameter– Comparison between various 20 kg rotorcraft configurations (Helicopter, Coaxial, Tandem Cases, 2 Isolated Rotors). a) Shows BMF for rotor diameters from 0 to 9 m on the x-axis. b) Shows a zoomed-in view, focusing on BMF for rotor diameters from 1.5 to 4.5 m on the x-axis for clarity 173

Fig. 3.25 BMF Forward Level Flight Segment (at 55.56 m/s for 3 minutes) vs Rotor Disk Diameter – Comparison between various 20 kg rotorcraft configurations (Helicopter, Coaxial, Tandem Cases, 2 Isolated Rotors).. 174

Fig. 3.26 Power required [Graph a) Vertical Climb at 8.33 m/s. Graph b) Level Forward Flight at 55.56 m/s] vs Rotor Disk Diameter (rotor diameter range - 1.5m to 4.5m) – Comparison between various 20 kg rotorcraft configurations (Helicopter, Coaxial, Tandem Cases) 176

Fig. 3.27 Case 3 Tandem rotorcraft with a 3 m rotor disk size based on initial sizing (CAD model illustration: the left side is a front isometric view and the right side is a top view. Not to scale) 178

Fig. 4.1 Rotorcraft Configurations Illustration 194

Fig. 4.2 Planform of the Mars Science Helicopter blade for a coaxial helicopter (R = 1.25 m) and a hexacopter (R = 0.64 m), with a typical 9%R root cutout (not shown). Adapted from [4], with graph plot images overlaid on a blank graph with minor axes for clarity. Not to scale. 206

Fig. 4.3 MSH components: (top left) skin, (top right) spar, (bottom left) foam, (bottom right) root insert. Image Source [4]. 207

Fig. 4.4 Simplified representation of segmented blade components along the radial span. The inner region ($0.09 \leq rR \leq 0.5$) contains the root insert, spar, and foam, while the outer region ($0.5 \leq rR \leq 1.0$) consists only of the skin. (Bars are not representation of the thickness) 207

Fig. 4.5 Scaling trends of blade component thickness with rotor radius, plotted on a logarithmic scale (base 2). 215

Fig. 4.6 Blade Mass vs. Rotor Blade Radius – Comparison between scaling models for blade mass estimation 218

Fig. 4.7 Close-up view of the graph plot - Blade Mass vs. Rotor Blade Radius (Rotor Radius Limits – 0.25 m to 2.25 m). Showing comparison of scaling models for blade mass estimation and empirical rotor blades data points, including the Ingenuity MH rotor (radius 0.61 m, mass 0.043 kg). 219

Fig. 4.8 Blade mass composition as a function of rotor blade radius, illustrating the contributions of individual components (spar, root insert, skin, and foam) to total blade mass using 3D MSH blade mass scale. 220

Fig. 4.9 Rotor Mass vs Rotor Diameter - Comparison between rotors with varying number of blades (2 to 5)..... 221

Fig. 4.10 Schema of the positioning of rotor hubs of tandem rotorcraft Cases 1, 2, and 3, on the fuselage placed inside an aeroshell [28]. (Not to scale). On the right is the aeroshell of NASA's Mars Science Laboratory mission, which was sent to Mars in 2011. Image Credit: NASA/JPL-Caltech 223

Fig. 4.11 Diagrammatic illustration of the rotor positioning of tandem rotorcraft Cases 1, 2, and 3 in operational mode [28]. (Not to scale)..... 224

Fig. 4.12 Diagram (not to scale) of the rotor hub positioning of quadrotor configuration with nonoverlapping equal-sized rotors. Top: stowed inside aeroshell. Bottom: operational mode 226

Fig. 4.13 Schematic illustration (not to scale) of the rotor hub positioning of hexarotor configuration with nonoverlapping equal-sized rotors. Top: stowed inside aeroshell. Bottom: operational mode..... 227

Fig. 4.14 Flight profile for the performance analysis..... 229

Fig. 4.15 Power Required (Hover & Vertical Climb) vs Rotor Disk Diameter - 20 kg & 40 kg Martian Conventional Helicopters..... 232

Fig. 4.16. Hover Power Required vs Rotor Disk Diameter – Comparison between various 20 kg rotorcraft configurations (Helicopter, Coaxial, 2 Isolated Rotors, and Cases of Tandem, Quadcopter, Hexacopter) 233

Fig. 4.17. Vertical Climb Power Required (at 8.33 m/s) vs Rotor Disk Diameter – Comparison between various 20 kg rotorcraft configurations (Helicopter, Coaxial, 2 Isolated Rotors, and Cases of Tandem, Quadcopter, Hexacopter) 234

Fig. 4.18. Forward Flight Power Required (at 55.56 m/s) vs Rotor Disk Diameter - 20 kg Martian Conventional Helicopter..... 234

Fig. 4.19 Forward Level Flight Power Required (at 55.56 m/s) vs Rotor Disk Diameter (Area) - 20 kg Martian Various Rotorcraft Configurations 235

Fig. 4.20. Forward Flight Power Required (at 55.56 m/s) vs Rotor Disk Diameter (Rotor Diameter Limits – 1 m to 4.5m) – Comparison between various 20 kg rotorcraft configurations (Helicopter, Coaxial, Tandem Cases, 2 Isolated Rotors, Quadcopter, Hexacopter)..... 236

Fig. 4.21. Vertical Climb (at 8.33 m/s for 2 mins) BMF vs Rotor Disk Diameter - 20 kg Martian rotorcrafts. Top - BMF for rotor diameters from 0 to 9 m. Bottom – Close-up view, focusing on BMF for rotor diameters from 1 m to 4.5 m on the x-axis for clarity..... 238

Fig. 4.22. Forward Level Flight (at 55.56 m/s for 3 mins) BMF vs Rotor Disk Diameter (Area) - 20 kg Martian rotorcrafts 239

Fig. 4.23. Power Required (Vertical Climb at 8.33 m/s) vs Rotor Disk Diameter (Rotor Diameter Limits – 1 m to 4.5m) – Comparison between various 20 kg rotorcraft configurations 240

Fig. 4.24. Power Required (Forward Level at 55.56 m/s) vs Rotor Disk Diameter (Rotor Diameter Limits – 1 m to 4.5m) – Comparison between various 20 kg rotorcraft configurations 241

Fig. 4.25 CAD Model illustration of a Case 2 Hexacopter configuration with a 1.5 m rotor disk size. Bottom left image shows the Hexacopter flying on Mars. (Not to scale) 244

List of Tables

Table 2.1 Summary of Mars 2020 mission landing site engineering constraints & safety criteria for sky crane-based EDL, and main scientific objectives [35] 54

Table 2.2: Summarised comparison between Aerobot and Rover 93

Table 3.1 Summary of Mars 2020 mission landing site engineering constraints & safety criteria, and main scientific objectives [22] 131

Table 3.2 A comparison of requirements and capabilities between Perseverance Rover [26], Ingenuity Helicopter [2], Mars Science Helicopter (MSH) [5], and the Potential Aerobot (PA) according to the mission specification. Mars 2020 mission data is based on its completion of 1000 sols on Mars. 1 Martian year = 668 sols. 136

Table 3.3 Summary of Tandem Rotorcraft Cases 156

Table 3.4 Parameters and variables used in the forward flight, vertical climb, and hover power analysis of various rotorcraft configurations. 158

Table 4.1 Relative chord (cR) values at key radial positions (rR) for the blades of rotor radius (R) 1.25 m and 0.64 m. 206

Table 4.2 Comparison of blade components mass composition 210

Table 4.3 Comparison of blade material components volume composition 211

Table 4.4 Comparison of blade material components thickncss composition 213

Table 4.5 Thickness-to-chord scaling exponents ($e\mathrm{cmpt}, \mathrm{seg}$) for blade components in a segment. 214

Table 4.6 Configuration Summary of Tandem, Quad & Hexa Rotorcraft Cases 228

Table 4.7 Parameters utilised in analysing power requirements for forward flight, vertical climb, and hover across various rotorcraft configurations. 230

List of Equations

(2.1) 68
(2.2) 68
(2.3) 68
(2.4) 76
(2.5) 78
(3.1) 138
(3.2) 138
(3.3) 138
(3.4) 142
(3.5) 144
(3.6) 145
(3.7) 146
(3.8) 146
(3.9) 147
(3.10) 147
(3.11) 148
(3.12) 149
(3.13) 149
(3.14) 151
(3.15) 151
(3.16) 152
(3.17) 153
(3.18) 153
(3.19) 153
(3.20) 153
(4.1) 195
(4.2) 195
(4.3) 197

(4.4)..... 197
(4.5)..... 198
(4.6)..... 198
(4.7)..... 199
(4.8)..... 199
(4.9)..... 199
(4.10)..... 200
(4.11)..... 201
(4.12)..... 201
(4.13)..... 203
(4.14)..... 203
(4.15)..... 204
(4.16)..... 204
(4.17)..... 208
(4.18)..... 208
(4.19)..... 208
(4.20)..... 208
(4.21)..... 208
(4.22)..... 209
(4.23)..... 211
(4.24)..... 212
(4.25)..... 212
(4.26)..... 213
(4.27)..... 214
(4.28)..... 215
(4.29)..... 215
(4.30)..... 216
(4.31)..... 216
(4.32)..... 216
(4.33)..... 216

(4.34)..... 216
(4.35)..... 216
(36)216
(4.37)..... 216
(4.38)..... 217
(4.39)..... 217

List of Abbreviations

BMF - Battery Mass Fraction

CAD – Computer Aided Design

CFD - Computational Fluid Dynamics

CNSA - China National Space Administration

EDL - Entry, Descent, and Landing

ESA - European Space Agency

GIS - Geographic Information System

JAXA - Japan Aerospace Exploration Agency

MOLA - Mars Orbiter Laser Altimeter

NASA - National Aeronautics and Space Administration

PA - Proposed Aerobot

RTG - Radioisotope Thermoelectric Generator

UAV - Unmanned Aerial Vehicle

VTOL - Vertical Take-off and Landing

MEPAG - Mars Exploration Program Analysis Group

MOLA - Mars Orbiter Laser Altimeter

MRO - Mars Reconnaissance Orbiter

HiRISE - High-Resolution Imaging Science Experiment

MSL - Mars Science Laboratory

MAEV - Mars Airborne Exploration Vehicle

GMM-3 - Goddard Mars Model-3 (high-resolution gravity field map of Mars).

SEP - Solar Energetic Particles (high-energy particles from the Sun affecting radiation levels).

MER - Mars Exploration Rover (e.g., Spirit, Opportunity).

List of Definitions of Key Terms

Aerobot: An autonomous aerial robotic system designed for planetary exploration, capable of sustained flight in extraterrestrial atmospheres (e.g., Mars).

Aeroshell: A protective casing used during spacecraft entry, descent, and landing (EDL) on Mars. Limits the stowed dimensions of spacecraft.

Areography: The study of Mars' physical geography, including topography, geology, and surface features.

Battery Mass Fraction (BMF): The proportion of the aerobot's total mass allocated to its battery system.

Disk Loading (W/S): The ratio of the aerobot's weight (*W*) to the total rotor disk area (*S*).

Entry, Descent, and Landing (EDL): The phase of a Mars mission where the spacecraft enters the atmosphere, descends, and lands on the surface.

HiRISE (High-Resolution Imaging Science Experiment): A camera on the Mars Reconnaissance Orbiter that provides detailed images of Mars' surface, aiding in aerobot mission planning.

Ingenuity Helicopter: NASA's first operational aerobot on Mars, part of the Mars 2020 mission. It demonstrated the feasibility of powered flight in Mars' thin atmosphere, serving as a technology demonstrator for future aerial missions.

Lander: A stationary robotic platform that lands on the Martian surface to conduct scientific research. Unlike rovers, landers remain fixed in one location, often carrying instruments for atmospheric analysis, seismic studies, and surface composition evaluation.

Mars 2020 Mission: NASA's mission that delivered the Perseverance rover and Ingenuity helicopter to Mars.

Mars Aerobot Design Thinking Matrix: A structured framework guiding the design of Martian aerobots by integrating mission requirements, environmental

constraints (e.g., atmospheric density, topography), and engineering trade-offs (e.g., power sources, rotor configurations).

Mars Climate Database (MCD): A European-developed computational tool providing atmospheric data (e.g., air density, temperature, wind speeds) for Martian locations and seasons, essential for aerobot design and simulation.

Mars Exploration Program Analysis Group (MEPAG): A NASA-led group that defines scientific goals and objectives for Mars exploration, including the search for life, climate studies, and preparation for human missions.

Mars Global Reference Atmospheric Model (Mars-GRAM): A NASA-developed atmospheric model used for mission planning and aerobot design.

Mars Orbiter Laser Altimeter (MOLA): An instrument on NASA's Mars Global Surveyor that provided high-resolution topographic maps of Mars, essential for understanding Martian terrain and selecting landing sites.

Mars Reconnaissance Orbiter (MRO): A NASA spacecraft orbiting Mars, equipped with high-resolution cameras (e.g., HiRISE) for mapping the planet's surface.

Mars Science Laboratory (MSL): NASA's mission that delivered the Curiosity rover to Mars. Its aeroshell design influences the size constraints for aerobots.

Mid-Air Deployment (MAD): A deployment strategy where aerobots are released from a spacecraft or lander during descent, bypassing the need for ground-based take-off.

Momentum Theory: A simplified aerodynamic model for rotary based propulsion, adapted for Martian rotorcraft to estimate power requirements for hover, climb, and forward flight.

Parametric Analysis: A method used to systematically evaluate multiple design variables and configurations by altering key parameters to determine their effects on performance. In the context of this study, parametric analysis is applied to rotorcraft configurations to optimise power efficiency, lift capacity, and feasibility for Martian exploration.

Photovoltaic (PV) Systems: Solar power systems that convert sunlight into electricity.

Planetary Boundary Layer (PBL): The lowest layer of Mars' atmosphere, directly influenced by surface interactions. Critical for predicting flight dynamics and turbulence.

Power Loading (W/P): The ratio of weight (*W*) to power (*P*), used to assess energy efficiency during flight phases (hover, climb, forward flight).

Reynolds Number: A dimensionless value indicating the ratio of inertial to viscous forces in a fluid flow. Low Reynolds numbers on Mars affect rotor aerodynamics, increasing drag and reducing lift efficiency.

Rotor: A rotating component consisting of blades that generate lift and thrust by interacting with the surrounding air. In rotorcraft, rotors are the primary mechanism for achieving controlled flight, and their design significantly impacts stability, efficiency, and power consumption.

Rotorcraft Configurations: Different arrangements of rotors on an aerial vehicle, including single-rotor, coaxial, tandem, quadcopter, and hexacopter setups, each with specific advantages in stability, power efficiency, and payload capacity.

Rover: A ground-based robotic vehicle designed for planetary exploration. Rovers are equipped with scientific instruments to analyse surface compositions, gather geological samples, and conduct environmental assessments while navigating Mars' terrain.

Valles Marineris: The largest canyon system in the solar system, located on Mars. A region of high scientific interest due to its geological complexity.

VTOL (Vertical Take-Off and Landing): A flight capability enabling aircraft to ascend and descend vertically without requiring runways. Critical for Mars missions due to the lack of infrastructure and rugged terrain.

1 Introduction

1.1 Background and motivation

Mars exploration has been a primary objective in planetary science due to its potential to reveal critical insights into the planet's geological history, climate evolution, and the potential for life. The evolution of Mars missions, from early flybys and orbiters to the advanced landers and rovers of today, has significantly expanded our understanding of the planet. These missions have uncovered a complex history involving water activity, diverse geological formations, and an environment that, although harsh, may have once supported life. However, despite the advancements made by surface-based exploration tools, significant challenges remain in exploring Mars' diverse and often inaccessible terrain. The limitations of rovers and landers, while valuable in their contributions to Mars exploration, have become increasingly apparent as the need arises to investigate more remote and scientifically important regions of the planet. Rovers, despite their ability to conduct detailed analyses of the Martian surface, are slow and constrained by the planet's rugged terrain, limiting their capacity to cover large distances and access difficult-to-reach sites. Similarly, landers are stationary platforms that can only study their immediate surroundings, preventing the exploration of broader areas or the investigation of distant features.

In response to these limitations, NASA introduced a new approach to Mars exploration with the deployment of the Ingenuity Helicopter as part of the Mars 2020 mission [1]. In April 2021, Ingenuity achieved the first powered flight on another planet, demonstrating the feasibility of aerial exploration in Mars' thin atmosphere. With an atmospheric density approximately 1% of Earth's at sea level, the successful operation of Ingenuity provided a proof of concept for the use of aerial vehicles to enhance Mars exploration. Ingenuity’s flights showed that aerial platforms could complement landers and rovers by providing overhead reconnaissance, scouting terrain, and accessing regions that ground-based vehicles cannot reach.

While Ingenuity's accomplishments have expanded the possibilities for Mars exploration, they have also highlighted the limitations of current aerial technology. As a technology demonstrator, Ingenuity was designed with constraints that reflect its primary goal of validating powered flight on Mars. Its small size, limited range, and modest payload capacity make it unsuitable for more ambitious scientific missions. The helicopter's restricted endurance and payload capabilities prevent it from conducting comprehensive scientific investigations, such as transporting advanced instruments, covering extensive distances, or operating in more diverse and challenging Martian environments. These limitations indicate the need for more advanced aerial platforms, known as aerobots, specifically designed to meet the rigorous demands of future Mars missions. Next generation aerobots must be capable of carrying larger scientific payloads, flying over greater distances, and withstanding the harsh conditions of the Martian environment. Developing such aerobots presents significant engineering challenges, particularly in lift generation, power management, and thermal control.

The unique atmospheric conditions on Mars pose one of the most significant challenges to rotorcraft design. The planet's thin atmosphere, with its low air density, necessitates generating substantially more lift to achieve flight. This requirement drives the need for larger rotors or higher rotor speeds, which subsequently increases power demands. Additionally, although Mars' gravity is only about 38% of Earth's, it still requires that the aerobot's structure is robust enough to withstand the stresses of flight, particularly during landing on rough terrain. Achieving an optimal balance between lift generation and structural integrity is critical in the design of Martian aerobots. The design of Martian aerobots is further constrained by the need to fit within the spacecraft aeroshell used for transport to Mars. The aeroshell's size limits the dimensions of the rotorcraft, particularly the rotor blades, which must either be compact enough to fit within the aeroshell or designed to fold and deploy after landing. This constraint necessitates innovative design solutions, such as foldable rotor blades or compact rotor configurations, to optimise the aerobot's performance while adhering to the size limitations imposed by the aeroshell. These design

challenges require a systematic approach to the conceptualisation and optimisation of rotorcraft configurations, ensuring that the final designs are both feasible and capable of meeting mission objectives.

This thesis addresses these challenges by advancing the design of aerobots for Mars exploration. The research builds on the foundational work of the Ingenuity Helicopter and other aerial concepts, proposing new rotorcraft configurations optimised for the Martian environment. The study focuses on the design and analysis of rotor systems—such as single, dual, quad, and hexarotor configurations—to identify the most efficient and effective designs for future Mars aerobots. The exploration of different rotorcraft configurations is based on a comprehensive parametric analysis rooted in simplified rotorcraft momentum theory. This analysis evaluates the power requirements of various rotorcraft designs during different flight phases, including hover, vertical climb, and forward flight. The study examines factors such as rotor disk diameter, power loading, and the impact of aerodynamic interference between rotors to determine the overall benefits of different rotorcraft configurations and propose suitable designs for further investigation. For instance, the research considers the power efficiency of conventional single main rotor designs compared to more complex configurations, such as coaxial rotors, tandem rotors, quadcopters, and hexacopters. Preliminary findings suggest that while single main rotor designs may be simpler, they are less efficient in terms of power consumption and payload capacity compared to multirotor configurations. Among the multirotor designs, hexacopters have demonstrated superior stability, redundancy, and power efficiency, particularly when designed to operate within the constraints of the aeroshell size.

The goal of this research is to develop aerobots that can significantly enhance the capabilities of Mars exploration missions. By providing a versatile and mobile platform for scientific investigations, these advanced aerial systems have the potential to enable new areas of research, support the identification of future landing sites, and facilitate the in-situ study of Mars' most remote and challenging terrains. The findings of this thesis are expected to contribute to the development

of next-generation Mars aerobots, capable of supporting more ambitious missions with enhanced scientific payloads, greater range, and improved operational flexibility. This work represents a critical step in advancing planetary exploration technologies, with the aim of enabling the scientific community to explore and study Mars more comprehensively and efficiently.

In summary, the research systematically addresses the design challenges associated with Martian aerobot configurations and optimises their performance, contributing to the advancement of planetary exploration technologies. The development of aerobots that can operate reliably and efficiently in Mars' unique environment is crucial to the success of future missions, enabling a more thorough and effective exploration of the Red Planet.

1.2 Research Gap, Aim and Objectives

1.2.1 Research Gap

Mars exploration has predominantly relied on landers and rovers, which, while successful, are limited in their ability to access the planet’s diverse and challenging terrains. This restriction has left vast areas of scientific interest unexplored. Aerobots offer a promising solution by enabling access to difficult and varied regions of Mars. However, the design and development of aerobots capable of sustained flight in Mars' thin atmosphere face multiple challenges. These include adapting to the planet's low-density atmosphere, ensuring energy efficiency, maintaining structural resilience in extreme conditions, and accommodating the size constraints imposed by the aeroshell used for deployment. Furthermore, there is a lack of systematic frameworks to guide the evaluation and optimisation of aerobot designs under these constraints. Martian rotorcraft designs in literature can be broadly classified into two categories: conceptual designs without feasibility validation and high-fidelity mission-specific studies. Conceptual studies propose novel configurations but lack detailed practicality assessments, while high-fidelity studies provide rigorous performance evaluations but are computationally intensive and limited to specific configurations, restricting broader applicability. Addressing these interconnected challenges is essential for advancing Mars exploration capabilities.

1.2.2 Aim

This research aims to develop a scalable conceptual design framework for an aerobot capable of sustained flight in Martian challenging atmospheric conditions, that bridges the exploratory strengths of conceptual studies with the practicality of high-fidelity analyses with a focus on identifying optimal rotorcraft configurations and accommodating deployment size constraints.

1.2.3 Objectives

To achieve the specified aim, the research is structured around the following objectives:

1) Conduct a literature review and identify research gaps in the domain of Martian aerial robot designs.

2) Develop a conceptual sizing framework to evaluate and compare different rotorcraft configurations under the environmental conditions of Mars and the constraints imposed by the aeroshell used in deployment.

3) Conduct a detailed parametric analysis of rotorcraft configurations to identify the most viable design in terms of power efficiency, lift capacity, and operational feasibility in the Martian atmosphere.

4) Produce a preliminary design and specifications for the aerobot, ensuring it meets the operational requirements for sustained flight and fits within the size constraints of a Mars mission aeroshell.

1.3 Contribution to Knowledge

This research makes contributions to the field of Martian exploration and aerospace engineering through the following:

1) Based on the conducted literature analysis, the proposed novel **Strategic Design Framework** in Chapter 2 introduces the Mars Aerobot Design Thinking Matrix, a strategic and systematic methodology for guiding the development of aerobots specifically adapted to the harsh and unique

conditions of Mars. This matrix assists in making key design decisions such as mission type (reusable or disposable), power sources, take-off mechanism and dependency on other systems (rover/lander or independent), ensuring that aerobot configurations are optimised for specific mission challenges. By integrating environmental factors (like atmospheric pressure and topography) and operational constraints, the matrix enhances the reliability and effectiveness of aerobots, making them better suited for future Mars exploration missions.

2) The proposed **Generalised Methodology** in Chapter 3, including the customised application of simplified momentum theory, enables the estimation of power requirements for Martian rotorcraft. This methodology is adapted to Mars' unique atmospheric and gravitational conditions, providing an efficient and practical way to calculate power consumption for various flight segments. By facilitating trade-off analyses between rotorcraft configurations, the methodology helps optimise rotor size and power efficiency, supporting more effective early-stage design decisions for aerobots. This technique complements the broader strategic design framework, described in Chapter 2, enabling mission-specific adaptations for future Mars exploration missions.

3) The **Comprehensive Parametric Analysis of Martian Rotorcraft Configurations** in chapters 3 and 4, is the application of the generalised methodology and the strategic design framework developed earlier. Chapter 4 extends the performance analysis by applying it to a range of rotorcraft configurations, including single, coaxial, tandem, quadcopter, and hexacopter designs. This detailed parametric analysis evaluates power requirements for different flight segments (hover, vertical climb, forward flight) under Martian conditions. The results demonstrate that hexacopters offer the best balance between stability, payload capacity, and power efficiency. By integrating the power estimation methodology with practical rotorcraft design optimisation, this contribution enhances the ability to make informed, mission-specific design decisions, further supporting the early-stage design process for Martian aerobots.

4) The created **Martian Rotorcraft Design Variants** for tandem, quadcopter, and hexacopter configurations set within the planetary transport size constraints, in Chapters 3 and 4, provide viable options for future Martian rotorcraft. These designs offer a practical foundation for further development, optimising rotorcraft performance for Mars missions.

1.4 Thesis Structure

This thesis is presented as a thesis by publication, comprising a series of interconnected research papers that contribute to the principal aim of advancing the design and optimisation of rotary VTOL aerobots for Mars exploration. Each of the main chapters (Chapters 2, 3, and 4) is structured as a stand-alone research publication, complete with its own literature review, methodology, results, and discussion. Although each chapter is self-contained, they collectively build upon one another to form a coherent and comprehensive study.

Chapter 2 includes a particularly extensive literature review, which contextualises the research within the broader field while establishing the scientific and technical constraints of Martian exploration. A key contribution of this chapter is the introduction of the Mars Aerobot Design Thinking Matrix, a novel framework that integrates environmental constraints, mission requirements, and design considerations to guide the systematic development of aerobots for Mars. Building upon this foundation, Chapter 3 develops a systematic methodology for the preliminary design of rotary VTOL aerobots within a structured framework using an example case study, integrating adapted rotorcraft momentum theory to estimate power requirements and assess feasibility under Martian conditions. Chapter 4 then applies this methodology to a parametric analysis of multirotor configurations, identifying optimal designs based on power efficiency, lift capacity, and operational feasibility. Finally, Chapter 5 concludes the thesis by summarising key findings and outlining recommendations for future research, including refinements in aerodynamic modelling, experimental validation, and advancements in power and autonomy for Mars aerial missions.

The rationale behind the thematic focus of this PhD thesis, titled Conceptual Design of Martian Aerial Robots, is visually summarised in Fig. 1.1. This figure

systematically illustrates the foundational questions driving the research, progressing from broad scientific objectives to specific technical challenges, while highlighting how each "why" question serves to justify critical decisions made throughout the theses and addresses a key research gap. Starting with the broad objectives of space exploration and the selection of Mars as a prime target, the figure narrows down to the specific design and operational needs of Martian aerobots. Chapter 2 discusses the importance of space exploration and Mars' significance, while also exploring how aerobots can navigate Mars' terrain more efficiently than rovers. The development of specific design frameworks in Chapters 2 and 3 addresses the lack of tailored guidelines for Martian aerobots. Chapters 3 and 4 then focus on the choice of solar-powered rotary VTOL systems, filling the gap for efficient, reusable systems in Mars' thin atmosphere. Finally, the parametric analyses in these chapters provide streamlined methods to quickly optimize rotorcraft designs. This dual perspective shows how specific technical solutions are guided by broader scientific goals, with each chapter of the thesis addressing different aspects of the overarching research problem.

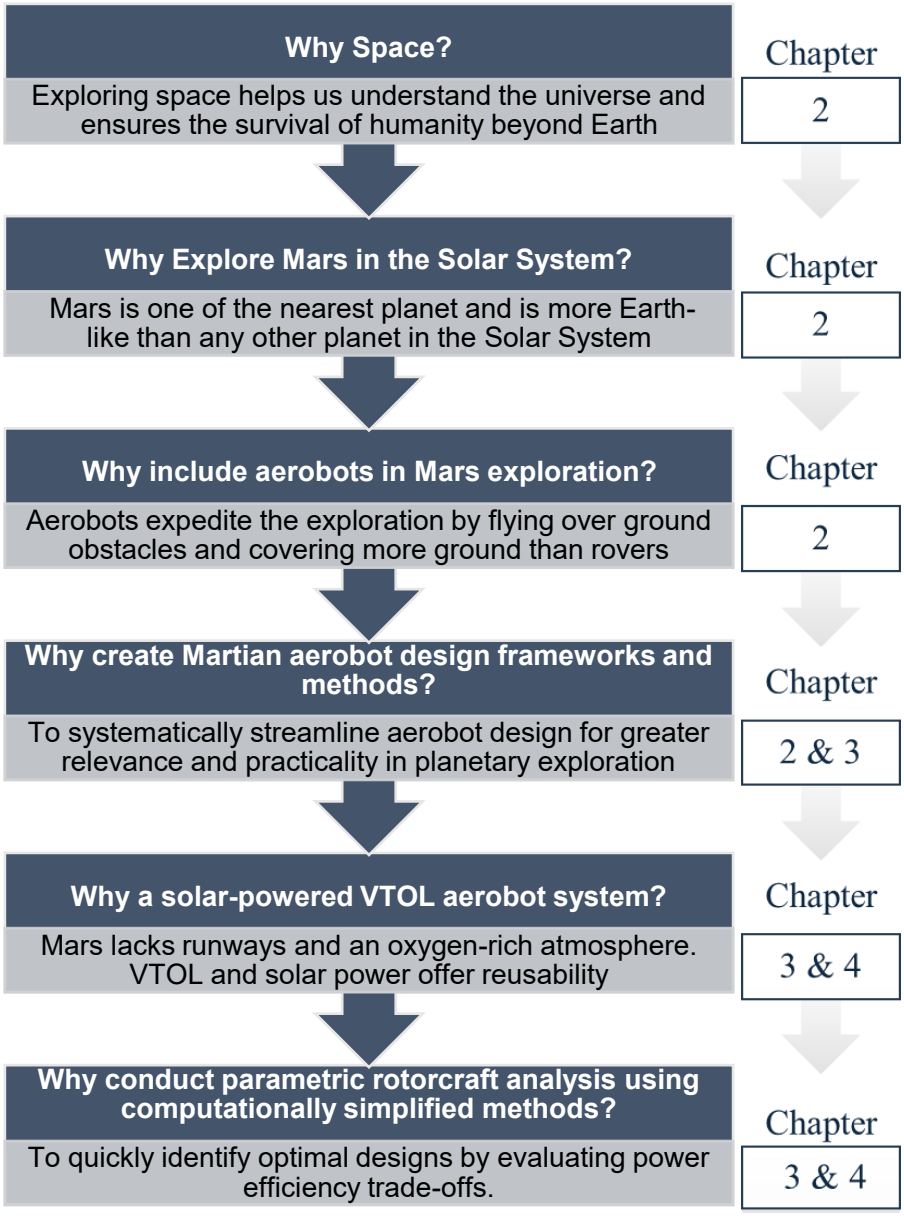


Fig. 1.1 Six whys and rationale for the PhD Thesis theme 'Conceptual Design of Martian Aerial Robots

1.4.1 Chapter 1: Introduction

This chapter establishes the foundation for the thesis by providing the necessary background and motivation for the research. It discusses the significance of Mars exploration and the limitations of existing surface-bound technologies, such as landers and rovers, which are constrained by their inability to traverse diverse and challenging terrains. The chapter identifies the critical research gap in the current technologies, particularly the need for aerial robotics capable of operating

in Mars' harsh environment. It then articulates the primary aim and objectives of the research, which focus on developing a comprehensive design framework for rotary VTOL aerobots optimised for Martian conditions. The chapter concludes by outlining the contributions to knowledge and providing a brief overview of the thesis structure.

1.4.2 Chapter 2: Mars Planetary Insights and Design Framework for Future In-Situ Aerial Robotic Missions

This chapter provides a detailed exploration of the environmental conditions on Mars, such as atmospheric composition, gravity, and temperature variations, all of which significantly influence the design and operation of aerial robots. It begins with a comprehensive literature review that situates the research within the broader context of Mars exploration and addresses the current technological challenges. Beyond the literature review, the chapter discusses critical planetary insights that inform the aerobot design process, including the impact of dust storms, surface topology, and potential landing sites. The chapter also introduces the Mars Aerobot Design Thinking Matrix, a novel framework developed to systematically incorporate these planetary conditions into the design process of aerial robots. This matrix is one of the key contributions of the thesis, offering a structured approach to designing aerobots that are optimised for Mars' unique environment. Additionally, the chapter presents various case studies and hypothetical mission scenarios to demonstrate the practical application of the matrix, highlighting how it can be used to develop aerobot designs that are both innovative and mission-ready.

1.4.3 Chapter 3: Systematic Methodology for the Preliminary Design of Future Rotary VTOL Martian Aerobots

Building on the foundation established in Chapter 2, this chapter introduces a comprehensive framework specifically for the Preliminary Martian Rotary VTOL Aerobot Design Methodology. This framework is crucial for systematically guiding the design process of rotary VTOL aerobots, addressing the unique challenges posed by Mars' thin atmosphere and low gravity. The chapter begins with a targeted literature review that explores the theoretical foundations of helicopter

momentum theory and discusses the necessary modifications to adapt it to Martian conditions. The core of the chapter is dedicated to developing and applying this framework, which encompasses a parametric analysis of various rotorcraft configurations—such as single-rotor, coaxial, and tandem systems. These configurations are evaluated for their power efficiency, lift capacity, and suitability for the Martian environment. Rotary VTOL systems are chosen due to their ability to operate without runways and their potential for reuse in multiple missions, making them ideal for Mars' diverse and challenging terrain. The findings from this chapter guide the selection and optimisation of the most promising designs, providing a solid methodological foundation for further refinement in the subsequent chapters.

1.4.4 Chapter 4: Parametric Analysis of Multirotor Aerobot Configurations for Mars

This chapter focuses on the parametric analysis of multirotor configurations, specifically quadcopters and hexacopters, which are valued for their stability and redundancy in the harsh Martian environment. Through several case studies, the chapter evaluates the performance of these configurations under Mars-like conditions, including power requirements during critical flight segments such as hovering, vertical climbing, and forward flight using the method developed in chapter 3. The analysis reveals that hexacopter configurations, particularly those with non-overlapping rotors, offer superior performance in terms of power efficiency and payload capacity. The chapter also addresses the practical challenges of deploying these systems on Mars, such as the need for folding mechanisms to accommodate larger rotors within the aeroshell. The insights gained from these studies are critical for refining aerobot designs, ensuring they meet the rigorous demands of future Mars exploration missions.

1.4.5 Chapter 5: Conclusion and Future Work

This final chapter outlines the key findings from the thesis, providing a concise summary of the research conducted in Chapters 2, 3, and 4. It reflects on the broader implications of these findings for Mars exploration and aerial robotics, reinforcing the importance of the Mars Aerobot Design Thinking Matrix and the

optimised rotorcraft configurations developed throughout the thesis. The chapter concludes with recommendations for future research, addressing the limitations identified in the study and proposing directions for further advancement in the field. This chapter ensures that the thesis concludes with a clear and forward-looking perspective, guiding future innovation in planetary exploration technologies.

1.5 Key Assumptions for Problem Definitions

This research rests on several core assumptions regarding Martian atmospheric properties, aerobot propulsion and autonomy, and the spacecraft packaging constraints. Outlined below, these assumptions set the scope of the study and reflect practical realities derived from existing planetary mission data and technologies.

1) *Applicability of Momentum Theory:* Simplified helicopter momentum theory, adapted to Mars's low-density conditions, can reliably estimate power requirements for hover, climb, and forward flight. While compressibility effects at high rotor tip speeds may arise, corrective factors keep early-stage predictions sufficiently accurate for conceptual design. Higher-fidelity aerodynamic tools remain a possible next step.

2) *Autonomous Navigation Requirement:* A ~20-minute one-way communication delay necessitates an aerobot capable of executing pre-programmed flight paths and real-time hazard avoidance without continuous Earth-based oversight. This level of onboard autonomy includes sensor-based obstacle detection and failsafe protocols for in-flight anomalies.

3) *Battery-Electric Power Source:* The aerobot utilises a battery-electric powertrain in this study, recharged primarily by solar panels. This choice reflects both heritage from prior technology demonstrators (e.g., Ingenuity) and the relative simplicity of battery-based power storage on Mars, where nuclear or other energy alternatives are more complex or restricted.

4) Battery Performance in Extreme Temperatures: Lithium-ion batteries are assumed to sustain an high energy density (~230 Wh/kg in this study) under typical Martian ambient temperatures (−40°C to −20°C). Thermal management systems (insulation, heaters) are assumed in the design for the aerobot performance evaluation, to mitigate cold-induced capacity loss, acknowledging minor mass/power trade-offs for these systems.

5) *Environmental Stability During Flight:* Short-duration flights (on the order of minutes) allow the assumption of stable atmospheric conditions in density, wind, and temperature. Any significant transient phenomena (e.g., global dust storms) suspend flight operations rather than requiring complex real-time adjustments. The aerobot must still function across a wide thermal range (−153°C to +20°C) and withstand periodic dust exposure and elevated radiation levels.

6) *Rotor Interaction Simplification:* In overlapping rotors in such as coaxial or tandem configurations, aerodynamic interference is approximated using empirical correction factors drawn from terrestrial rotorcraft statistical data. These factors strike a balance between model simplicity and accuracy for initial trade-off studies, with more refined models reserved for advanced design phases.

7) *Size and Deployment Constraints:* The aerobot must fit within a spacecraft aeroshell (of 4.5 m diameter in this study), as used in current Mars EDL missions. Folding or retractable rotors are essential to meet these packaging constraints. Although future heavy-lift vehicles could support larger aeroshells, the thesis scope aligns with near-term technology.

8) *Mission Architecture Context:* The aerobot operates either independently or in tandem with surface assets (e.g., rovers) to augment science data collection. It can carry sensors for site surveys, imaging, or atmospheric sampling, but it does not replace the functionality of larger ground-based platforms. Command and telemetry paths may involve an orbiter or lander as an intermediary.

9) *Short-Duration Flights per Sol:* Flight durations are generally limited to a few minutes, primarily by battery capacity and thermal factors. Frequent short sorties enable recharging cycles, repeated data gathering, and incremental mapping of terrain. Scheduling flights around peak solar availability and local weather forecasts maximises operational efficiency.

1.6 List of Research Outputs

1.6.1 Journal Papers – Peer Reviewed

- Youhanna, V., Felicetti, L., & Ignatyev, D. (2024). Mars planetary insights and design framework for future in-situ aerial robotic missions. Advances in Space Research - manuscript targeted at for publication. (chapter 2)

5) Youhanna, V., Felicetti, L., & Ignatyev, D. (2024). Systematic methodology for the preliminary design of future rotary VTOL Martian aerobots. Acta Astronautica. Manuscript accepted for publication, in press. https://doi.org/10.1016/j.actaastro.2025.01.059 (chapter 3)

- Youhanna, V., Felicetti, L., & Ignatyev, D. (2024). Parametric analysis of multirotor aerobot configurations for Mars. MDPI Aerospace- manuscript targeted at for publication. (chapter 4)

1.6.2 Conference Papers – Peer Reviewed

Throughout the course of this research, several conference papers were published and presented, contributing to the dissemination of the findings and receiving valuable feedback that helped refine the work, particularly in the journal papers presented in Chapters 3 and 4. Below is a list of the key conference papers, along with a brief overview of their content and the impact they had on the research development.

- Youhanna, V., Ignatyev, D., Felicetti, L., (2022). Futuristic Martian Aerobot Design. In: *UKRAS22 Conference "Robotics for Unconstrained Environments" Proceedings*, 64-65. doi: http://doi.org/10.31256/Ec2Na5W

This short paper introduced a foldable rotary VTOL winged aerobot concept for Martian exploration. The insights from this work played a key role in guiding the later research, particularly in developing methods to identify the most efficient and optimal configuration within the constraints of the aeroshell used for transporting spacecraft beyond Earth.

- Youhanna V, Felicetti L & Ignatyev D (2023) Parametric analysis of battery-electric rotorcraft configurations to fly on Mars. In: *Aerospace Europe Conference Joint 10th EUCASS - 9th CEAS Conference 2023, Lausanne, 9-13 July 2023.* DOI: 10.13009/EUCASS2023-319

  This paper performed a parametric analysis on the hover and vertical flight capabilities of single, tandem, and isolated rotors. It provided insights into the performance of different rotorcraft configurations, helping refine power efficiency and rotor size considerations for Mars exploration.

- Youhanna V, Felicetti L & Ignatyev D (2024). Conceptual Design Study based on Defined Parameters for Next Generation Martian Rotorcrafts. In: *IEEE Aeroconf 2024, Montana, US, 2-9 March 2024.* DOI: 10.1109/AERO58975.2024.10521441

  In this paper, the analysis was expanded to include the forward flight segment, providing a more comprehensive understanding of rotorcraft performance across various flight modes. This broadened scope contributed to a deeper exploration of the capabilities of rotorcraft for Martian missions.

- Youhanna V, Felicetti L & Ignatyev D (2024). Preliminary Investigation into Future Martian Multicopter Configurations. In: *Vertical Flight Society's 80th Annual Forum & Technology Display, Montréal, Québec, Canada, May 7-9, 2024.* DOI: 10.4050/F-0080-2024-1266

  This paper introduced a quadcopter case alongside dual and single rotor configurations. The inclusion of multiple configurations demonstrated a more diverse and adaptable approach to rotorcraft design for Mars, improving the understanding of multicopters capabilities.

- Youhanna V, Felicetti L & Ignatyev D (2024). Preliminary Design Exploration of Prospective Multirotor Aerobots for Mars. In: *34th Congress of the International Council of the Aeronautical Sciences (ICAS 2024), Florence, Italy*, September 9-13, 2024.

  This paper introduces a hexacopter configuration, further advancing the previous designs. This addition significantly enhances stability, payload capacity, and power efficiency, marking a key step in optimising rotorcraft for Mars exploration.

- Youhanna V, Felicetti L & Ignatyev D (2024). Systematic Selection of the Next Generation Martian Rotorcraft Configurations. *In: 75th International Astronautical Congress (IAC 2024), Milan, Italy,* October 14-18, 2024.

  This paper intends to introduce systematic selection framework (chapter 2) of the next generation Martian aerobot configurations along with the application of such framework (chapter 4) to the space community. The shortlisted rotorcraft configuration from the previous study is further mechanically developed and presented.

- Youhanna V, Felicetti L & Ignatyev D (2024). Parametric Analysis of Rotary VTOL Aerobot Design Configurations to Fly on Titan*. In: 75th International Astronautical Congress (IAC 2024), Milan, Italy,* October 14-18, 2024.

  This paper performed a parametric analysis on the hover and vertical flight capabilities of rotorcraft configurations such single, coaxial, tandem, isolated rotors and quad in the environmental conditions of Titan (Saturn's planet). The paper intends to introduce the versatility of the parametric study methodology developed for Martian aerobots in this thesis. By updating planetary parameters such as air density and gravitational acceleration, the framework and methodology can be applied to other atmospheric environments.

References

[1] NASA. (2024) Mars Helicopter - NASA Mars. Retrieved April 22, 2024, from https://mars.nasa.gov/technology/helicopter/#Flight-Log

2 Mars Planetary Insights and Design Framework for Future In-Situ Aerial Robotic Missions[2]

Vishal Youhanna, Dmitry Ignatyev, Leonard Felicetti

Faculty of Engineering and Applied Sciences, Cranfield University, UK

Abstract:

This paper presents a comprehensive framework for the design and deployment of aerobots as a pivotal tool for future Mars exploration. The Martian environment, characterised by its thin atmosphere, extreme temperature fluctuations, and challenging topography, poses significant obstacles to traditional ground-based exploration robots such as rovers and landers. Aerobots, with their ability to navigate diverse terrains and conduct in-situ scientific investigations, offer a transformative approach to overcoming these challenges. Through a detailed analysis of past Mars missions, this paper identifies the key scientific objectives driving current and future exploration, including the search for biosignatures, understanding Mars' climate and geology, and preparing for human exploration. The research integrates advanced aerospace engineering principles, including aerodynamics, materials science, and autonomous systems, to develop aerobots capable of sustained operation in Mars' harsh conditions. This paper underscores the importance of adaptive design, robust structural integrity, and precise mission planning in enhancing the efficacy of aerobots, thereby expanding the possibilities of Mars exploration. By addressing the complex relationship between Mars' environment and aerobot design, this work contributes to the advancement of planetary exploration technologies, paving the way for more ambitious and scientifically rewarding missions.

2 This is an adapted version of the article targeted at Advances in Space Research journal for publication: Youhanna, V., Felicetti, L., & Ignatyev, D. (2024). Mars Planetary Insights and Design Framework for Future In-Situ Aerial Robotic Missions

Keywords: Mars Exploration, Planetary Science Mission, Martian Drones, Aerobots

2.1 Introduction

The exploration of Mars represents one of the most ambitious scientific endeavours of the 21st century, driven by a profound curiosity about the potential for life beyond Earth and the desire to understand the history and geology of our closest planetary neighbour. As Earth's closest neighbour, with conditions that might have once supported life, Mars presents unique challenges and opportunities for scientific discovery. Over the decades, numerous missions have been launched to study Mars. These missions have revealed the planet's dynamic history and its current state as a cold, dry world with a thin atmosphere and frequent dust storms. Interplanetary missions to Mars are characterised by their high stakes and inherent risks, requiring not only advanced technological solutions but also an in-depth understanding of the Martian environment. The success of these missions hinges on the ability to design and develop exploration tools that are both robust and precisely adapted to the planet’s extreme conditions.

Traditional Mars exploration has relied heavily on landers and rovers, which, while successful, are limited in their ability to traverse diverse and challenging terrains. Future missions seeks to explore more of Mars' surface, particularly its less accessible regions, autonomous aerial robots (aerobots) become essential. Aerobots can overcome the limitations of ground-based exploration by providing aerial surveys, accessing difficult-to-reach areas such as steep cliffs, deep canyons, and cave entrances, and covering large distances more quickly. They can also serve as scouts for future manned missions, gathering critical data on potential landing sites and environmental conditions. The ability to conduct in-situ scientific missions from the air makes aerobots a crucial component of future Mars exploration strategies. However, designing aerobots for Mars is a complex project that demands careful consideration from the earliest stages of development. The success of NASA's Ingenuity helicopter, the first powered flight

on another planet, demonstrated the feasibility of aerial exploration in Mars' thin atmosphere, paving the way for more advanced aerial platforms.

This paper presents a comprehensive framework for the design, development, and deployment of aerobots in future Mars missions, integrating insights from past explorations with advanced aerospace technologies to address the unique challenges posed by the Martian environment. It bridges the gap between aeronautics and planetary science, emphasising the necessity of thoroughly understanding the Martian environment: captured in the metaphor that one must imagine breathing on Mars before planning to fly on Mars. This concept underscores the importance of aligning aerobot designs with Mars' specific challenges, ensuring they are not only theoretically feasible but also practical, mission-ready, and capable of withstanding the planet's harsh conditions. The existing literature often presents innovative concepts for Mars exploration, yet many of these fail to address the practical challenges of deployment on the planet. This paper tackles this issue by providing a scientifically grounded framework designed to ensure that future aerobot designs are both innovative and operationally viable. By examining the influence of Martian topography and climatology on aerobot performance, it offers a systematic approach to meet the rigorous demands of Mars exploration. The Mars Aerobot Design Thinking Matrix, introduced in this work, serves as a strategic tool for refining aerobot design, taking into account the atmospheric, topographical, and climatological challenges unique to Mars, and ultimately ensuring mission success. This integrative approach not only aids mission planners and engineers but also advances our broader understanding of Mars, facilitating more effective exploration strategies and driving significant advancements in Mars exploration technology.

The paper is structured as follows. The Section 2.2 discusses the broader context of planetary exploration, emphasising the importance of Mars in the pursuit of scientific knowledge and technological advancement. The subsequent section (2.3) outlines the scientific objectives of Mars exploration, including the search for life, understanding the planet's climate and geology, and preparing for future human exploration. This is followed by an exploration of how Mars' diverse

topography (Section 2.4.1) influences the design and operation of aerobots, with an emphasis on the need for mission-specific adaptations. The discussion then moves to the impact of Mars' surface features on the mechanical design of aerobots, highlighting the challenges posed by the planet's varied terrain. The influence of Mars' climate (Section 2.4.2), including its thin atmosphere and extreme temperature variations, on the performance and reliability of aerobots is examined next. The paper then provides a detailed analysis of the practical aspects of designing and deploying aerobots on Mars (Section 2.5), including materials, autonomous operation, and delivery systems. Finally, the paper introduces a structured approach to aerobot design through the Mars Aerobot Design Thinking Matrix (Section 2.6), which helps balance the various engineering and operational challenges associated with Mars missions. This structure ensures a comprehensive understanding of the role of aerobots in Mars exploration, offering valuable insights for future mission planning and technology development.

2.2 Comprehending Planetary Exploration Development

Planetary exploration is a fundamental scientific vocation that enhances understanding of the solar system and addresses profound questions about the origins of the universe, the potential for extraterrestrial life, and Earth's place in the cosmos [1]. This pursuit drives technological innovation, inspires the next generation of scientists and engineers, and fosters international collaboration, uniting global efforts to expand the frontiers of knowledge [2]. The continued development of planetary exploration programs not only advances scientific insights with significant societal implications but also prepares for sustainable human presence in space, essential for future exploration and survival beyond Earth [1],[2].

Appreciation for past and ongoing planetary missions is critical, as each mission has contributed to an evolving understanding of planetary environments, surface conditions, and atmospheric dynamics. These efforts have shaped technological advancements that enable further exploration. In particular, Mars has remained a primary target due to its potential for past habitability, the presence of water in

various forms, and its similarities to early Earth. The motivation to explore Mars extends beyond scientific curiosity, as it represents a stepping stone for future human exploration and interplanetary travel. Understanding the complexities of the Martian environment, including its geology, climate, and atmospheric constraints, is essential for designing aerial robotic systems capable of operating efficiently in such conditions.

This section examines the historical evolution of planetary exploration, particularly the comparative exploration of Mars and Venus, and the lessons learned from past missions. It then discusses Mars' exploration history in detail, highlighting key scientific findings and technological advancements that shape the future of aerial robotic systems. These discussions reinforce the core objective of this thesis: developing an aerobot optimised for Martian conditions. By analysing planetary exploration development, the section establishes a clear link between past missions and the technological advancements necessary for integrating aerobots into future planetary missions.

2.2.1 Earth's Two Neighbours – First to Most Explored

Earth is surrounded by two adjacent planets, Venus and Mars. Despite Venus being the closest and often labelled as its twin, it is surpassed by Earth's second nearest neighbour, Mars, in terms of human curiosity and passion for planetary exploration. Though Mars, for now, holds the record of being the most explored planet besides Earth [3], Venus is the first-ever planet to be closely observed by a spacecraft in 1962 – NASA's Mariner 2 Flyby – that provided substantial data about its atmosphere and surface [4]. Later, the Soviet Union's Venera program took the lead in sending the first-ever successful planetary probe, lander, and lander/orbiter missions to Venus [5]. The beginning of Venus' exploration soon led to the observation that its hostility towards alien bodies increases as one moves closer to its surface, as the longest any spacecraft has survived its functionality on the planet's surface is 127 minutes – a record that is held by Venera 13 lander which is also the first spacecraft to capture coloured pictures of Venus' surface and sound on another planet in March 1982, Fig. 2.1 [6].

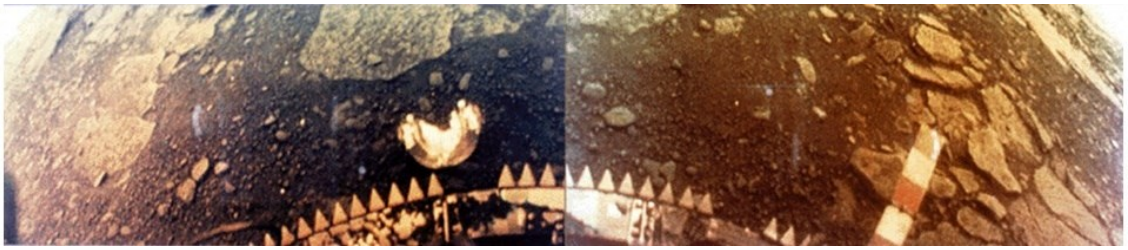


Fig. 2.1Colour picture of the surface of Venus from the Venera 13 Lander. Image credit: NASA/NSSDC (ID -VG00261,262)

In shape and size, Venus looks like Earth, but there are far more dissimilarities between the two planets that make them the opposite twins of each other [7]. Being the hottest planet in the Solar System, it sustains an average surface temperature of 464 °C due to intense volcanic activity and a dense atmosphere rich in carbon dioxide and sulphuric acid, which generates atmospheric pressures up to 92 bar, creating an environment that crushes and corrodes spacecraft [8],[9]. While no land rover has been sent to Venus, the first and only balloon aerostats ever deployed on any other planet were by two Soviet Vega spacecrafts in 1985. These transmitted data for 46 hours from around 50 km altitude, where conditions are more Earth-like, with temperatures ranging from 30 to 70 °C and atmospheric pressure equal to Earth's sea level [10]. These conditions could potentially host extremophile microbial life, sparking interest in future Venusian aerobot missions, although no such missions are currently planned [9]. For a future settlement of humans on Venus, besides the environmental challenges are a few more reasons that would make humans experience drastic disorientation. The rotation of Venus is extremely slow it takes 243 Earth days for it to complete one day, and its day is, in contrast, longer than its year which is 225 Earth days. The Sun sets in the east and rises in the west as it rotates backwards, and because Venus lacks a prominent tilt in its spin axis, one cannot experience perceptible seasonal changes [9]. For these characteristics of Venus and the challenges they bring along, planetary exploration preference has been shifted towards Earth's second-closest neighbour, Mars.

Planet Mars is about half the size and two-fifth the gravity with a total surface area equalling nearly all dry land of Earth. Much like Earth, its rotation on its axis takes 24.6 Earth hours which makes a Martian day, also called 'sol' [11]. Local

hours are 1/24th fraction of a sol and a year is 668.6 sols, almost double the Earth year due to Mars' larger solar orbit given its 1.5 times relative distance away from the Sun [11]. The planet completed its 37th Martian year on 26th December 2022, based on its calendar starting with the 0th Year in 1953 [12]. The temperature on Mars on average can vary from 20 °C to -153 °C [11], depending on the time of the sol, locality, and season. A Human on Mars can experience relief from the home-like four seasons, though longer and varied in length, caused by the planet's Earth-like tilted rotational axis. The current thin atmosphere is mostly Carbon dioxide, and the rest is nitrogen, argon, oxygen and water vapours [11]. Over 4 billion years ago Mars lost its global magnetosphere while replacing it with a phenomenon called the induced magnetosphere – caused by the interaction between its top atmosphere and solar wind – that triggered the continuous loss of its once-thick atmosphere into space, depriving the land of its water over time and leaving it exposed to higher cosmic radiation [13]. Microbial life as known on Earth has not yet been discovered by any of the current spacecrafts on the surface of Mars, but the promising ExoMars mission in 2028 (previously 2022) by the European Space Agency will carry Rosalind Franklin rover, equipped with the first-ever drill on wheels for digging 2 meters into the Mars ground to investigate its geology and signs of life [14]. Mars caves and lava tubes are natural shields against radiation and cold temperatures, that might be inhabiting Mars life and can also offer an underground residence for future Human settlers. The goal of sending humans to Mars by the 2030s was officially reiterated by the US governance in 2016, which has enticed people's interest, accelerated public-private sector partnerships to work on new space habitat technologies, and challenged researchers to bring innovative solutions for future Mars missions [15].

The exploration of Venus demonstrated the feasibility of long-duration atmospheric flight, as seen in the Vega balloon missions, despite the planet's extreme surface conditions. This contrasts with Mars, where its thin atmosphere poses significant aerodynamic challenges, requiring innovative lift solutions for sustained flight. Understanding these planetary differences is crucial for

developing aerobots optimised for Martian flight conditions, which will be discussed in detail in Section 2.5.

2.2.2 Standing on the Shoulders of the Giants – Mars Exploration History

Mars can be spotted from Earth as a reddish globe due to the colour of oxidised iron dust spread across its atmosphere that rises from its surface; but unlike Venus' opaque whitish thick atmosphere, Mars' atmosphere is less than 1% of what Earth has at sea level – giving the orbiting spacecrafts a visual advantage of mapping its surface [8],[11]. NASA's Mariner 4 Flyby became the first spacecraft in 1964 that had ever come closest to Mars and also was the first to take pictures of another planet in deep space [16]. This close observation led to exposing the popular misinterpreted theory of the existence of intelligent life and their giant irrigation canal systems on Mars – based on the astronomer Giovanni Schiaparelli's detailed map of the red planet that he drew in 1877 with the aid of a telescope in Italy, Fig. 2.2 [17]. The concept of a rational life living on Mars was further demystified when NASA's Mariner 9 orbiter performed the first detailed global mapping of the planet and its two moons; meanwhile grabbing the title of becoming the first spacecraft to orbit another planet in 1971[18],[19]. Two distinct features, Olympus Mons and Valles Marineris, later to be known as the wonders of the solar system that are high-interest regions for future in-situ scientific research missions, were discovered by the first orbiter [20],[21]. Olympus Mons is the largest shield volcano in the solar system; for comparison, it is about 3 times the height of Mt Everest and 100 times the volume of Mouna Lao on Earth. Valles Marineris, named to honour the Mariner orbiter, is the largest canyon of our solar system that delves around 8 km deep and is about the width of Australia [22].

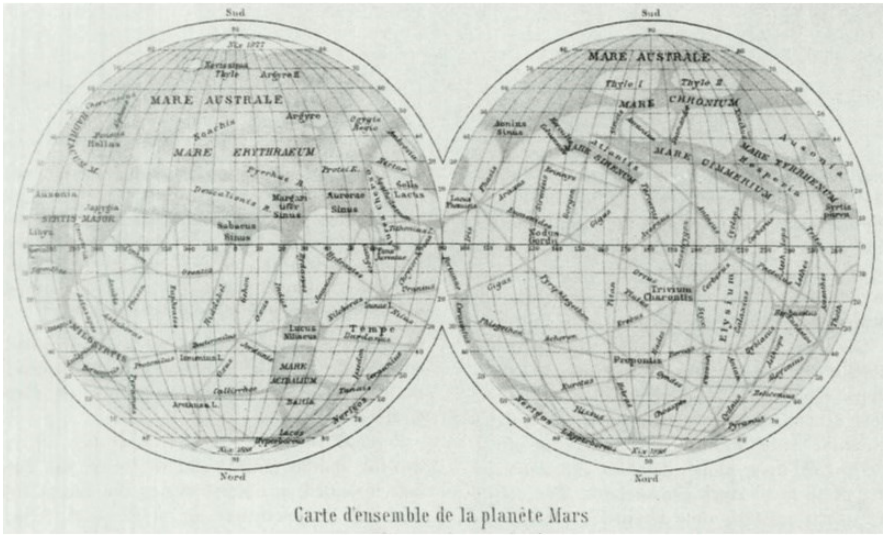


Fig. 2.2. Schiaparelli's 1877 surface map of Mars. (Image Source [17])

Another popularity of Mars is its dust storms; Mariner 9 when first reached the planet was welcomed by a global dust storm of a scale ever recorded that covered the entire globe as if it had mistakenly reached Venus, Fig. 2.3. Only the tips of the giant volcanoes are prominently visible from the orbit during global storms on Mars [17]. Consequently, the first orbiter took advantage of its reprogrammable software to delay the surface imaging of the red planet until the dust settled in the next couple of Earth months, marking the importance of adaptable software in space missions [17],[19]. This principle extends to Martian aerobots, which require autonomous decision-making capabilities to adjust flight paths and mission objectives in response to environmental conditions.

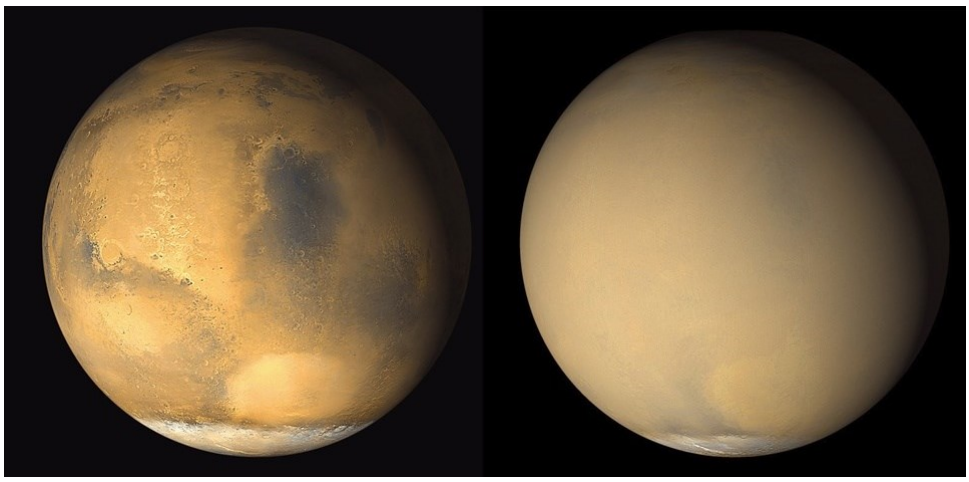


Fig. 2.3 (left) before and (right) after one month of the global storm in 2001 captured by NASA's Mars Global Surveyor orbiter. Image credit: NASA/JPL/MSSS (ID- PIA03170)

The Soviet's Mars 2 and Mars 3 were two ambitious spacecrafts carrying an orbiter and a rover secured inside a lander, that followed Mariner 9 after a couple of weeks; but due to the software inflexibility and limited fuel, their descent modules were ejected amidst the dust storm that led to their ill-fated instant death – still achieving the record of the first objects to impact and soft-land on Mars, respectively [23]. The Soviet Mars missions were the pioneers in deep space exploration, starting even a year before Venera Missions in 1960, nevertheless also were unduly unfortunate in their success rate due to multiple factors linked to individual missions [18]. However, the unavailability of sophisticated software yet again caused the loss of another Mars mission to the Soviets in 1988, when the control system lacking fail-safe features became a victim of human error and disoriented Phobos 1 spacecraft during the cruise phase; thus, shattering its objective of investigating the Martian moon, Phobos [23]. Landing on Mars is hard because its thin atmosphere is unable to provide the cushioning effect to slow down a spacecraft upon its entry, as experienced on Earth or Venus. Moreover, it takes about 5 to 20 minutes for a one-way signal to reach Earth from Mars and vice versa, depending on the planet's orbital orientation [24]. Often deemed as 7 minutes of terror for mission operators – the time it takes for a spacecraft to enter, descent and land (EDL) on Mars ground from its top atmosphere, cannot be controlled in real-time. Along with mechanisms such as aerobraking, heat shields, parachutes and thrusters to make EDL successful, it is of utmost importance that the autonomous capacity of the control systems is well matched. Lessons learnt in the past decades of Mars missions, both from the failures and successes, have advanced human expertise along with evolving technology to a level that in early 2021, China National Space Administration (CNSA) deployed one of its kind mission on Mars called Tianwen 1 – carrying an orbiter, landers and a rover [25].

The Martian environment offers challenges to the alien exploratory bodies, unlike the hostile ones of Earth's twin, which have been manageable by scientists to explore Mars the most. Viking 1, the first successful Mars lander, was launched

in 1975 to operate primarily for just over 90 Earth days to observe the red planet but lasted for around 6 and half years, Fig. 2.4 [26]. The record was further lifted by Opportunity, the Mars Exploration Rover B, which began its operation after landing on Mars in 2004 and could have continued to travel beyond 45 km if the global dust storm in 2018 had not left its solar panels incapable [27]. Such life expectancy of Martian terrestrial spacecrafts has led NASA to expand the primary operational duration of their recent Mars missions from days to a couple of Earth years, with the exclusion of Ingenuity – the first Mars aerobot launched in the Mars 2020 mission. A conservative approach, similar to the first successful rover Sojourner in 1997, was applied to the helicopter for being a technology demonstrator, with an allocation of about 30 days for the primary phase [28]. Ingenuity, with a forward flight velocity of 20 m/s but capped at a maximum of 2 m/s for energy efficiency [28], was in its operational phase of aerial scouting, until retiring in February 2024, to aid its mission companion Perseverance – the most advanced Martian rover with a top speed of 0.04 m/s on hard flat ground [29], that travelled over 27 km by mid-2024 since its landing in February 2021 [30]. Being the predecessor of Perseverance in terms of design, Mars Science Laboratory's (MSL) Curiosity rover comparatively has covered a distance of around 32 km in its career of around 12 years on Mars [31]. Relatively, Martian spacecrafts are slow by Earth transport standards but well achievers for planetary exploration. Ingenuity has become a step forward in increasing the pace of Mars exploration via aerial survey, and this pace can be further increased with the next-generation aerobot designs.



Fig. 2.4 First Colour Image from Viking Lander 1 of the Mars ground. Image credit: NASA/JPL (ID- PIA00563)

The historical evolution of planetary exploration underscores the growing need for high-mobility systems capable of overcoming terrain and atmospheric challenges. The next sections introduce a structured design framework that systematically addresses these constraints, ensuring that future aerobots are optimized for sustained Martian flight.

2.3 Comprehending Mars Exploration Science Goals and Requirements

Past, present and future space missions to Mars are guided by the detailed scientific goals, objectives, investigations, and priorities set by NASA's Mars Exploration Program Analysis Group (MEPAG) in its first published report of 2001. The document, updated biennially, represents a consentaneous statement of the Mars scientific community that has established the following four major scientific goals: 1. Life 2. Climate 3. Geology 4. Preparation for Human Exploration [32]. Liquid water is a necessary prerequisite to life on Earth, therefore 'following the water' traces has been a key strategy for the missions sent to Mars to search for evidence of biosignatures and habitability environment of ancient or present life. The initial selection of the landing sites is based on scientific merit but is finalised once the engineering constraints of the whole operation are matched [33]. The objective of understanding the Martian atmospheric characteristics for safe robotic and human spacecraft flight was first included under the Climate Goal of MEPAG 2005 report, but in later editions it was moved under the fourth Goal of Human Exploration to treat it as an engineering application rather than a scientific objective [34].

The Ingenuity Helicopter has significantly expanded the understanding of the flight characteristics of rotorcraft in the Martian atmosphere with multiple in situ demonstrations. Historically, the selection team has conservatively opted for plain terrains as landing sites for the past rover missions that offer smooth travel; for instance, Valles Marineris was shortlisted multiple times in the landing site selection process for both Curiosity 2012 and Perseverance 2020 rovers but has been continuously rejected despite its geological importance because of its harsh rocky surface and long traverse to the desired scientific points [33]. However,

these engineering safety constraints can be loosened to include challenging surfaces when the use of an aerobot is included in a Mars Mission [33]. Like aircraft on Earth, a reusable aerobot on Mars will not remain in continuous flight but will spend a significant amount of time on the ground. During this time, it may be stationed, recharging its batteries, conducting science experiments (if equipped with a dedicated payload), or moving with the aid of mobile landing gear. The red planet has a diverse landscape with local environmental variations, that though offers numerous opportunities for future in situ exploration missions but also demands a certain level of familiarity with its areography, a specific name for Mars physical geography, for the designing of a mission-specific Martian aerobot.

The design of the Martian aerobot must be adapted to the specific region targeted by the mission. Mars features a variety of potential mission zones, each with distinct territorial characteristics such as plains, highlands, polar regions, underground caves, steep hills, and deep valleys. The selection of a landing site begins with meeting engineering constraints, ensuring safe Entry, Descent, and Landing (EDL), and supporting the operational needs of the in-situ spacecraft. Once these criteria are satisfied, the focus shifts to identifying scientifically significant sites that align with the mission's scientific objectives and the four science goals established by MEPAG [34]. One effective way to understand the landing site selection process is by examining the engineering parameters and requirements, alongside the scientific objectives of recent Mars missions. For instance, the Mars 2020 mission's landing site, Jezero Crater, was chosen from a database of 55 candidates. It met all engineering constraints and was selected for its astrobiological significance, aligning with the scientific goals of the mission as outlined in Table 2.1. It summarises engineering constraints such as latitude range, elevation limits, landing ellipse size, terrain roughness, and atmospheric wind conditions, which ensured a safe and stable landing. Additionally, the table highlights scientific objectives, including geological diversity, astrobiological potential, sample collection opportunities, and considerations for future human exploration. These factors collectively influenced site selection to maximise both mission safety and scientific return.

Table 2.1 Summary of Mars 2020 mission landing site engineering constraints & safety criteria for sky crane-based EDL, and main scientific objectives [35]

Engineering Parameters	Landing Sites Requirements	Science Objectives		
Latitude	30°N to 30°S (due to surface thermal limitation)	Perform thorough in-situ science	Geology: Analyse the geological processes in a selected Martian area linked to ancient environments and diverse geology, indicating potential astrobiological importance.	Potential Sample Return: Collect scientifically chosen samples with documented context, highlighting astrobiological importance and site geological diversity.
Elevation	<-0.5km (Relative to datum)			
Landing Ellipse	≤16.0 km (West-East) 14 km (North-South)			
Rock Height	≤0.6 m			
Terrain Relief/Slopes	(length scale) 2-10 km: <20° 1-1000 m: ≤100 m relief			
Radar Reflectivity	Ka band reflective			
Load Bearing Surface	Not dominated by dust		Astrobiology: Evaluate the habitability of a historic Martian setting, examine materials conducive to preserving signs of life, and search for potential evidence of past life.	Human Exploration/ Technology: Aid in preparing for Mars human exploration by addressing key knowledge gaps
Atmosphere	Up to 25 m/s horizontal and 20 m/s vertical winds during EDL			
Surface Winds for Thermal Environment for Rover Science Operations	During Operation: < 15 m/s (steady) <30 m/s (gusts) Non-Operation (sleeping): < 40 m/s (steady)			

2.4 Martian Aerobot Science Missions Subject to Areography

The success of Martian aerobots relies on their ability to adapt to the planet's unique geography (areography), which directly shapes mission design, operational feasibility, and scientific return. This section explores how Mars' topography, climate, and environmental conditions impose constraints and opportunities for aerial robotic missions, emphasising the need for mission-specific adaptations to navigate the planet's diverse and often extreme terrain.

2.4.1 Mars Topography Influencing Aerobot Mechanical Design

Mars' topography, from vast plains to towering volcanoes and deep canyons, presents distinct mechanical and operational challenges for aerobots. This subsection examines how elevation differences, surface roughness, and geological features dictate design choices, including structural sizing, resilience,

and obstacle avoidance systems, ensuring aerobots can safely traverse and explore the varied landscapes of the planet.

2.4.1.1 Mars Global Topography

The global topography of Mars has a sharp contrast feature known as Martian Dichotomy, which depicts a division between the lowlands of the northern hemisphere and the highlands of the southern hemisphere with a ratio of 1 to 2, respectively, as mapped in Fig. 2.5 [36]. The geological age of the red planet is divided into 3 main timelines, namely: Noachian is 3.9 - 3.5 billion years (bn yrs) ago, Hesperian is 3.5 - 1.8 bn yrs ago, and Amazonian is 1.8 bn yrs ago to present. Southern highlands are the oldest surface that is heavily cratered and elevated, preserving the bombardment impacts of the Noachian period, whereas comparatively Northern lowlands are smooth and renewed by volcanic lava flows [37]. Like Earth, Mars has been assigned an areographic grid with its prime meridian passing through a point named Airy-0, inside a small crater Airy [38]. Similar to the concept of Earth's geoid, Mars has the zero elevation datum defined by its areoid, below where the oceanic water accumulated with thick atmospheric conditions in the past [39]. Notably, this datum encompasses the regions where successful Mars missions have landed, aiming to detect evidence of past or present life.

United States Geological Survey (USGS) has divided the surface of Mars into 30 cartographic quadrangles Mars Chart (MC) map each having a number and a name based on classical albedo features covering a specified array of latitudes and longitudes, used as a standard desktop reference, shown in Fig. 2.6 [40]. The major topographic and gravitational anomaly that covers about one-fourth of the planet's surface is the Tharsis bulge or rise (about 170° W to 40° W, -50° to 50°), which elevates up to 10 km above the surrounding terrain, excluding the giant volcanoes it embeds [41].

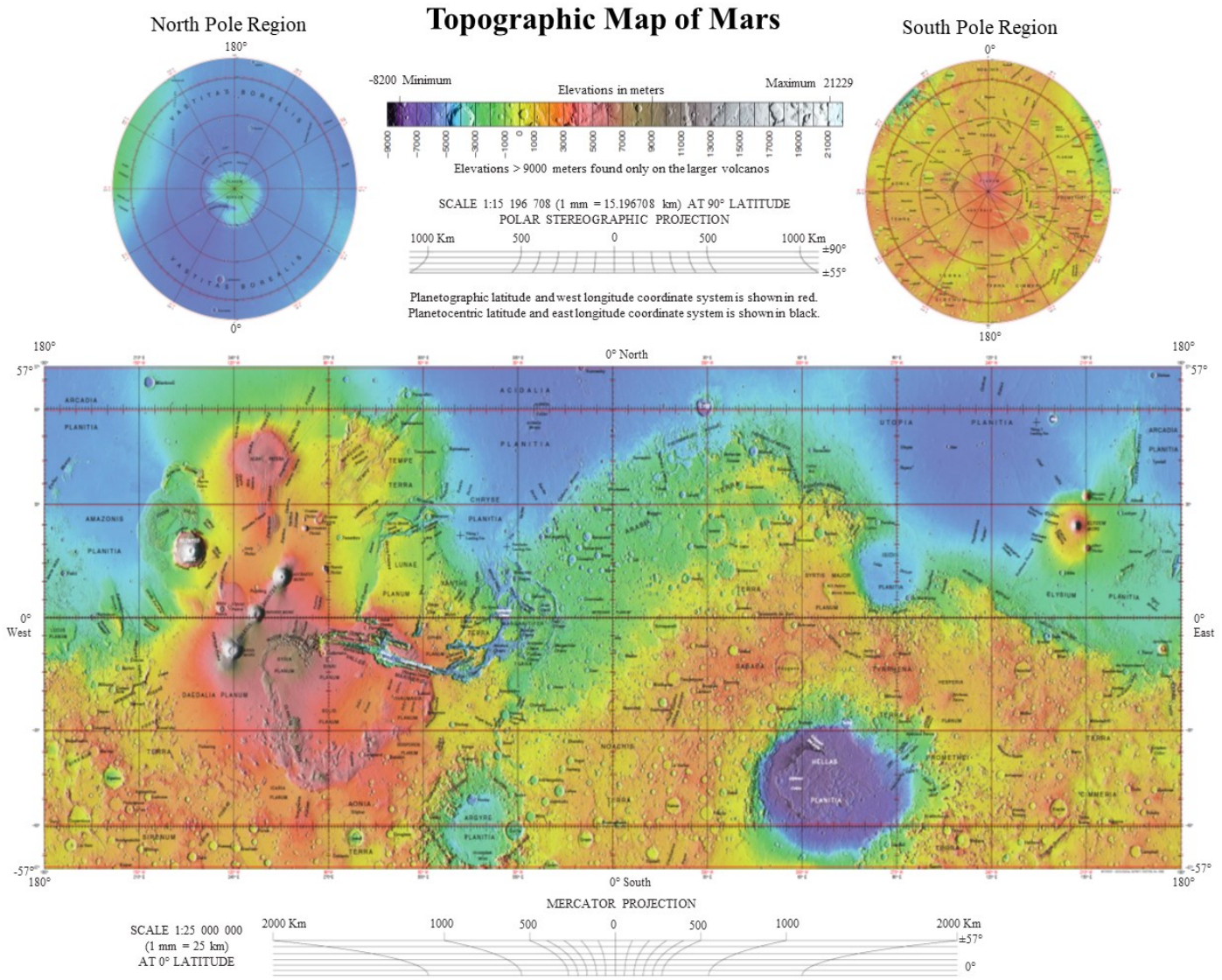


Fig. 2.5 Topographic Map of Mars - M 25M RKN, by USGS 2003 based on data from the Mars Orbiter Laser Altimeter (MOLA) an instrument on NASA's Mars Global Surveyor (MGS) [36]

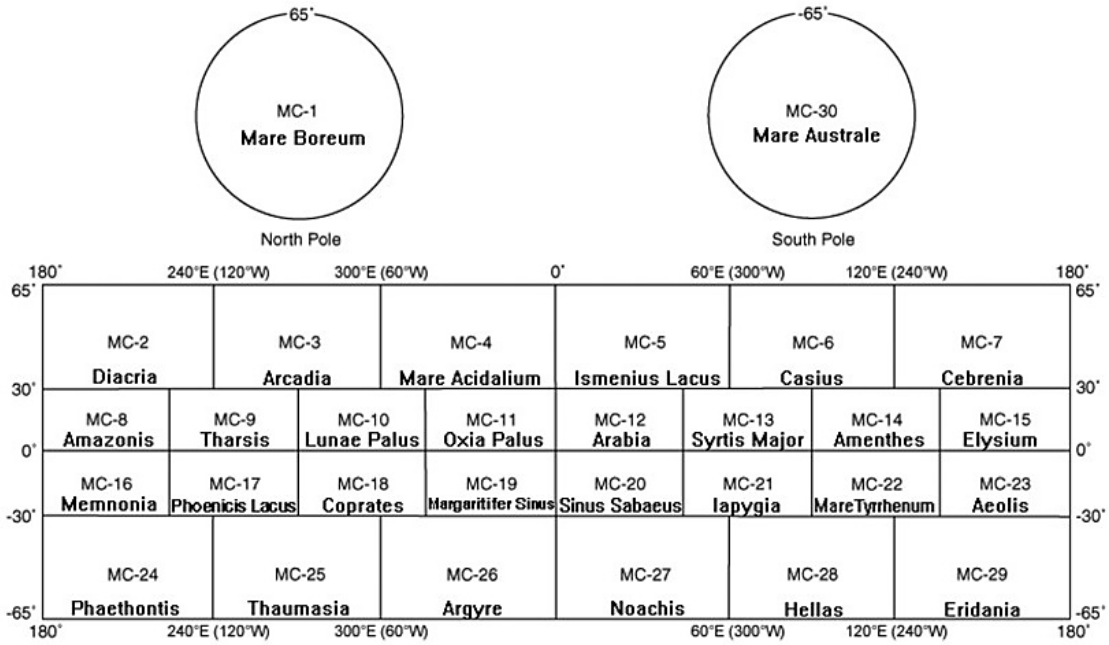


Fig. 2.6 Mars Cartographic Chart [42]

There is a generic distinctive difference of about 6 km in elevation from North to South which can be visualised as a slope of 0.036° in a slice run along the prime meridian, shown in Fig. 2.7 [39]. This elevation gradient affects atmospheric density variations, which influence aerobot flight performance, aerodynamic efficiency, and landing feasibility, making it a critical consideration for mission planning. Additionally, it highlights regions of scientific interest, such as transition zones between highlands and lowlands, which may hold clues to Mars' geological and climatic history.

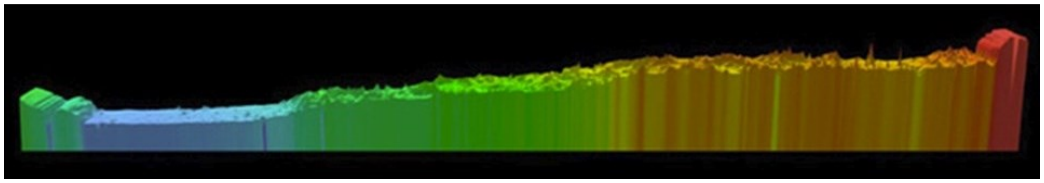


Fig. 2.7 Slice runs showing a slope of 0.036° from the north pole (left) to the south pole (right) at 0° Longitude. Image credit: NASA/MOLA Science Team

2.4.1.2 Mars Orders of Relief

Orders of relief is a 5-level scheme to capture the Mars landscape in a vivid mental map, analogous to the one of Earth, taught by the Department of Geography at California State University Long Beach [37]. The first order of relief

highlights the apparent global Martian Dichotomy, and the third order discusses the geological age history of the planet. Whereas the second, fourth, and fifth orders of relief manifest a descriptive flow from the largest planetary features to the regional and then to the small local features, as shown in the non-exhaustive chart list of Fig. 2.8. This hierarchical framework serves a dual purpose: it guides the design of mission-specific aerobots adapted to specific landing sites (e.g., high-power rotors for volcanic provinces) and informs the selection of optimal sites for pre-designed aerobots (e.g., avoiding boulder fields for compact rotorcraft). Fig. 2.9 further contextualises this relief classification by depicting real Martian topographic features, highlighting their impact on aerobot propulsion requirements for elevation changes, obstacle avoidance in rugged landscapes, and mission feasibility in complex terrain.

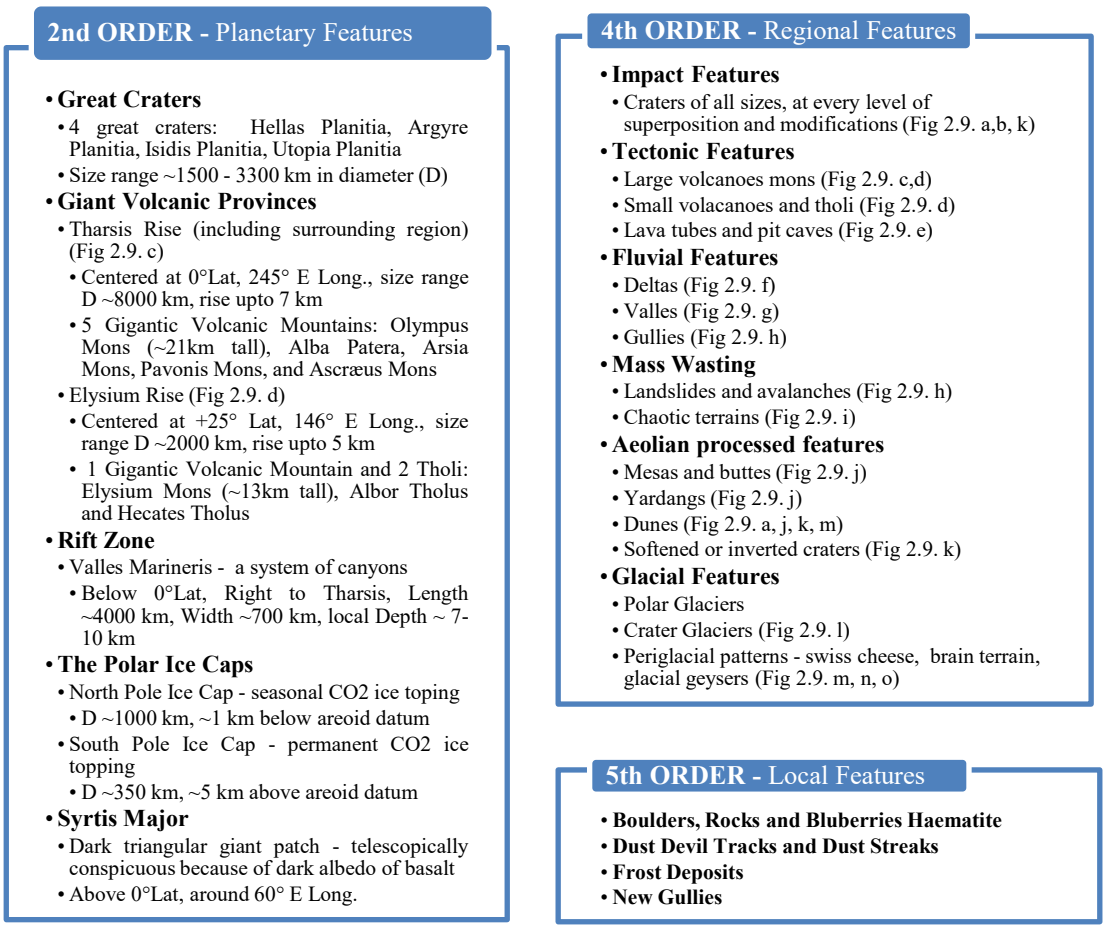


Fig. 2.8 A non-exhaustive chart list diagram of the 2nd, 4th and 5th orders of relief of Mars, based on [37]. Some features listed have picture examples shown in Fig. 2.9.

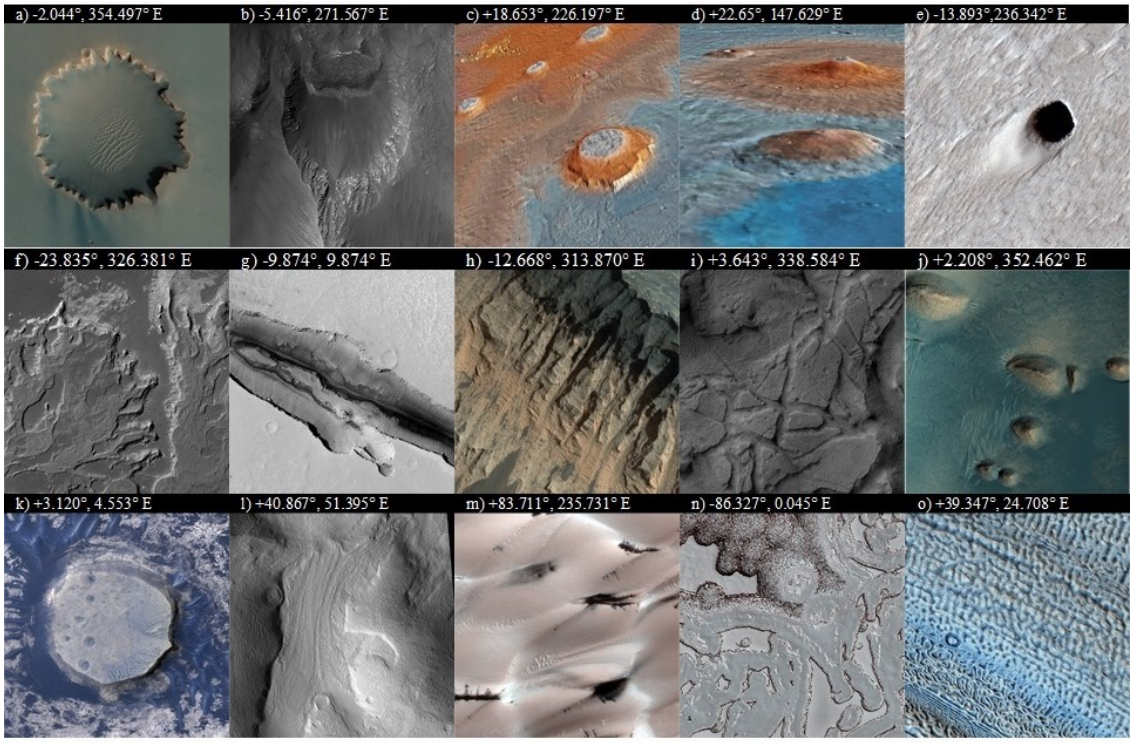


Fig. 2.9 Distinct topographic features and terrains of Mars with a potential for future science missions by aerial robots. Mars Reconnaissance Orbiter images are publicly accessible on the HiRISE web catalogue [44]. a) Victoria Crater at Meridiani Planum with scalloped shaped rim and floored with dunes (TRA_000873_1780). b) Non-circular 3 km impact crater on Tithonium Chasma's inclined wall (ESP_044998_1745). c) False coloured 3D rendered view of Olympus Mons, Arsia Mons, Pavonis Mons & Ascræus Mons. (generated in JMars5 (GIS) [45]) d) False coloured 3D rendered view of Elysium Rise showing Hecates Tholus (front), Elysium Mons & Albor Tholus. (generated in JMars) e) A pit crater about 50m across formed over an underground lava tube (ESP_065887_1660). f) Delta structure showing distributary network including lobes, inverted channels, & meander cutoffs in Eberswalde Crater (PSP_001336_1560). g) Cerberus Fossae East of the Head of Athabasca Valles (ESP_016216_1900). h) Gully-like landslides, including alcoves and channels, on the interior wall of Valles Marineris (ESP_022632_1670). i) Chaotic terrain of Aram Chaos showing rough floor topography with large, slumped blocks & fractures (PSP_008311_1835). j) Mesas, buttes & yardangs surrounded by sand dunes in Meridiani Planum (ESP_034129_1820). k) Inverted Crater and dunes in Arabia Terra (ESP_016459_1830). l) Alpine glaciers, common at middle latitudes (ESP_019213_2210). m) Dunes in the North covered primarily with ice, during

springtime get topped with dark sand streaks due to geyser-like eruptions of carbon dioxide (ESP_017043_2640). n) Swiss cheese terrain formed by circular & blob-shaped depressions at the South Pole due to the gradual ongoing sublimation of the CO2 ice layer (PSP_005095_0935). o) Brain terrain is icy lobate features, in the image layering a small hill (ESP_033165_2195). Images Credit: NASA/JPL-Caltech/UArizona (image id number next to each image caption)).

The fourth order of relief features of the region will be one of the key driving factors in determining the mechanical design of an aerobot for a Mars science mission. In contrast, the local features of the fifth order are less of a challenge for an individual aerial drone unless it is accompanied by a rover, as it can fly over obstacles such as rocks, boulders, soft sand deposits, or small gullies. Notable Mars mission landing sites over the past decade, including Utopia Planitia (Tianwen 1 Mission 2020), Jezero Crater (Mars 2020 Mission), Elysium Planitia (InSight Mission 2018), and Gale Crater (MSL Mission 2012), share similarities in surface flatness and local roughness with Chryse Planitia (+22°, 312° E), the landing site of the Viking 1 lander in 1975 (Fig. 2.4) [18]. Although Mars 2020 mission incorporated two new technologies, Range Trigger and Terrain Relative Navigation, for a precision landing in rougher terrain [43], near-future missions are likely to continue favouring flatter sites for safer landings until high-resolution mapping of riskier but scientifically desirable regions is completed. This conservative approach highlights the importance of endurance and speed in aerobot designs, as they must be capable of flying from the landing site to the desired operational area. It also suggests that the primary function of next-generation drones will be to produce high-resolution maps of unexplored Martian terrains.

On Mars, various terrains are observed that contain multiple relief features of the 4^{th} order. Fretted terrain is one such region that lies on the Martian Dichotomy, shaping a sharp transition between lowlands and highlands by featuring 1 to 2 km high cliffs standing on the smooth flat land, covered with several mesas, buttes, and yardangs [46]. A series of mensae can be seen in Fig. 2.5, forming the fretted terrain along the border; however, part of Aeolis Mensae is covered by another distinctive collection of features called Medusae Fossae Formation

(MFF) that starts at the south of Olympus Mons, surrounding the equatorial region. MFF is hypothetically a soft layered field of volcanic ash, wrapped with yardangs, ridges, and grooves; also labelled as the single largest source of global dust on Mars [47]. In contrast to the fretted terrain is the chaotic terrain, probably the most challenging for in situ exploration, featuring a rough floor landscape enveloped with a patterned mesh of large blocks, hills, and fractures, Fig. 2.9i. A network of chaotic terrains exits at the outflow channel region of Valles Marineris, Fig. 2.5, leading to speculation that the origin of such rough landform came from a catastrophic burst of water from the surface in Martian history [46]. Numerous pit craters, also called skylight caves such as in Fig. 2.9e, are spotted on the surface of volcanic provinces that open into undiscovered underground lava tube terrains of Mars – an exploratory mission demanding bespoke sophisticated aerobot designs. Thousands of high-resolution stamp images of Mars topography are publicly accessible through the HiRISE program, captured from the telescopic camera mounted on the Mars Reconnaissance Orbiter since 2006 [44]. Most of these regional features discovered can be compared to the similar naturally occurring features on Earth, to simulate design mission scenarios for Martian aerobots. However, the Martian atmosphere, which is subject to Mars' global and regional climate, is the other key driving factor in defining the aerodynamic design of such aerobots.

2.4.1.3 Mars Gravity Anomalies

Mars' average surface gravity acceleration is 3.73 m/s² [48], approximately 38% of Earth's gravity. However, it varies significantly due to the planet's uneven topography and internal structure. The latest NASA's Goddard Mars Model-3 (GMM-3) free-air gravity map, with a high resolution of 120 km, displays detailed gravitational anomalies across Mars [49]. This map supports identifying stable geological regions and avoids hazardous terrains such as cliffs and large boulders, while also revealing potential subsurface features like lava tubes and ice deposits, which is crucial for selecting safe landing sites for future in-situ spacecrafts missions [49]. This map enhances spacecraft navigation and landing precision on Mars, allowing mission controllers to plan descent and landing trajectories more accurately.

The gravity map quantifies gravitational variations in milliGals, a unit of acceleration (Gal=0.01 m/s²), with most anomalies falling within ±500 mGal and only the major volcanic regions resulting in higher gravity anomalies [50]. The variations from average gravity, though less than 1%, are significant enough to impact the design and planning of Martian aerial missions. In Mars' low-gravity, thin-atmosphere conditions, even minor gravitational differences can affect flight dynamics, causing deviations in flight paths and increased energy consumption, making precise calculations crucial for mission success.

The GMM-3 map enhances the design and performance of aerial robots for Martian exploration by providing high-resolution, location-specific gravitational data, which is crucial because the weight of an aerobot directly depends on the gravitational force at a given location, affecting its flight dynamics. This data can support precise navigation and control systems, enabling real-time adjustments to flight paths, altitude, and speed, with onboard sensors integrating GMM-3 data to enhance responsiveness to gravitational variations through adaptive algorithms. Particularly for long-range Martian aerobots, the map can improve flight stability by enabling gravity compensation, adjusting lift and propulsion according to local gravity changes, and helping design optimal flight paths to enhance energy efficiency and reduce system wear. It can also aid in selecting safe landing and takeoff sites by identifying areas with minimal gravitational anomalies and ensures accurate scientific measurements by allowing real-time calibration of onboard instruments.

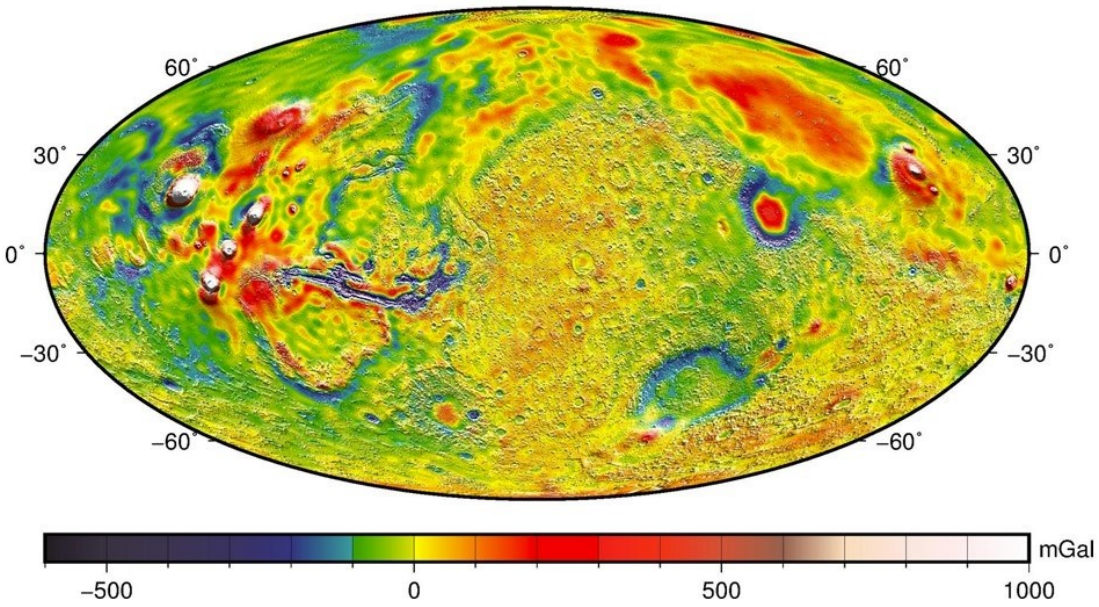


Fig. 2.10 NASA's Goddard Mars Model-3 (GMM-3) free-air gravity anomaly map. (mGal=0.00001 m/s²). Image: NASA/GSFC [49]

2.4.2 Mars Climatology Influencing Aerobots Performance

The Martian climate, characterised by a thin atmosphere, extreme temperature fluctuations, and frequent dust storms, profoundly impacts aerobot performance. This subsection analyses how atmospheric density, wind patterns, solar irradiance, and radiation levels influence power requirements, flight stability, and operational endurance, underscoring the need for robust environmental adaptability in mission planning.

2.4.2.1 Orbital Mechanics Driving Martian Environment

The orbital and axial characteristics of Mars significantly shape its climate and atmosphere. Present Mars shares a similar obliquity to Earth, resulting in four yearly seasons. The Martian calendar comprises 12 months ranging from 46 to 67 sols each, based on solar longitude (Ls) which is a measure of the eccentric orbital position of Mars from the Sun. Each month spans 30° of Ls, with seasons changing every 90° interval, starting from the Northern Hemisphere's Spring equinox (Ls=0°), as illustrated in Fig. 2.11 [51]. Orbital eccentricity, a dimensionless parameter (0 for circular, 0-1 for elliptical orbits), quantifies orbit deviation from circularity. Mars' orbital eccentricity of 0.1 is significantly higher

than Earth's 0.02 [48], leading to substantial variations in insolation as Mars orbits the Sun. Elliptical orbits are characterised by perihelion (closest point to the Sun) and aphelion (farthest point), with the planet moving faster at the former and slower at the latter, as described by Kepler's Second Law. Unlike on Earth, this variation creates a significant seasonal asymmetry between the red planet's hemispheres: the southern hemisphere's spring (142 sols) and summer (154 sols) are shorter, but more intense, whereas the northern spring (194 sols) and summer (178 sols) are longer, but milder [37]. These unique orbital characteristics create distinct environmental conditions, such as seasonal temperature variations, atmospheric pressure fluctuations, wind patterns, and dust activity, across Mars' surface throughout its year. These factors directly influence aerobot lift generation, flight stability, power efficiency, and navigation, requiring adaptive flight control strategies and energy management systems to ensure reliable operation in varying environmental conditions.

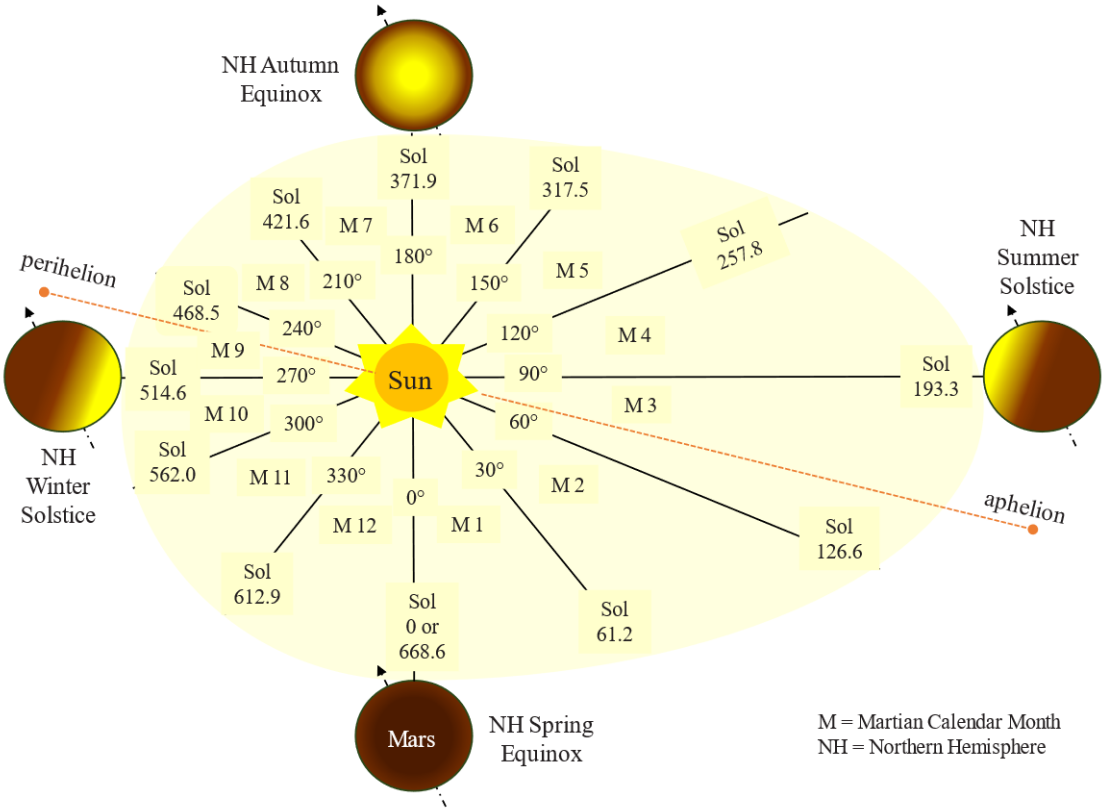


Fig. 2.11 Mars positions in the solar orbit. Illustration not to Scale.

Mars' surface temperature averages -73 °C [52] globally, with significant variations from 20 °C to -153°C [11]. The coldest temperatures occur in the polar regions during winter, while the warmest in the southern subtropics when Mars is closest to the Sun. In the tropical regions, diurnal temperature variations can exceed 100°C in a single day [52]. Mars's surface atmospheric pressure varies with elevation such that the pressure in the deepest crater Hellas Planitia averages 14 mbar whereas the pressure at the top of Olympus Mons is 0.7 mbar [53]. Around the areoid datum (Mars sea-level), the average pressure is approximately 6.1 mbar [39], which is about 0.6% of Earth's sea-level pressure, fluctuating by 60% annually due to seasonal variations compared to a 20% variation on Earth [37]. This happens because Mars' polar caps display pronounced semiannual variations in pressure, with deeper minima observed during southern winter compared to northern winter. Driven by Mars' orbital eccentricity, this asymmetry is influenced by the dynamics of carbon dioxide gas, which is 95% of the Martian air composition [48]. During southern winter, CO_2 freezes onto the south polar cap as temperatures drop below negative 123 °C, reducing global atmospheric pressure by 25-30% [53]. This cycle reverses during southern summer raising the global pressure to the highest during the process. This process reverses during southern summer, causing a rise in global pressure to its highest point. These seasonal changes in mass at the poles also result in minor temporal variations in the gravity field. Despite seasonal changes, polar caps persist year-round but with differing compositions. During Martian summer, the north pole's CO2 frost sublimes to reveal a water ice cap, whereas the south pole maintains its CO_2 frost cover, creating compositionally different polar caps [52]. Clouds of water and CO_2 ice form over polar regions during winter, with CO_2 snow detected by NASA’s Phoenix lander in year 2008, which sublimated before reaching the surface [53]. These drastic atmospheric pressure, temperature and composition variations necessitate aerobots to adapt to changing lift and drag conditions throughout their missions. For instance, lower atmospheric pressure during southern winter reduces lift generation, requiring higher rotor speeds, while extreme temperature changes demand robust thermal management systems to maintain operational stability throughout their missions.

2.4.2.2 Mars Atmospheric Structure

Mars has a vertical atmospheric structure similar to Earth's but lacks a stratosphere layer due to the absence of ozone (O_3), which is typically found between the troposphere and mesosphere [37][52]. The Martian troposphere, where most weather phenomena occur, extends up to approximately 45 km above the surface - about three times higher than Earth's [37]. Within this layer is the planetary boundary layer (PBL), the lowest and most dynamic level, characterised by dominant atmosphere-surface interactions and significant influence from local topography [54]. Understanding the PBL is crucial for predicting environmental conditions, ensuring mission safety, optimising aerobot design, and navigating the challenges of Mars' diverse terrain and atmospheric conditions during spacecraft EDL and aerobot operations [53]. Likewise, aerial robots can provide high-resolution data on the Martian atmosphere, particularly within the PBL, contributing to our understanding of Mars' climate and surface-atmosphere interactions. This capability is critical for refining atmospheric models, predicting dust storm behaviour, and optimising future mission designs, as ground-based instruments and orbiters often lack the spatial and temporal resolution needed to capture fine-scale dynamics in the PBL. The following subsections within this discussion explore key atmospheric characteristics that influence aerobot performance, including boundary layer turbulence, wind patterns, and air density variations.

2.4.2.2.1 Planetary Boundary Layer

The planetary boundary layer, which influences heat, momentum, and mass exchanges between the surface and the atmosphere, directly impacts flight conditions, sensor operations, and mission planning. The PBL significantly impacts Martian weather and climate across various scales, with effects amplified by the planet's thin, clear atmosphere, where changes in surface temperature and drag have disproportionately large effects due to the atmosphere's low thermal and dynamical inertia [54]. During the day, the PBL experiences intense convection, with plumes and vortices rising to 10 km and exhibiting a dry adiabatic lapse rate of 4.3 °C/km, the rate at which the temperature of air without moisture decreases with altitude [52]. In contrast, the average lapse rate on Mars is lower

(about 2.5 °C/km) due to suspended dust particles that absorb solar radiation and heat the air [52]. At night, convection diminishes, and radiative cooling creates a stable shallow PBL, primarily influenced by turbulence generated near the surface [54]. The PBL tends to be deeper over elevated terrain due to stronger surface-atmosphere interactions and increased solar heating, causing increased turbulence and complex wind patterns [54].

The dynamics of the PBL have has direct implications for the Mid-Air Deployment (MAD) concepts being proposed for the next generation of Martian science rotorcraft [55]. Unlike traditional landers, which require flat terrain for touchdown, MAD systems allow rotorcraft to be deployed from an aeroshell at low altitudes (a few hundred meters above the surface), minimising the risks associated with Mars' thin atmosphere, reduced aerodynamic braking efficiency, and high-impact landing forces. This method is particularly advantageous for reaching highland regions over 5 km above datum, where steep slopes, rough terrain, and unstable ground make conventional landing nearly impossible. By bypassing these challenges, MAD enables rotorcraft to begin operations in locations that were previously inaccessible, significantly expanding the range of scientific exploration on Mars.

2.4.2.2.2 Winds

Wind shear and turbulence within the PBL pose challenges for maintaining stable flight. The atmospheric circulation on Mars is less complex than on Earth, mainly due to the absence of oceans. In the equatorial regions, atmospheric pressure on Mars is relatively lower due to solar-induced convective uplift, while the cold polar areas exhibit higher pressures resulting from air subsidence over the caps [37]. This leads to Hadley circulation (or cell) at low latitudes, where heated air rises near the equator, moves poleward to approximately 30° latitude, descends, and returns equatorward [53]. This process generates surface winds predominantly from the northeast in the northern hemisphere and from the southeast in the southern hemisphere, while at higher latitudes, polar air masses interact with Hadley cells to create weather fronts and storms [53]. Generally, wind velocities on Mars vary seasonally, ranging from 2-7 m/s in summer to 5-10

m/s in fall [48]. When winds exceed 17 m/s, these can lift and transport sand and fine rock particles, potentially leading to dust storms with speeds reaching up to 30 m/s [48][56]. However, despite these high wind velocities, the force exerted would feel like a light breeze to human perspective, due to Mars' thin atmosphere [57].

2.4.2.2.3 Air Density

The key parameter upon which most of the aerodynamic calculation of the aircraft depends is the air density at which it will typically fly. The air density on Mars is much lower than on Earth. Earth's sea-level air density is approximately 1.225 kg/m³, while Mars' average air density at the surface is only about 0.020 kg/m³, less than 2% of Earth's [48]. This low density poses significant challenges for generating lift, necessitating larger rotor blades or wings for aerial vehicles to achieve flight on Mars. This 0.020 kg/m³ value reflects an overly optimistic atmosphere condition because the regional air density depends on the location, and altitude from the datum (sea level) and varies across seasons and times of the day. One of the methods for determining the air density involves a more specific approach based on NASA's Mars atmospheric mathematical model, which considers altitude effects and consists of separate equations for the lower atmosphere (<7 km) and the upper atmosphere (>7 km). In both zones, the temperature decreases linearly, and the pressure decreases exponentially with respect to the change in altitude. By inserting the desired altitude (*H*) value, measured above the ground, into Eq. (2.1) and Eq. (2.2), both temperature (T) and pressure (p) can be calculated, respectively. Different values of constants a and b are used in equations for the lower and upper atmosphere zones in Eq. (2.1) to determine temperature. Air density (ρ) is then calculated using Eq. (2.3) by inputting the corresponding values of temperature and pressure.

$$T_{\text{Celsius}} = -a - bH\,, \tag{2.1}$$

$$p = p_0 \mathrm{e}^{-H/H_0}\,, \tag{2.2}$$

$$= \frac{p}{R(T_{\text{K}})}, \tag{2.3}$$

where $T_{℃}$ $(\mathrm{Celsius})$ is the temperature on the Celsius scale; H (m) is the altitude from the ground; p (kPa) is the atmospheric pressure; ρ $(\mathrm{kg/m^3})$ is the air density; a $(℃)$ is a temperature intercept constant (=31 ℃ when H<7000 m; =23.4 ℃ when H >7000 m); b $(℃/\mathrm{m})$ is a lapse rate constant (=0.000998 $℃/\mathrm{m}$ when H<7000 m, =0.00222 $℃/\mathrm{m}$ when H >7000 m); $p_0(\mathrm{kPa})$ is a reference pressure constant (=0.699 kPa); H_0 (m) is an atmospheric scale height constant (=11111.1 m); R $(\mathrm{kJ/kg/K})$ is a gas constant (=0.1921 $\mathrm{kJ/kg/K}$); T_{K} (K) is the temperature on the Kelvin scale ($= T_{\mathrm{Celsius}} + 273.15$)

The resulting values using NASA's Mars atmospheric mathematical model can be rather overly conservative estimates because although the model considers altitude effects, it does not account for atmospheric variations related to regional attributes such as datum level, seasons, and time of day.

The third technique for obtaining a more precise estimate of the local air density involves the utilization of the Mars Climate Database (MCD Version 6.1) software [58], a publicly accessible and reliable European-developed resource used in various aerobot design concepts, for instance as in Refs [59], [60]. Alternatively, the Mars Global Reference Atmospheric Model (Mars-GRAM) provides detailed atmospheric data, though it is primarily used by NASA and authorised collaborators [61]. These models require environmental input parameters, such as time of flight, to generate accurate density estimates. The MCD can present air density data output in two formats: a range presentation or distinct curves. Similarly, many other environmental parameters, including air viscosity data, can be extracted from MCD. Kinematic viscosity (=viscosity/density) influences the Reynolds number, a fundamental aerodynamic parameter used to predict flow characteristics over an aerobot’s surfaces. In Martian conditions, where air density is significantly lower than on Earth, the Reynolds number helps assess whether airflow remains laminar or transitions to turbulence, directly impacting propulsions systems efficiency, lift generation, and overall aerobot stability.

Fig. 2.12 generated using the Mars Climate Database (MCD v6.1) based on the average solar conditions for Martian climatology, serves as an example of key atmospheric parameters, including air density, viscosity, wind speed, and

temperature. These factors directly affect aerobot flight by influencing lift, drag, stability, and power requirements. Variations in density and viscosity impact aerodynamic efficiency, while wind speed affects flight control. Temperature fluctuations influence battery performance and material durability, making thermal management essential. Understanding these conditions helps optimise aerobot design for stable and efficient operation in varying Martian environments.

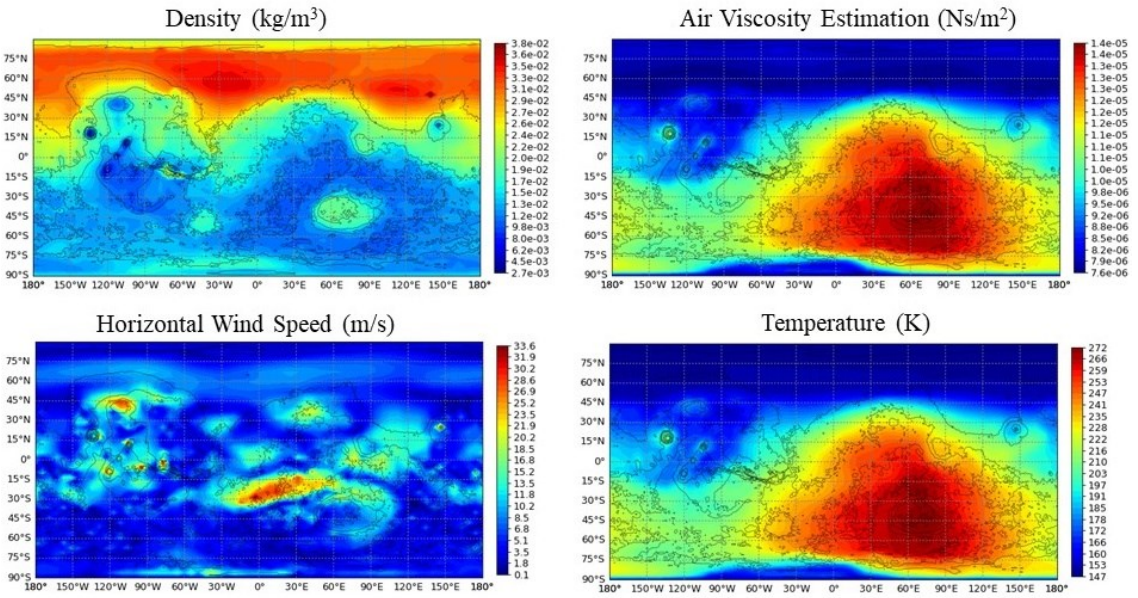


Fig. 2.12 The graphs show global environmental parameters on Mars at the altitude of 10 m above the local surface of Mars at Longitude 0° Local time 11:00 on Sol 514.6 (Ls 270) during the Northern Hemisphere Winter Solstice. The parameters a) Air Density b) Air Viscosity c) Horizontal Wind Speed d) Temperature are based on the climatology average solar scenario generated in MCD_v6.1 [58].

2.4.2.3 Martian Dust Effects

Mars experiences dust devils (area covering <10 m²) and dust storms (~10^6 m²) on daily frequency lasting for short periods, driven by strong daytime turbulence that stirs surface dust [37][52]. Dust devils, small swirling dust columns sometimes reaching altitudes over 12 km, are significantly larger and more vigorous than on Earth, occurring commonly during warm, clear afternoons [54]. While crucial in lifting dust into the atmosphere, they contribute less to global dust storms due to a negative feedback mechanism where increased atmospheric dust leads to surface cooling and reduced convection [54]. However, dust storms

create a complex environment where dust, radiation, temperature, and wind influence each other, occasionally escalating into regional (~10^6 km²) or global (>10^6 km²) events lasting for weeks and months, respectively [52]. These typically begin in the southern hemisphere during spring and summer, impacting sunlight and temperatures, which challenges solar-powered missions [54]. Overall, Mars' global atmospheric patterns are simpler and more predictable than those on Earth [57], with NASA's long-term temperature monitoring revealing consistent seasonal regional dust storms [62], which develops our understanding of the Martian climate and offers potential advantages for aerial robot operations.

Besides naturally occurring dust events, rotorcrafts on Mars can generate substantial dust clouds during flight operations. The Ingenuity helicopter lifted about 0.1% of its mass in dust per flight due to the Martian environment and dust properties, significantly more than terrestrial helicopters, which elevate dust up to 0.02% of their mass [63]. Larger rotary VTOL Martian aerobots are expected to lift an even greater proportion of dust relative to their mass. These dust clouds pose challenges for future rotary aerobot operations, including potential mechanical wear due to abrasive dust particles, potential clogging or degradation of moving parts, and reduced aerodynamic efficiency caused by dust adhesion on rotor blades and control surfaces.

The weathering and wind erosion of Martian rocks produce fine dust particles averaging around 3 microns, which can damage machinery by infiltrating non-sealed components, requiring robust protective measures essential for Mars aerial robots [56]. This is particularly critical for future crewed Martian aerial and ground vehicles, as inhaling dust containing harmful chemicals like silicates and oxychlorine compounds can cause serious health issues, including lung disease, cancer, and blood disorders [64]. This is one reason the Mars soil sample-return mission has been a key focus for NASA, ESA, and other global space agencies for over a decade, as it is essential for evaluating the planet's suitability for future human exploration missions [35].

Martian dust storms and dust devils are predicted to generate significant electric fields and potentially produce electric discharges, similar to those observed on

Earth, due to charge transfer during particle collisions and charge separation by atmospheric dynamics [54] [65]. These discharges are limited by the weak fields of the Martian atmosphere, which are about 20 kiloV/m compared to Earth's 3 MegaV/m [65]. In addition to dust storms, rotorcraft like Ingenuity Helicopter could create electrical phenomena on Mars through triboelectric charging, where friction between spinning blades and dust generates an electric charge, leading to small electric fields or faint glows around the rotorcraft [66]. On Earth, moist ground naturally dissipates electric charges, preventing large potential differences and electrical discharges. Whereas, the dry surface of Mars lacks this grounding, potentially allowing significant charge accumulation and electrical sparking, especially with fast-moving vehicles [67][68]. Historical observations revealed that rover wheels could accumulate significant electrical charges through ground friction, leading to the addition of ultrathin tungsten needles that concentrated the electric field, allowing the thin Martian atmosphere to ionize and safely discharge the charges [68]. The current discovery indicates that Martian static electricity does not impose a significant risk to the present spacecraft operations [65] [66], but future missions must account for its effects with robust shielding for electronics and communication systems, as little electric sparks could damage circuitry or trigger false signals in high-speed larger aerial vehicles, causing mission disruptions [67].

In addition to electrical concerns, Martian dust adhesion challenges aerobots as dust can adhere to surfaces majorly through electrostatic forces, with additional effects from magnetic attraction from minerals like magnetite in dust, and weak intermolecular van der Waals forces [67]. Dust accumulation on sensors and optical systems impairs visibility and data collection, affecting guidance, navigation, and control (GNC) by reducing sensor accuracy. Adhering to dust affects the aerobots' performance by altering aerodynamics and adding weight. Additionally, it accelerates wear on moving parts, raising the risk of mechanical failures, which impacts mission effectiveness and longevity. For solar-powered spacecrafts, such as the Insight lander and Opportunity rover, it significantly reduces solar panel efficiency, limiting power generation and operational time, especially during Martian winter. Similarly, the Ingenuity helicopter has

encountered power issues due to dust on its solar panels, including a loss of contact with Earth when dust covered its panels, reducing sunlight absorption and hindering battery charging [69].

2.4.2.4 Martian Radiation Effects

Radiation, the emission of energy as electromagnetic waves or moving subatomic particles, is a fundamental aspect of space environments that affects Mars, exposing it to two primary forms: particle radiation and electromagnetic radiation [67][70]. Particle radiation includes energetic particles that can penetrate deep into materials and biological tissues, such as the regular high-energy Galactic Cosmic Rays (GCRs) from outside the solar system, and the comparatively less energetic Solar Energetic Particles (SEPs) from the Sun, which occur irregularly during solar storms events [67]. The Sun experiences an approximately 11-year solar cycle that affects Mars' radiation exposure, with solar maximum increasing SEPs and suppressing GCRs due to the stronger solar magnetic field, while solar minimum allows more GCRs to reach the surface, increasing radiation levels [71]. Electromagnetic radiation spans a broad spectrum, including the damaging ultraviolet (UV) light, which primarily affects surfaces over prolonged time [70][72]. On Earth, the ozone layer filters out UV radiation, while the planet's magnetic field protects against particle radiation [13]. Mars, lacking these protective shields [13], is exposed to higher levels of harmful radiation, compounding the challenges for unmanned and manned missions, including material degradation, electronic failures, and increased health risks for human explorers [67][70][72].

Radiation poses significant risks to spacecraft electronics and materials, leading to effects such as Total Ionizing Dose (TID), displacement damage, and Single Event Effects (SEE) [71]. TID results from cumulative ionization over time, causing shifts in voltage thresholds and increased leakage currents, which degrade the performance of electronic components. Displacement damage occurs when energetic particles displace atoms, creating defects that impair devices like solar cells. SEE involves a single radiation particle causing temporary errors or permanent damage in electronic circuits, ranging from minor glitches to

complete system failures [71]. Ionizing radiation on Mars breaks down perchlorate salts into reactive compounds in the Martian regolith, accelerating corrosion in aluminium alloys commonly used in ground spacecraft by compromising protective oxide layers, especially when they are mechanically damaged [73]. Moreover, prolonged exposure to UV radiation can weaken the structural materials used in spacecraft, leading to a reduced lifespan of equipment [70][72].

To mitigate radiation risks, spacecraft often use aluminium shielding, although its effectiveness is limited by factors like weight constraints and the potential generation of secondary particles from the shielding itself [71]. Advanced alternatives under development, such as hydrogen-rich carbon fibre composites and hydrogenated boron nitride nanotubes, aim to enhance radiation resistance and durability in space environments[74]. Radiation Hardening Assurance is the process of designing, selecting, and testing space electronics to ensure they can withstand the harsh radiation environment, incorporating strategies like using radiation-hardened components, redundancy, and shielding to maintain system reliability [75]. For example, NASA’s Perseverance rover relies on specialised radiation-hardened components, such as the AD590S temperature sensor, which has been crucial in managing the extreme temperature variations experienced in space [76]. However, the trend toward using Commercial Off-The-Shelf (COTS) components, driven by their superior performance in terms of size, power, and speed, introduces new risks [75]. For instance, NASA's Ingenuity helicopter used a cell-phone grade processor, 150 times faster than Perseverance's processor, within a three-layer system [77]. It placed a radiation-tolerant FPGA at the base for low-level tasks, dual-redundant automotive-grade processors in the middle for flight control, and the Qualcomm Snapdragon 801 processor at the top for high-level functions, compensating for its lack of radiation hardening with redundant, parallel processing to ensure reliability [28]. As spacecraft electronics become more complex, advanced testing methods using higher energy particle beams and precise irradiation are crucial for developing hardened components that can withstand intense radiation environments [75]. Consequently, designing spacecraft for Mars necessitates robust shielding, materials resistant to UV

degradation, and electronics that can endure high-energy particles to ensure mission success and longevity on the Martian surface.

Beyond uncrewed aerial systems, there have been conceptual studies such as in Ref. [78] and [79], exploring the feasibility of manned Martian rotorcraft. In such scenarios, radiation exposure becomes a critical factor in vehicle design, influencing shielding requirements, mission duration, and operational altitude constraints. The absorbed dose of particle radiation is defined as the absorption of one joule of energy per kilogram of matter, measured in unit gray (Gy) [80]. To account for varying biological effects of different particle types, the absorbed dose is adjusted to does equivalent rate expressed in sieverts (Sv), reflecting the potential damage to living tissues [80]. A cumulative 1 Sv radiation exposure increases fatal cancer risk by 5%, which motivated NASA to set a 0.6 Sv astronaut career limit, while ESA and RSA set 1 Sv limits[81]. The average dose equivalent rate measured by instrument on the Curiosity rover at Gale Crater on Mars ranges from 0.64 to 0.721 milli-Sv/day, based on the respective solar minimum and maximum [80]. For comparison, astronauts on the ISS are exposed to about 0.5 mSv/day (182.5 mSv/year), as Earth's magnetic field offers some protection, whereas the average background radiation on Earth is only 0.007 mSv/day (or 2.4 mSv/yr) [80]. For a typical round-trip Mars mission, including 180 days each way and 500 days on the Martian surface, the total radiation dose could exceed 1 Sv, mainly because during their cruise to Mars, astronauts are exposed to radiation levels of approximately 1.84 mSv/day due to limited shielding in deep space [80]. Estimates from NASA's Mars Odyssey orbiter suggest that global surface radiation on Mars ranges from 100 to 200 mSv/year, with the lowest levels found at lower elevations where the thicker atmosphere offers more shielding (Fig. 2.13) [82]. These values are crucial for determining aerobot shielding thickness for safer radiation levels [80], particularly in systems designed for manned missions or biological payloads. Operating in lower Martian elevations with natural atmospheric shielding can further enhance protection.

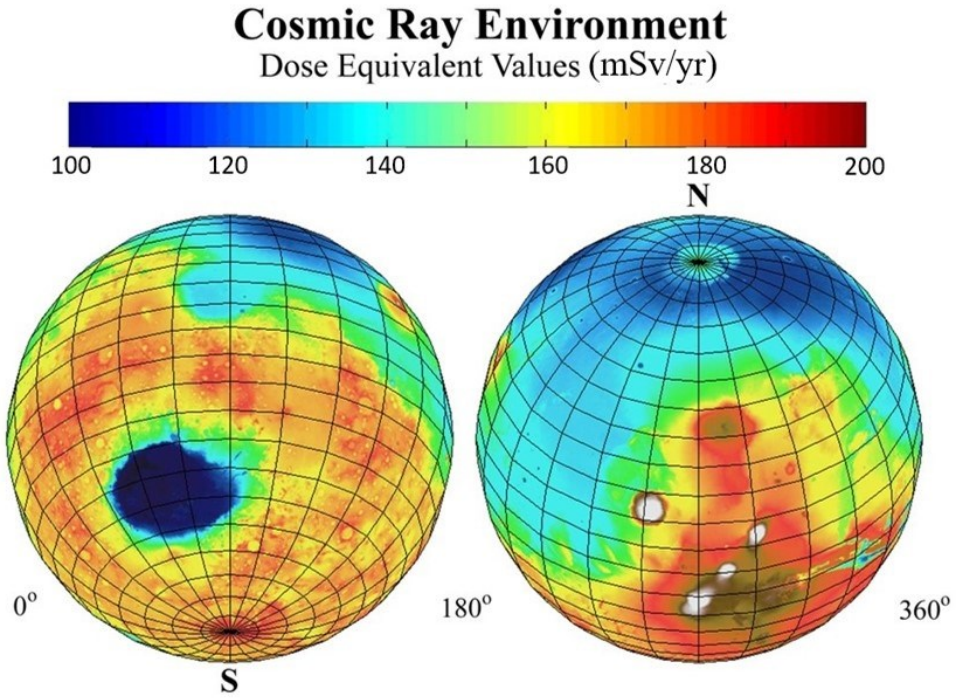


Fig. 2.13 The colours in the map refer to the annual dose equivalent in milli sievert (mSv) estimated utilising NASA's Mars Odyssey orbiter data. The range is generally from 100 Sv (colour-coded dark blue) to 200 Sv (colour-coded dark red) [82]. Original Image Credit: NASA/JPL/JSC. Modification: Altered equivalent units.

2.4.2.5 Martian Solar Irradiance

Solar irradiance, also referred to as solar flux, is the power per unit area received from the Sun in the form of electromagnetic radiation. The Martian solar constant (I_0), defined as the average solar irradiance received at the top of the atmosphere, is about 590 W/m² [83], about 57% [48] lower than that of Earth due to Mars' greater distance from the Sun. The mean irradiance reaching the Martian surface is often much lower due to atmospheric dust, which absorbs and scatters sunlight. This effect is quantified by the atmospheric optical depth (τ), ranging from 0.5 in clear conditions to over 3.0 during severe dust storms [83]. In a clear atmosphere, direct straight sunlight is vital for maximizing energy capture. The direct solar irradiance on a surface that is perpendicular to the Sun's rays ($I_\perp$) is given by [83]:

$$I_\perp = I_0 \exp\left(-\frac{\tau}{\cos\theta_z}\right), \tag{2.4}$$

where I_0 $(\mathrm{W/m^2})$ is the solar constant, τ is the atmospheric optical depth, and θ_z (degree°, solar zenith angle) is the angle between the Sun and the vertical direction above the surface point.

During dust storms, when direct sunlight is minimal, diffuse irradiance, which is sunlight scattered by atmospheric particles, becomes important as it reaches the surface from all directions. Global irradiance measures the total available solar energy by combining both direct and diffuse components along with surface-reflected sunlight [83]. The solar global irradiance on a horizontal surface at ground level on Mars can reach up to 400 W/m² at midday during a clear summer day and drop to as low as 80 W/m² at noon during a winter dust storm [83]. This measure is especially relevant for optimizing energy strategies and ensuring reliable power supply for solar-powered Mars aerobot systems, which might not always be oriented directly towards the Sun. Mars Climate Database (MCD) software [58] can be used to incident solar flux data in any region, space and time on Mars.

2.4.2.5.1 Photovoltaic Systems

Photovoltaic (PV) systems, which convert sunlight directly into electricity using solar cells, are particularly suitable for Martian aerobots due to being much lighter compared to nuclear power systems used in rovers. Maximising solar panel efficiency on Mars involves optimizing tilt and orientation [83]. Near the equator, lower tilt angles are effective, while steeper angles are necessary closer to the poles. Panels can be fixed or equipped with tracking systems. Fixed panels are simpler but less efficient, while tracking systems, which adjust panel orientation to follow the Sun's movement, offer higher energy capture but greater complexity [83]. Flat-plate solar arrays, a common type of PV system, are particularly effective as they can capture both direct and diffuse radiation, providing reliable power even during dust storms when diffuse light dominates [83]. In contrast, solar concentrators PV system, which uses reflectors to focus sunlight, are more efficient under clear conditions but are highly susceptible to the scattering effects of Martian dust, making them less ideal for consistent energy production [83].

Third-generation advanced thin-film III-V multi-junction solar cells, made from stacked materials in groups III and V of the periodic table, are used in space and Mars missions due to their broader spectrum capture, superior efficiency, radiation resistance, and lightweight flexibility, compared to the first-generation Crystalline Silicon cells predominantly used on Earth [84][85]. Ingenuity Helicopter was equipped with Inverted Metamorphic Quadruple Junction solar cells [28], capable of efficiencies up to 33% [86]. Ongoing research aims at the theoretical 68.2% efficiency limit [85] for multijunction cells under standard sunlight, with the current record at 39.5% [87]. Interestingly, the significantly lower ambient temperatures on Mars reduce thermal losses and improve the overall energy conversion efficiency of solar cells; for instance, the efficiency of the Gallium Arsenide component in III-V multi-junction cells increases by about 10-30% compared to their performance on Earth [83][88]. The following simplified equation can estimate the generic electrical power output (P_{el}) of the PV solar panel:

$$P_{\mathrm{el}} = \eta I_{\mathrm{G}} A\,, \tag{2.5}$$

where I_{G} $(\mathrm{W/m^2})$ is the global solar irradiance $(= I_{\mathrm{direct}} + I_{\mathrm{diffuse}} + I_{reflected})$ [83], A $(\mathrm{m^2})$ is the area of solar panel, and η is the overall efficiency of the solar cell (includes losses due to factors like conversion inefficiencies, reflection, and thermal effects).

For future aerobot missions, reliability is paramount. Despite their resistance, III-V solar cells degrade over long missions on Mars due to cumulative radiation exposure, which displaces atoms within the lattice and causes defects, as well as thermal and mechanical stress, and material ageing [85]. However, dust deposition is the major issue, significantly affecting the lifetime, maintenance, and energy output of solar power systems, as evidenced by the 0.28% performance degradation per sol observed on the Pathfinder solar arrays [83][88]. The findings from the long-term Mars Exploration Rovers (MER) mission suggest that the degradation rate decreased to about half as additional dust layers had a diminishing impact [88]. While winds can temporarily remove dust, leading to reversible effects, the study [89] on MER-B found an irreversible degradation rate

of 0.6% per year due to cell cracking, surface abrasion, and interconnect failures, resulting in a 1.9% annual power loss. The most severe damage comes from global dust storms, equivalent to approximately 77 sols of standard exposure [89]. Although various dust mitigation technologies exist, they are excluded from spacecraft designs due to trade-offs in complexity, power consumption, weight, and limited effectiveness [90]. Mechanical wipers, like those used on Earth, physically sweep dust off surfaces but can cause surface abrasion over time, leading to reduced solar panel efficiency and potential material degradation. Air-blast cleaning systems rely on high-pressure gas to dislodge dust, but in Mars' low-pressure atmosphere, the reduced air density limits their effectiveness. Electrostatic dust removal systems use electric fields to repel or move dust particles, a promising technology; however, they require additional power, precise surface integration, and complex control mechanisms, making them less practical for current Martian aerobot designs [90].

To ensure the long-term efficiency of solar panels on Martian aerobots, practical strategies must be cautiously integrated with mission constraints. System redundancy mitigates power loss by incorporating multiple energy sources or backup panels. Real-time data monitoring allows dynamic power adjustments based on dust accumulation trends. Durability testing ensures materials can withstand repeated dust exposure over extended missions. Anti-reflective coatings reduce dust adhesion, improving light absorption, while optimising panel tilt angles (45°–60°) enhances passive dust shedding by leveraging Martian wind dynamics and gravity [89]. This comprehensive approach to managing solar flux is crucial for the success and longevity of solar-powered aerobot missions in Mars' challenging environment.

2.5 Design, Development and Delivery Considerations for Martian Aerobots

Understanding Mars' atmospheric and environmental conditions is crucial for designing in-situ aerial robotic missions. These insights guide the development of exploration technologies adapted to the planet's unique challenges. Mars' thin atmosphere necessitates careful consideration of aerodynamics, requiring

efficient lift mechanisms and robust structural integrity to function effectively in low-pressure conditions. Autonomous operation is imperative due to the communication delays between Mars and Earth, necessitating lightweight, energy-efficient, and radiation-hardened systems capable of independent navigation without a Global Positioning System (GPS) [91]. In an environment characterised by limited digital maps and frequent dust storms, onboard sensors and real-time terrain mapping are crucial for maintaining stable flight. Navigational systems must adapt to varying atmospheric conditions, including pressure changes and wind patterns, to ensure operational stability. Seasonal mission planning plays a vital role in optimising aerobot performance, taking advantage of periods with higher atmospheric pressures and more stable environmental conditions. Ingenuity Helicopter operated autonomously during its flights on Mars, managing navigation, stability, and landing without human intervention, while still relying on human input for mission planning and flight parameter definition, making it semi-autonomous in its overall operation [28].

Structurally, aerobots must be constructed from ultra-lightweight, durable materials capable of withstanding extreme temperature fluctuations (-153°C to 20°C [11]) and resisting dust-induced corrosion. Martian dust can also disrupt electronic systems through triboelectric charging, risking signal interference and component failure. Reliable energy management is crucial, particularly for solar-powered aerobots, as dust accumulation and atmospheric conditions can diminish solar efficiency over time. Thermal management systems are necessary to protect against extreme cold, especially during the Martian winter. Furthermore, Mars' varied topography and gravitational anomalies present additional challenges to maintaining flight stability and energy efficiency. Advanced methods and technologies across fields such as aerodynamics, propulsion, materials, autonomous systems and space science, are vital to ensuring these vehicles can reliably perform under Martian conditions and lead to the successful deployment of next-generation aerobots.

2.5.1 Ingenuity into the Design and Development Considerations

Integrated design methodologies that combine mission requirements, vehicle design, and environmental factors are essential for developing Martian aerobots. This involves specialised software tools for design and simulation, along with rigorous testing using simulated Mars environments and Earth-based analogues. The design of the first Mars Helicopter, Ingenuity, presented significant challenges, requiring a precise balance of structural integrity, thermal management, aerodynamic efficiency, and contamination control to prevent particulate interference with sensitive components and ensure planetary protection compliance within strict mission constraints [92]. Innovative engineering solutions, including rotor system optimisation, lightweight durable landing gear, and ruggedised electronics built for extreme Martian conditions, enabled Ingenuity to operate effectively in Mars' harsh environment. Rigorous design, testing, and validation processes, including flight, structural, and environmental assessments, validated the helicopter's ability to withstand space travel, Martian conditions, and operational stresses, establishing it as a technology demonstrator for future missions [92]. The following subsections will explore the challenges and detail the design and development considerations, including testing, necessary for the successful deployment of Mars aerobots.

2.5.1.1 Flight Dynamics Considerations

Mars' atmosphere, at about 1% of Earth's density, poses significant challenges for aerial vehicle design. Terrestrial combustion engines are impractical due to the lack of free oxygen, although the thin atmosphere still allows for rotary propulsion systems like rotors or propellers [91]. The thin air significantly reduces the Reynolds number, which measures the ratio between inertial and viscous forces in the atmosphere, leading to decreased aerodynamic efficiency. A lower Reynolds number increases the possibility of flow separation and drag over the flight surfaces, making it more difficult to generate lift and maintain stable flight in Mars' atmosphere [98]. Additionally, the speed of sound on Mars is 70% lower than on Earth [33], meaning that rotary aerodynamic surfaces are more prone to approaching supersonic speeds, potentially causing compressibility effects like

shock waves that further degrade performance. While existing literature, including data from Ingenuity's flights, offers valuable insights into these phenomena, empirical data remains limited. This limitation complicates the design process, necessitating extensive research and specialised airfoil designs optimised for Mars' unique aerodynamic conditions [91]. Another significant challenge is the reduced aerodynamic damping in Mars' thin atmosphere, which affects the rotor blades' ability to control blade flapping, the up-and-down motion of the blades caused by cyclic aerodynamic and inertial forces during flight. On Earth, the denser atmosphere provides sufficient aerodynamic resistance to manage this flapping motion, but on Mars, this damping is reduced by about ten times, leading to oscillatory flap modes that could destabilise the rotary aerobot by coupling with its body during flight [92].

To address Mars' thin atmosphere, the Mars Helicopter's rotor blades were designed using advanced rotor aerodynamics tools to optimise performance under low Reynolds numbers [92]. The initial geometries were refined for structural integrity and efficiency, with specialised software predicting aerodynamic performance. Thin laminar flow airfoils were utilised to minimise drag while ensuring structural strength, which is critical for stable flight in the Martian environment. To mitigate the reduced aerodynamic damping, the rotor blades were made extremely stiff, raising the natural flap mode frequencies to a higher range, where they are less likely to interfere with the helicopter's control system [92].

2.5.1.1.1 Flight Testing

The flight testing of the Mars Helicopter, Ingenuity, was conducted in the JPL Space Simulator, a cylindrical chamber 7.6 m in diameter and 24.4 m in height, designed to replicate Mars' low atmospheric pressure and gravity [92]. The chamber was evacuated to a near-vacuum and filled with CO_2 gas to simulate the Martian atmosphere. The facility was equipped with advanced instrumentation, including the multi-directional force and torque sensor and motion tracking systems, ensuring precise evaluation of Ingenuity's performance under the extreme conditions it would face on Mars. Initial testing evaluated the

helicopter's ability to generate lift, maintain stable hover, and respond to control inputs and external forces in simulated Martian conditions, including low-speed flight and aerodynamic stability under controlled wind speeds of up to 10 m/s [92]. Unique to Mars rotorcraft, the testing involved a gravity offload system designed to simulate Mars' gravity, about 38% of Earth's (3.71 m/s² compared to 9.81 m/s²). This system, using pulleys and counterweights, reduced the helicopter's effective weight, allowing it to perform free-flight tests within the chamber [92]. This setup enabled Ingenuity to simulate flight conditions on Mars, including take-off, hovering and manoeuvring in a controlled environment. Additional testing related to spacecraft environmental conditions, such as vibration and shock from launch and landing, was performed in a smaller 3-meter chamber.

Some other institutions have developed advanced facilities to study flight in the Martian atmosphere. At Tohoku University in Japan, researchers constructed a specialised wind tunnel designed to simulate low Reynolds numbers and high subsonic flows [93]. This facility allows for detailed studies of aerodynamic behaviours, such as flow separation and compressibility effects, which are critical for optimising aircraft design for the Martian environment. Meanwhile, the low-density multi-fan wind tunnel at the California Institute of Technology focuses on forward flight dynamics and wind interaction, providing a more dynamic testing environment that can simulate varying wind conditions and their impact on flight stability [94]. Additionally, at the Harbin Institute of Technology in China, a novel reflux subsonic low-density dust wind tunnel offers the unique capability to simulate Martian dust storms [95]. This facility replicates the erosive and abrasive effects of Martian dust, allowing researchers to better understand the impact of these harsh conditions on rotorcraft performance, which is critical for the design of long-lasting spacecraft and aerial vehicles for Mars exploration.

2.5.1.2 Structural Material and Design Considerations

The Martian environment presents significant thermal challenges and requires strict planetary protection to prevent contamination with Earth-based microorganisms [91]. Aerobots designed to operate in Mars' extreme cold, where temperatures can drop below -100°C at night, require materials that can

withstand extreme cold without becoming brittle or contracting excessively. Minimising outgassing, where trapped gases are released from materials when exposed to the vacuum of space or low-pressure environments like Mars, is crucial, as is reducing the risk of microcracking at low temperatures [92].

Mars Helicopter Carbon fibre composites, known for their high strength-to-weight ratio, were used for critical structural components like rotor blades and landing gear, with a specially formulated resin to minimise outgassing [92]. The landing gear was designed for stability on uneven terrain, with long deployable composite legs that create a broad base to minimise the risk of tipping. The legs incorporate flexures and dampers to absorb landing impacts, and the deployment mechanism ensures reliable leg extension and locking during descent. The solar array, mounted above the rotor blades (Fig. 2.14), recharges the lithium-ion batteries and is structurally similar to the rotor blades, featuring moulded carbon fiber composite skins and a foam core, with the central hub interfacing with the rotor system [92].

Thermal management is vital due to Mars' low atmospheric density, which limits heat dissipation [91]. For example, the Mars Helicopter uses a beryllium-aluminium motor hub that acts as a heat sink, managing excess heat from the propulsion system and electronics while stabilising thermal expansion to maintain operational integrity [92]. The Helicopter Warm Electronics Box (HWEB) on Ingenuity provided thermal insulation for sensitive electronics and batteries while serving as an environmental barrier to prevent contamination and comply with planetary protection requirements. It is constructed from a polyamide film membrane with high solar absorptivity and low emissivity, wrapped around a lightweight composite frame that creates an insulating gas gap to minimise heat loss. While optical windows in the HWEB ensured clear views for the helicopter’s cameras and laser altimeter.

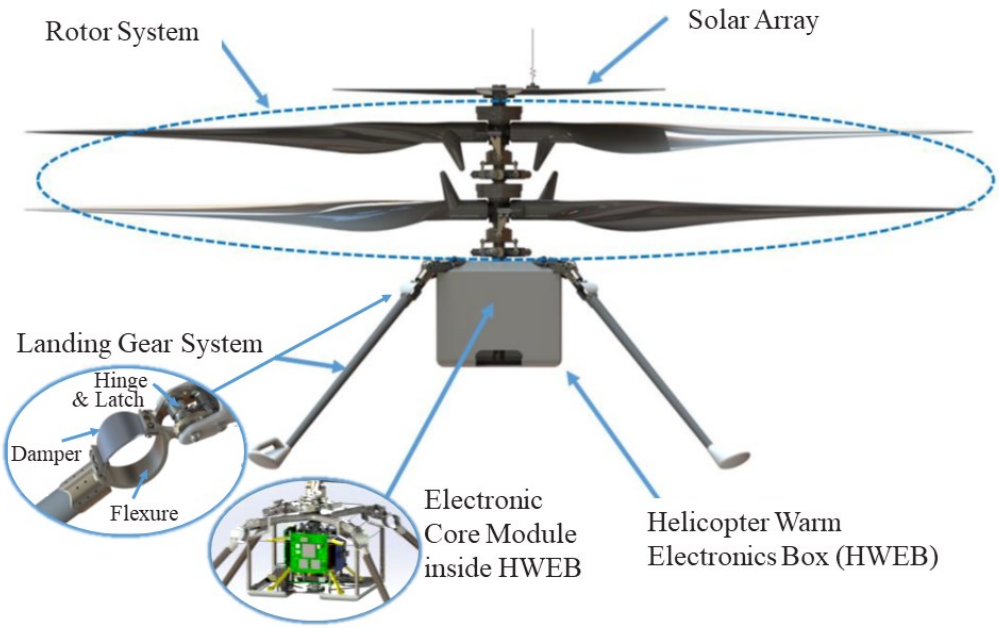


Fig. 2.14 Mars Helicopter Technology Demonstrator Subsystem Classification. Modified Image from source [92]

2.5.1.2.1 Structural Testing

Structural testing is essential for verifying the mechanical strength and durability of aerobot components under mission-specific loads and stresses. Finite Element Analysis (FEA) is commonly used to simulate and predict structural behaviour under conditions such as launch forces, centrifugal forces on rotor blades, and thermally induced stresses from material expansion differences. For the Mars Helicopter, these simulations were validated through experimental tests to ensure the design could endure the interplanetary journey, deployment on Mars and operational stresses of the Martian environment [92].

The integrity of the rotor system is confirmed through destructive load testing, which evaluates the structure's ability to withstand extreme forces, and modal testing, which identifies the natural frequencies and vibration modes. In the case of Ingenuity, rotor blades were tested to ensure they could withstand the high centrifugal forces experienced during flight [92]. Landing gear, designed for stability on uneven terrain, undergoes drop tests with scale models to emulate various landing scenarios. For the Mars Helicopter, these tests, using the similar gravity offload system used in the flight testing, included evaluations on surfaces

like concrete, sand, and rocks, as well as sloped terrain, ensuring the gear could absorb impacts without tipping. Its solar array was tested at JPL's Environmental Test Laboratory to verify its structural resilience through both modal and random vibration tests, ensuring it could withstand launch and operational vibrations.

Thermal vacuum testing is critical for ensuring an aerobot can operate in extreme Martian conditions. The Mars Helicopter was tested in a chamber that simulated Mars' environment by creating a near-vacuum and backfilling it with carbon dioxide to simulate the thin atmosphere [92]. The temperature within the chamber was cycled to simulate the daily temperature variations on Mars, with diurnal changes exceeding 100 °C [52]. This testing was vital for verifying the function of HWEB for insulating the sensitive electronics packaged inside it.

2.5.2 Interplanetary Delivery Considerations

2.5.2.1 Interplanetary Travel Stresses

Aerobots designed for planetary exploration must withstand extreme forces during launch and throughout their journey to the target planet. During the launch phase, spacecraft can experience steady-state accelerations of 5 to 7g, while during Entry, Descent, and Landing (EDL) on Mars, g-loads can peak between 9 and 16g, depending on the launch vehicle, its mass and specific mission configurations [96]. The Mass Acceleration Curve is a critical guideline that determines the maximum acceleration forces components must endure based on their mass, ensuring robustness against these intense conditions. The Mars Helicopter was designed to endure up to 60G quasistatic acceleration [92], a limit providing a high safety margin which accounts for extreme scenarios such as hard landings, deployment shocks, and unexpected impacts. In addition, the root mean square of acceleration (Grms), measures the intensity of vibrations and addresses the continuous vibrational stresses experienced during launch. Ingenuity was sized for 7.9 Grms to help prevent components from entering resonance, which could lead to structural failure [92]. These factors necessitate significantly more structural mass for an aerobot than would be required for flight operations alone.

Ingenuity underwent rigorous testing at the JPL to ensure its structural integrity, including vibration tests to simulate launch forces, modal tests to avoid resonance, and shock tests to replicate impacts during separation and landing. It was mounted on a vibration table and subjected to random vibration levels simulating launch conditions, including attachment to its delivery system beneath the Perseverance rover [92]. Post-test inspections confirmed the helicopter's durability. Shock testing simulated the forces during separation from the launch vehicle and deployment from the rover, using controlled devices to replicate the detachment process [92]. These comprehensive tests validated the components of the rotorcraft could withstand these mechanical shocks, ensuring its readiness for the most challenging phases of the mission.

2.5.2.2 Spacecraft Transport Package Sizes

The size and design of aircraft for Mars missions are critically constrained by the EDL system. As the spacecraft enters Mars' atmosphere with a descending speed of 6 km/s, the protective covering called aeroshell shields it from extreme heat and shock waves while also imposing strict geometric limitations on the aerobot's maximum size [97]. Historically, NASA has utilised three different aeroshell sizes for successful EDL systems, as illustrated in Fig. 2.15. The smallest aeroshell, 2.65 m in diameter, is used in several key missions, including the Mars Exploration Rovers (2003) and InSight (2018). The next size up is 3.5 m, which was used exclusively for the Viking 1 and 2 Landers (1975) [98]. The largest aeroshell, first used in the Mars Science Laboratory (2011) and later in the Mars 2020 mission [98], sets the current size limits for Mars aerobots, constraining them to a maximum diameter under 4.5 meters and a height of approximately 2.2 meters [99].

The unique challenge for aerial vehicles due to the thin atmosphere on Mars, necessitates larger wings or rotor blades for heavier-than-air craft and oversized balloons for lighter-than-air craft to achieve sufficient lift. For instance, NASA's Ingenuity helicopter, which weighs only 1.8 kilograms, has long rotor blades measuring 1.2 meters in diameter [28]. While Ingenuity's compact design was adequate for its limited mission as a rover appendage, carrying a more

substantial payload would require a significantly larger aircraft, which in turn demands more space for larger wings or blades. To accommodate these larger flying surfaces within the constraints of the aeroshell, it becomes essential to incorporate folding mechanisms into the aerobot's design, allowing efficient stowage and deployment upon arrival. As shown in Fig. 2.15, different aerobot configurations, including winged VTOL and coaxial rotorcraft designs, demonstrate how folding structures enable compact packing while maintaining structural integrity and operational efficiency. These mechanisms allow wings or blades to remain stowed during transit and deploy once the aerobot reaches Mars. Since the constraint is on the physical size of an aerobot rather than its weight, which must remain light to fly on Mars, there is sufficient space to accommodate a smaller lander or rover alongside the aerobot. The petal lander, utilised in earlier missions like Pathfinder and MER rovers, can provide additional support to aerobots by absorbing loads during the liftoff and landing (Fig. 2.15 b.i) [98]. The selection of landing systems, whether powered deceleration thrusters, airbag systems, or sky cranes, depends on specific mission requirements, such as payload size, terrain, and precision needed during the final descent and landing phases of soft EDL [97]. Although developing a new aeroshell and lander would be optimal, space missions often favour existing designs for their proven reliability [98].

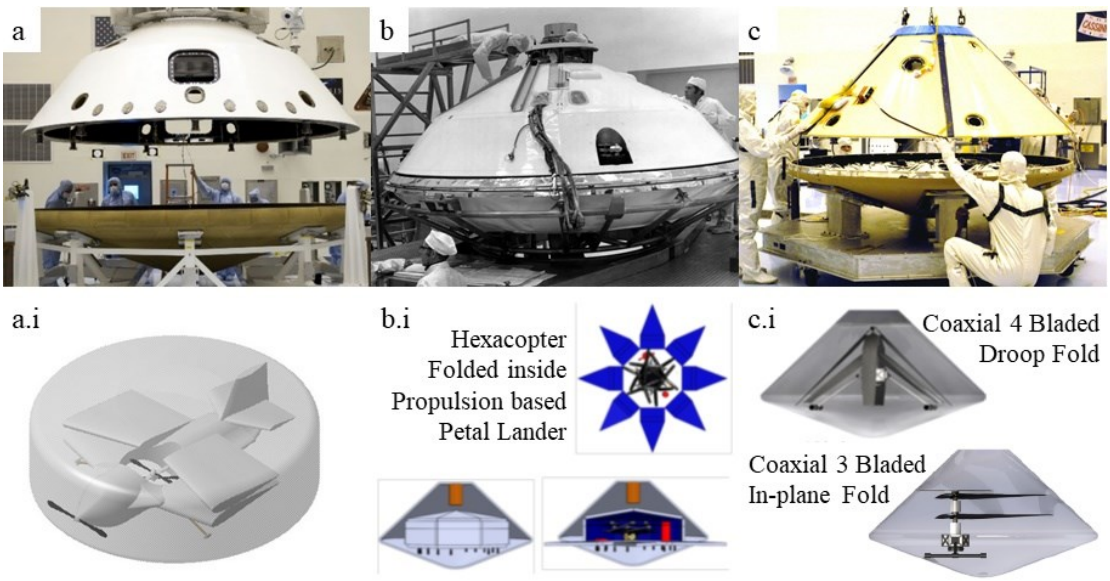


Fig. 2.15 The top images depict Mars's past mission aeroshells during the testing phase: a) Mars Science Laboratory aeroshell (2011, size 4.5 m). b) Mars Viking 1 aeroshell (1975, size 3.5 m). c) Mars Exploration Rover 2 aeroshell (2003, size 2.65 m). Images Credit: NASA. The bottom images are CAD model illustrations showing different aircrafts folded and packed inside the respective aeroshell shown at the top a.i) Winged VTOL concept CAD model 4.5 m aeroshell [100]. b.i) Folded hexacopter concepts folded inside a petal lander comprising thrusters which are packed inside the Viking aeroshell (3.5 m) [98]. c.i) Coaxial rotorcraft with 3 and 4 blades variants packed inside 2.65 aeroshells [98]

2.5.2.3 Futuristic Transportation

As Martian aerobot technology advances, its feasibility is inherently linked to improvements in interplanetary transportation. Larger transport systems, including expanded aeroshells, could enable the delivery of heavier aerobots and advanced aerial systems, supporting extended mission durations and in situ resource utilisation. While current aerobots, such as Ingenuity, are constrained by the size and weight limitations of existing Mars aeroshells, future large-scale transportation could facilitate high-endurance aerial platforms for scientific exploration over vast distances. This would allow aerobots to carry more advanced instrumentation, enhanced power sources, and improved mobility systems, significantly impacting mission design and scientific output.

SpaceX's Starship spacecraft and Super Heavy rocket, collectively known as Starship (Fig. 2.16), represent a future solution for Mars missions with their planned fully reusable transportation system for both crew and large cargo [101]. Designed to carry up to 150 metric tonnes in a reusable configuration or up to 250 metric tonnes in an expendable mode, the Starship cargo variant offers a payload volume of up to 8 meters in diameter and 17 meters in height [102]. SpaceX is actively advancing Starship's development, focusing on rapid iteration and testing to bring this vision to reality [103]. The plan includes in-orbit refuelling and the use of Martian in situ resources for refuelling, enabling sustainable round trips and supporting more ambitious missions [104], including those requiring larger and more capable aerial vehicles essential for advanced exploration. However, given the inherent challenges and the typically slow pace of space

technology development, it may take a significant amount of time before these capabilities are fully realized.

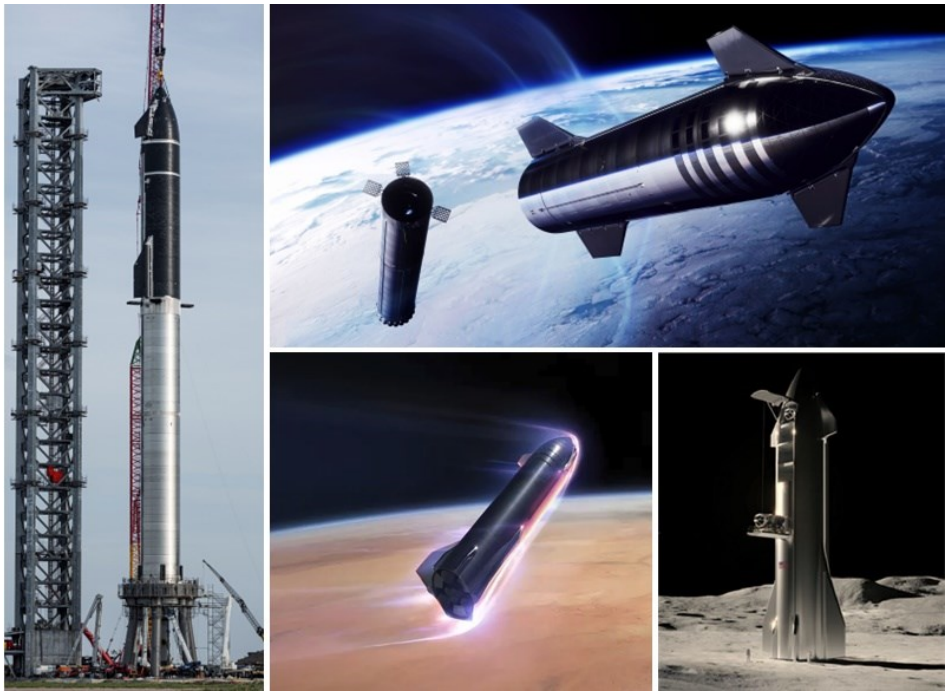


Fig. 2.16 The image at the left shows the reusable SpaceX Starship, currently in development, standing at the launch pad. The rendered images at the right illustrate the concept of a Starship spacecraft (stage 2) separating from a Super Heavy Rocket (Stage 1) in the near-Earth orbit and travelling to Mars, where it enters the atmosphere and lands on the ground with its payload door open. Images Credit: SpaceX

2.5.2.4 Launch Budget

The optimal window that space agencies always use for launching a spacecraft to Mars, typically a 6-9-month journey, occurs every 26 months when Earth and Mars align near Mars' closest approach to Earth, sometimes coinciding with its perihelion (Fig. 2.11) [99]. For Mars robotic missions, Young et al. [91] estimated that adding 1 kg to an air vehicle increases the lander mass by 21.5 kg, the entry mass by 13 kg, and the launch mass by 20 kg (as illustrated in graph Fig. 2.17). These figures, derived from the 1998 Mars Pathfinder mission, show that the 16 kg rover and its equipment led to a total launch mass of 890 kg.

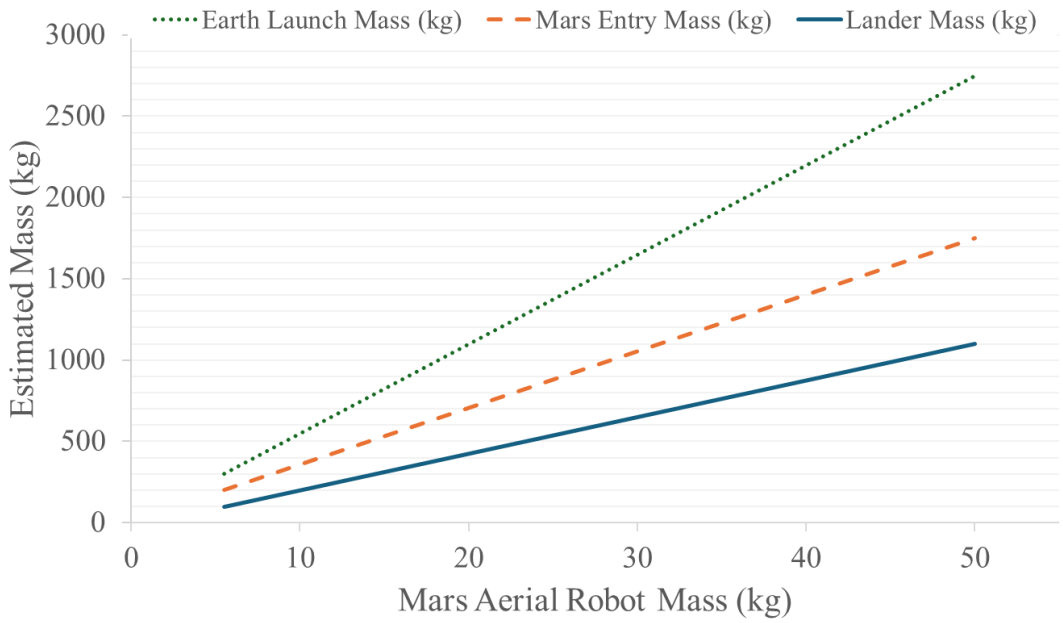


Fig. 2.17 Estimated increases in Earth launch, Mars entry, and lander mass as a function of Mars aerial robot mass. Graph recreated from source [91].

Mission costs were estimated with a fixed launch vehicle cost of $70 million and an incremental mission development cost of $180,000 per kg of launch mass (in 1997 USD), resulting in a total cost of about $230 million for Mars Pathfinder [91]. Adjusted for inflation, $230 million in 1997 is equivalent to about $451 million today (2024), reflecting a cumulative price increase of 96% over 27 years due to an average annual inflation rate of 2.52% [105]. While the inflation-adjusted figure provides a base estimate, the increased complexity and advanced technology required for modern Mars missions could raise costs by an additional 20-30%, potentially bringing the budget to $541 to $586 million. This estimate method aligns closely with the cost of the Phoenix mission (2007), which totalled $407 million, including $321 million for spacecraft development and $86 million for its launch, using the same Delta II rocket and a 2.65-meter aeroshell [106]. Launch service costs can increase by 2.5 times for missions using larger rockets such as the Atlas V, as seen with the Mars Science Laboratory (MSL) and Mars 2020 projects, where development costs exceeded $2 billion due to large payloads and new methodologies [107]. Ultimately, the escalating costs and narrow launch window available only about every two years, highlight the importance of efficient mass management and strategic planning in future Martian aerobot missions.

Limited payload capacity and high transportation costs demand that Martian aerobots be designed for maximum functionality with minimal weight, optimising energy efficiency, material selection, and payload integration to ensure mission feasibility within these constraints.

2.6 Mars Aerobot Design Thinking Matrix

The Mars Aerobot Design Thinking Matrix is a structured framework developed to guide the systematic design and selection of aerobots for Martian exploration. Given the extreme environmental constraints of Mars, such as its thin atmosphere, variable terrain, and limited energy availability, designing an aerobot requires careful consideration of multiple interdependent factors. This matrix serves as a decision-making tool, integrating insights from planetary science and aerospace engineering to optimise aerobot configurations based on mission objectives, energy efficiency, flight stability, and environmental adaptability.

This section begins by establishing the rationale for incorporating aerobots in Mars exploration, comparing their capabilities to traditional rovers through a qualitative evaluation of key performance parameters. It then introduces a hierarchical selection framework for aerobot design, categorising mission types, take-off mechanisms, power sources, and aerobot configurations. By providing a structured approach to balancing engineering trade-offs and operational constraints, the Mars Aerobot Design Thinking Matrix ensures that future aerobot designs are both viable and optimised for Martian exploration.

2.6.1 The Rationale for Aerobots Inclusion

The development of a Mars aerobot design involves an analytical thought process that is primarily based on the mission requirement to customise an optimised overall design by prudently examining the trade-offs amongst the numerous parameters, design configurations and technologies. A reasonable first step before such a process would be a quick justification of the inclusion of aerobots in the Mars missions against current rovers. To remove any ambiguity, an aerobot here is defined as any kind of autonomous robot with lifting capability into the air. Table 2.2 shows the comparative analysis between aerobot and rover, by

allocating a qualitative rating on a 5-point scale of very low to very high, against eight selected attributes. The ratings assigned are according to Martian vehicle standards, and some parameters could be rated in the form of a range, such as traversing speed can be ranged from high to very high, but the single most likely rating is mentioned for simplicity.

Table 2.2: Summarised comparison between Aerobot and Rover

Attributes	Aerobot	Rover
Traverse Speed	High	Very Low
Obstacle Overpassing	High	Very Low
Dynamic Agility	High	Very Low
Specific Range	High	Very Low
Operational Endurance	Low	Medium
Payload Capacity	Low	High
Shape & Size Flexibility	Low	High
Robotic Capability	Low	High

The lateral velocity of the small Ingenuity Helicopter is capped at 2 m/s, with a capacity of going up to 20 m/s, whereas its companion Perseverance rover can travel across a hard flat surface with a speed of 0.04 m/s [28] [29]. This great disparity between travelling speed combined with the ability to travel upwards further gives aerobots a high edge against the rover in obstacle overpassing, dynamic agility, and specific range. Dynamic agility, in the context of Mars exploration, refers to an aerobot's ability to perform rapid, precise manoeuvres to adjust flight paths, avoid obstacles, and adapt to wind disturbances. Mars' thin atmosphere provides less aerodynamic damping, making stability and control more challenging than on Earth. Unlike rovers, which are confined to ground traversal, aerobots leverage their agility to explore diverse terrains efficiently, access high-priority scientific sites, and cover greater distances in shorter timeframes.

Rovers are heavy which limits their speed and movement but have greater flexibility in shape and size that benefits in accommodating more power, science payloads, and experimenting capabilities; for instance, the Perseverance rover is

about 1025 kg, but it is a walking lab of volume size of 3 x 2.7 x 2.2 meters, carrying 7 science instruments, a long robotic hand, and a samples storage system [99]. Flying a rotary-propelled vehicle in the Martian thin atmosphere consumes a lot of power and produces in-system heat, due to the requirement of going above 2000 RPMs to generate lift; therefore, Ingenuity has flying endurance of only over a couple of minutes [28]. Rovers on the other hand are slow but have higher operational endurance regarding continuous travel and experimentation. Given that rovers can last over a decade, they can overall cover a wider land when compared to a short-term aerobot mission. For missions that would include a combination of both land and aerial robots, the individual attributes of each machine need to be counted and coordinated in such a way that they justify and enhance the overall mission performance and output.

2.6.2 Orders of Martian Aerobot Preliminary Design

The formation of the Mars Aerobot Design Thinking Matrix is majorly based on the trends observed in the research literature [108] on Martian aerobot designs. These studies highlight key constraints such as aerodynamic performance in Mars' thin atmosphere, energy efficiency, take-off mechanisms, mission longevity, and mission types based on energy resources and operational objectives. Incorporating these insights, the matrix establishes a hierarchical selection process to define prerequisites for a preliminary aerobot design, as shown in Fig. 2.18 and discussed in the following subsections.

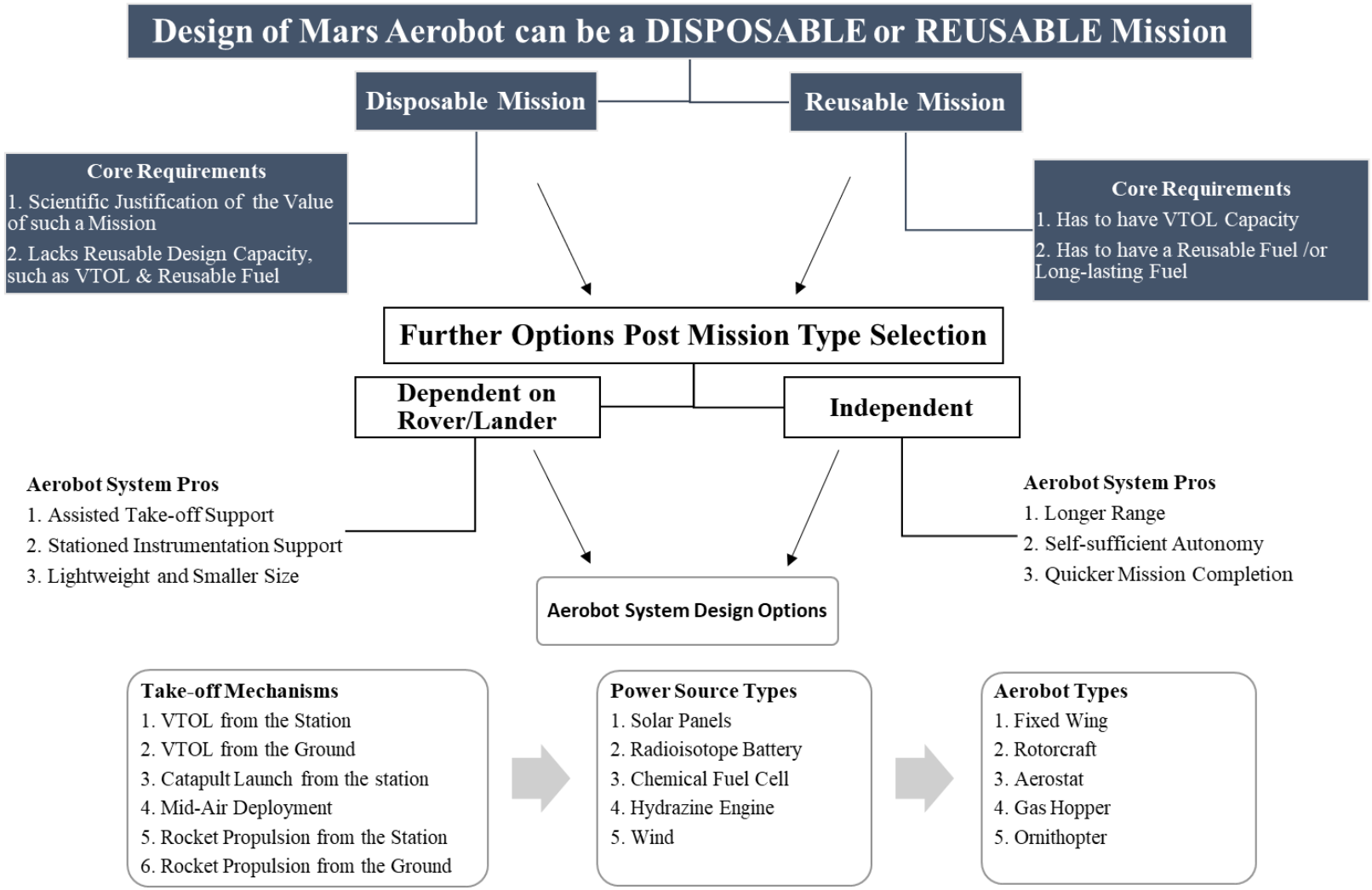


Fig. 2.18 The Mars Aerobot Design Thinking Matrix Flow Chart

2.6.2.1 Mission Types

In this order of selection shown in Fig. 2.18, the foremost choice to make is between a disposable and reusable Mars mission-type aerobot design. The reusable mission type requires an aerobot that would be capable of VTOL and uses long-lasting or reusable fuel, as there are no runways and refuelling infrastructure on Mars; whereas the mission is deemed disposable when the aerobot lacks such reusable capability. However, a disposable mission would essentially require a scientific justification for its value in terms of planetary exploratory budget and resources. Each mission type influences the next choices in the series, accordingly.

After selecting the mission type, the next key decision is whether the aerobot will be rover/lander-dependent or fully independent, as this influences its design, launch mechanism, and power system. A rover/lander-dependent aerobot offers advantages like assisted launches, on-ground instrumentation, and reduced weight due to shared resources. However, the slower pace of traditional rovers can limit the aerobot's efficiency and range. Recent advancements, such as NASA and Boston Dynamics' Mars Dog robot [109], could resolve this issue by matching the aerobot’s speed, allowing for more efficient, synchronized operations. Nevertheless, this approach requires adapting the rover/lander to accommodate the aerobot. In contrast, an independent aerobot, while lacking support from a rover/lander, offers greater range, autonomy, and potentially faster mission completion because it is not constrained by the need to return to a fixed ground base for recharging, data transfer, or operational coordination. This allows it to cover larger areas in a shorter time, making it particularly advantageous for reconnaissance and large-scale mapping missions. The decision between dependency and independence should consider the specific mission objectives, balancing the benefits of support against the flexibility of autonomy.

Next in the order series is the aerobot system design that includes a set of 3 primary sub-systems at this level, each allocated with the known possible options.

These subsystems are arranged in one of the feasible rational orders, comprising the launch mechanism, power source type, and aerobot type.

2.6.2.2 Take-off Mechanism

The take-off mechanism, or system, for flight, is a good starting point in the preliminary design phase as it helps to think of the best way of take-off as per mission requirements and hence, the required technology. There are 6 ways of launching an aerobot, as mentioned in Fig. 2.18 and choosing one of them depends on the previous selections made. For instance, VTOL can only be for a reusable mission and VTOL from the station is only possible if the aerobot is developed to be rover/lander dependent. VTOL from the ground is a versatile option that can be effective for both rover/lander-dependent aerobots, such as the NASA Mars Electric Reusable Flyer concept shown in Fig. 2.19 [110][111], and independent aerobots, as demonstrated by the Ingenuity Helicopter, which successfully took off from the ground after being deployed from the belly of the Perseverance Rover [99].

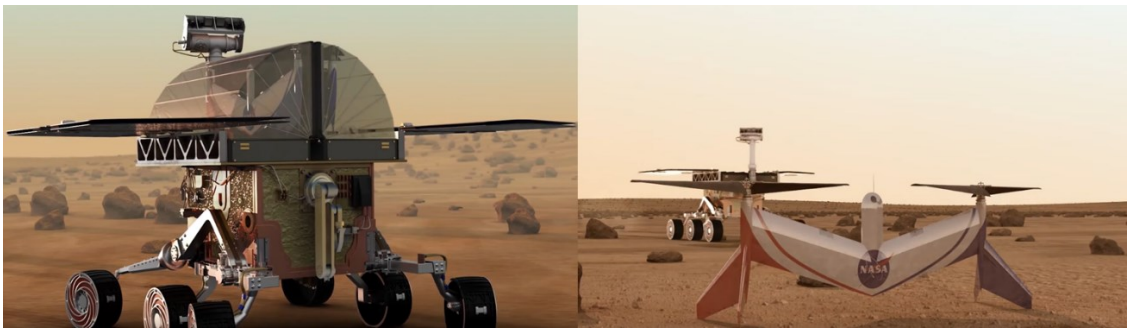


Fig. 2.19 NASA's Mars Electric Reusable Flyer concept proposed a rover-dependant tail-sitter rotorcraft deployed by the rover with a robotic arm to explore caves and canyons. After each mission, it returns to the rover for recharging. Still images from the NASA Langley Research Center's YouTube post [110]

A catapult launch from a station, suitable for both disposable and reusable aerobots, involves propelling the aerobot into the sky. This method requires a rover or lander on the ground to support the launch mechanism, similar to those used in terrestrial tactical aerial drone systems [112]. Recovery of the drone can be a challenge in such take-offs, as drones without VTOL will be disposed of unless they make a return back to the station within the same flight. Reuseable

drones, on the other hand, can utilise this strategy to increase range and altitude for specific missions. Similarly, aerobots launching from the station carrying rocket or propellant-based propulsion, are designed to be one-time missions. A terrestrial canister launched small OUTRIDER drone by Lockheed Martin is an example of such an unmanned aerial system [113].

Both mid-air deployment and rocket propulsion from the ground take-off mechanisms can be applied to any combination of preliminary selections within the Mars Aerobot Design Thinking Matrix. Mid-air deployment, especially for disposable aerobots, is one of the earliest concepts in planetary exploration, traditionally involving an independent, rocket-fuelled aerobot [114][115]. Recent research has focused on using mid-air deployment of VTOL aerobots to explore Mars' highlands before landing and re-flying [55]. Alternatively, rocket propulsion from the ground offers a more controlled and time-specific launch option. A reusable VTOL drone with an auxiliary rocket-fuelled propulsion system for high-altitude flight could also benefit from this ground-based launch mechanism when needed.

2.6.2.3 Power Source Types

The next step in the aerobot system design process (Fig. 2.18) is selecting the appropriate power source. In the earliest Mars aerobot design concepts, the Hydrazine Engine has been a popular choice for a disposable mission-type aircraft due to its ability to provide high energy and propulsion thrust at a temperature of 926 °C with a minimal engine design complexity and monopropellant property, which is of advantage in an oxygen-deprived atmosphere that is not physically accessible by humans [116]. However, hydrazine's high toxicity requires careful handling, as demonstrated in one of the early concepts, the fixed-wing aircraft called Mini-Sniffer (Fig. 2.20), studied by NASA's Dryden Research Center in 1977 [114] [116]. Alternatively, some design concepts, such as the Japanese Mars Airplane [117] and BIG BLUE inflatable-wing aircraft [118], proposed to utilise pre-charged electric batteries to power aerobots for a limited duration suitable for disposable missions.



Fig. 2.20 Mini-Sniffer III. The image on the right shows the crew wearing self-contained suits and oxygen tanks because the engine was fueled with toxic hydrazine fuel. Image Credit: NASA.

In the recent literature, solar panels in combination with rechargeable batteries have been a popular choice of Martian aerobot researchers, with pioneering concepts such as solar-powered long-endurance Mars aircraft [119] and Martian Airborne Exploration Vehicle (MAEV) [120], because of the abundant renewable solar energy on the planet that makes the drone self-sustaining for a reusable mission type. Solar panels are lighter in weight when compared to the other power system options, and do not essentially require dedicated storage space in the fuselage, as they can embed in the top surfaces of the plane, particularly in winged aircraft. Over time, the panels get covered with dust and need cleaning for optimal efficiency, but unlike Earth, it does not rain on Mars and the winds are inefficient in wiping off the stubborn layer closest to the skin, which causes the land spacecrafts to have a limited life expectancy. Whereas, aerial spacecrafts would have a comparatively longer life because their high-speed flight works like a self-cleaning mechanism for the panels; however, global dust storms can be a terminator of spacecraft by blocking the sunlight for months from approaching the solar panels, as such in the case of Opportunity Rover's demise [27]. Moreover, solar energy is not fully accessible in the polar regions of Mars or areas that are hidden from sunlight (such as lava tubes), and the solar flux has both diurnal and seasonal variations.

For greater reliability, a radioisotope battery is a considerable but highly expensive option as a power source. Plutonium (Pu) 238 fuel-based radioisotope

thermoelectric generator (RTG) has been used in several deep space spacecrafts, including Perseverance rover which carries a 4.8 kg Pu in a 45 kg multi-mission-RTG system with an ability to produce 110 Watt of electricity at a life expectancy of 14 years [99]. There are some preliminary Martian aerobot concepts in the literature that have opted for a radioisotope battery, such as Ballistic Mars Hopper [121], radioisotope powered long-endurance Mars aircraft [119] and ARMaDA (Advanced Reconnaissance Martian Deployable Aircraft) [122]. An advanced alternative to the RTG is the Advanced Stirling Radioisotope Generator (ASRG), which, though still in NASA's testing phase, is proposed to produce several times more power with the same amount of radioisotope fuel and is being considered for future deep space missions, including the Mars Geyser Hopper [123]. However, these systems have significant drawbacks, including the heavier power system, the limited availability of nuclear fuel, and stringent regulations surrounding nuclear energy. Incorporating both a radioisotope battery and a solar power system on an independent, reusable aerobot could address certain mission requirements but at the cost of increased mass, size, propulsion power, and overall system complexity. This approach is more suitable for heavier aerobots, such as balloons and hoppers like the Mars Aerial Platform (MAP) balloon [124] and Mars Geyser Hopper [123]. Alternatively, an aerobot accompanied by a lander or rover equipped with a radioisotope battery can be used as an optional recharging station.

Another power source introduced in the Martian aerobot literature is fuel cells, an electrochemical device that converts the chemical energy of a reaction directly into electrical energy. Particularly, proton exchange membrane (PEM) fuel cells with oxygen and hydrogen gas as a fuel stored at cryogenic temperature and supercritical pressure, are chosen for use in the cold Martian environment because of their low-temperature operation, faster start-ups, swift response to changes in power demand, and high power density with a lower weight and volume than other fuel cell types. An aerobot equipped with a fuel cell system would be transported to Mars with a limited fuel supply, making the mission either a disposable or short-term reusable type, as demonstrated in the MARV (Martian Autonomous Rotary-Wing Vehicle) concept [125] and MIRAGE (Mars Intelligent

Reconnaissance Aerial and Ground Explorer) [126]. Continuous operation could only be achieved if a regenerative fuel cell (RFC) is used in combination with a solar power system, as considered in concepts like GTMARS (Georgia Tech Martian Autonomous Rotorcraft System) [127] and Mars Airship-Rover System [128]. The RFC system utilises electricity that is generated and stored diurnally via solar energy to dissociate liquid water, gathered as a by-product during the electricity generation process, back into gaseous hydrogen and oxygen through water electrolysis, thus creating a closed-loop system. RFC can be a superior electricity storage unit alternative to batteries for solar electric power on Mars due to its high specific energy, storage capacity, and power delivery, as it is deemed that longer discharge periods (such as nocturnal) along with higher energy storage requirements add a huge penalty to the battery mass and complexity [129]. Alternatively, a solid oxide fuel cell (SOFC) can generate power from carbon monoxide and oxygen, using Mars' CO_2, making it ideal for long-term missions that minimize reliance on Earth-supplied resources. However, SOFCs operate at over 800 °C, requiring complex thermal management and added system mass, which likely confines them to lander-based applications [83] [129].

Power generation using wind turbines has not been widely considered for Martian aerobots, though studies are exploring wind turbines to complement solar power for human settlements, especially during global dust storms when winds are high but sunlight is minimal. Wind turbines alone cannot generate sufficient energy in Mars' thin atmosphere, and ground-based systems would require massive structures, such as a 50-meter hub with a rotor diameter of over 80 meters [130]. Modern airborne wind energy systems are proposed as a better alternative [130]; these systems involve tethered airborne devices, such as kites or drones, that capture wind energy at higher altitudes where winds are stronger and more consistent. Aerobots could either serve as part of these systems or assist in their deployment and maintenance. Alternatively, NASA is reviewing a smaller, foldable turbine with 2-meter diameter blades, called the Planet Turbine Anemometer (PTA) [131]. Although wind energy harvesting on Mars is still an underdeveloped field, it has the potential to recharge Martian aerobots, particularly in polar regions and during global dust storms.

2.6.2.4 Aerobot Types for Mars

The final step in the Mars Aerobot Design Thinking Matrix, shown in Fig. 2.18, involves deciding on the type of aerobot most suitable for the specific Mars mission. Fig. 2.21 Categories Chart of Aerobot Types for Mars illustrates a comprehensive categorisation of aerobot types, showcasing the various aerial vehicle designs proposed in the literature to fly on Mars. The classification is divided into five main categories: Fixed Wing, Rotorcraft, Aerostat, Gashopper, and Ornithopter, each representing a distinct approach to overcoming the unique challenges posed by Mars' thin atmosphere and harsh environmental conditions.

Fixed-wing is the oldest and most commonly proposed design, with many variants in the list of conceptual aerobots for Mars. Fixed-wing aerobots rely on traditional winged structures to generate lift. This category includes subtypes such as Conventional, Rotary-VTOL, Jet-VTOL, Rotary-Tailsitter, and Glider, highlighting the versatility within fixed-wing configurations. Conventional designs might be suited for long, sustained flights, while VTOL (Vertical Take-Off and Landing) variants combine the benefits of fixed wings with the ability to take off and land vertically, crucial in Mars' varied terrain. Gliders, which do not rely on continuous propulsion, could exploit Mars' atmospheric conditions for energy-efficient flight over extended distances.

Rotorcraft aerobots, including Unicopter, Multicopter, Coaxial Multicopter, and Gyrocopter, are characterised by their rotating blades, which provide lift and thrust. These designs offer superior manoeuvrability and the ability to hover, making them ideal for detailed surface exploration and navigation through complex landscapes. Multicopter designs, with their multiple rotors, provide enhanced stability and control, crucial for precise operations in Mars' unpredictable wind patterns.

Aerostats are lighter-than-air vehicles that rely on buoyancy rather than aerodynamic lift. This category includes Uncontrolled Balloons, Controlled Balloons, and Airships. These vehicles are particularly suited for long-duration missions, where energy efficiency and the ability to remain aloft for extended periods are paramount. Controlled balloons and airships can navigate more

effectively, allowing for targeted exploration of specific areas on Mars, such as canyons or craters.

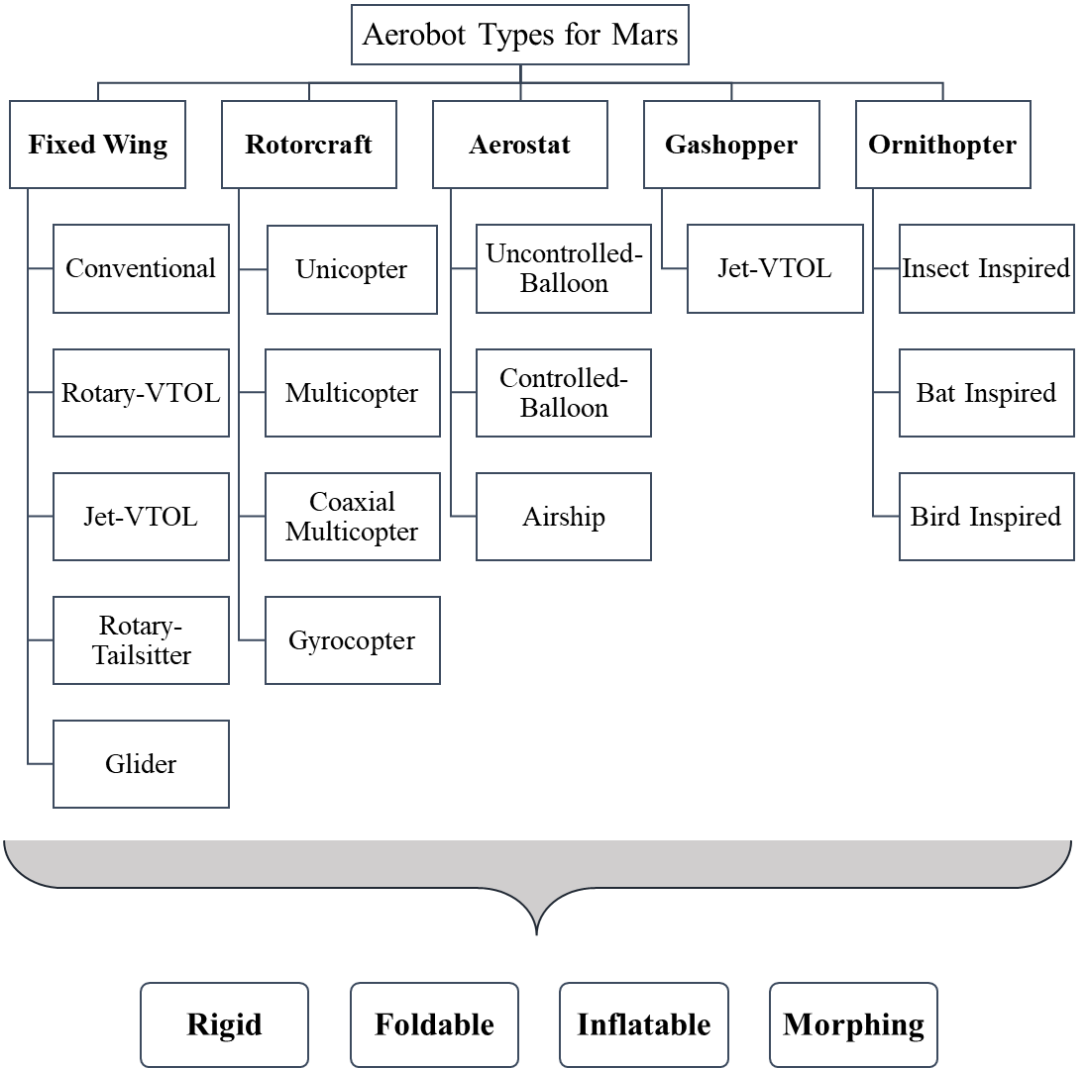


Fig. 2.21 Categories Chart of Aerobot Types for Mars proposed in the literature

The Gashopper category is represented by Jet-VTOL designs, which are capable of vertical take-off and landing using jet propulsion. These aerobots could potentially use Martian resources, such as carbon dioxide from the atmosphere, to generate thrust. This type of vehicle could enable quick hops from one location to another, facilitating rapid exploration of Mars' diverse terrain.

Ornithopters are bio-inspired designs that mimic the flapping wings of birds, bats, or insects. Subtypes include Insect-Inspired, Bat-Inspired, and Bird-Inspired designs. These vehicles could take advantage of Mars' thin atmosphere by using

flexible wings that adapt to changing conditions, offering a unique approach to flight that combines agility with energy efficiency. Ornithopters could be particularly useful for navigating through narrow spaces or for missions requiring a combination of hovering and gliding.

Beneath these categories, the diagram also highlights potential structural configurations of these aerobots: Rigid, Foldable, Inflatable, and Morphing. Rigid designs provide structural stability, Foldable designs offer compact storage and deployment capabilities, Inflatable designs can expand upon reaching Mars, reducing the space required during transport, and Morphing structures can dynamically change shape to adapt to varying flight conditions or mission requirements. This flexibility in design allows for a tailored approach to addressing the specific challenges of Mars exploration, enabling a wide range of mission types and operational strategies.

Overall, the diversity of potential aerobot designs underscores the importance of selecting the right configuration to meet the specific demands of Mars' environment, whether for detailed surface mapping, atmospheric sampling, or long-distance exploration. Each type offers unique advantages, and the choice of design will depend on the mission objectives, the specific environmental challenges, and the resources available for the mission.

2.7 Conclusion

The exploration of Mars represents a critical frontier in our understanding of the solar system, with aerobots emerging as indispensable assets in this mission. This paper presents a comprehensive framework for the design, development, and deployment of Martian aerobots, addressing the complex challenges inherent in Mars exploration. The pursuit of scientific objectives on Mars, such as the search for life, climate analysis, and geological investigation, necessitates the deployment of specialised aerial platforms capable of navigating the planet’s unique environmental conditions. Mars’ thin atmosphere, extreme temperature variations, and rugged topography impose stringent requirements on aerobot design, necessitating innovative approaches in aerodynamics, propulsion, and materials science. A detailed examination of Mars' topography and atmospheric

conditions underscores the importance of optimising aerodynamics and propulsion systems. These systems must generate sufficient lift and maintain stability in a low-density atmosphere, requiring the precise design of rotor blades and airfoils, as well as efficient propulsion mechanisms. Structural integrity is paramount, demanding lightweight yet robust materials capable of withstanding Mars' harsh climate, including dust storms and temperature fluctuations. The integration of advanced thermal management and dust mitigation strategies is crucial for long-term operational viability. Furthermore, the design of aerobots must consider the constraints imposed by the aeroshell during the entry, descent, and landing phases, which limit the size and shape of the aerobot. Autonomous navigation and real-time adaptability are essential features, given the communication delays between Earth and Mars. Aerobots must be capable of independent decision-making, responding dynamically to environmental changes. The Mars Aerobot Design Thinking Matrix introduced in this study provides a strategic tool for optimising design choices, ensuring that the final aerobot configuration aligns with both mission objectives and the practical constraints of Martian operations. This framework represents a significant contribution to the field, offering a structured approach to the development of aerial robotic systems tailored for Mars exploration.

Future research should prioritise advancements in aerodynamics and propulsion systems, focusing on refining designs that optimise performance within the constraints of Mars’ low-density atmosphere and aeroshell limitations. Enhancing autonomous systems will be critical to improving aerobot navigation and adaptability in the unpredictable Martian environment. Additionally, further innovation in energy management, including the development of more efficient power sources and storage solutions, will be essential for extending mission durations. Continued emphasis on the development of materials capable of enduring Mars' extreme conditions will ensure the reliability and longevity of aerobots, thereby supporting the broader objectives of future Martian missions.

References

[1] Vernikos, J. (2008). Human Exploration of Space: why, where, what for? Hippokratia, 12(Suppl 1), 6-9.

[2] Shea, G (NASA Web Editor). (2023.). Why Go to Space? Retrieved September 3, 2024, from https://www.nasa.gov/humans-in-space/why-go-to-space/.

[3] NASA SMD Content Editors. (2024) Mars - NASA Science. Retrieved September 03, 2024, from https://science.nasa.gov/mars/

[4] Williams, D. R. (NASA Web Editor). (2022) Mariner 2 NASA - NSSDCA - Spacecraft - Details. Retrieved September 03, 2024, from https://nssdc.gsfc.nasa.gov/nmc/spacecraft/display.action?id=1962-041A

[5] Williams, D. R. (NASA Web Editor). (2024) Venus Exploration Timeline. Retrieved September 03, 2024, from https://nssdc.gsfc.nasa.gov/planetary/chronology_venus.html

[6] Williams, D. R. (NASA Web Editor). (2022) Venera 13 Descent Craft NASA - NSSDCA - Spacecraft - Details. Retrieved September 03, 2024, from https://nssdc.gsfc.nasa.gov/nmc/spacecraft/display.action?id=1981-106D

[7] Svedhem, H., Titov, D., Taylor, F. et al. Venus as a more Earth-like planet. Nature 450, 629–632 (2007). https://doi.org/10.1038/nature06432

[8] Williams, D. R. (NASA Web Editor). (2024) Planetary Fact Sheet. Retrieved September 03, 2024, from https://nssdc.gsfc.nasa.gov/planetary/factsheet/

[9] NASA SMD Content Editors. (2024) Venus: Facts - NASA Science. Retrieved September 03, 2024, from https://science.nasa.gov/venus/venus-facts/

[10] Williams, D. R. (NASA Web Editor). (2022) Vega 1 Balloon NASA - NSSDCA - Spacecraft - Details. Retrieved September 03, 2024, from https://nssdc.gsfc.nasa.gov/nmc/spacecraft/display.action?id=1984-125F

[11] NASA SMD Content Editors. (2024) Mars: Facts - NASA Science. Retrieved September 03, 2024, from https://science.nasa.gov/mars/facts/

[12] Piqueux, S., Byrne, S., Kieffer, H. H., Titus, T. N., & Hansen, C. J. (2015). Enumeration of Mars years and seasons since the beginning of telescopic exploration. Icarus, 251, 332-338. https://doi.org/10.1016/j.icarus.2014.12.014

[13] Tamsyn Brann. (2020) MAVEN Maps Electric Currents around Mars that are Fundamental to Atmospheric Loss - NASA. Retrieved September 03, 2024,

from https://www.nasa.gov/news-release/maven-maps-electric-currents-around-mars-that-are-fundamental-to-atmospheric-loss/

[14] Williams, D. R. (NASA Web Editor). (2022) ExoMars Rover NASA - NSSDCA - Spacecraft - Details. Retrieved September 03, 2024, from https://nssdc.gsfc.nasa.gov/nmc/spacecraft/display.action?id=EXOMARS22

[15] Hanneke Weitering. (2016) US Will Send People to Mars by 2030s, Barack Obama Says | Space. Retrieved September 03, 2024, from https://www.space.com/34351-obama-says-america-will-send-people-to-mars.html

[16] Williams, D. R. (NASA Web Editor). (2022) Mariner 4 NASA - NSSDCA - Spacecraft - Details. Retrieved September 03, 2024, from https://nssdc.gsfc.nasa.gov/nmc/spacecraft/display.action?id=1964-077A

[17] Hartmann, W. K., Raper, O. (1974). The New Mars: The Discoveries of Mariner 9 : Prepared for the NASA Office of Space Science. United States: Scientific and Technical Information Office, NASA. Retrieved September 03, 2024, from https://ntrs.nasa.gov/citations/19750005657

[18] Williams, D. R. (NASA Web Editor). (2024) Mars Exploration Timeline. Retrieved September 03, 2024, from https://nssdc.gsfc.nasa.gov/planetary/chronology_mars.html

[19] Williams, D. R. (NASA Web Editor). (2022) Mariner 9 NASA - NSSDCA - Spacecraft - Details. Retrieved September 03, 2024, from https://nssdc.gsfc.nasa.gov/nmc/spacecraft/display.action?id=1971-051A

[20] Cox, B. (Presenter). (2010). Wonders of the Solar System, Original Series, Dead or Alive, Olympus Mons on Mars [Video]. BBC Two. Retrieved September 03, 2024, from https://www.bbc.co.uk/programmes/p0073lg1

[21] Cox, B. (Presenter). (2010). Wonders of the Solar System, Original Series, Dead or Alive, Valles Marineris on Mars [Video]. BBC Two. Retrieved September 03, 2024, from https://www.bbc.co.uk/programmes/p0070j7d

[22] Gulf Times. (2018, March 11). The long Venusian day. Gulf Times. Retrieved September 3, 2024, from https://www.gulf-times.com/story/585526/the-long-venusian-day

[23] Messier, D. M. (1996). Soviet/Russian Mars program. Instituto de Física da UFRGS. Retrieved September 3, 2024, from http://astro.if.ufrgs.br/solar/sovmars.htm

[24] Samuelson, A (NASA JPL Web Editor). (2019) How an Atomic Clock Will Get Humans to Mars on Time. NASA JPL Caltech. Retrieved September 03, 2024,

from https://www.jpl.nasa.gov/news/how-an-atomic-clock-will-get-humans-to-mars-on-time

[25] Osnat Katz. (2021) Landing on Mars is difficult, often fails, and will never be risk-free. Retrieved September 3, 2024, from https://phys.org/news/2021-05-mars-difficult-risk-free.html

[26] NASA SMD Content Editors. (2024) Viking Project - NASA Science. Retrieved September 03, 2024, from https://science.nasa.gov/mission/viking/

[27] NASA SMD Content Editors. (2024) Spirit And Opportunity By The Numbers - NASA Science. Retrieved September 03, 2024, from https://science.nasa.gov/resource/spirit-and-opportunity-by-the-numbers/

[28] Balaram, J., Aung, M., Matthew, ·, Golombek, P., Farley, K. A., Williford, K. H., Stack, K. M., Aung, M., & Golombek, M. P. (2021). The Ingenuity Helicopter on the Perseverance Rover. https://doi.org/10.1007/s11214-021-00815-w

[29] NASA SMD Content Editors. (2024) Perseverance Rover Components - NASA Science. Retrieved September 03, 2024, from https://science.nasa.gov/mission/mars-2020-perseverance/rover-components/

[30] NASA SMD Content Editors. (2024) Perseverance Rover Location Map - NASA Science. Retrieved September 03, 2024, from https://science.nasa.gov/mission/mars-2020-perseverance/location-map/

[31] NASA SMD Content Editors. (2024) Curiosity Rover Location Map - NASA Science. Retrieved September 03, 2024, from https://science.nasa.gov/mission/msl-curiosity/location-map/

[32] Banfield Et Al. Mars Science Goals, Objectives, Investigations, and Priorities: 2020 Version Mars Exploration Program Analysis Group (MEPAG) Prepared by the MEPAG Goals Committee. Retrieved September 3, 2024, from https://mepag.jpl.nasa.gov/reports.cfm?expand=science

[33] Radotich, M., Withrow-Maser, S., Gelhar, S., & Gallagher, H. (2021). A study of past, present, and future Mars rotorcraft. Vertical Flight Society's 9th Biennial Autonomous VTOL Technical Meeting, Virtual, January 26-28, 2021. NASA. Retrieved September 3, 2024, from https://ntrs.nasa.gov/api/citations/20210000448/downloads/1459_Radotich_011321.pdf

[34] Yu-Yan Sara Zhao , Disheng Zhou , Xiongyao Li, Jianzhong Liu, Shijie Wang , Ziyuan Ouyang. (2020). The evolution of scientific goals for Mars exploration

and future prospects. National Science Review, 65, 7. https://doi.org/10.1360/TB-2019-0638

[35] Grant, J. A., Golombek, M. P., Wilson, S. A., Farley, K. A., Williford, K. H., & Chen, A. (2018). The science process for selecting the landing site for the 2020 Mars rover. Planetary and Space Science, 164, 106–126. https://doi.org/10.1016/J.PSS.2018.07.001

[36] U.S. Geological Survey. (1998). Topographic map of Mars (USGS I Map 2782). U.S. Department of the Interior. Retrieved January 7, 2022, from https://pubs.usgs.gov/imap/i2782/

[37] Rodrigue, C. M. (2024). Areography: A regional geography of Mars. Department of Geography, California State University. Retrieved July 10, 2024, from https://home.csulb.edu/~rodrigue/mars/finallect.html

[38] NASA/JPL-Caltech Web Team. (2001). Airy-0: The Martian Prime Meridian Crater. NASA Photojournal. Retrieved September 3, 2024, from https://photojournal.jpl.nasa.gov/catalog/PIA03207

[39] Smith, D. E., Zuber, M. T., Frey, H. v, Garvin, J. B., Head, J. W., Muhleman, D. O., Pettengill, G. H., Phillips, R. J., Solomon, S. C., Zwally, H. J., Banerdt, Ø. B., Duxbury, T. C., Golombek, M. P., Lemoine, F. G., Neumann, G. A., Rowlands, D. D., Aharonson, O., Ford, P. G., Iranov, A. B., … Sun, X. (2001). Mars Orbiter Laser Altimeter: Experiment summary after the first year of global mapping of Mars. JOURNAL OF GEOPHYSICAL RESEARCH, 106, 689–712. https://doi.org/10.1029/2000JE001364

[40] NASA/JPL-Caltech Web Team. (2002). MGS MOC Mars Digital Map. NASA Photojournal. Retrieved September 3, 2024, from https://photojournal.jpl.nasa.gov/catalog/PIA03467

[41] Solomon, Sean & Head, James. (1982). Evolution of the Tharsis Province of Mars: The importance of heterogeneous lithospheric thickness and volcanic construction. Journal of Geophysical Research. 87. https://doi.org/10.1029/JB087iB12p09755

[42] U.S. Geological Survey. (no date). Mars 1:5,000,000 THEMIS quadrangles. USGS Astrogeology Science Center. Retrieved September 3, 2024, from https://planetarynames.wr.usgs.gov/Page/mars1to5mTHEMIS

[43] Farley, K. A., Williford, K. H., Stack, K. M., Bhartia, R., Chen, A., de la Torre, M., Hand, K., Goreva, Y., Herd, C. D., Hueso, R., Liu, Y., Maki, J. N., Martinez, G., Moeller, R. C., Nelessen, A., Newman, C. E., Nunes, D., Ponce, A., Spanovich, N., … Liu, Y. (2020). Mars 2020 Mission Overview. Space Sci Rev. https://doi.org/10.1007/s11214-020-00762-y

[44] HiRISE. (2024). High Resolution Imaging Science Experiment – Catalog (use search box). University of Arizona. Retrieved September 03, 2024, from https://www.uahirise.org/catalog/

[45] Christensen, P.R.; Engle, E.; Anwar, S.; Dickenshied, S.; Noss, D.; Gorelick, N.; Weiss-Malik, M.; JMARS – A Planetary GIS, http://adsabs.harvard.edu/abs/2009AGUFMIN22A..06C

[46] Sharp, R. P. (1973), Mars: Fretted and chaotic terrains, J. Geophys. Res., 78(20), 4073–4083, doi:10.1029/JB078i020p04073

[47] Ojha, L., Lewis, K., Karunatillake, S., & Schmidt, M. (n.d.). The Medusae Fossae Formation as the single largest source of dust on Mars. https://doi.org/10.1038/s41467-018-05291-5

[48] Williams, D. R. (NASA Web Editor). (2024) Mars Fact Sheet. Retrieved September 06, 2024, from https://nssdc.gsfc.nasa.gov/planetary/factsheet/marsfact.html

[49] Antonio Genova. (2017) PGDA - Mars Gravity Field: GMM-3. Retrieved September 06, 2024, from https://pgda.gsfc.nasa.gov/products/57

[50] Wörner, Lisa & Root, Bart & Bouyer, Philippe & Braxmaier, Claus & Dirkx, Dominic & Encarnarcao, Joao & Hauber, Ernst & Hussmann, Hauke & Karatekin, Ozgur & Koch, Alexander & Kumanchik, Lee & Migliaccio, Federica & Reguzzoni, Mirko & Ritter, Birgit & Schilling, Manuel & Schubert, Christian & Thieulot, Cedric & Klitzing, Wolf & Witasse, Olivier. (2023). MaQuIs - Mars Quantum Gravity Mission. 10.22541/essoar.167397424.46877056/v1

[51] MCD Team. (2024) Martian Seasons and Solar Longitude Ls. Retrieved September 06, 2024, from https://www-mars.lmd.jussieu.fr/mars/time/solar_longitude.html

[52] North, Gerald R. Pyle, John Zhang, Fuqing. (2015). Encyclopedia of Atmospheric Sciences, 6 Volume Set (2nd Edition) - 34.2 Planetary Atmospheres: Mars. Elsevier. Retrieved September 06, 2024 https://app.knovel.com/hotlink/pdf/id:kt011A9C71/encyclopedia-atmospheric/planetary-atmospheresb

[53] Mars Education Program (ASU) Team. (2024) Mars Education | Atmosphere. Retrieved September 06, 2024, from https://marsed.asu.edu/mep/atmosphere

[54] Petrosyan, A., et al. (2011), The Martian atmospheric boundary layer, Rev. Geophys., 49, RG3005, doi:10.1029/2010RG000351

[55] Delaune, J., Izraelevitz, J., Sklyanskiy, E., Schutte, A., Fraeman, A., Scott, V., Leake, C., Ballesteros, E., Aaron, K., Young, L. A., Johnson, W., Withrow-Maser, S., Cummings, H., Bhagwat, R., Veismann, M., Wei, S., Lee, R., Madrid, L. P., Gharib, M., … Rapin, W. (2020). Motivations and preliminary design for mid-air deployment of a science rotorcraft on mars. Accelerating Space Commerce, Exploration, and New Discovery Conference, ASCEND 2020. Virtual Event. https://doi.org/10.2514/6.2020-4030

[56] Mars Education Program (ASU) Team. (2024) Mars Education | Dust. Retrieved September 06, 2024, from https://marsed.asu.edu/mep/dust

[57] Mars Education Program (ASU) Team. (2024) Mars Education | Wind. Retrieved September 06, 2024, from https://marsed.asu.edu/mep/wind

[58] Millour, E., Forget, F., Spiga, A., Pierron, T., Bierjon, A., Montabone, L., Vals, M., Lefèvre, F., Chaufray, J.-Y., Lopez-Valverde, M., Gonzalez-Galindo, F., Lewis, S., Read, P., Desjean, M.-C., and Cipriani, F. and the MCD Team: The Mars Climate Database (Version 6.1), Europlanet Science Congress 2022, Granada, Spain, 18–23 Sep 2022, EPSC2022-786, https://doi.org/10.5194/epsc2022-786

[59] Lavagna, M., Colagrossi, A., Pesce, V., Punzi, C., & Ciarambino, M. (2015). ARMONIA: Feasibility Study on Aerobots in Martian Atmosphere to Enhance Science Return. Presented at the 66th International Astronautical Congress, Jerusalem, Israel.

[60] Youhanna V, Felicetti L & Ignatyev D (2024). Preliminary Investigation into Future Martian Multicopter Configurations. In: Vertical Flight Society's 80th Annual Forum & Technology Display, Montréal, Québec, Canada, May 7-9, 2024. https://doi.org/10.4050/F-0080-2024-1266

[61] NASA. (2021). Mars Global Reference Atmospheric Model (Mars-GRAM): User Guide. NASA Technical Reports Server. Retrieved September 06, 2024 https://ntrs.nasa.gov/api/citations/20210023957/downloads/Mars-GRAM%20User%20Guide.pdf

[62] Guy Webster, JPL NASA. (2024) NASA Mars Orbiters Reveal Seasonal Dust Storm Pattern. Retrieved July 25, 2024, from https://www.jpl.nasa.gov/news/nasa-mars-orbiters-reveal-seasonal-dust-storm-pattern

[63] Lemmon, M. T., Lorenz, R. D., Rabinovitch, J., Newman, C. E., Williams, N. R., Sullivan, R., Golombek, M. P., Bell, J. F., 3rd, Maki, J. N., & Vicente-Retortillo, A. (2022). Lifting and Transport of Martian Dust by the Ingenuity Helicopter Rotor Downwash as Observed by High-Speed Imaging from the

Perseverance Rover. Journal of geophysical research. Planets, 127(12). https://doi.org/10.1029/2022JE007605

[64] Wang, Justin & Rosenbaum, Jeremy & Prasad, Ajay & Raad, Robert & Putman, Esther & Aintablian, H & Hynek, B. (2024). Geological Health Hazards from Martian Dust and Appropriate Countermeasures for the Human Exploration of Mars. In: 55th Lunar and Planetary Science Conference. Texas and virtually on March 11–15, 2024.

[65] University Of Oregon. (2024) Experiments Find That Electrical Sparks Are Possible on Mars. Retrieved July 27, 2024, from https://scitechdaily.com/experiments-find-that-electrical-sparks-are-possible-on-mars/

[66] Nancy Atkinson. (2024) Glowing Helicopters on Mars - Universe Today. Retrieved September 06, 2024, from https://www.universetoday.com/154356/glowing-helicopters-on-mars/

[67] National Research Council. 2002. Safe on Mars: Precursor Measurements Necessary to Support Human Operations on the Martian Surface. Washington, DC: The National Academies Press. Chap 3. https://doi.org/10.17226/10360

[68] Fraser Cain. (2005) Static Electricity... in Space - Universe Today. Retrieved September 06, 2024, from https://www.universetoday.com/10830/static-electricity-in-space/

[69] Nancy Atkinson. (2022) Martian Dust is Starting to Darken Ingenuity's Solar Panels - Universe Today. Retrieved September 06, 2024, from https://www.universetoday.com/155864/martian-dust-is-starting-to-darken-ingenuitys-solar-panel/

[70] Clavé, E., et al. (2024). Radiation-induced alteration of apatite on the surface of Mars: first in situ observations with SuperCam Raman onboard Perseverance. Scientific Reports, 14, 11284. https://doi.org/10.1038/s41598-024-61494-5

[71] I. Jun, H. Garrett, W. Kim et al. (2024) A review on radiation environment pathways to impacts: Radiation effects, relevant empirical environment models, and future needs, Advances in Space Research, 2024, ISSN 0273-1177 https://doi.org/10.1016/j.asr.2024.03.079

[72] Larson, K., & Fries, M. (2017). Ultraviolet Testing of Space Suit Materials for Mars. In 47th International Conference on Environmental Systems. Charleston, South Carolina. NASA Johnson Space Center.

https://ntrs.nasa.gov/api/citations/20170002050/downloads/20170002050.pdf

[73] Calle, L. M. (2019). Corrosion on Mars: Effect of the Mars environment on spacecraft materials (NASA Technical Publication No. 2019–220238). National Aeronautics and Space Administration, John F. Kennedy Space Center. Available at https://ntrs.nasa.gov/citations/20190027256

[74] Abd El-Hameed, A. M. (2022). Radiation effects on composite materials used in space systems: A review. NRIAG Journal of Astronomy and Geophysics, 11(1), 313-324. https://doi.org/10.1080/20909977.2022.2079902

[75] Web Team (Aerospace Testing International). (2020) How enigneers test the radiation shielding of electronics in space vehicles | Aerospace Testing International. Retrieved September 06, 2024, from https://www.aerospacetestinginternational.com/features/requirements-are-changing-for-the-testing-of-electronics-used-on-board-space-vehicles.html

[76] Analog Devices, Inc (Team). (2023) Mars Perseverance and Hardened Technology in Extreme Environments | Analog Devices. Retrieved August 15, 2024, from https://www.analog.com/en/signals/articles/mars-perseverance-hardened-technology.html

[77] Evan Ackerman. (2021) JPL's Plan for the Next Mars Helicopter - IEEE Spectrum. Retrieved August 15, 2024, from https://spectrum-ieee-org.cdn.ampproject.org/c/s/spectrum.ieee.org/amp/the-next-mars-helicopter-2654506042

[78] Young, L. A., Aiken, E. W., Lee, P., & Briggs, G. A. (2004). Mars rotorcraft: Possibilities, limitations, and implications for human/robotic exploration. NASA Technical Reports Server. Retrieved January 21, 2025, from https://ntrs.nasa.gov/citations/20090028805

[79] Young, L., Cummings, H., Withrow-Maser, S., Pisanich, G., Lee, P., Briggs, G., & Aiken, E. (2021). The future of rotorcraft and other aerial vehicles for Mars exploration. In: Vertical Flight Society's 77th Annual Forum & Technology Display, Virtual, 2021 May 10-14. https://doi.org/10.4050/F-0077-2021-16699

[80] Guo, J., Hassler, D.M., Zeitlin, C., Wimmer-Schweingruber, R.F., et al. (2022). The Martian Surface Radiation Environment at Solar Minimum Measured with MSL/RAD. Icarus, 384, 115035. https://doi.org/10.1016/j.icarus.2022.115035

[81] Ramos RL, Carante MP, Ferrari A, Sala P, Vercesi V, Ballarini F. A Mission to Mars: Prediction of GCR Doses and Comparison with Astronaut Dose

Limits. International Journal of Molecular Sciences. 2023; 24(3):2328. https://doi.org/10.3390/ijms24032328

[82] Michael McAuley (NASA/JPL). (2002) Catalog Page for PIA03480. Retrieved August 15, 2024, from https://photojournal.jpl.nasa.gov/catalog/PIA03480

[83] Badescu, V. (2009). Mars: prospective energy and material resources (1st ed. 2009.). Springer. Chaps. 1,2,3. https://doi.org/10.1007/978-3-642-03629-3

[84] Shubbak, M., 2019. Advances in solar photovoltaics: Technology review and patent trends. Renewable and Sustainable Energy Reviews, Vol. 115(Nov), pp. 109383. https://doi.org/10.1016/j.rser.2019.10938

[85] Li, J. & Aierken, Abuduwayiti & Liu, Y. & Zhuang, Yu & Yang, X. & Mo, J. & Fan, R. & Chen, Q. & Zhang, S. & Huang, Y. & Zhang, Q.. (2021). A Brief Review of High Efficiency III-V Solar Cells for Space Application. Frontiers in Physics. 8. https://doi.org/10.3389/fphy.2020.631925

[86] Solaero Technologies Corp. (2021) SolAero Technologies' Solar Panel Powers NASA's Mars Helicopter - Ingenuity. Retrieved August 11, 2024, from https://www.prnewswire.com/news-releases/solaero-technologies-solar-panel-powers-nasas-mars-helicopter---ingenuity-301271650.html

[87] National Renewable Energy Laboratory. (2024) Best Research-Cell Efficiency Chart | Photovoltaic Research | NREL. Retrieved August 10, 2024, from https://www.nrel.gov/pv/cell-efficiency.html

[88] Landis, G. A., Kerslake, T. W., Jenkins, P. P., & Scheiman, D. A. (2004). Mars solar power (NASA/TM—2004-213367). National Aeronautics and Space Administration, Glenn Research Center. https://ntrs.nasa.gov/citations/20040191326.

[89] McMillon-Brown, L., Peshek, T. J., Pal, A., & McNatt, J. (2020). A study of photovoltaic degradation modes due to dust interaction on Mars. Solar Energy Materials & Solar Cells, 221, 110880. https://doi.org/10.1016/j.solmat.2020.110880

[90] Afshar-Mohajer, Nima & Wu, Chang-Yu & Curtis, Jennifer & Gaier, James. (2015). Review of dust transport and mitigation technologies in lunar and Martian atmospheres. Advances in Space Research. 56(6), 1212-1229. https://doi.org/10.1016/j.asr.2015.06.007

[91] Young, L. A., Chen, R. T. N., Aiken, E. W., Briggs, G. A. (2019) "Design Opportunities and Challenges in the Development of Vertical Lift Planetary Aerial Vehicles," Proceedings of the American Helicopter Society International Vertical Lift Aircraft Design Specialist's Meeting, January 2000. Retrieved September 06, 2024

https://rotorcraft.arc.nasa.gov/Publications/files/Young_AHS_Design2000.pdf

[92] Benjamin T. Pipenberg, Matthew Keennon, Jeremy Tyler, Bart Hibbs, Sara Langberg, J. (Bob) Balaram, Håvard F. Grip and Jack Pempejian. (2019) "Design and Fabrication of the Mars Helicopter Rotor, Airframe, and Landing Gear Systems," AIAA 2019-0620. AIAA Scitech 2019 Forum. January 2019. https://doi.org/10.2514/6.2019-0620

[93] Anyoji, M., Nagai, H., & Asai, K. (2009). Development of low-density wind tunnel to simulate atmospheric flight on Mars. Proceedings of the 47th AIAA Aerospace Sciences Meeting Including The New Horizons Forum and Aerospace Exposition, January 5-8, 2009, Orlando, Florida. https://doi.org/10.2514/6.2009-1517

[94] Veismann, M., Dougherty, C., Rabinovitch, J., Quon, A., & Gharib, M. (2021). Low-density multi-fan wind tunnel design and testing for the Ingenuity Mars Helicopter. Experiments in Fluids, 62(9). https://doi.org/10.1007/s00348-021-03278-5

[95] Wu, H., Liu, M., Mi, Y., Wang, J., & Guo, M. (2022). Key parameters of a design for a novel reflux subsonic low-density dust wind tunnel. Aerospace, 9(662). https://doi.org/10.3390/aerospace9110662

[96] Schuerger, Andrew C., and Adriana V. Borrell. (2023). "Shock-Impacts and Vibrational g-Forces Can Dislodge Bacillus spp. Spores from Spacecraft Surfaces" Microorganisms 11, no. 10: 2421. https://doi.org/10.3390/microorganisms1110242

[97] ESA Web Team. (2019) ESA - Robotic Exploration of Mars - The hazards of landing on Mars. Retrieved August 20, 2024, from https://exploration.esa.int/web/mars/-/58307-the-hazards-of-landing-on-mars

[98] Johnson, W., Withrow-Maser, S., Young, L., Malpica, C., Koning, W. J. F., Kuang, W., Fehler, M., Tuano, A., Chan, A., Datta, A., Chi, C., Lumba, R., Escobar, D., Balaram, J., Tzanetos, T., & Fjaer Grip, H. (2020). Mars Science Helicopter Conceptual Design. http://www.sti.nasa.gov

[99] NASA. (2020) Mars 2020 Perseverance Launch Press Kit | Mission Overview. Retrieved August 20, 2024, from https://www.jpl.nasa.gov/news/press_kits/mars_2020/launch/mission/

[100] Youhanna, V., Ignatyev, D., Felicetti, L., (2022). Futuristic Martian Aerobot Design. UKRAS22 Conference “Robotics for Unconstrained Environments” Proceedings, 64-65. doi: http://doi.org/10.31256/Ec2Na5W

[101] SpaceX Web Team. (2024) SpaceX - Starship. Retrieved August 20, 2024, from https://www.spacex.com/vehicles/starship/

[102]SpaceX Team. (2020) Starship Users Guide. SpaceX. Retrieved August 20, 2024, from https://www.spacex.com/media/starship_users_guide_v1.pdf

[103]Lee Mohon. (2024) NASA Artemis Mission Progresses with SpaceX Starship Test Flight - NASA. Retrieved August 20, 2024, from https://www.nasa.gov/directorates/esdmd/artemis-campaign-development-division/human-landing-system-program/nasa-artemis-mission-progresses-with-spacex-starship-test-flight/aceX Media Team. (2024) SpaceX - Updates - ON THE PATH TO RAPID REUSABILITY. Retrieved August 20, 2024, from https://www.spacex.com/updates/

[104]SpaceX Media Team. (2024) SpaceX - Missions: Mars. Retrieved August 20, 2024, from https://www.spacex.com/humanspaceflight/mars/

[105]Ian Webster. (2024) $230 in 1997 → 2024 | Inflation Calculator. Retrieved August 22, 2024, from https://www.officialdata.org/us/inflation/1997?amount=230

[106]The Planetary Society Team. (2024) The Cost of NASA's Phoenix Mission to Mars | The Planetary Society. Retrieved August 22, 2024, from https://www.planetary.org/space-policy/phoenix-cost

[107]The Planetary Society Team. (2024) Cost of Perseverance | The Planetary Society. Retrieved August 22, 2024, from https://www.planetary.org/space-policy/cost-of-perseverance

[108]Hassanalian, M., Rice, D., & Abdelkefi, A. (2018). Evolution of space drones for planetary exploration: A review. Progress in Aerospace Sciences, 97, 2018. 61–105. https://doi.org/10.1016/J.PAEROSCI.2018.01.003

[109]Mindy Weisberger. (2021) Meet Au-Spot, the AI robot dog that's training to explore caves on Mars | Space. Retrieved September 02, 2024, from https://www.space.com/ai-mars-robot-dogs-agu

[110]NASA Langley Research Center. (2017) NASA Langley Engineers Propose Mars Flyer Concept - YouTube. Retrieved September 01, 2024, from https://www.youtube.com/watch?v=9xjHCHR5_50

[111](NASA) Alesyn Lowry . (2018) NASA TechPort - Project Data. Retrieved September 01, 2024, from https://techport.nasa.gov/view/93850

[112]Novaković, Z., Vasić, Z., Ilić, I., Medar, N., & Stevanović, C. (2016). Integration of тactical-medium range UAV and catapult launch system. Scientific Technical Review, 66(4), 22-28. DOI:10.5937/STR1604022N

[113]Tamir Eshel. (2017) Lockheed Martin UK Developed a Submarine-Launched UAV - Defense Update:. Retrieved September 01, 2024, from http://defense-update.com/20170912_outrider.html

[114]Colozza, A., Landis, G., & Lyons, V. (2003, July). Overview of innovative aircraft power and propulsion systems and their applications for planetary exploration. In International Air and Space Symposium and Exposition (No. E-13998).

[115]Stocking, P., and Summer, L., “M-4 Minerva Mars Atmospheric Flight Vehicle and CRATER Drop Test Vehicle Project Executive Summary,” Department of Power, Propulsion, and Aerospace Engineering, School of Engineering, Cranfield University, UK, May 2005.

[116]National Aeronautics and Space Administration (NASA). (2010). NASA's contributions to aeronautics: Flight environment, operations, flight testing and research (Vol. 2). Washington, DC: NASA/SP-2010-570-Vol 2.

[117]Nagai, H., & Oyama, A. (2016). Development of Japanese Mars Airplane. In 67th International Astronautical Congress (IAC), Guadalajara, Mexico, 26-30 September 2016

[118]Smith, S. W., LeBeau, R. P., Seigler, T. M., Reasor, D. A., Jacob, J. D., Gleeson, D., & Scarborough, S. (2008). Testing of compact inflatable wings for small autonomous aircraft. 49th AIAA/ASME/ASCE/AHS/ASC Structures, Structural Dynamics, and Materials Conference, Schaumburg, IL, April 7-10, 2008. American Institute of Aeronautics and Astronautics. https://doi.org/10.2514/6.2008-2216

[119]Colozza, A. (1990). Preliminary design of a long-endurance Mars aircraft. 26th Joint Propulsion Conference, Orlando, FL, July 16-18, 1990. American Institute of Aeronautics and Astronautics. https://doi.org/10.2514/6.1990-2000

[120]Malla, R., Loo, S. H., Liew, L. Y., Wai, N. S., Edmonston, D., Dinh, T., & Mahathalagalage, N. (2000). Martian Airborne Exploration Vehicle (MAEV). Wichita State University, Department of Aerospace Engineering, HEDS-UP Forum, May 2000.

[121]Sercel, J. C., Blandino, J. J., & Wood, K. L. (1987). The Ballistic Mars Hopper: An Alternative Mars Mobility Concept. 23rd Joint Propulsion Conference, San Diego, CA, June 29-July 2, 1987. American Institute of Aeronautics and Astronautics. https://doi.org/10.2514/6.1987-1901

[122]Perez Lebbink, L. (2006). UAV mission design for the exploration of Mars – ESA/EUROAVIA Design Workshop 2006. Proceedings of the Design

Workshop 2006, Noordwijk, The Netherlands. Delft University of Technology. Retrieved September 2, 2024, from http://hdl.handle.net/1853/26454

[123]Landis, G. A., Oleson, S. J., & McGuire, M. (2012). Design study for a Mars Geyser Hopper. 50th AIAA Aerospace Sciences Conference, Nashville, TN, January 9-12, 2012. American Institute of Aeronautics and Astronautics. https://doi.org/10.2514/6.2012-631

[124]Greeley, R., Christensen, P. R., Cantrell, J., Clark, B. C., Price, R. S., Zubrin, R. M., Cutts, J. A., Oberto, R. E., Haberle, R. M., & Malin, M. C. (1996). The Mars Aerial Platform (MAP) concept. 34th AIAA Aerospace Sciences Meeting and Exhibit, Reno, NV, January 15-18, 1996. American Institute of Aeronautics and Astronautics. https://doi.org/10.2514/6.1996-335

[125]Datta, A., Roget, B., Griffiths, D., Pugliese, G., Sitaraman, J., Bao, J., Liu, L., & Gamard, O. (2003). Design of a Martian autonomous rotary-wing vehicle. Journal of Aircraft, 40(3), 461-472. https://doi.org/10.2514/2.3141

[126]Aguirre, J., Casado, V., Chamie, N., & Zha, G. C. (2007). Mars Intelligent Reconnaissance Aerial and Ground Explorer (MIRAGE). 45th AIAA Aerospace Sciences Meeting and Exhibit, Reno, NV, January 8-11, 2007. American Institute of Aeronautics and Astronautics. https://doi.org/10.2514/6.2007-244

[127]O'Brien, P. C. (2012). Using a robotic helicopter to fuel interest in and augment the human exploration of the planet Mars. American Institute of Aeronautics and Astronautics. https://doi.org/10.2514/6.2003-6275

[128]Li, Y. (2007). Information Gathering Strategies for a Combined Martian System of Aerobots and Rovers (Master's thesis). Luleå University of Technology & Cranfield University. Retrieved September 2, 2024, from https://www.diva-portal.org/smash/get/diva2:1022648/FULLTEXT01.pdf

[129]Guzik, M. C., Jakupca, I. J., Gilligan, R. P., Bennett, W. R., Smith, P. J., & Fincannon, J. (2017). Regenerative Fuel Cell Power Systems for Lunar and Martian Surface Exploration (AIAA 2017-5368). AIAA SPACE and Astronautics Forum and Exposition, September 2017. https://doi.org/10.2514/6.2017-5368

[130]Schorbach, V., & Weiland, T. (2022). Wind as a back-up energy source for mars missions. Acta Astronautica, 191, 472–478. https://doi.org/10.1016/J.ACTAASTRO.2021.11.013

[131]Bruce Dorminey. (2020) NASA Eyes Wind Turbines To Power Martian Weather Stations. Retrieved September 02, 2024, from

https://www.forbes.com/sites/brucedorminey/2020/08/30/nasa-eyes-tiny-wind-turbines-to-power-martian-weather-stations/

3 Systematic Methodology for the Preliminary Design of Future Rotary VTOL Martian Aerobots[3]

Vishal Youhanna, Leonard Felicetti and Dmitry Ignatyev

Faculty of Engineering and Applied Sciences, Cranfield University, UK

Abstract:

This paper proposes and describes a methodology for the preliminary design of aerobots for future Martian exploration missions within a framework. The methodology takes into account inputs derived from top-level mission requirements and site locations to obtain the critical mission parameters that affect the performance of the rotorcraft. The proposed methodology allows for incorporating multi-rotor configurations into the trade-offs based on the required power to perform flight profiles. The equations, based on momentum theory for conventional helicopters, are derived and generalised to estimate the required power for flight segments such as hover, vertical climb, and forward flight for rotorcraft with both overlapping and non-overlapping rotors such as coaxial, tandem, and multirotor configurations. The resulting performance data is used for sizing and selecting the critical components of the aerobot in a mission scenario, such as rotor and battery sizes. Notably, the analyses conducted on rotorcraft with single and dual rotors identified a tandem rotorcraft configuration without folding mechanisms as the optimal choice due to its superior power efficiency and mechanical simplicity. Through calculated equations for battery mass and available empty mass estimation, this framework enables the optimisation and selection of an efficient rotary VTOL aerobot for Martian missions in the years to come.119

Keywords: Mars Exploration, Martian Drone Framework, Planetary Aerobots, Rotorcraft Conceptual Design, UAV,

[3] This is an adapted version of the article accepted by Acta Astronautica journal for publication: Youhanna, V., Felicetti, L., & Ignatyev, D. (2024). Systematic methodology for the preliminary design of future rotary VTOL Martian aerobots.

3.1 Introduction

The predominant approach to in-situ exploration of Mars has historically relied on landers and rovers, but their limitations have sparked interest in designing specialised aerial robots known as aerobots. The concept of unmanned aerial vehicles has gained prominence due to their advantages over surface rovers, including increased speed, broader range, obstacle avoidance capabilities, and improved visibility [1]. While chronological planetary exploration mainly explored the use of lighter-than-air airships or fixed-wing planes, recent advancements in drone technology have rekindled interest in rotorcraft for Mars exploration. These technological advancements culminated in the successful deployment of the first operational aerobot on Mars by NASA's Ingenuity Mars Helicopter. The vehicle, having landed on Mars in February 2021, completed 72 short autonomous pre-commanded flights before retiring in January 2024, accumulating approximately 129 minutes of flight time, covering 17 km, reaching altitudes of up to 24 meters, and achieving ground speeds of up to 10 m/s [2]. These flight tests marked the transition of Ingenuity from the Technology Demonstration phase to the Operations Demonstration phase, demonstrating the potential for collaboration between future rovers and aerial surveyors [2]. The insights gained from designing and operating the Mars Helicopter offer valuable knowledge for developing advanced aerobots for Mars exploration.

3.1.1 Martian Flight Conditions

The unique features of Mars pose challenges for rotorcraft design, primarily due to its atmospheric conditions. Despite the lower gravity of Mars, its average atmospheric density is approximately 100 times lower than that of Earth [3], leading to a very low Reynolds number during rotor operations, especially for small-scale helicopters. However, the Mach number on Mars would be significantly higher due to two main factors: the necessity for higher tip speeds to compensate for the lower atmospheric density, and the reduced speed of sound on the Martian surface, which is only about 70% of that on Earth. These conditions significantly constrain the rotorcraft design [4]. Another challenge in sustaining the flight of Martian drones involves managing the heat generated by

the propulsion system while generating the required lifting thrust. This task is exceptionally demanding given the low Reynolds number involved. Furthermore, the size constraint set by an aeroshell required to transport the aerobot to Mars introduces additional complexities [5]. These factors have historically cast doubt on the feasibility of using rotating-wing aerobots on Mars, a scepticism dispelled by the first Mars Helicopter.

The success of Ingenuity, while groundbreaking, exposes the inherent limitations of small-sized, basic-configured aerobots on Mars. These constraints limit their ability to conduct expansive scientific missions that demand extended flights, larger payloads, advanced communication systems, or robust propulsion for high-altitude endeavours. Addressing these limitations necessitates reimagining the parameters of Martian aerobot missions. Enhancing the Ingenuity Helicopter could involve augmenting its size or integrating fixed wings into its configuration, aiming to extend endurance, and payload capacity and accommodate more solar panels.

3.1.2 Literature

Diverse proposals for Mars exploration have explored VTOL aircraft with rigid or adaptable body configurations [6]-[16]. The first rotary VTOL planetary aerial vehicle design concepts were pioneered by Young et al. (2000) [6], particularly promoting a Mars tiltrotor that represents a good compromise between hover performance and cruise range as both attributes are critical for Mars exploration. Y-4 Tilt-Rotor VTOL Aerobot [7], the fourth and final design iteration studied at the University of Surrey from 2004 to 2016, was such a concept that used two smaller tractor tiltrotors to provide the thrust needed for both vertical and horizontal flight, and a coaxial rotor embedded at the centre of the blended wing for VTOL. Whereas another configuration, called MIRAGE [8], used a fan embedded in the centre of the blended wing body (4.8 m wingspan) for VTOL and a propeller on the nose for forward thrust. Among these types of transitioning aircraft is the tailsitter configuration, which takes off and lands vertically on its tail, and for forward flight the whole body tilts horizontally in midair. Martian Twin Rotor Tailsitter design [9] and Mars Electric Reusable Flyer (MERF) [10] are dual-rotor

VTOL tailsitter concepts proposed with a reusable option and foldable body, which when deployed would have a wingspan of 7.5 m and 0.9 m, respectively. VITAS [11] is another tailsitter concept with 4 coaxial rotors positioned at the tips of an x-wing configuration with a wingspan of about 2 m and is equipped with a canard for pitch control. Besides using vertical propulsion generated by rotary blades, there are concepts such as Mars Gashopper [12] and Marshopper [13], that propose to utilise local carbon dioxide to store and pressurise the gas inside the aircraft system and then propel it out to hop above the surface of Mars for VTOL. Both these designs are equipped with wings to glide around for increased endurance during forward flight. Among large foldable and small rigid fixed wing rotorcraft, there is an inflatable wing concept that offers the advantage of transporting the aircraft to Mars in the limited aeroshell size. VALKERIE (Vertical-takeoff And Landing Kompact Electric Reusable Inflatable Explorer) [14] is such a design which has merged the above-mentioned tailsitter MERF with BIGBLUE (Baseline Inflatable-wing Glider, Balloon-Launched Unmanned Experiment). BIGBLUE is an inflatable wing glider technology that was introduced and worked on by the students at the University of Kentucky for low air density environments such as Mars. The LILI (Long-term Ice-field Levitating Investigator) concept [15] further expands on foldable hybrid mobility by integrating a tandem rotor configuration with a ground-based sled system. This approach allows for efficient navigation of polar ice fields on Mars, leveraging the tandem rotors for aerial capability while optimising power use through surface mobility. NASA started developing the second generation of Mars Helicopters such as the Mars Science Helicopter (MSH) and Advanced Mars Helicopter (AMH), even before Ingenuity Helicopter had landed on Mars. MSH had two short-listed designs with foldable mechanisms and each weighed 20 kg, namely a coaxial rotorcraft with 2.5 m diameter rotors and a hexacopter design with 1.28 m diameter rotors [5], whereas AMH is a similar design to Ingenuity with 1.2 m diameter rotors but weighs 4.6 kg and is equipped with improved airfoils and science payload [16], on which attitude control and autonomous navigation are investigated in Ref.[17].

Among these concepts, the Valles Marineris Explorer (VaMEx) initiative evaluated coaxial helicopters and transition coaxial tailsitter configurations as

part of a robotic swarm for Mars high ranges exploration [18]. For a mission with a 30 km cruise range and a 1.4 kg payload, the study shows that the 3.83 m wingspan transition tailsitter, while offering better cruise efficiency and enabling longer range through reduced battery weight, is outweighed by the added mass of its wings and stabilisers, resulting in a heavier and more complex design. In contrast, the coaxial helicopter, with 1.52 m rotors, is simpler, lighter, and more efficient, making it better suited for shorter missions. These findings highlight the need for comprehensive assessments to optimise rotorcraft designs for Martian conditions, particularly within aeroshell size constraints, assuming the stability of launch and re-entry technologies in the coming decades. Accommodating larger craft may require alternative solutions, such as separate transport, packaging with a smaller ground spacecraft, or innovative folding mechanisms within the aeroshell. However, aircraft design constraints imposed by practical aeroshell sizes are frequently disregarded in studies, particularly those not conducted by space agencies. For instance VaMEx study [18] defers the selection of aeroshell size and relative dimensions for future research and MIRAGE [8] proposed 5 m diameter aeroshell, which currently does not exist. Although the development of new aeroshells could provide greater flexibility, space missions prioritise established designs, such as the 4.5 m diameter aeroshells utilised in the Mars Science Laboratory (2011) and Mars 2020 missions, due to their proven reliability [5].

Previous studies in Martian rotorcraft design can be broadly classified into two categories: conceptual designs without feasibility validation and high-fidelity mission-specific studies. Conceptual studies often propose novel configurations, such as tiltrotors or hybrid rotorcraft models proposed in [4] and Coaxial Tri-rotor and Jumping Flying Aircraft concepts proposed in [19], but lack detailed analyses to quantify their practicality under Martian conditions. High-fidelity studies, while providing detailed performance evaluations, are computationally intensive and limited to predefined configurations. For instance, study such as in Ref. [20] used blade element theory and experimental validation for quadrotor designs but do not generalise findings to other configurations. Similarly, studies on coaxial and transition vehicles for the Valles Marineris Explorer (VaMEx) [18] missions are

modified to specific operational scenarios and do not extend to broader mission profiles. Multidisciplinary design frameworks, such as the one illustrated in [6], focus on vertical lift planetary aerial vehicles but emphasise spacecraft integration over rotorcraft design scalability.

3.1.3 Proposed Research

This research introduces a scalable framework that combines the exploratory strengths of conceptual studies with the practicality of high-fidelity analyses. The framework integrates multidisciplinary design considerations, such as mission requirements, environmental constraints, and spacecraft integration, into a systematic process for preliminary rotorcraft design. A fundamentally novel aspect of this framework is its parametric analysis methodology, which is based on rotorcraft momentum theory and enables rapid evaluation of power requirements, rotor sizing, and payload capacities for configurations such as single rotors and dual-rotor systems, including coaxial and tandem rotors. Although this paper focuses on these configurations, the methodology is extended to multirotor systems. This methodology integrates mission constraints, such as aeroshell size and power limitations, into a streamlined design process. It is inherently adaptable to varying planetary environments. By updating planetary parameters such as air density and gravitational acceleration, the framework can be applied to other atmospheric environments, such as Titan [21] and Venus, making it a versatile tool for future exploration efforts. By simplifying aerodynamic analyses while maintaining computational efficiency, the framework accelerates decision-making and supports iterative design refinements. The performance outcomes, such as rotor and battery sizing, provide actionable insights for researchers and engineers, ensuring that the preliminary designs are grounded in theoretical rationale and aligned with mission requirements. Consequently, this approach addresses the limitations of small-sized aerobots while advancing scalable, mission-specific designs, paving the way for the next generation of Martian rotorcraft.

The structure of this research article is such that it begins with an overview (section 3.2) of the framework for preliminary Martian aerobot design

methodology, a systematic approach on which the rest of the sections are constructed. This is succeeded by the development of a mission statement and requirements (section 3.3), and a definition of relative parameters (section 3.4). The outlined specifications and objectives highlight the complexity of Martian missions and the innovative strategies necessary to overcome challenges, providing insights into the potential outcomes of employing an aerobot in Mars exploration, and emphasising the advancements and challenges involved in planning and executing missions beyond Earth. A generalised methodology rooted in simplified momentum theory (section 3.5) is explained that enables the calculation of the required flight power of diverse Martian rotorcraft configurations, including overlapping rotors. Likewise, a methodology for the initial sizing of battery-electric aircraft (section 3.6) is introduced which inputs the flight required power to estimate the required battery mass and hence, provides insights into determining the total mass of the rotorcraft. After the description of the methodologies, study cases for parametric analysis are established (section 3.7) by forming a basic flight profile mission and locking necessary parameters to perform analysis on a single conventional helicopter, coaxial rotorcraft, and three created cases of tandem rotorcraft configurations. Subsequently, the results are demonstrated from the analysis performed (section 3.8) using the above-mentioned methodology to examine the relationship between rotor disk size and the power demands for hover, vertical climb, and forward flight across the selected rotorcraft configurations in the Martian environment. The insights from the rotorcraft power requirement analysis allow for the identification of the most power-efficient configurations for aerobot design. However, certain theoretical optima may introduce complexities due to design constraints, a factor pivotal in the selection and refinement of these configurations. Hence, based on this analytical approach the most suitable rotorcraft design is rationalised and shortlisted for the preliminary sizing and further discussion (section 3.9).

3.2 Framework for Preliminary Martian Rotary VTOL Aerobot Design Methodology

The flow chart in Fig. 3.1 illustrates the framework of the systematic methodology proposed and applied in this research for the preliminary design of future rotary VTOL Martian aerobots. The methodology is generalised with the aim of developing a rational case for the design of a Martian aerobot customised to a specific mission. Interplanetary space missions, given their one-shot nature with minimal margin for error, involve high stakes owing to the complexities involved in their operations. Any proposed advanced solution addressing current space exploration challenges must align with the existing state-of-the-art space infrastructure, as a mismatch could result in lengthy implementation timelines and render the solution obsolete before it can be deployed. Therefore, the first step in the framework is to identify the mission aim for the future aerobot, which should align with the priorities of global space agencies for upcoming Mars exploration missions. The second step is choosing a possible landing site that meets the engineering constraints and scientific goals and requirements set by the Mars scientific community. The next stage is to define the top-level mission profile for the operation of the aerobot. The subsequent step is to determine the flight operations and profile for the primary mission. Setting the performance criteria for the aerobot will follow as the fifth stage in the design. The sixth step in the process is to specify the localised values of the key parameters that are essential for the flight of the aerobot.

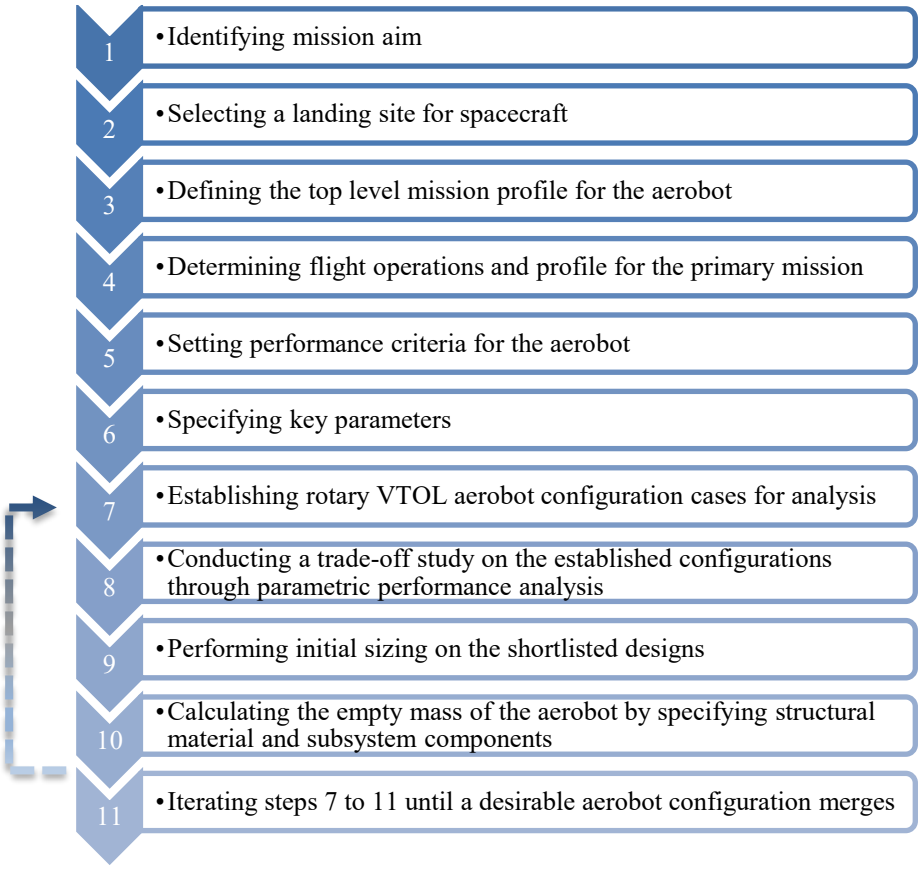


Fig. 3.1 Flow chart of the framework for the preliminary Martian aerobot design methodology

The seventh step in the flow chart is to establish possible rotary VTOL aerobot configuration cases, along with specifying all the parametric values required for the performance analysis. The next stage is to perform the parametric performance analysis based on the methodology explained in section 3.5 for estimating the required flight power of rotorcraft configurations. In this eighth step, a trade-off study is conducted based on the results. The ninth step is to perform initial sizing on the shortlisted designs using the methodology explained in section 3.6 for the initial sizing, given it is a battery-electric aircraft. The second-last step is to calculate the empty mass (mass exclusive of payload and fuel) of the aerobot by identifying the components and material of the structure of the whole system. Once the empty mass is determined, it will be utilised to balance the initial sizing equation. The outcome is unlikely to be desirable the first time and thus, it would require step 11 which is an iteration of steps 7 to 11 until an acceptable outcome is achieved. The subsequent sections provide detailed explanations and methods

for each step using an example case, except for step 10, which is beyond the scope of this paper because it involves advanced structural analysis and detailed mass buildup, requiring iterative refinements and additional data that are better addressed in future detailed design studies.

3.3 Mission Statement and Requirements

The first 5 steps of the framework for preliminary Martian aerobot design introduced in Fig. 3.1 are exemplified in this section by forming a mission scenario supported by relevant tools and methodologies. Starting with the identification of the mission aim and the justification of the selected landing site of the spacecraft, the top-level mission profile is defined using a mapping tool. Next, the flight operations and profile are determined based on the primary mission profile and current standard capabilities of an aerial drone in the Martian environment. Subsequently, the performance criteria of the potential Martian aerobot are framed by comparing its capabilities with those of recent mobile spacecrafts operating on the surface of Mars.

3.3.1 Mission Aim Identification

For over a decade, the Mars sample-return mission has remained a primary focus for NASA, ESA, CNSA, JAXA, Roscosmos, and other global space agencies. This mission not only enhances human understanding of Martian astrobiology but also lays the groundwork for future human exploration on Mars [22]. To mitigate mission risks and optimise scientific output, selecting a previously investigated region for the sample-return mission is imperative [23]. An aerial robot on the Martian surface, equipped with advanced scientific surveillance capabilities and significantly greater speed than a rover, stands as a crucial asset, accelerating the safe and efficient execution of the Mars sample collection mission. Therefore, the mission aim for this research project is to generate high-resolution aerial mapping of the area and mark potential experimental/sample collection points for future rover missions using a reusable VTOL aerobot, leveraging the aerobot's speed and vantage point to efficiently identify high-priority sites that rovers can later examine in detail.

3.3.2 Mission Location Requirement and Justification

The design of the Martian aerobot must be adapted for the selected mission region. There can be numerous mission zones that can have one or more distinct territorial characteristics such as plains, highlands, arctic poles, underground caves, steep hills, and deep valleys. The selection of a landing site first requires fulfilling the criteria of engineering constraints and safe Entry, Descent, and Landing (EDL), as well as operation of the spacecraft. Post fulfilment of engineering constraints, the focus shifts to identifying scientifically significant sites. The Mars scientific objectives revolve around the major science goals namely life, climate, geology, and preparation for human exploration, that are set by NASA's Mars Exploration Program Analysis Group (MEPAG) [24]. One of the ways to understand the selection of the landing site process is to look at the engineering parameters and requirements, particularly for sky crane-based EDL as it has been the preferred system in recent Mars missions for delivering heavy payloads with high landing precision, alongside the science objectives of missions such as Mars 2020 (summarised in Table 3.1). Jezero Crater was selected from a database of 55 candidate landing sites for this mission because of its astrobiological importance while meeting engineering constraints.

Table 3.1 Summary of Mars 2020 mission landing site engineering constraints & safety criteria, and main scientific objectives [22]

Engineering Parameters	Landing Sites Requirements	Science Objectives		
Latitude	30°N to 30°S (due to surface thermal limitation)	Perform thorough in-situ science	*Geology:* Analyse the geological processes in a selected Martian area linked to ancient environments and diverse geology, indicating potential astrobiological importance.	*Potential Sample Return:* Collect scientifically chosen samples with documented context, highlighting astrobiological importance and site geological diversity.
Elevation	<-0.5km (Relative to datum)			
Landing Ellipse	≤16.0 km (West-East) 14 km (North-South)			
Rock Height	≤0.6 m			
Terrain Relief/Slopes	(length scale) 2-10 km: <20° 1-1000 m: ≤100 m relief			
Radar Reflectivity	Ka band reflective			
Load Bearing Surface	Not dominated by dust		*Astrobiology:* Evaluate the habitability of a historic Martian setting, examine materials conducive to preserving signs of life, and search for potential evidence of past life.	*Human Exploration/ Technology:* Aid in preparing for Mars human exploration by addressing key knowledge gaps
Atmosphere	Up to 25 m/s horizontal and 20 m/s vertical winds during EDL			
Surface Winds for Thermal Environment for Rover Science Operations	During Operation: < 15 m/s (steady) <30 m/s (gusts) Non-Operation (sleeping): < 40 m/s (steady)			

The selected landing site on Mars for this study is the Southwestern (SW) Melas Basin within Valles Marineris which is the largest canyon system in the solar system (see Fig. 3.2.a). Although ranked among the top 8 sites for previous NASA missions by planetary scientists [22], it was often rejected due to its rugged terrain and the extensive distances required to reach specific scientific locations [4]. However, now EDL in such terrain is possible because the Mars 2020 mission incorporated two new technologies, Range Trigger and Terrain Relative Navigation, for a precision landing in rougher terrain [25]. Accessing the designated Regions of Interest (ROIs) highlighted in Fig. 3.2.b, such as delta and hydrated silica deposits, would require a rover drive of approximately 6 km, with travel times of less than 50 sols (Martian day) with a driving efficiency of 35–75

m/sol estimated in [22]. However, these evaluations were overly optimistic, as the actual driving efficiency observable from the Perseverance rover track record indicates values of < 25 m/sol [26]. Thus, employing an aerial drone to map routes to ROIs aims to enhance rover driving efficiency, underscoring the necessity for a functional Martian aerobot equipped with scientific instruments in future.

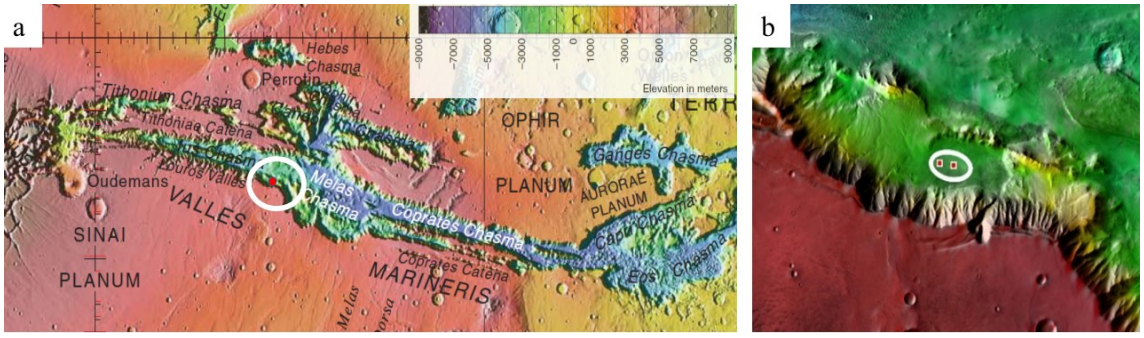


Fig. 3.2 a) Map showing SW Melas basin (red spot) in Valles Marineris. Cropped Topographic Map of Mars (M 25M RKN) by USGS 2003 based on data from the Mars Orbiter Laser Altimeter, an instrument on NASA's Mars Global Surveyor. b) Close-up of SW Melas Basin perches on the southwestern rim of Melas Chasma, with two ROI (red dots). The white outline (not to scale) is the 9.7 x 8.7 km landing ellipse centred at - 9.81° N, - 76.46° E, elevation -1.92km [22]. Image created using JMars 5 (GIS) [28].

3.3.3 Top-Level Mission Profile Definition

Valles Marineris extends over 4000 km, covering about one-fifth the circumference of Mars, with some parts running as deep as 7 km and as wide as 200 km [27]. Fig. 3.3 shows the mission operation profiles, including the estimated pathway of the aerobot and traverse distance calculated using JMars 5, a publicly available geospatial information system (GIS) software [28]. The overall mission can be divided into three geographical sub-missions, marked with magenta, orange and yellow lines, that enable comprehensive coverage of the expansive canyon region systematically. This hierarchical approach aims to progressively boost confidence in the capabilities of the aerobot. Notably, other sections of the canyon, like East Melas Chasma, are among the 55 candidate landing sites [22]. The fundamental design of the aerobot is required to be based on the primary mission, which also includes the demonstration phase. Although,

the longevity history of the spacecrafts that have landed successfully on Mars has shown that these do surpass expectations and carry on the scientific investigation for many years. Hence, the secondary and extended missions of an aerobot can be a good practice to be added to the list of design considerations.

The definition of mission in terms of time and distance sets the foundation of the preliminary design and function of the aerobot, with estimates based on expected flight capabilities, operational constraints, and insights from Ingenuity's performance and Mars Science Helicopter (MSH) [5] design studies for extended Mars helicopter missions. The primary mission of the aerobot would be to explore the SW Melas Basin, traversing a total of ~ 100 km, in the first ~ 30 sols after deployment. The secondary mission would explore the boundary of Melas Chasma, traversing a total of ~ 1500 km, in the next ~ 450 sols. The extended mission would explore the in-between of Melas Chasma and Coprates Chasma, traversing a total of ~ 2500 km, in the next ~ 750 sols. From this specified mission plan further specifications and parameters can be derived.

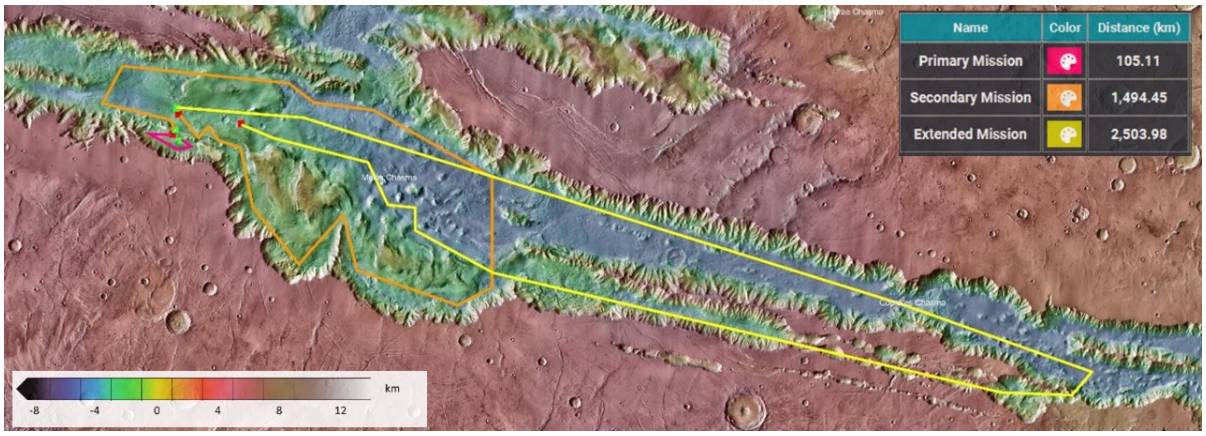


Fig. 3.3 Mission Profile Map showing Valles Marineris created in JMars5 (GIS) [28]. The green and red dots on each mission profile line depict the start and finish, respectively.

3.3.4 Flight Operations and Profile Definition

Terrestrial mid-level electric battery-powered aerial drones commonly sustain an average flight time of ~20 minutes, while high-end consumer drones typically achieve ~30 minutes, with exceptions in some high-end drones and fixed-wing aircraft that can fly for several hours [29]. The flight duration on Mars is limited to

short bursts (2-10 mins) due to the necessity of ensuring a sufficiently charged helicopter battery to avoid electrical issues during high-power manoeuvres. Effective energy management on Mars is important, with much energy allocated for temperature control, posing flight endurance challenges due to poor thermal dissipation in the thin Martian atmosphere [30]. The 20-minute communication delay between Earth and Mars hinders real-time monitoring [31], relying on Earth station commands for aerobot navigation, limiting daily flights. Consequently, flight activities may occur intermittently, with much mission time devoted to tasks like charging, data transmission, and flight planning.

According to the primary mission objectives, the aerobot aims to traverse 100 km in 30 sols, translating to a total of 10 sols allocated for flight, with one sol dedicated to flying and two sols for data transmission and planning. This arrangement results in a range of 10 km per sol for flight operations. Flight time range can be between 5 to 10 minutes, depending on the capability of the aircraft. Both estimates are consistent with Ingenuity's scaled performance and design studies from the Mars Science Helicopter [5]. A flight altitude of 1 km is selected, as aerial mapping at this altitude will ensure extensive coverage to bridge the gap between satellite and rover imaging, an altitude demonstrated as achievable in previous Mars mission studies [1][7]. Fig. 3.4 summarises the selected specifications of the flight profile at which the aerobot would fly normally in pursuit of completing the missions defined above.

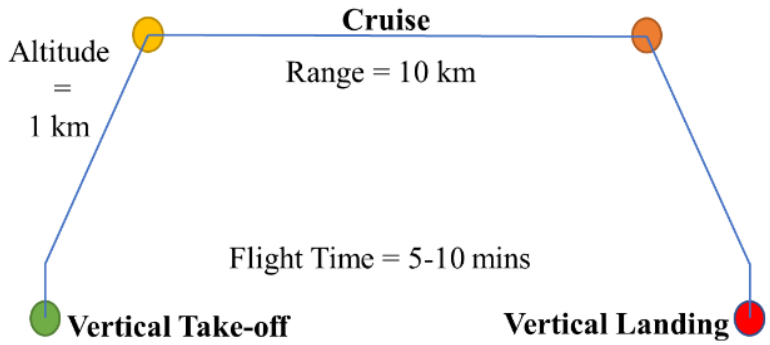


Fig. 3.4 Flight specifications and profile of an aerobot for the proposed Mars mission

3.3.5 Aerobot's Performance Criteria Establishment

The Potential Aerobot (PA) represents a hypothetical case study within the mission scenario, designed to evaluate the feasibility of long-range aerial exploration on Mars. This conceptual, battery-electric, rotary VTOL vehicle aims to extend traverse range and speed beyond current existing ground systems on Mars, while also offering comparative insights against the advanced Martian aerobot concepts. A concise performance comparison in Table 3.2 highlights key mobility capabilities and mission related requirements, defining a non-exhaustive set of metrics that establish top-level performance requirements and guide the preliminary design of the aerobot. Mars 2020 mission data is sourced and then calculated from online logs based on its completion of 1000 sols on Mars [2] [26]. The Potential Aerobot's estimated yearly traverse distance is based on a total planned traverse of 4100 km over 1230 sols (developed in Section 3.3.3), giving an average range of ~3.33 km per sol, which scales to 2227 km over a full Martian year (668 sols).

Notably, the Potential Aerobot demonstrates capabilities exceeding those of the Mars 2020 mission, which included both the Perseverance Rover and the Ingenuity Helicopter. Compared to the rover, the Potential Aerobot can cover around 150 times more distance per Martian year and per sol on average, with about 550 times greater specified traverse speed, marking a significant advancement. When compared to the Ingenuity Helicopter, the Potential Aerobot's traverse speed is 11 times greater. However, it can be noticed that Ingenuity covered far less distance per Martian year than the rover. This inconsistency arose from the helicopter's lack of an independent communication system and its confinement to the vicinity of the Perseverance Rover, which restricted its mobility. Conversely, the Potential Aerobot is intended to possess higher traverse speed and fully equipped communication and navigation systems, enabling multiple long-range flights. As the design progresses, additional metrics for performance criteria will be necessary to delve into more specific design considerations.

A comparable future mission concept, the Mars Science Helicopter (MSH) by NASA JPL [5], was designed for Jezero Crater to conduct mapping and remote sensing, followed by landing and recharging over one sol using onboard solar cells. Its flight profile consists of a 30-second hover-powered takeoff, a climb to 200 m, and a 1 km cruise to the science site, followed by a 2-min hover before landing. With a traverse speed of 30 m/s, total flight time is ~3 mins. Since the Potential Aerobot's flight profile excludes hover, an adjusted MSH profile is required for direct comparison. Based on the developed MSH concept's energy use, each minute of hover time equates to approximately 2 km of cruise distance [5]. By excluding hover, the MSH's effective cruise distance increases from 1 km to 5 km (1 km original cruise + 4 km hover equivalent), making it more comparable to PA's extended range under similar energy constraints. With this adjusted profile, assuming one flight every two sols due to recharging requirements, the MSH would cover ~1670 km per Martian year (5 km per flight × 334 flights), resulting in a Mean Operational Range of 2.5 km per sol.

While the Potential Aerobot differs in specific design goals, the realistic nature of its expected performance aligns closely with current trends in Mars aerial vehicle research, including the capabilities being explored in MSH studies. The PA with range per flight of 2 times greater (10 km vs. 5 km for MSH), endurance about 2.5 times longer, and total yearly traverse distance (2227 km vs. 1670 km) suggest that a higher-performance aerial vehicle is within reach, assuming continued advancements in battery efficiency, aerodynamic design, and autonomous flight control. Rather than exceeding MSH's capabilities outright, the PA represents a feasible extension of the capabilities being explored in conceptual mission studies, further bridging the gap between current Mars aerial platforms and future long-range reconnaissance missions.

Table 3.2 A comparison of requirements and capabilities between Perseverance Rover [26], Ingenuity Helicopter [2], Mars Science Helicopter (MSH) [5], and the Potential Aerobot (PA) according to the mission specification. Mars 2020 mission data is based on its completion of 1000 sols on Mars. 1 Martian year = 668 sols.

Metrics	Mars Spacecrafts				PA times (x) to		
	Perseverance Rover	Ingenuity Helicopter	MSH	Potential Aerobot (PA)	Rover	Ingenuity	MSH
Distance travelled per Martian year (km)	15	10	1670	2227	149	222	1.3
Predefined Traverse Speed (m/s)*	0.04	2	30	22	556	11	0.7
Mean Operational Range per sol (km/sol)	0.022	0.015	2.5	3.33	149	222	1.3
Mean Number of Flights per Martian year (flights/yr)	NA	45	334	223	NA	5	0.7
Mean Operational Range per flight (km/flight)	NA	0.23	5	10	NA	44	2
Mean Operational Endurance per flight (min)	NA	1.5	3	7.5	NA	5	2.5

*Traverse speed of PA is based on the average flight time (i.e. 7.5 mins)

3.4 Specification of Key Parameters

Specifying the parametric values that are central to the flight performance of the aerobot is the sixth step in the preliminary Martian aerobot design framework (Fig. 3.1). This section discusses methods and tools utilised to determine the values or a set of values of parameters such as air density, air viscosity, flight speed, rotor spin rate and rotorcraft size constraints. The key parameter upon which most of the aerodynamic calculations of the aircraft depends is the air density at which it will typically fly. The variation between air densities appears negligible, but a minute change can significantly impact the flying capability of rotorcraft in low-density environments like Mars. For instance, NASA's Ingenuity helicopter's thrust margin could drop from 30% to 8% with a slight decrease in air density from 0.0145 kg/m³ to 0.012 kg/m³ [34]. To compensate, the rotor speed must be maximised, leading to challenges such as encountering higher Mach numbers and addressing structural resonances. This highlights the sensitivity of rotorcraft operations to changes in air density, underscoring the requirement for precise measurements and adaptation of Martian rotorcraft designs to local atmospheric conditions for reliable performance. Overly optimistic values could falsely indicate superior performance in the aerobot design process, while overly conservative values may limit the demonstration of its full potential.

3.4.1 Approaches to Local Air Density Determination

Three approaches are presented to determine the air density on Mars for the design of the aerobot. The first approach provides the most generic estimate using the mean surface air density, which is 0.02 kg/m^3 on Mars [32]. This value

reflects an overly optimistic atmospheric condition because regional air density depends on location, and altitude from the datum (sea level), and varies across seasons and time of day. The second method for determining the air density involves a more specific approach based on NASA's Mars atmospheric mathematical model, which considers altitude effects and consists of separate equations for the lower atmosphere (<7 km) and the upper atmosphere (>7 km) [33]. In both zones, the temperature decreases linearly, and the pressure decreases exponentially with respect to the change in altitude. By inserting the desired altitude (*H*) value, measured above the ground, into Eq. (3.1) and Eq. (3.2), both temperature (T) and pressure (p) can be estimated, respectively. Different values of constants a and b are used in equations for the lower and upper atmosphere zones in Eq. (3.1) to determine temperature. Air density (ρ) is then calculated using Eq. (3.3) by inputting the corresponding values of temperature and pressure.

$$T_{\text{Celsius}} = -a - bH\,, \tag{3.1}$$

$$p = p_0 \mathrm{e}^{-H/H_0}\,, \tag{3.2}$$

$$\rho = \frac{p}{R(T_{\text{K}})}\,, \tag{3.3}$$

where T_{Celsius} (℃) is the temperature on Celsius scale; H (m) is the altitude from the ground; p (kPa) is the atmospheric pressure; ρ (kg/m^3) is the air density; a (℃) is a temperature intercept constant (=31 ℃ when H<7000 m; =23.4 ℃ when H >7000 m); b (℃/m) is a lapse rate constant (=0.000998 ℃/m when H<7000 m, =0.00222 ℃/m when H >7000 m); p_0(kPa) is a reference pressure constant (=0.699 kPa); H_0 (m) is an atmospheric scale height constant (=11111.1 m); R (kJ/kg/K) is a gas constant (=0.1921 kJ/kg/K); T_{K} (K) is the temperature on Kelvin scale ($= T_{Celsius} + 273.15$)

Continuing with the case study developed in the previous section 3.3, the Potential Aerobot requires flying from 0 to 1 km altitude according to the standard flight profile (Fig. 3.4). The application of this mathematical model at the surface (H=0) and 1 km (H=1000) altitudes gives an air density of 0.015 kg/m^3 and ~0.014 kg/m^3, respectively. These values are rather overly conservative estimates

because although the model considers altitude effects, it does not account for atmospheric variations related to regional attributes such as datum level, seasons, and time of day.

The third technique for a more precise estimate of the local air density involves the utilisation of the Mars Climate Database (MCD Version 6.1) software [35]. This method requires additional knowledge about the red planet and inputs such as time of flight. Mars' calendar year has 12 months, which can be of varying numbers of sols depending on the solar longitude (*Ls*), which is a measure of the eccentric orbital position of Mars from the Sun. The span of 30° in *Ls* represents a month and the season on Mars changes after each 90° span, starting from the Northern Hemisphere's Spring equinox (*Ls*=0°) [35]. When applying this method to the Potential Aerobot mission scenario, the air density is estimated by taking the average of Mars regional air density spread across one Martian year with MCD's standard climatology scenario, for the altitude of up to 1 km from the surface of SW Melas Basin. For a solar-powered autonomous aircraft, optimal flight times typically lean towards later in the day, allowing solar panels to recharge the battery after overnight heater use. However, a conservative local flight time of around 11 am is used on Mars for regions in the middle latitudes, as delaying too long risks subjecting the rotorcraft to intensified winds due to increased solar heating in the lower atmosphere [30]. The MCD can present air density data output in two formats: a range presentation or distinct curves, as illustrated in Fig. 3.5. The graph in Fig. 3.5a depicts a visually coloured presentation of air densities over the range of 0 to 1000 m altitude at the 11^{th} hour at SW Melas Chasma for a full Martian solar longitude range based on the climatology average solar scenarios. Conversely, Fig. 3.5b shows two distinct curves of air densities at 0 m and 1000 m altitudes under the same set of conditions.

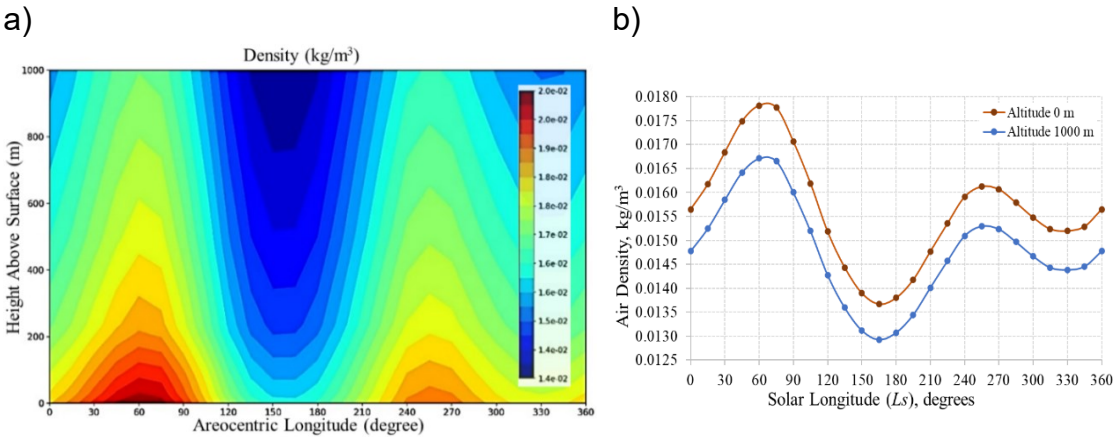


Fig. 3.5 The graphs show air density over the altitude above the local surface of SW Melas Chasma (Latitude -9.81N. Longitude 283.5E.) at a local time of 11.0h, spread over the full range of Martian Solar Longitude. a) altitude range of 0 m to 1000 m. b) at altitude 0 m and 1000 m. MCD_v6.1 with climatology average solar scenario [35].

The MCD is a publicly available reliable source, however, a discrepancy was found between these two graphs, as in Fig. 3.5b the maximum value of air density is about 0.0178 kg/m^3 (at 60° *Ls* and altitude 0 m), whereas in Fig. 3.5a it is 0.02 kg/m^3. Similarly, the minimum value of air density is about 0.0129 kg/m^3 (at 165° *Ls* and altitude of 1000 m) in the graph (b), as opposed to 0.014 kg/m^3 in the graph (a). Therefore, the average of the maxima and minima from both graphs is taken first, from which the mean value 0.016 kg/m^3 of the air density is determined that will be used in the initial aerobot sizing. Similarly, air viscosity data can be extracted from MCD. The viscosity estimates coinciding with the maxima and minima (at *Ls* of 60° and 165°, respectively) of air density are taken and then averaged. Hence, kinematic viscosity (=viscosity/density) is used to calculate the Reynolds number, which is required to define the accurate airfoil and streamlined aerodynamic body of the aerobot in the later stages of the design. For the secondary mission at East Melas Chasma (Latitude -12.22°N, Longitude 290.9°E), approximately 4 km below the datum, estimates for regional air density and air viscosity for various altitudes above the surface can be obtained using the same method. Air density reaches 0.025 kg/m³ at the surface, indicating potential for improved flight performance during secondary missions.

3.4.2 Aerobot's Size Constraints Definition

Another critical parameter is the geometric restriction imposed by the maximum allowable size of the aerobot. This constraint stems from the dimensions of the protective heat shield required for the Entry, Descent, and Landing (EDL) system, known as the aeroshell, which encases the spacecraft during transportation to Mars. Past successful EDL systems by NASA, such as the Pathfinder aeroshell (1997, 2.65 m diameter), Viking aeroshell (1976, 3.5 m), and Mars Science Laboratory (MSL) aeroshell (2012, 4.5 m), serve as benchmarks [5]. Fig. 3.6a shows the actual MSL aeroshell during testing, along with two Mars aerobot concept case studies in the literature with folding mechanisms to fit into the Pathfinder aeroshell (Fig. 3.6b) and Mars 2020 mission aeroshell (Fig. 3.6c).



Fig. 3.6 a) Mars Science Laboratory aeroshell during testing (2011, size 4.5 m). Credits: NASA/Kim Shiflett. b) Folding option for coaxial helicopter concept in Pathfinder Aeroshell (size 2.65 m) [5]. c) Winged VTOL concept CAD model called FuMAD, folded and packed in Mars 2020 mission aeroshell (size 4.5) [37]

The aeroshell size of the Mars 2020 mission was the same as that of MSL, which is currently the biggest existing aeroshell. Thus, this predefined limit sets the aerobot's maximum dimensions at 4.5 m in diameter and approximately 2.2 m in height. For the parametric performance analysis (step 8, Fig. 3.1) of potential design configurations in the Potential Aerobot case study, the rotor disk size range considered, excluding any rotor folding mechanism, spans from 5% to 100% (i.e., 0.23m to 4.5m) of the aeroshell diameter.

3.4.3 Rotor Speed Limits Determination

On Mars, where the speed of sound is approximately 240 m/s [4], operational constraints are imposed on rotor tip speed and forward velocity to mitigate the

formation of transonic compression waves. In forward flight, the speed of the advancing blade is required to be approximately three times the airspeed of a helicopter to maintain lift on the retreating blade [36]. Typically, maximum rotor tip speed is constrained to be around 0.75 Mach (180 m/s). Therefore, a maximum forward velocity of 60 m/s is proposed, aligning with one-quarter of Mars' average speed of sound and conforming to one-third of the allowable maximum rotor tip speed. This means that the RPM of the rotor must adjust so that the Mach number at the rotor advancing blade tip (M_{at}) does not exceed the maximum rotor tip speed during the forward flight. The term revolution per minute (*RPM*) is the rate at which the rotor spins and is calculated using the following equation:

$$RPM = \frac{60\omega}{2\pi} = \frac{60v}{2\pi r}, \tag{3.4}$$

where RPM $(\mathrm{rev/min})$ is revolution per minute; ω $(\mathrm{rad/s})$ is the angular velocity; v $(\mathrm{m/s})$ is the rotor tip speed; r (m) is the rotor radius.

Smaller rotors require higher *RPM* than larger rotors to generate a similar amount of thrust. At the maximum permitted rotor tip speed (i.e., 180 m/s), the *RPM* ranges from approximately 15000 for a 0.23 m rotor to 800 for a 4.5 m rotor. Ingenuity, with a 1.2 m rotor disk, had a maximum allowable *RPM* of ~2800 [30].

3.5 Methodology for Estimating Required Flight Power of Rotorcraft Configurations

The section introduces a generalised methodology derived to estimate the power requirements of by various rotorcraft configurations for the conceptual design of a next-generation Martian drone. This estimation is important for the trade-off analysis, step 8 of the design framework illustrated in Fig. 3.1, later applied in sections 3.8 and 3.9 to select an appropriate configuration for the developed example of the Potential Aerobot (the hypothetical case study) on Mars. The analysis uses conservative values for most of the coefficient-type variables. Fig. 3.7 depicts possible configurations with single and dual rotors, extensively utilised as VTOL aircraft for terrestrial applications. A standard/conventional helicopter is

equipped with a single main rotor situated on top and a tail rotor positioned at the rear. While the main rotor provides lift and propulsion, the tail rotor counteracts the torque generated by the rotation of the main rotor. Conversely, a coaxial helicopter features two rotors stacked on the same axis, rotating in opposite directions, eliminating the need for a tail rotor. This design enhances stability and manoeuvrability. Tandem rotorcraft have dual main rotors, one placed in front of the other on the same body. This configuration offers substantial lift capacity and efficient load-carrying capabilities. Side-by-side rotorcraft have multiple rotors positioned next to each other, typically on the same horizontal plane. This category includes versatile configurations like tiltrotors and tiltwings, allowing for both hovering and forward flight. Quadcopters and hexacopters, types of multicopters, feature four and six rotors, respectively, and are well-known for their simplicity, stability, redundancy and ease of control. This paper focuses on estimating the power requirements and comparing configurations, including conventional rotorcraft, coaxial rotorcraft and tandem rotorcraft.

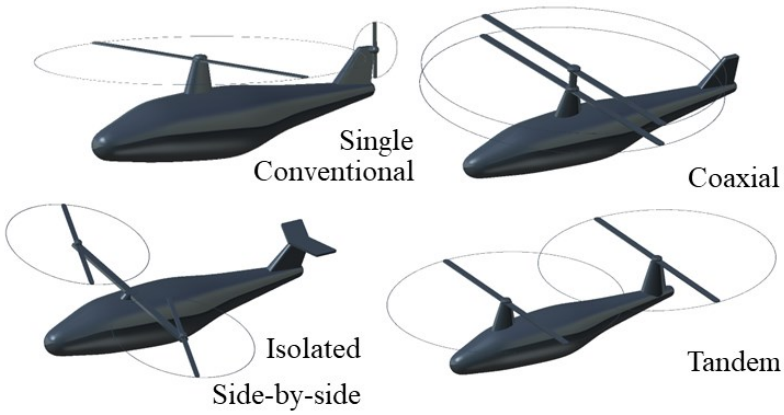


Fig. 3.7 Illustration of existing rotorcraft configurations: (top left) Single Conventional, (top right) Coaxial, (bottom left) Isolated Side-by-Side, and (bottom right) Tandem rotorcraft

3.5.1 Single Rotor Conventional Rotorcraft

For a reusable Martian aerobot to achieve successful flight, its ability to execute vertical takeoff and landing (VTOL) is critical, as runways are unavailable on Mars. This capability hinges entirely on the rotary propulsion system of the rotorcraft. Momentum theory is utilised to estimate the power (P) consumption of

the rotor during hover, vertical climb, and forward flight. This theory assumes that spinning rotor blades act as an actuator disk with minimal thickness and a specific disk area (S). The model also assumes a uniform airflow across the rotor disk and instantaneous energy transfer to the airflow. Additionally, factors like airfoil profile drag losses, tip losses, and residual rotational velocities are disregarded. To adjust for these losses, a parameter called the figure of merit (M) is introduced. This figure (M = P_{ideal} / P_{actual}) represents the ratio of ideal power to actual power and serves as an indicator of rotor efficiency. The following equation provides the necessary power for vertical (vert) climb or hover (when the climb velocity is zero), specifically formed for a conventional helicopter [36].

$$P_{(\text{Vert Climb or Hover})} = \left[\left(\frac{fW}{M}\sqrt{\frac{fW/S}{2\rho}}\right) + \frac{WV_{\text{Climb}}}{2}\right]\left[\frac{(1 + P_{\text{tail rotor}}/P_{\text{main rotor}})}{\eta_{\text{mechanical}}}\right], \tag{3.5}$$

where P (Watt) is the power required; W (N) is the rotorcraft weight (=mg, where m (kg) is the mass of the rotorcraft and g (m/s^2) is the surface gravity acceleration on Mars for the sake of this paper); S (m) is the rotor disk area; M is the figure of merit; V_{Climb} (m/s) is vertical climb velocity (=0 for hover); f is the adjustment for downwash on the fuselage (=1.06 typically); ρ (kg/m^3) is the local air density on Mars; $\eta_{\text{mechanical}}$ is mechanical losses adjustment due to driving of the tail rotor (=0.97 typically)

The calculated total power encompasses the power requirement for the tail rotor as well. Generally, the ratio of power needed by the tail rotor to that required by the main rotor ($P_{\text{tail rotor}}/P_{\text{main rotor}}$) ranges between 0.14 to 0.22, as tail rotors usually have a diameter of approximately 15-20% of the main rotor's diameter [36].

During forward flight, the rotor functions similarly to a circular wing. The aspect ratio of such a wing stands at $4/\pi$, featuring an equivalent Oswald efficiency

factor between 0.5 and 0.8, based on empirical observations [36]. The Oswald efficiency factor defines the efficiency of the wing concerning induced drag and is calculated as the ratio between the wing's induced drag coefficient to that of an equal aspect ratio elliptic wing at the same lift coefficient. Parasitic drag can be quantified using the drag area (D/q), where 'q' denotes the dynamic pressure. The following equation integrates these elements to generate required power approximations for forward climb or level flights [36].

$$P_{(\mathrm{Fwd_{climb}\ or\ Fwd_{level}})} = \left[\frac{V}{\eta_{\mathrm{p}}}\left\{q(D/q) + \frac{W^2}{4eqS} + W\sin(\gamma)\right\}\right]\left[\frac{(1 + P_{\mathrm{tail\ rotor}}/P_{\mathrm{main\ rotor}})}{\eta_{\mathrm{mechanical}}}\right], \tag{3.6}$$

where $V\ (\mathrm{m/s})$ is the forward flight speed; $\gamma\ (\mathrm{Deg})$ is the climb path angle (=0, when levelled); $q\ (\mathrm{Pa})$ is the dynamic pressure; e is the equivalent Oswald's efficiency factor (=0.5 to 0.8 typically); $D/q\ (\mathrm{m^2})$ is the component drag area; η_{p} is the propeller efficiency (=0.6 to 0.85 typically).

In this equation, $W\sin(\gamma)$ represents the climb component, contingent upon the climb path angle γ (which is 0 for level flight). The rotor, while generating lift, also serves as a propeller for forward propulsion. Hence, to provide a reasonable estimate of the rotor in forward thrust, the propeller efficiency factor η_{p} is incorporated into the calculation.

3.5.2 Coaxial Rotorcraft

In a traditional helicopter setup, the primary function of the tail rotor is to counteract the torque produced by the rotation of the main rotor. It is achieved by generating an opposing thrust force, effectively balancing the torque. An alternative solution is to use another similarly sized rotor that spins in the opposite direction. This secondary rotor generates thrust parallel to the main rotor, offering the added benefit of increased lift. This concept is employed in the coaxial rotorcraft configuration, where two rotors are situated on the same shaft within a more complex hub arrangement. This configuration may suggest a doubling of

the lift force; however, the close proximity of the rotors results in the loss of some lift due to airflow wake interference. Theoretically, when the two rotors entirely overlap, known as a 100% overlapping case with zero vertical separation, the overlapping interference factor (K_{ov}) raises power consumption by √2, or approximately 41%, compared to two isolated rotors that are unaffected by the upper rotor's wake [38]. When the rotors are aligned without any vertical spacing in a coaxial setting, it is termed an equivalent single rotor. This equivalent single rotor equates to a system of smaller paired rotors with identical total thrust and total projected area (disk loading). This equivalence is due to their shared rotor solidity, defined as the ratio of total blade area to total disk area [39].

In practical applications, coaxial rotor systems maintain a physical separation between the two rotors. With increased vertical separation, the wake of the upper rotor affects a smaller area of the lower rotor, leading to a reduction in the overlapping interference factor (K_{ov}). For instance, with large separation (indicated as LS in section 3.8), typically around 10% of the rotor diameter, the K_{ov} decreases to 1.281 under the assumption of uniform disk loading [38] [39]. Hence, to calculate vertical climb and hover power for a coaxial rotor system with equally sized rotors sharing the total rotorcraft weight, Eq. (3.5) is adjusted by multiplying it by the overlapping interference factor (K_{ov}), resulting in Eq. (3.7). Similarly, Eq. (3.6) for a forward flight of a traditional helicopter is adapted to form Eq. (3.8) for a coaxial helicopter [38].

$$P_{(\text{Vert Climb or Hover})} = \left[\left(\frac{fW}{(2\sqrt{2})M}\sqrt{\frac{fW/S}{2\rho}}\right) + \frac{WV_{\text{Climb}}}{4}\right]\left[\frac{2}{\eta_{\text{mechanical}}}\right][K_{\text{ov}}] \quad (3.7)$$

$$P_{(\text{Fwd}_{\text{climb}}\text{ or Fwd}_{\text{level}})} = \left[\frac{V}{\eta_p}\left\{q(D/q) + \frac{W^2}{16eqS} + \frac{W\sin(\gamma)}{2}\right\}\right]\left[\frac{2}{\eta_{\text{mechanical}}}\right][K_{\text{ov}}] \quad (3.8)$$

In this configuration, there is no tail rotor; instead, a second rotor is utilised. Consequently, the ratio of power required by the two equal-sized rotors ($P_{\text{second rotor}}/P_{\text{main rotor}}$) becomes 1.

3.5.3 Isolated Rotors (Non-Overlapping Rotors e.g., Rotorcraft with Side-by-Side Rotors)

The K_{ov} factor, signifying the degree of overlapping interference between two identically sized rotors, changes from √2 to 1 when the shared area between them in the same plane shifts from full to zero. In the latter case, these rotors essentially function as isolated entities. Although there might be a minor degree of either beneficial or detrimental interference when there is a vertical separation between the rotors without any overlap, this aspect is usually disregarded in preliminary studies [38] [39]. For example, one subtype of side-by-side rotors is transverse rotorcraft, including tiltrotors and tiltwings, where smaller rotors are mounted horizontally on the tips of side wings or an extended support frame of the fuselage. Typically, these smaller rotors are positioned to avoid overlap and function similarly to isolated rotors. During the cruise flight, they transition into forward propellers. In scenarios involving configurations with multiple non-overlapping rotors, Equations (3.5) and (3.6) can be modified to accommodate a multirotor system with an 'N' number of equally sized rotors. In such an arrangement, the total thrust required for the rotorcraft is assumed to be evenly distributed among all the rotors, as described in Equations (3.9) and (3.10).

$$P_{(\text{Vert Climb or Hover})} = \left[\left(\frac{fW}{(N\sqrt{N})M}\sqrt{\frac{fW/S}{2\rho}}\right) + \frac{WV_{\text{Climb}}}{2\text{N}}\right]\left[\frac{N}{\eta_{\text{mechanical}}}\right] \quad (3.9)$$

$$P_{(\text{Fwd}_{\text{climb}} \text{ or } \text{Fwd}_{\text{level}})} = \left[\frac{V}{\eta_{\text{p}}}\left\{q(D/q) + \frac{W^2}{(N^2)4eqS} + \frac{W\sin(\gamma)}{N}\right\}\right]\left[\frac{N}{\eta_{\text{mechanical}}}\right] \quad (3.10)$$

However, in forward flight setups where the rotors align in front of each other, there is an additional downwash effect generated by the front rotor onto the rear rotor. To estimate the actual power required, this downwash must be considered and factored into the rear rotor/s [38], as explained in the following subsection 3.5.4 about the tandem rotorcraft. As there is no tail rotor in this configuration, but all equal sizes of rotors, thus the segment $[1 + (P_{\text{tail rotor}}/P_{\text{main rotor}})]$ of the original equation is replaced by $[N]$ in the modified equation to reflect the number of rotors involved.

3.5.4 Rotorcraft with Partial Overlapping Rotors (e.g., Tandem Rotorcraft)

The longitudinal configuration of a tandem rotorcraft involves aligning two equal-sized rotors along the fuselage, with one rotor situated in front of the other. The theoretical analysis of this setup resembles that of coaxial rotors as it generally includes a certain degree of overlapping disk area, determined by the horizontal gap between the rotors. Maximum tandem overlap occurs when one rotor's blade tip touches the hub centre of the other rotor. Therefore, the initial assessment for vertical climb or hover power in tandem rotors employs the same equation Eq. (3.7) as used for coaxial rotors. However, the determination of the overlapping interference factor (K_{ov}) in a tandem configuration is influenced by the ratio (d/D), representing the horizontal distance (d) between the two rotor axes and the rotor diameter (D), as illustrated in the tandem rotor configuration top view in Fig. 3.8. When the rotors are in the same plane (i.e., no vertical gap between rotors), demonstrated in Fig. 3.8 side view (a), K_{ov} can be approximated using Eq. (3.11) [38]. In scenarios where rotors operate in separate planes (side view (b), Fig. 3.8), and the lower rotor functions within the contracting wake of the upper rotor, determining the overlapping area necessitates numerical integration to ascertain a solution for K_{ov}.

$$K_{\mathrm{ov}} = \left[\sqrt{2} - \frac{\sqrt{2}}{2}\left(\frac{d}{D}\right) + \left(1 - \frac{\sqrt{2}}{2}\right)\left(\frac{d}{D}\right)^2\right] \tag{3.11}$$

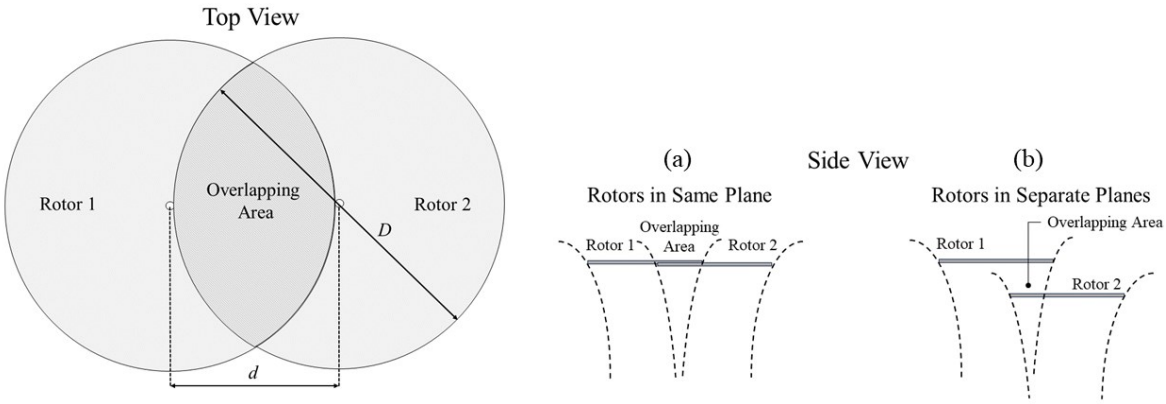


Fig. 3.8 Schematic illustration of tandem rotors overlapping area showing a generic top view and side view of rotors in the (a) same plane and (b) separate planes. (Not to scale)

In forward flight estimation for tandem rotorcraft, the downwash from the front rotor affects the rear rotor, which requires calculation and must be added to the power loss. For preliminary theoretical analysis, this downwash (dw) is presumed to reach the maximum value of the overlapping interference factor (max K_{ov} = K_{dw}) [38], calculated as 1.134 with maximum tandem overlap using Eq. (3.11). Therefore, the total power (P) required for forward flight is described in Eq. (3.12) [38]. For initial assessments, it is assumed that the two equally sized rotors generate identical thrust and thus, necessitate equal power. Hence, this expression is formulated into Eq. (3.13), where the total power of two isolated rotors is halved, and then one-half is multiplied by the downwash factor.

$$P_{(\mathrm{Forward})} = P_{\mathrm{Front\ Rotor}} + P_{\mathrm{Rear\ Rotor}}(K_{\mathrm{dw}})\,, \tag{3.12}$$

$$P_{(\mathrm{Forward})} = (1 + K_{\mathrm{dw}})\frac{1}{2}P_{2\ \mathrm{Iso}}K_{\mathrm{ov}}\,, \tag{3.13}$$

where $P_{2\ \mathrm{Iso}}$ (Watt) is the required forward flight power of rotorcraft with 2 isolated rotors; K_{dw} is the downwash factor (=1.134); K_{ov} is the overlapping interference factor (=1, when no overlapping).

When there is an overlap between the rotors, the equations (3.7) and (3.13) incorporate the parameter K_{ov}, which is calculated using Eq. (3.11), to estimate hover, vertical climb and forward power, respectively. However, in scenarios where there is no overlap between the rotors, such as in non-overlapping same-

plane tandem rotors, the K_{ov} factor is either omitted or the value is set to 1 in equations (3.7) and (3.13). This adjustment is necessary because using Eq. (3.11) for K_{ov} estimation is invalid when there is no overlap between the rotors.

Additionally, side-by-side rotor configurations with overlapping rotors can utilise a comparable approach to evaluate the overall power required. One such configuration is the synchropter, characterised by two counter-rotating rotors set at outward-tilting angles and a single gearbox to prevent blade collisions. This configuration would require numerical integration, and, for this reason, it is not considered a viable configuration for this study. Each of these rotorcraft configurations possesses distinct characteristics and aerodynamic considerations, and the selection among them is based on specific mission requirements and design objectives [38] [39].

3.6 Methodology for the Initial Sizing of Battery-Electric Aerobot

In this section, methodologies are outlined for estimating battery mass based on flight power requirements and conducting initial sizing for aerobot mass estimation, essential for step 9 of the design framework (Fig. 3.1). These methods are applied in section 3.9 using the ongoing example study case to determine the Potential Aerobot's empty mass. The total mass of an aircraft at maximum take-off comprises three primary elements: the empty mass, the payload, and the fuel. In the case of conventional fuel-powered aircraft, mass decreases progressively during flight due to fuel consumption across multiple flight phases, including taxiing, take-off, ascent, cruising, and descent. This decrease in mass affects the performance of aircraft and aerodynamic properties, necessitating detailed calculations for each flight phase during initial sizing estimations. However, in the case of electric aircraft, there is no variation in battery mass during flight. Consequently, there is no need for integration across different flight segments. Instead of fuel, the total mass of the aircraft includes the mass of the battery (m_{b}). The necessary battery mass for the flight mission is determined through the Battery Mass Fraction (*BMF*), represented in Eq. (3.14) as the ratio of battery mass to the total aircraft mass (m_{b}/m_0) [36].

$$BMF = \frac{m_{\mathrm{b}}}{m_0} = \frac{W_{\mathrm{b}}}{W_0} = \frac{EP_{\mathrm{used}}}{E_{sb}\eta_{\mathrm{b2s}}m_0}, \tag{3.14}$$

where m_0 (kg) is the total take-off mass of the aerobot; m_{b} (kg) is the battery mass; W_0 (N) is the total take-off weight of the aerobot (=mg, where g $(\mathrm{m/s^2})$ is the surface gravity acceleration on Mars for this paper); W_{b} (N) is the battery weight; P_{used} $(\mathrm{Watt\ or\ W})$ is the power required; E $(\mathrm{hour\ or\ h})$ is the known run time; E_{sb} $(\mathrm{Wh/kg})$ is the battery-specific energy; η_{b2s} is the total system efficiency from the battery to the motor output shaft (=0.9 typically).

Equation (3.14) accounts for parameters such as the known endurance (E) and power consumption (P_{used}) during distinct flight segments, including vertical climb, hover, and forward flight for rotorcraft. To obtain the total required aircraft *BMF*, the *BMF*s for each flight segment are summed. This method enables a comprehensive evaluation of the battery mass required for different phases of the mission flight profile of the aerobot [36].

When calculating the Battery Mass Fraction for electric aircraft, it is important to later include nominal usage and discharge efficiency to improve the precision of battery mass estimations. Nominal usage refers to the usable portion of the battery's capacity, as batteries are typically not discharged from 0% to 100% to prevent degradation and extend lifespan. For instance, operating within a range of 10% to 80% state of charge limits usable capacity to 70%, reducing stress and enhancing longevity [40]. Discharge efficiency, defined as the ratio of energy output during discharge to energy input during charging, also influences battery sizing. A discharge efficiency of 95%, for example, indicates that 5% of the energy is lost, primarily as heat [41]. Incorporating these adjustments into the *BMF* ensures the aircraft achieves its performance objectives while safeguarding battery health and operational reliability.

The total aircraft take-off mass is determined by the sum of the empty mass (m_{e}), battery mass, and payload mass, as shown:

$$m_0 = m_{\mathrm{e}} + m_{\mathrm{b}} + m_{\mathrm{payload}} \tag{3.15}$$

To adjust this equation for battery-electric aerobot sizing, Ref. [36] applied a modification to derive the following equation:

$$m_0 = \frac{m_{\text{payload}}}{1 - BMF_{\text{total}} - \frac{m_{\text{e}}}{m_0}} \tag{3.16}$$

This adaptation involves considering the total Battery Mass Fraction and the ratio between the empty mass and the total take-off mass [36]. Within this framework, the payload can encompass instrumentation or delivery items, especially in the context of unmanned aircraft. Conversely, the term m_{e} comprises all the components apart from the payload or operational batteries. This includes the propulsion system, aircraft structure, avionics, navigation systems, and other critical components necessary for the functionality of the aerobot, along with a percentage contingency margin.

The initial sizing equation serves as a foundational reference, allowing for preliminary measurements based on factors like the empty mass ratio, payload mass (derived from statistical data or a particular package), and the calculated Battery Mass Fraction. This equation provides a starting point to determine the total take-off mass of the aerobot. Alternatively, known or predetermined parameters can be used to estimate unknown variables; for instance, the empty mass, when total take-off mass and payload are known, and the required battery mass is computed using calculated *BMF*. This iterative procedure permits multiple calculations and adjustments until a reasonably accurate estimate aligns with the desired objectives, thereby facilitating comprehensive preliminary design investigations.

3.7 Establishing Rotorcraft Configuration Cases for Parametric Analysis

As per step 7 of the framework for the preliminary Martian aerobot design (Fig. 3.1), this segment establishes the potential rotorcraft configuration cases and sets values for all parameters, and a range for variables, in alignment with mission requirements for parametric performance analysis for the example mission scenario developed in the earlier sections. For rotorcraft with multiple

equal-sized rotors, some generalisations can be made. When the rotor diameter (D) equals or falls below the half value of the maximum allowable diameter ($D_{\max}$) – the disk size beyond which the blade would hit the hub of the other rotor – the rotors do not overlap and are deemed isolated. Where the rotor size is above half $D_{\max}$, the rotors overlap and behave as an overlapping tandem rotor setup, as expressed by the following equation:

$$D_{\text{non-overlap}} \leq \frac{D_{\max}}{2} < D_{\text{overlap}} \tag{3.17}$$

The above relationship is expressed in Fig. 3.9 along with the rotor hub position (h), which represents the displacement from the reference point/line located in the middle of two adjacent rotors (i.e., the reference line shown), which when factored by 4 gives $D_{\max}$ as shown in Eq. (3.18) and when factored by 2 it estimates the horizontal distance (d) between the two rotor hubs, Eq. (3.19).

$$D_{\max} = 4h = 2d\,, \tag{3.18}$$

$$d = 2h\,, \tag{3.19}$$

where $D_{\max}$ (m) is the maximum allowable rotor diameter; h (m) is a displacement from the reference point/line located in the middle of two adjacent rotors; d (m) is the horizontal distance between the two rotor hubs.

For the given aeroshell dome size limit (A), the rotor hub position at which the maximum allowable rotor diameter is within the aeroshell without requiring any folding mechanism can be deduced by the following equation, which is valid for the rotors in tandem settings (e.g. Fig. 3.11, Case 3).

$$h = \frac{A}{6} \tag{3.20}$$

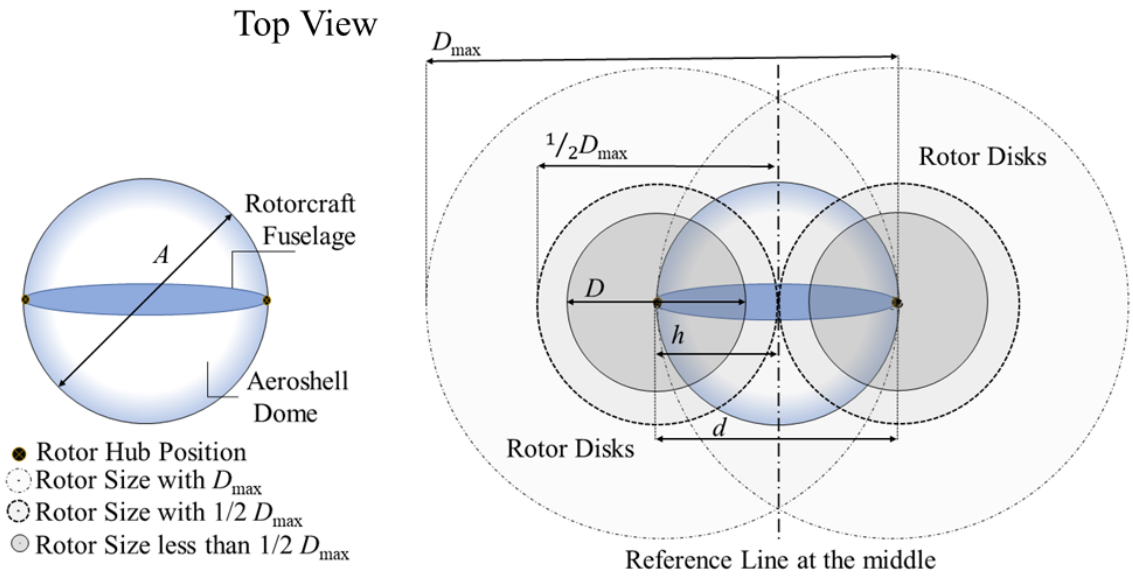


Fig. 3.9 Schematic diagram illustrating the terms A, D_{max}, h, d. Left side image shows a fuselage of the rotorcraft within a spacecraft aeroshell highlighting the size limit A. Right side image shows 3 different sizes of rotor disks at a fixed rotor hub position, demonstrating how changes in rotor diameter affect the degree of rotor overlap.

3.7.1 Tandem Rotorcraft Configuration Cases Formation

Tandem rotorcraft configurations can vary based on the longitudinal positioning of the rotors atop the fuselage. For power analysis, three cases are examined based on the structural limits of the aeroshell, assuming the fuselage matches the maximum aeroshell size of 4.5 m. The hubs of two equal-sized rotors are positioned at equal distances from the middle of the fuselage at 2.25 m, 1.125 m, and 0.75 m for Cases 1, 2, and 3, respectively as shown in Fig. 3.10. These positions represent extreme scenarios for parametric analysis, with Case 1 placing foldable rotors at the end of the fuselage with a maximum allowable diameter of 9 m, while Case 3 positions rotors to reach a maximum permitted diameter of 3 m that fits within the aeroshell boundary, and Case 2 setting lies between these two cases, which allows rotors to a maximum diameter of 4.5 m (Fig. 3.11). A summary of the defined parameters for all three tandem rotorcraft configuration cases is detailed in Table 3.3. Tandem Case 1 requires a folding

mechanism and possibly an articulated rotor hub system for storage within the aeroshell. Similarly, Case 2 would demand folding mechanisms and perhaps an articulated rotor hub system as well, if the rotor diameter exceeds 2.25 m. Contrary to this, Case 3 can utilise a rigid rotor hub system without requiring linkages. Notably, the practical design considerations, such as the clearance between rotor blades and aeroshell walls or rotor hubs, have not been factored into this theoretical analysis as the primary focus is on establishing fundamental performance trade-offs between different rotorcraft configurations of this study.

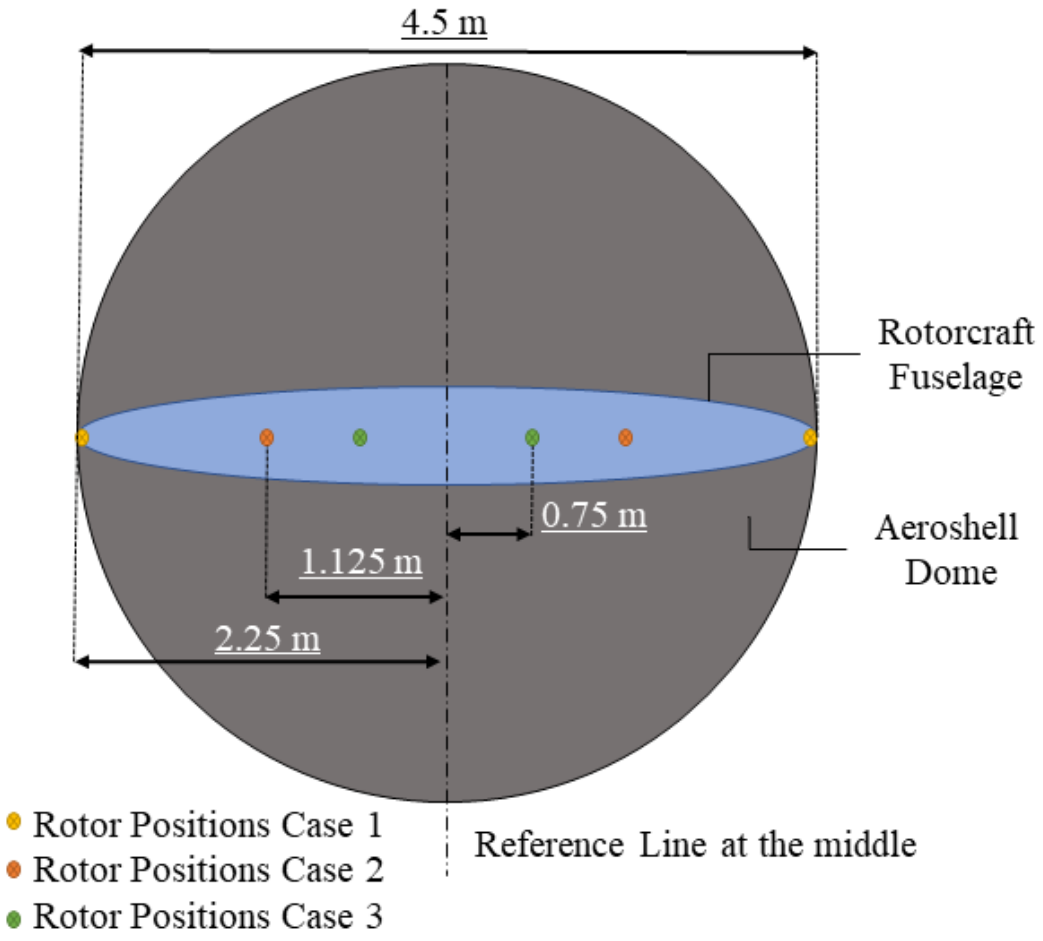


Fig. 3.10 Schematic illustration of three cases of tandem rotor hub positions on the fuselage placed inside the aeroshell. (Not to scale)

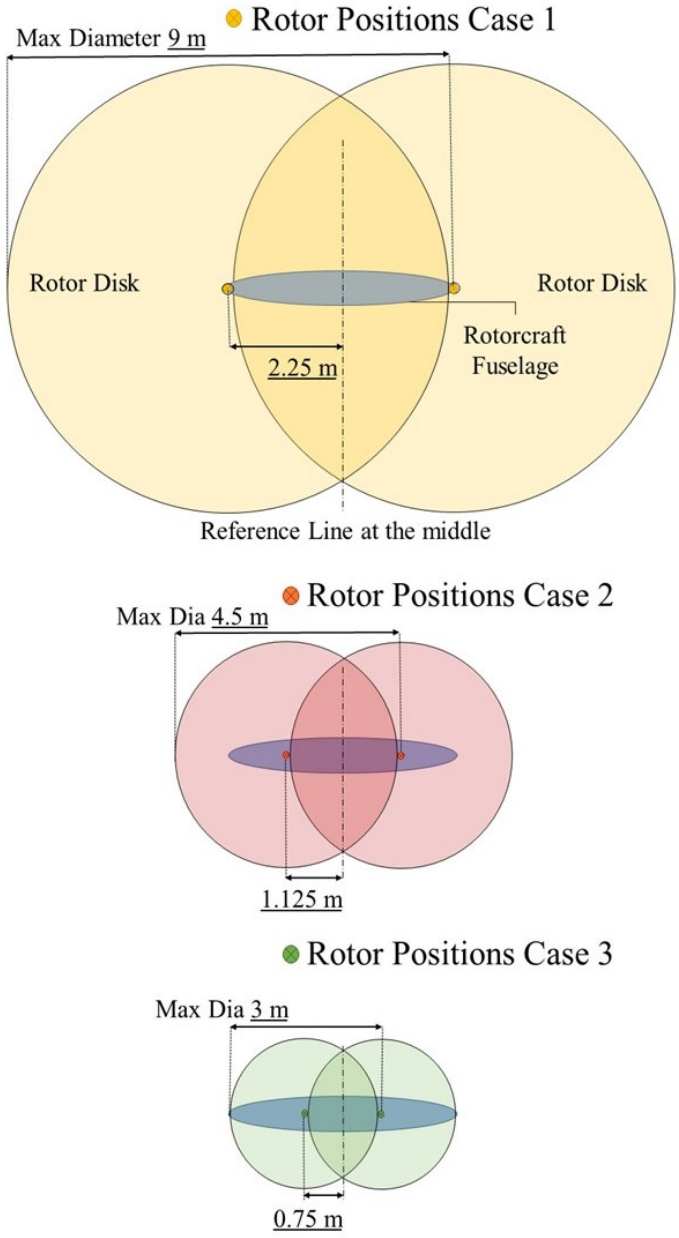


Fig. 3.11 Schematic illustration of the rotor positioning of tandem rotorcraft cases 1, 2 and 3 in operational mode. (Not to scale)

Table 3.3 Summary of Tandem Rotorcraft Cases

Case No.	Rotor System Type	Folding Mechanism	Maximum Diameter	Rotor Position*	Isolated Rotor behaviour
1	Articulated	Yes	9 m	2.25 m	$D \leq 4.5$ m
2	Articulated**	Yes**	4.5 m	1.125 m	$D \leq 2.25$ m
3	Rigid	No	3 m	0.75 m	$D \leq 1.5$ m

* Rotor hub position from the center of the fuselage

** When rotor D is > 2.25 m

3.7.2 Parameters and Variables Finalisation

The initial sizing of the rotorcraft incorporates the total flight mission duration based on range, cruise speed, takeoff, and climb, presuming continuous high-power operation. Descent and landing times are initially excluded to simplify the analysis, as their power requirements are significantly lower compared to ascent and cruise phases, thus having a minimal impact on overall energy consumption and sizing estimates [36]. Therefore, the flight profile considered in this analysis, Fig. 3.12, involves a 2-minute ascent to 1 km (resulting in an average vertical climb velocity (V_{climb}) of 8.33 m/s) and a 3-minute traverse of 10 km (yielding an average cruise velocity of 55.56 m/s) and vertical descent, totalling 5 minutes. These values are derived from the mission specifications and expected aerobot performance constraints discussed in Section 3.3.4, which consider power availability, achievable flight speeds, and energy efficiency.

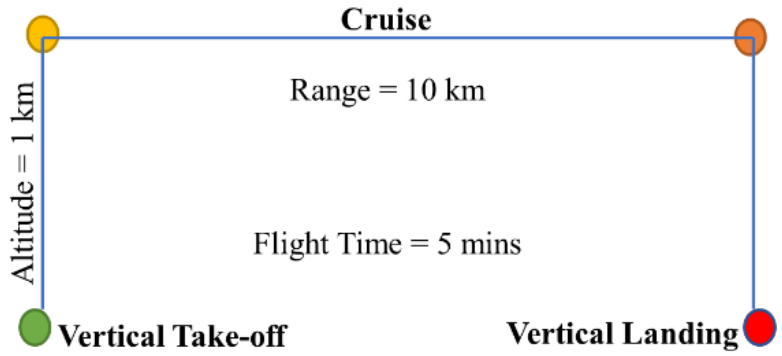


Fig. 3.12 Flight profile for the analysis

Table 3.4 summarises the parameters and variables defined for this research used in the parametric power analysis for various rotorcraft configurations during forward flight, vertical climb, and hover phases. For the Potential Aerobot case study, the Maximum Take-Off Gross (MTOG) mass of the aerobot for the mission is set to be 20 kg , aligning with advanced Mars rotorcraft like the MSH [5] and Y-4 Tiltrotor [7] to ensure feasibility within current power and payload constraints. The figure of merit (M), typically ranges between 0.6 to 0.8 for a full-scale helicopter on Earth [36]; however, because of the low Reynolds number on Mars the lowest value of 0.6 is used for this analysis as a conservative choice, consistent with experimental studies on low-Reynolds-number rotors for Mars

rotorcraft concepts [5]. The battery specific energy (E_{sb}) required for Battery Mass Fraction (*BMF*) calculations for flight is selected to be 230 Wh/kg pack (including battery management system), sourced from a JPL technology forecast [5].

Table 3.4 Parameters and variables used in the forward flight, vertical climb, and hover power analysis of various rotorcraft configurations.

Parameter	Values			Unit
Mars Mean Air Density at SW Melas Basin	0.016			kg/m^3
Average Speed of Sound on Mars	240			m/s
Surface Gravity Acceleration on Mars	3.73			m/s^2
Aircraft MTOG Mass, m_0	20			kg
Aircraft MTOG Weight, W_0	74.60			N
Allowable Maximum Rotor Advancing Blade Tip, M_{at}	0.75			Mach
Air Speed at Max M_{at} on Mars	180			m/s
Traverse Range as per Flight Mission	10			km
Cruise Flight Endurance, E	3.0			min
Cruise Flight Velocity, V	55.56			m/s
Dynamic Pressure at the Cruise Velocity, q	24.69			Pa
Flight Altitude as per Flight Mission	1			km
Vertical Climb Endurance, E	2.00			min
Average Vertical Climb Velocity, V_{climb}	8.33			m/s
Rotor Diameter, D	0.23	to	9.0	m
Rotor Disk Area, S	0.04	to	63.6	m^2
Battery Specific Energy, E_{sb}	230.00			Wh/kg
Measure (or figure) of Merit, M	0.6			
Mechanical efficiency factor, $\eta_{mechanical}$	0.97			
Fuselage downwash adjustment, f	1.06			
Helicopter Power ratio ($P_{tail\ rotor}/P_{rotor}$)	0.18			
Coaxial Power ratio ($P_{second\ rotor}/P_{main\ rotor}$)	1			
System efficiency battery to motor (η_{b2s})	0.9			
Propeller Efficicency, η_p	0.8			
Oswald Efficiency, e	0.5			
Parasitic Drag Area, *D/q* (Front Area x Drag data)	**Front Area**	**Drag Data**	***D/q***	
D/q Fuselage (radius 0.15 m)	7.1E-02	0.09	6.0E-03	m^2
D/q Tubular Landing 4 legs (0.002m x 0.03m, each)	2.4E-04	1.01	2.4E-04	m^2
D/q Unfaired Single Rotor (0.005m x 0.003m)	1.5E-05	1.20	1.8E-05	m^2
Downwash Interference Drag Fuselage	7.1E-02	0.02	1.4E-03	m^2
Leakage & Protuberance Drag (15% Total *D/q*)			1.2E-03	m^2

Concerning forward flight analysis, certain parameters are crucial, such as the frontal area of the aircraft body. For all configurations, the same frontal area

comprising the fuselage, landing legs, and an unfaired rotor hub is considered. Helicopter-specific drag data, outlined by D. Raymer [36] in terms of drag area (D/q) per unit frontal area, is used. This drag area data, when multiplied by the frontal area of the helicopter, provides specific values for the drag area of each component. The calculated total parasitic drag is subsequently integrated into the forward flight power Eq. (3.6) for conventional helicopters, and similarly included in the respective forward flight equations for other rotorcraft configurations. While this drag data method is not precise, it is sufficient for the initial sizing of the rotorcraft until the design matures for a comprehensive preliminary study. The theoretical method used aligns well with experimental data in the literature, particularly within an advance ratio range of 0.1 to 0.3 [38]. The advance ratio of rotorcraft is the ratio of its forward flight speed to its rotor tip speed.

3.8 Results and Analysis

Continuing within the framework for preliminary drone design for Mars (Fig. 3.1), the following stage (step 8) involves the evaluation and selection of various rotorcraft configurations based on their power consumption within a simplified flight envelope. This trade-off study, conducted through parametric performance analysis, utilises the methodology outlined in Section 3.5 to assess different configurations and parameters introduced in the previous section (3.7). The objective of the parametric analysis is to identify the most suitable configuration for the exemplar mission outlined in Section 3.3, although the same approach can be applied to any other VTOL aerobot mission on Mars. The subsequent subsections present results and analysis in terms of power requirements for hover, vertical climb, and forward flight segments, for rotorcraft configurations with single and dual rotors, including a single conventional, coaxial rotors with large separation (LS), three cases of tandem rotors (shown in Fig. 3.11) and 2 isolated rotors. These findings inform the sizing of battery packs and, consequently, the overall mass of the rotorcraft. Later, Section 3.9 will present a further discussion of the results and the practical implications of the analyses.

3.8.1 Hover and Vertical Climb Analysis

Fig. 3.13 shows the power demand for a Martian helicopter of conventional configuration plotted against the increasing diameter of the rotor disk. As the rotor size expands, the area of the rotor disk also increases, leading to a reduction in disk loading. Disk loading is the ratio of the total weight of the helicopter to the area of the rotor disk (*W/S*). This means that by using motor power on a larger air cross-section, the helicopter achieves greater thrust efficiency. Consequently, when disk loading decreases, there is a reduced requirement for battery and motor power during hovering or climbing. This reduction in power demand allows for a higher power loading (*W/P*), which represents the ratio of the helicopter's weight to its engine power. However, it is important to note that while lower disk loading, associated with larger rotor blades, can improve efficiency, it can also lead to increased weight, higher forward flight drag, and a greater potential for encountering shocks on the advancing blade [36], which are factors not addressed in this research. The graph demonstrates that smaller-sized rotors consume considerably more power than larger ones, showcasing a noticeable and substantial decrease in power as the rotor disk diameter increases (also discussed in [42] and [43]).

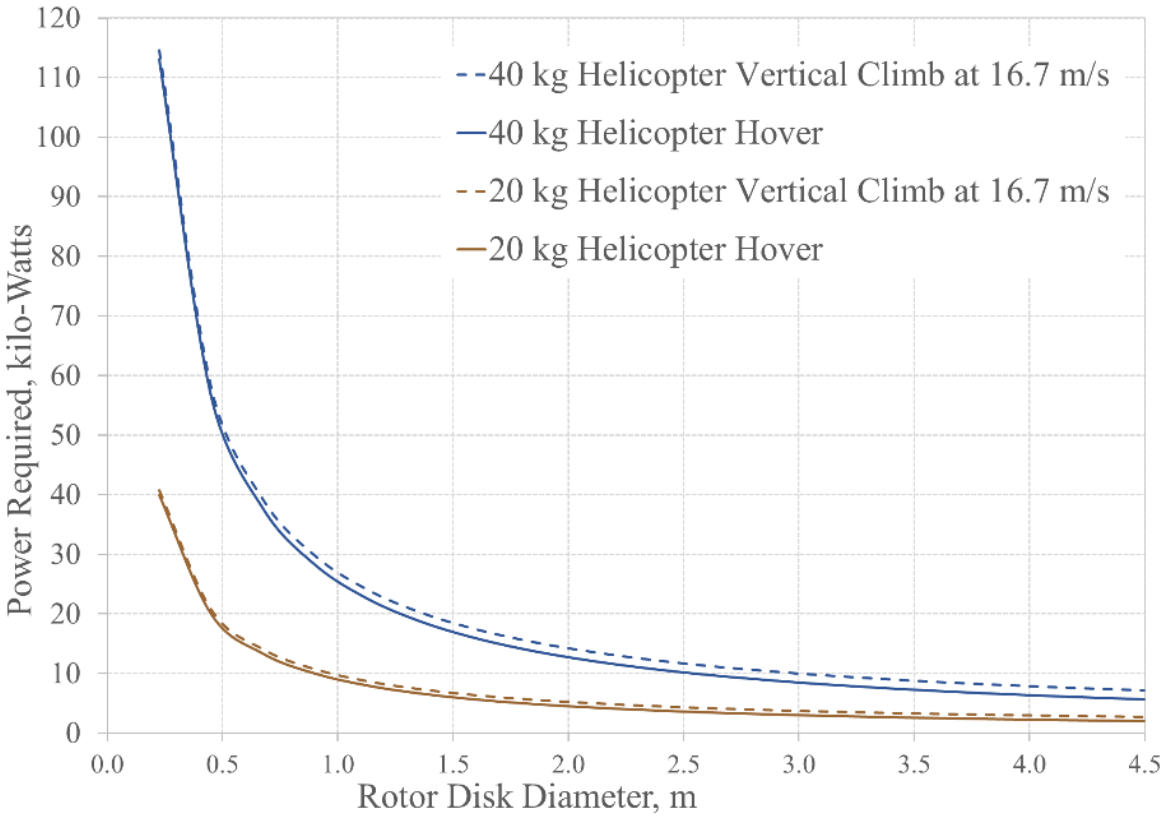


Fig. 3.13 Power Required (Hover & Vertical Climb) vs Rotor Disk Diameter – 20 kg & 40 kg Martian Conventional Helicopter

Moreover, if the total mass of the aerobot increases, the power required for smaller rotor disks significantly escalates, whereas, for larger rotor disk diameters, the power required reaches higher asymptotic values. This difference is demonstrated in the graph comparing a 40 kg to a 20 kg helicopter. Analysing the power requisites, it is apparent that vertical climbing demands slightly more power than hovering, as expected due to the energy needed for vertical forward propulsion. Nevertheless, with increasing rotor disk size, the divergence between the power demands for hovering and climbing becomes more noticeable over time.

Fig. 3.14 and Fig. 3.15 present graphical representations of hover power and vertical climb power relative to the rotor disk diameter, respectively, across various rotorcraft configurations: conventional helicopter, LS (large separation) coaxial rotorcraft, three tandem rotorcraft cases, and rotorcraft with two isolated rotors. It is worth noting that the extension of power data for two equal isolated

rotors beyond a rotor disk size of 4.5 m is for analytical comparison with tandem rotor Case 1, rather than for practical application. Across all configurations, vertical climbing consistently demands more power than hovering, with this difference progressively increasing as the rotor disk diameter grows. Among these setups, the conventional helicopter exhibits the highest power demand. Conversely, the power consumption of two equal-sized coaxial rotors is lower with smaller-sized rotors, notably at a diameter of 0.23 m, requiring approximately 9,000 Watts less power compared to the conventional helicopter. Similarly, other configurations demand roughly 16,000 Watts less power for both hovering and vertical ascent at this rotor size. At the maximum aeroshell size (corresponding to a rotor diameter of 4.5 m), hover and vertical climb power requirements range approximately between 1,000 to 2,500 Watts for all configurations. In the three tandem rotorcraft cases, it is evident that before rotor overlapping, the power needed aligns with that of isolated rotors. The graphs illustrate a trend where power requirements decrease in verse proportion to rotor diameter, initially decreasing rapidly and then levelling off as rotor diameter increases. This transition in power requirement becomes insignificant, particularly for tandem rotorcraft Case 1, with rotor disk sizes between 4.5 m and 9 m. Particularly smaller rotor sizes show tandem rotorcraft consuming notably less power than other rotorcraft configurations.

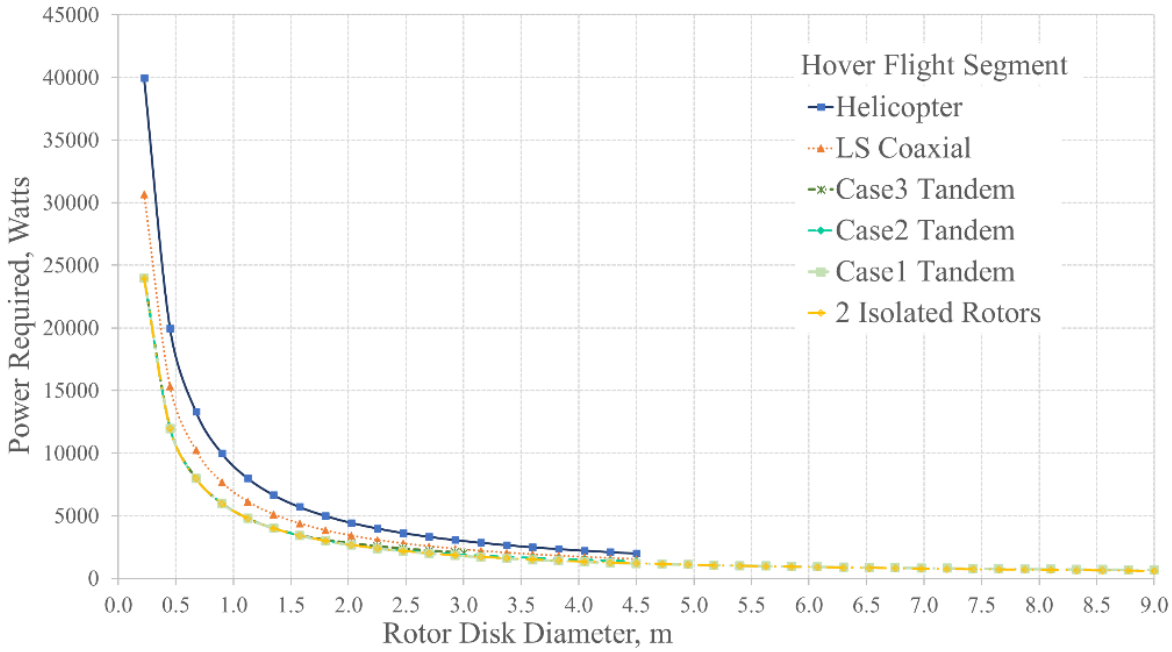


Fig. 3.14 Power required (Hover) vs Rotor Disk Diameter – Comparison between various 20 kg rotorcraft configurations (Helicopter, Coaxial, Tandem Cases, 2 Isolated Rotors)

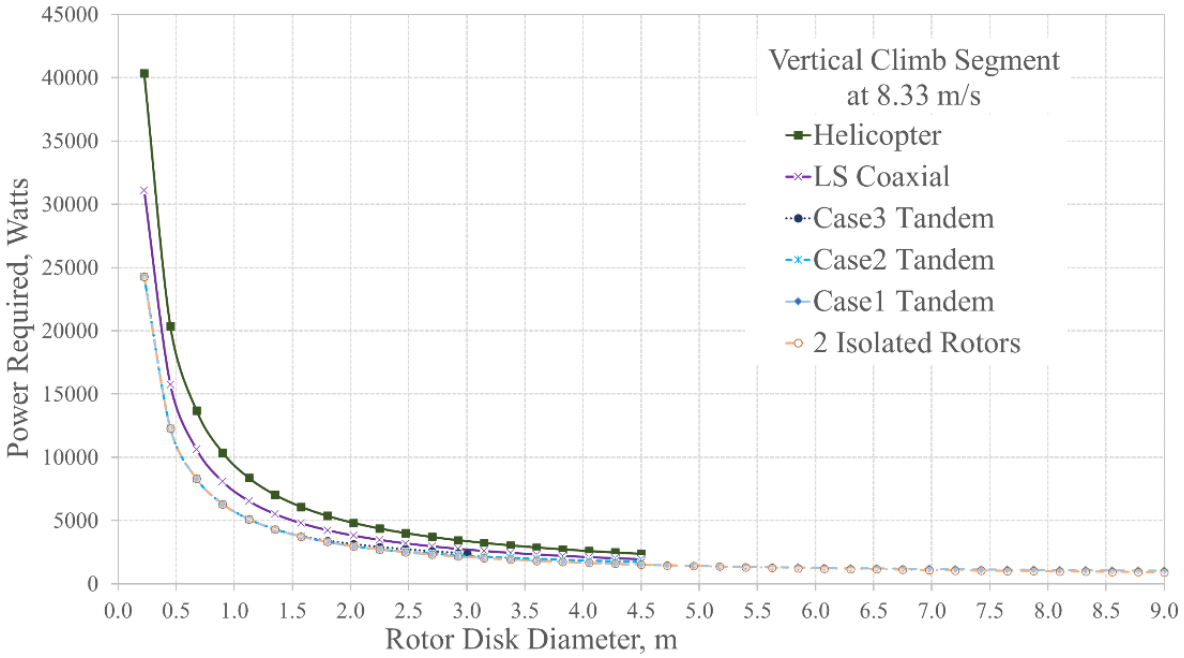


Fig. 3.15 Power required (Vertical Climb) vs Rotor Disk Diameter – Comparison between various 20 kg rotorcraft configurations (Helicopter, Coaxial, Tandem Cases, 2 Isolated Rotors)

Fig. 3.16 presents a graph of hover power required by the 20 kg rotorcraft configurations mentioned earlier, plotted against the rotorcraft disk loadings (*W/S*) on the logarithmic scale (base 2). These data provide insight into the trend in terms of disk loading, whereas earlier Fig. 3.14 showed hover required power in terms of rotor disk diameter. The nodes or markers on the graph lines indicate the corresponding rotor disk sizes related to the disk loading of the respective rotorcraft, increasing in 5% intervals of the 4.5m aeroshell size, starting at 0.23 m and going up to 9 m (particularly for the 2 isolated rotors and tandem Case 1). Some of these disk sizes are labelled across the graph, particularly the smallest and largest sizes. The helicopter uses a single rotor of mentioned disk size, whereas other rotorcraft uses dual rotors of labelled sizes; hence, it is apparent that the helicopter consumes the highest power followed by a coaxial rotor with tandem and isolated rotors. It is well established that the lower disk loading means that less power is required to hover, however, it is interesting to note that for the given rotorcraft weight, the rotorcraft with disk loading under 64 N/m^2 (rotor disk diameter >1 m) require substantially less power when compared to the rotor disk sizes lower than 1 m diameter. The disk loading increases rapidly, from 60 to 2000 N/m^2 (approx.), as the rotor disk diameter reduces from about 1m to 0.23 m, respectively. As shown in the previous graphs, the single-rotor helicopter consumes more power than the coaxial rotorcraft, while the tandem rotorcraft is the most efficient, with the disk loading graph highlighting these differences more prominently for smaller rotors.

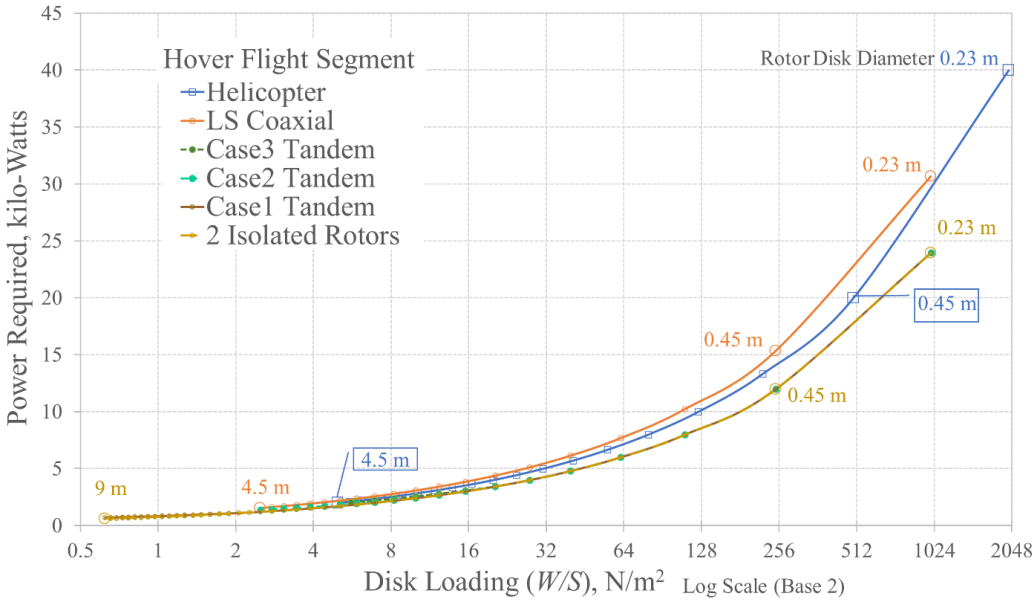


Fig. 3.16 Power required (Hover) vs Disk Loading (W/S - on log scale base 2) – Comparison between various 20 kg rotorcraft configurations (Helicopter, Coaxial, Tandem Cases, 2 Isolated Rotors)

Similarly, a graph of the power loading (*W/P*) of these 20kg rotorcraft configurations during hover is plotted against the rotorcraft disk loading, using log scale (base 2) for both axes for better clarity, as shown in Fig. 3.17. The more power-efficient the rotorcraft, the higher its power loading, as reflected in the plot, where the tandem and 2 isolated rotorcraft configurations have higher power loading than the coaxial, while the helicopter configuration has the lowest for similar disk sizes. The power loading inversely decreases with an increase in disk loading (appearing as a linear decrease on a log scale), reflecting a reduction in rotor disk size for a given mass.

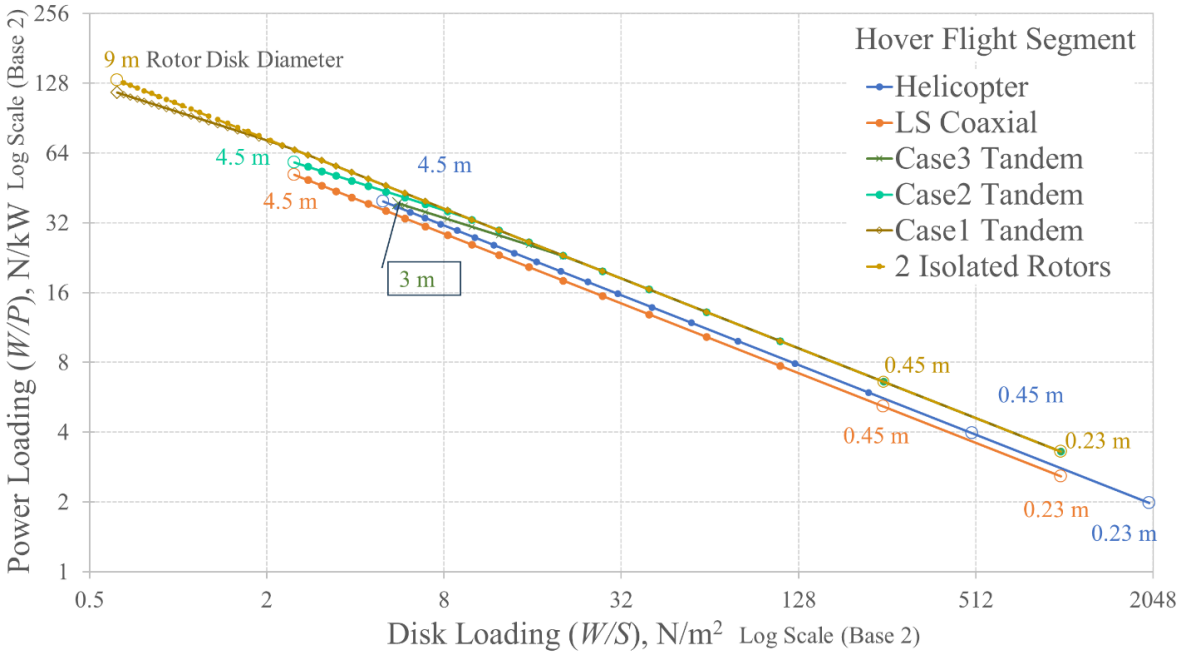


Fig. 3.17 Power Loading (W/P) (Hover) vs Disk Loading (W/S) (both axes on Log scale base 2) – Comparison between various 20 kg rotorcraft configurations (Helicopter, Coaxial, Tandem Cases, 2 Isolated Rotors)

3.8.2 Forward Flight Analysis

The analysis shown of a conventional helicopter for Mars in Fig. 3.18 includes forward-level flight and forward climb flight at a 20-degree climb path angle, flying at a cruise velocity of 55.56 m/s. A trend is apparent in the graph that climbing while flying forward demands higher power compared to straightforward forward flight. However, at smaller rotor disk sizes, both flight modes exhibit similar power consumption, with the difference becoming noticeable at and beyond a rotor disk diameter of about 0.5 m. Unlike levelled flight, the power requirement for forward climb flight does not decrease as significantly with increasing rotor disk size.

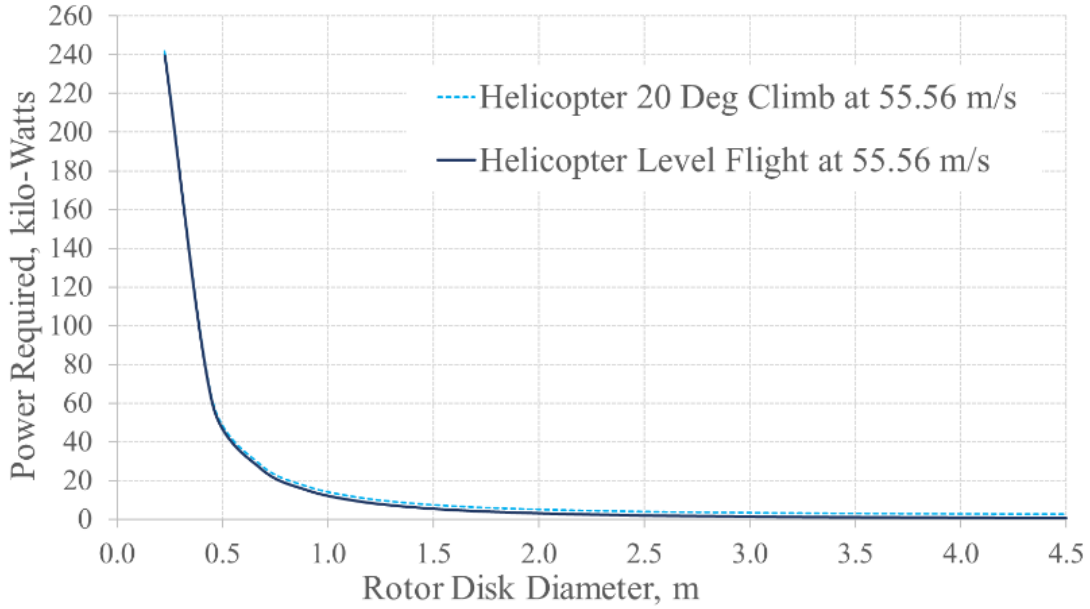


Fig. 3.18 Power Required (Forward Level & Climb Flight) vs Rotor Disk Diameter – 20 kg Martian Conventional Helicopter

Fig. 3.19 presents a snapshot of the required power for forward levelled flight among the discussed rotorcraft configurations, up to rotor disk sizes of 9 m. Notably, at the smallest rotor disk size, the conventional helicopter demonstrates the highest and unrealistic power demand, followed by the coaxial rotorcraft, tandem rotorcraft cases, and then the two isolated rotors. However, with a slight increase in rotor disk size, the power requirement dramatically decreases, until the reduction in power becomes negligible from a rotor size of about 2 m onward.

Fig. 3.20 displays a detailed observation of the power differences among various rotorcraft configurations for both forward levelled and climb flights, setting the rotor disk diameter from 1 m on the horizontal axis. During the forward climb of tandem rotorcraft Case 1, a notable observation arises: after initially reaching a minimum, the required power begins to increase as the tandem rotors start to overlap beyond a rotor diameter of 4.5 m, influenced by the introduction of an additional overlapping interference factor (K_{ov}) in conjunction with the downwash factor (K_{dw}). A similar trend is noted with Case 2 tandem rotorcraft but only at the upper limit of the rotor diameter.

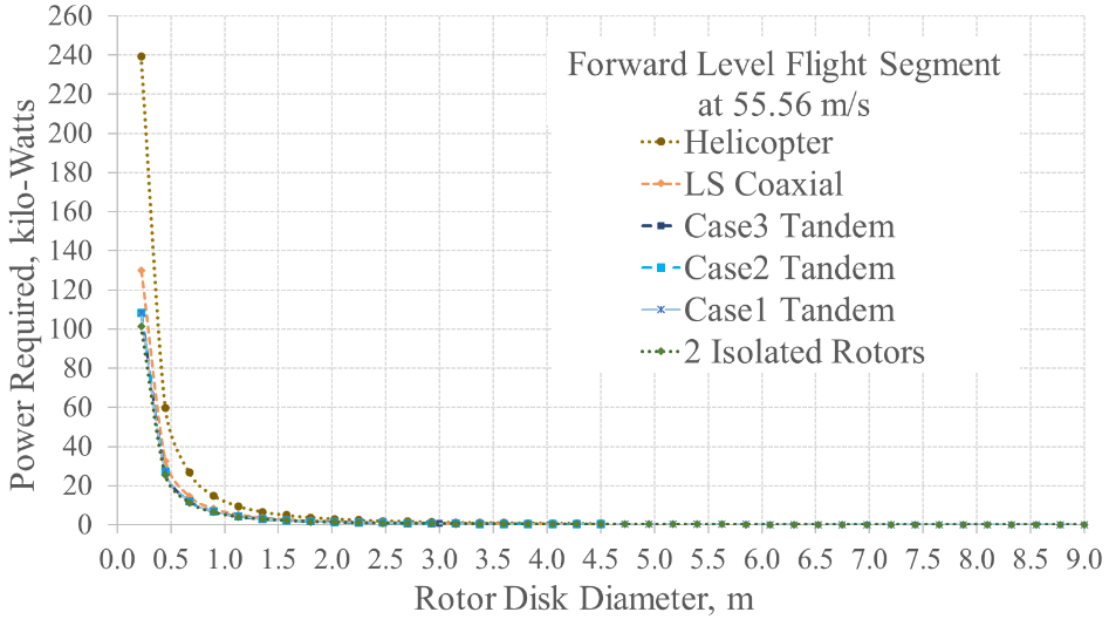


Fig. 3.19 Power Required (Forward Level) vs Rotor Disk Diameter– Comparison between various 20 kg rotorcraft configurations (Helicopter, Coaxial, Tandem Cases, 2 Isolated Rotors)

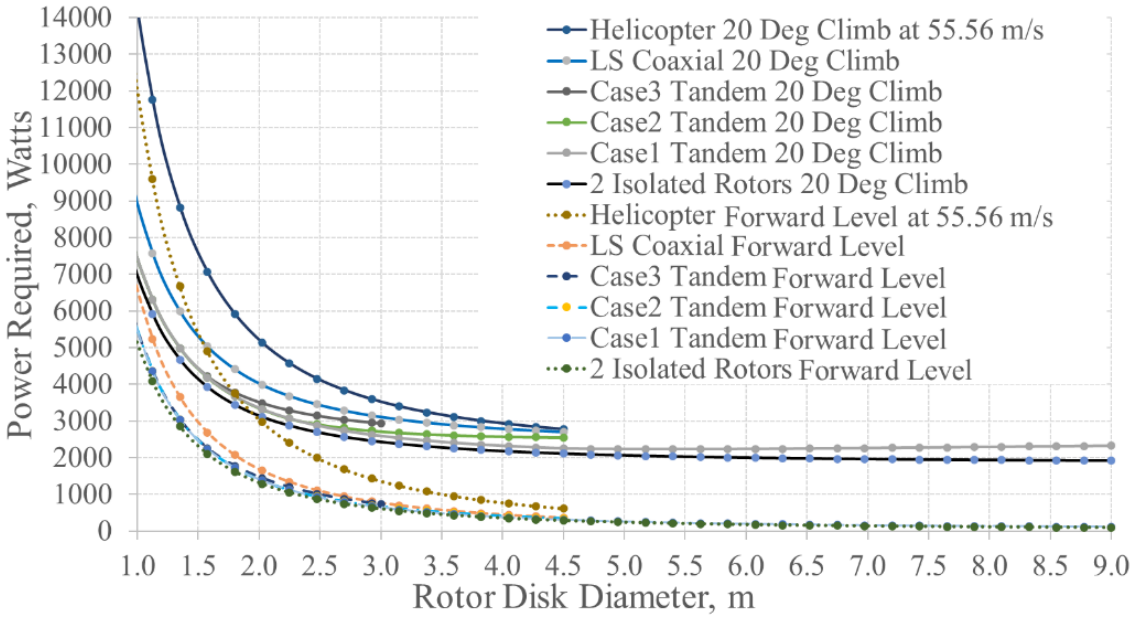


Fig. 3.20 Power required (Forward Level & Climb Flight at 55.56 m/s) vs Rotor Disk Diameter (Rotor Diameter Limits - 1 to 9 m) – Comparison between various 20 kg rotorcraft configurations (Helicopter, Coaxial, Tandem Cases, 2 Isolated Rotors)

It is apparent that beyond rotor disk sizes of 3 m, except for the helicopter, all other rotorcraft configurations for forward levelled flight require around or under 1000 Watts of power. Conversely, for forward flight at a 20-degree climb angle,

the power requirement ranges from approximately 2500 to 3500 Watts. Although climbing while flying forward demands more power than levelled flight, achieving height during forward flight is more energy efficient than vertical flight overall. Flying closer to the ground, known as ground effects, creates an air cushion under the aircraft, aiding in reaching optimal flight speed before ascending, thus reducing energy losses. This analysis is performed below the maximum allowed forward flight speed (60 m/s, refer to subsection 3.4.3) to prevent air shock buildup at the rotor tip speed; however, if we experiment with increasing the forward speed further, the required forward flight power will decrease. Additionally, a lower climb path angle would result in less power required for forward climb flight.

Fig. 3.21 presents a graph depicting the power required for forward level flight by the 20 kg rotorcraft configurations, plotted against rotorcraft disk loading (*W/S*) on logarithm scale (base 2). This analysis parallels the hover power analysis shown in Fig. 3.16. While Fig. 3.19 illustrated the power requirements for forward level flight as a function of rotor disk diameter, this data provides insight into the trends relative to disk loading. It is apparent from this disk loading graph that for smaller rotor sizes, helicopter configuration becomes significantly more inefficient during cruise than in hover when compared to other configurations. Additionally, the tandem configuration consumes more power during the forward flight compared to the ideal two isolated rotors, a contrast to the hover segment shown in **Fig.** 3.16. This loss in performance is attributed to the downwash interference experienced by the rear rotor from the wake of the front rotor, as described in Eq. (3.12). Similarly, Fig. 3.22 shows a graph of the forward level flight power loading (*W/P*) of these 20kg rotorcraft configurations plotted against the rotorcraft disk loading using logarithmic scale (base 2) for both axes for better clarity. The trends observed are similar to the hover power loading graph (Fig. 3.17) such that the helicopter has the lowest power loading, followed by coaxial rotorcraft, tandem and then the rotorcraft with the 2 isolated rotors.

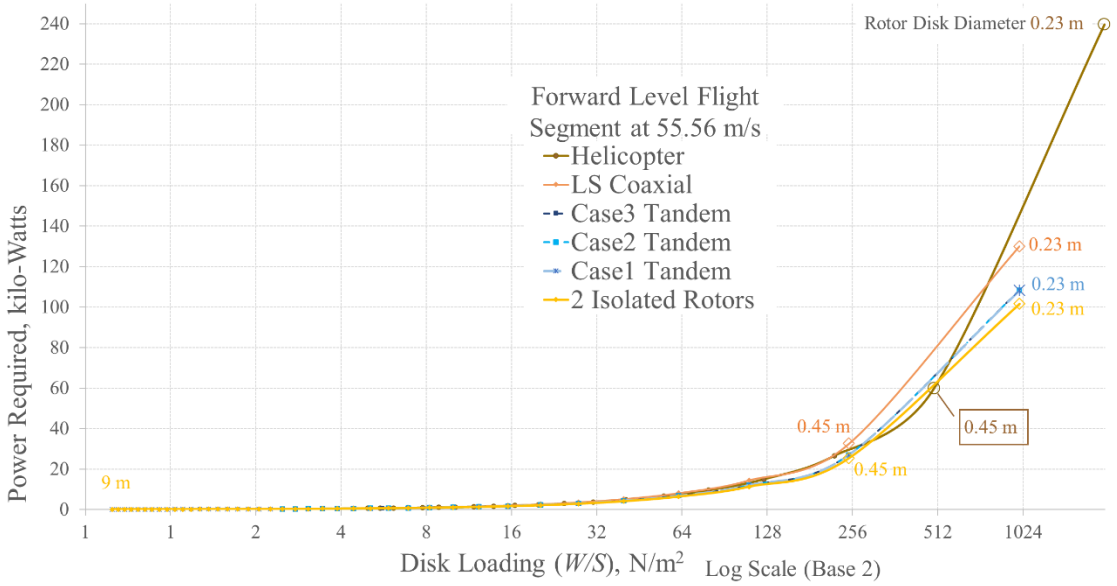


Fig. 3.21 Power required (Forward Level Flight) vs Disk Loading (W/S) – Comparison between various 20 kg rotorcraft configurations (Helicopter, Coaxial, Tandem Cases, 2 Isolated Rotors)

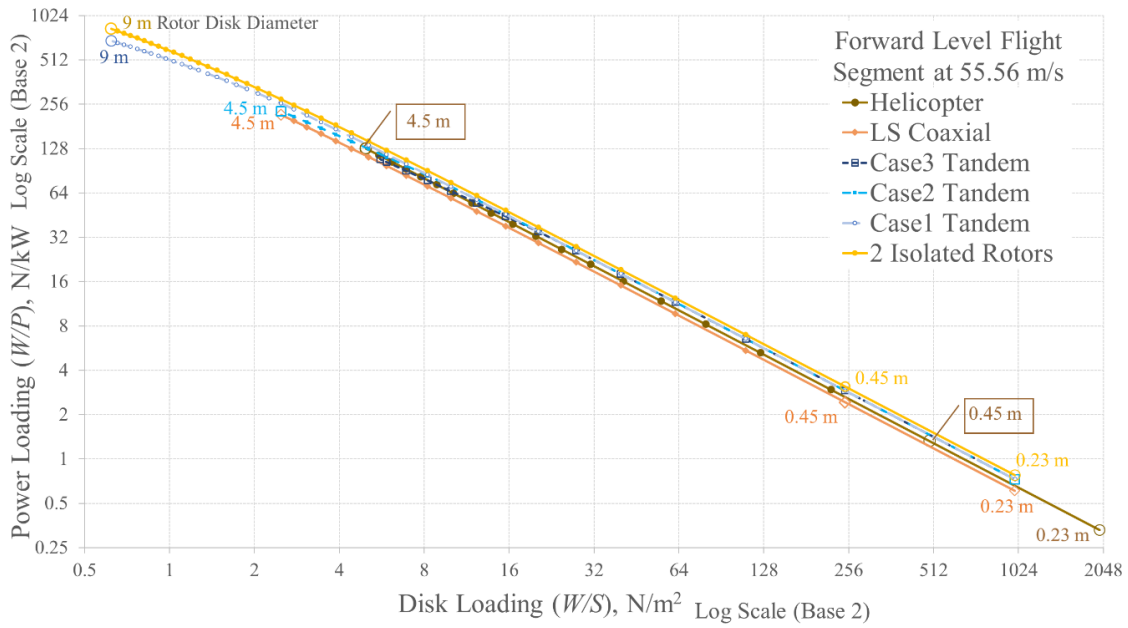


Fig. 3.22 Power Loading (W/P) (Forward Level Flight) vs Disk Loading (W/S) (both axes on Log scale base 2) – Comparison between various 20 kg rotorcraft configurations (Helicopter, Coaxial, Tandem Cases, 2 Isolated Rotors)

Fig. 3.23 illustrates the relationship between power required and rotor disk diameter for three rotorcraft configurations (Helicopter, LS Coaxial, and Case 1 Tandem) operating in Martian atmospheric conditions at two densities, 0.013

kg/m³ and 0.025 kg/m³. These density values account for seasonal and altitude-based variations discussed in Section 3.4.1, with the lower density corresponding to the primary mission location at SW Melas Chasma during the summer season and the higher density reflecting the secondary mission location (East Melas Chasma) approximately 2000 km lower in elevation during winter. The data corresponds to forward level flight at a velocity of 55.56 m/s. Across all configurations, the power required decreases as rotor disk diameter increases, driven by improved aerodynamic efficiency resulting from reduced disk loading with larger rotor sizes. The Helicopter configuration consistently demonstrates the highest power requirements, particularly under the lower density condition of 0.013 kg/m³, highlighting its relatively lower efficiency. In contrast, the LS Coaxial configuration shows improved efficiency over the Helicopter, while the Case 1 Tandem configuration is the most efficient, requiring the least power across all densities and rotor diameters.

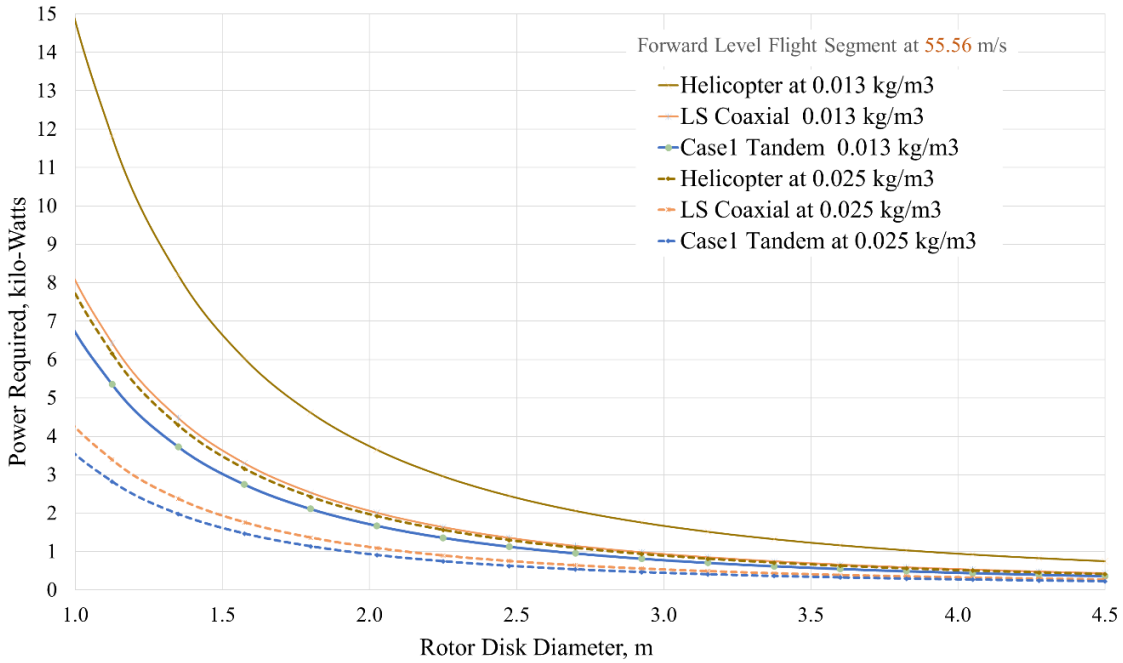


Fig. 3.23 21 Power Required (Forward Level) vs Rotor Disk Diameter (1 to 4.5 m)– Comparison between various 20 kg rotorcraft configurations (Helicopter, Coaxial and Tandem Case1) at 0.013 kg/m3 and 0.025 kg/m3

Atmospheric density significantly impacts power requirements, influenced by both seasonal and altitude-based variations. Higher density (0.025 kg/m³) reduces

power consumption for all configurations due to enhanced aerodynamic lift efficiency, with this effect being more pronounced for smaller rotor diameters. At larger rotor diameters (above 3 m), power requirements across all configurations converge, reflecting diminishing differences in efficiency. The graph highlights the tandem configuration's superior power efficiency, particularly in low-density Martian conditions, while emphasising the critical influence of rotor disk diameter on aerodynamic performance. These findings underscore the importance of optimising rotor size and configuration to meet mission-specific requirements under varying Martian atmospheric conditions influenced by both seasonality and altitude.

3.8.3 Battery Mass Fraction (*BMF*) Analysis

Fig. 3.23 illustrates the Battery Mass Fraction (*BMF*) concerning the vertical climb required power across various defined rotorcraft configurations, demonstrating its correlation with increasing rotor disk diameter. This *BMF* calculation, using the Eq (3.14), considers a 2-minute run time (*E*), a climb speed of 8.33 m/s, and a constant total mass of 20 kg. The trend observed in the vertical climb *BMF* lines aligns with the vertical climb power dependency outlined in Fig. 3.15. Essentially, as the required power increases, the *BMF* also increases, indicating the necessary battery weight for this specific flight segment. A similar *BMF* trend is observed for the forward-level flight segments depicted in Fig. 3.24, mirroring the forward-level flight power data from Fig. 3.19. The required battery mass can simply be determined by multiplying the total *BMF* by the total aircraft mass. For instance, with a 0.03 *BMF*, the battery mass would equal 0.6 kg (i.e., 0.03 x 20 kg). It is essential to aggregate the *BMF* of each segment with the BMF of other flight segments, as detailed in Section 3.6, to ascertain the total *BMF* and thus determine the overall battery mass necessary for a specific flight regime. Moreover, it is noteworthy that the *BMF* calculated for the flight mission excludes the battery mass required for avionics or electronic payload instruments. Separate calculations would be needed for these unless these have dedicated batteries of their own.

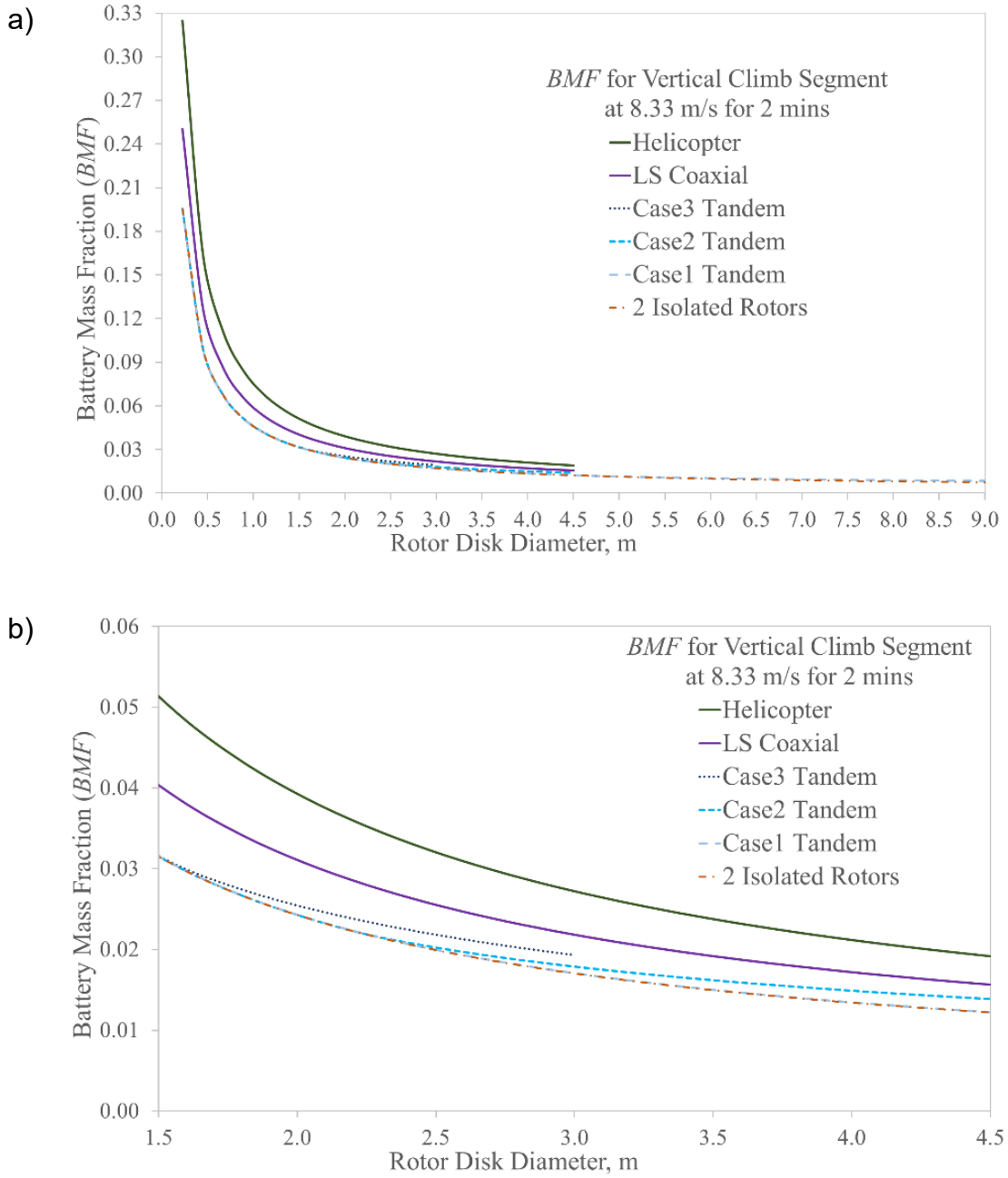


Fig. 3.24 BMF Vertical Climb Segment (at 8.33 m/s for 2 minutes) vs Rotor Disk Diameter– Comparison between various 20 kg rotorcraft configurations (Helicopter, Coaxial, Tandem Cases, 2 Isolated Rotors). a) Shows BMF for rotor diameters from 0 to 9 m on the x-axis. b) Shows a zoomed-in view, focusing on BMF for rotor diameters from 1.5 to 4.5 m on the x-axis for clarity

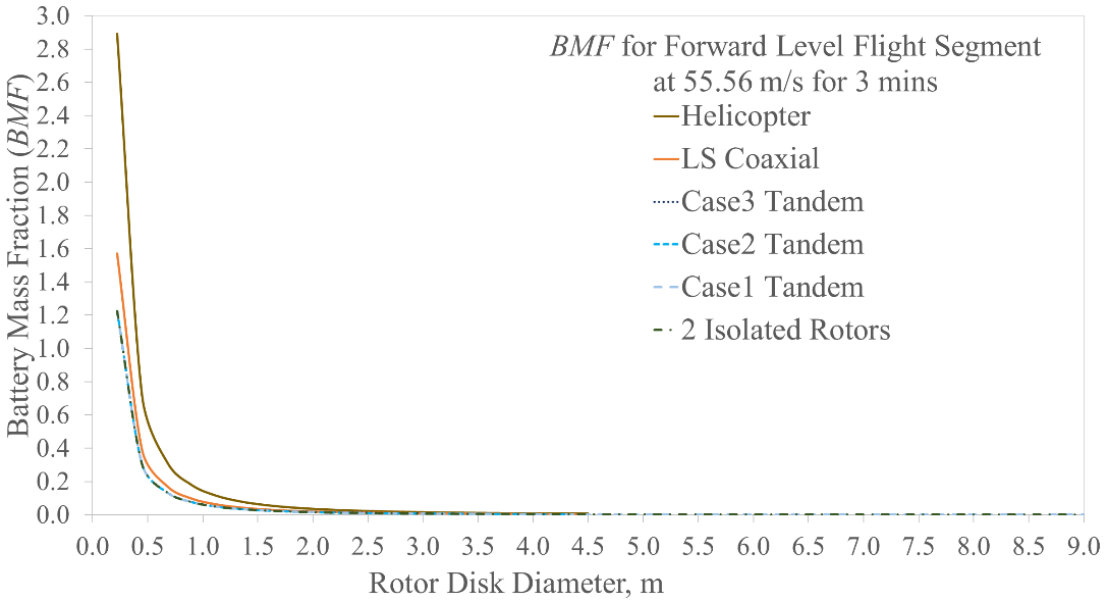


Fig. 3.25 BMF Forward Level Flight Segment (at 55.56 m/s for 3 minutes) vs Rotor Disk Diameter – Comparison between various 20 kg rotorcraft configurations (Helicopter, Coaxial, Tandem Cases, 2 Isolated Rotors)

3.9 Practical Application of the Analysis and Discussions

This penultimate section presents the concluding steps of the framework for the preliminary design of future rotary VTOL Martian aerobots (Fig. 3.1), applied in this research through an example case study in a systematic manner. The initial sizing method (step 9 within the framework) for the battery electric aircraft, introduced in Section 3.6, is conducted on the designs shortlisted based on power efficiency and specific design constraints discussed in the subsequent subsection. While the calculation of the aerobot's empty mass by specifying structural materials and subsystem components (step 10) is introduced here, the detailed execution of this step is beyond the scope of this paper, as mentioned in the introduction of the framework.

3.9.1 Efficient Rotor Configuration Shortlisting

Based on the power requirement analysis of rotorcraft with single and dual rotors, the lowest power-consuming rotorcraft configurations can be shortlisted for the aerobot design. However, specific design constraints are established to exclude certain theoretical findings that may seem optimal in theory but introduce design

complexities, including folding and stowing requirements, the need for heavy and robust materials, as well as control and stability concerns, exemplified by the 9 m rotor diameter of the Case 1 Tandem rotorcraft. Similarly, smaller-sized rotors, while lighter and mechanically simpler, demand higher power and are more suitable for small to medium-sized multicopters rather than large helicopters or rotorcraft. Therefore, Fig. 3.25 presents a zoomed-in view of the analytical graphs comprising the power required for vertical climb and level forward flight against the rotor disk diameter with limits set from 1.5 m to 4.5 m. As per the basic mission flight profile (Fig. 3.12), the rotorcraft must ascent vertically and cruise forward. Conventional helicopter within the set parameters consumes the highest power for both flight segments and therefore can rationally be omitted. The lowest power is required by Case 1 Tandem rotorcraft and then by Case 2, but both require a rotor folding mechanism and potentially a heavier articulated hub system as mentioned in Table 3.3 (for Case 2, when D>2.25). One of the important factors in designing a rotorcraft for an extraterrestrial application is keeping the operational capability as simple as possible to minimise any malfunction risk because maintenance or mechanical error correction by physical means is not possible. Thus, these two tandem rotorcraft cases are deprioritised. Case 2 of tandem rotorcraft with a rotor diameter of D<2.25 fits inside the aeroshell vessel without requiring any folding mechanism, while its rotors present the more efficient isolated behaviour due to the absence of overlapping. When doing trade-offs based on the complexity, weight and maintenance factors, such configurations are likely to be prioritised.

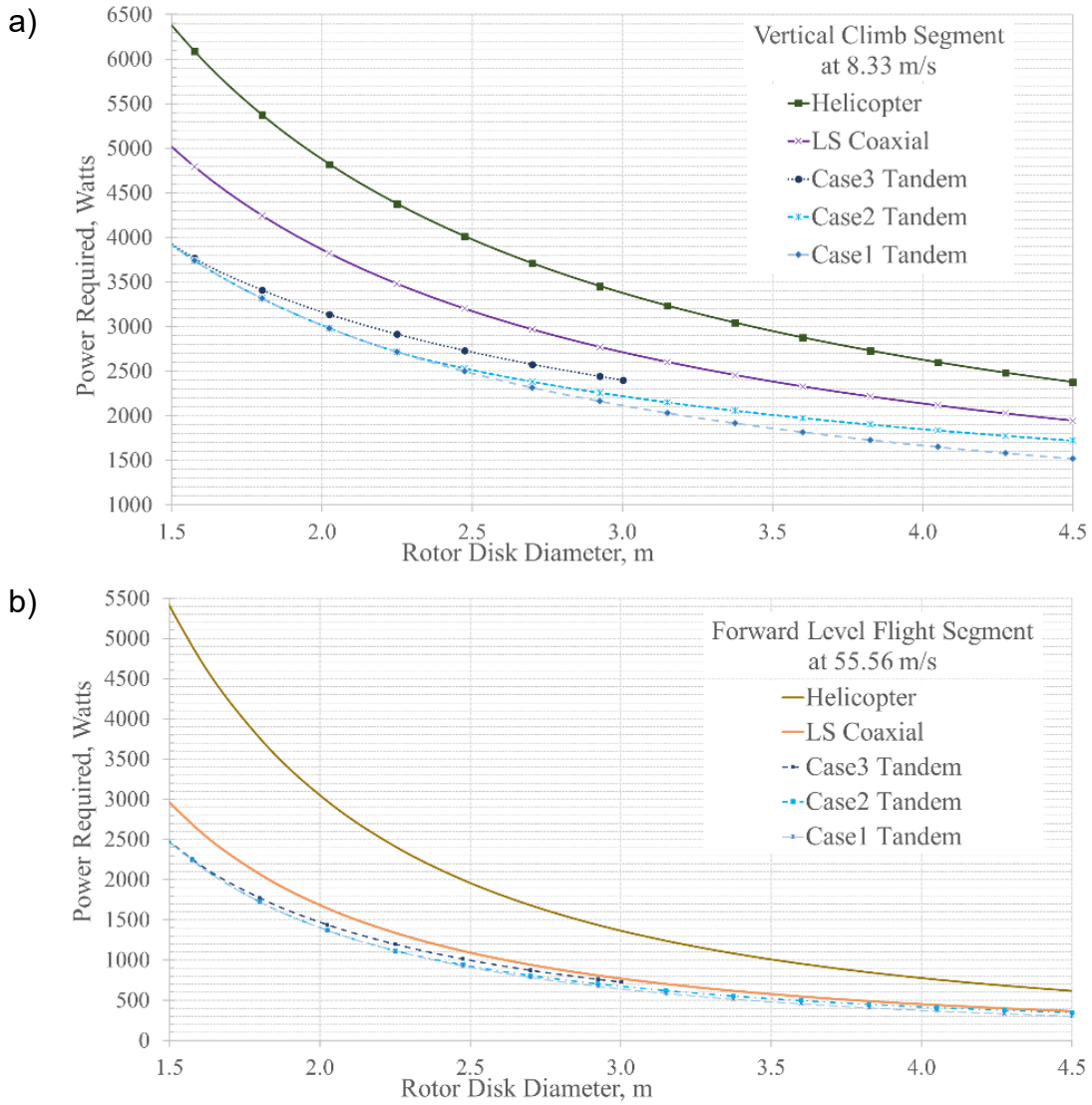


Fig. 3.26 Power required [Graph a) Vertical Climb at 8.33 m/s. Graph b) Level Forward Flight at 55.56 m/s] vs Rotor Disk Diameter (rotor diameter range - 1.5m to 4.5m) – Comparison between various 20 kg rotorcraft configurations (Helicopter, Coaxial, Tandem Cases)

Coaxial rotorcraft with large separation (LS) between rotors and Case 3 Tandem rotorcraft are the remaining choices. The overlapping interference factor (K_{ov}) for LS coaxial rotors is 1.281, while for Case 3 tandem rotorcraft at a maximum allowable rotor diameter of 3 m (resulting in a maximum tandem rotor overlapping), the K_{ov} is 1.134. The K_{ov} of Case 3 is lesser for rotor disks smaller than 3 m in diameter due to a decrease in rotor overlapping. A noticeable difference of around 1000 Watts is evident between the two configurations for vertical climb power at a rotor diameter of 1.5 m, where the tandem rotor shows

zero overlapping in this instance. Whereas, for a forward levelled flight the difference at 1.5 m disk size is about 400 Watts, which keeps becoming negligible with the increase in rotor size. Consequently, tandem rotor Case 3 emerges as a favourable configuration option, displaying higher hover and vertical climb power efficiency compared to the LS coaxial setup. Additionally, it is mechanically less complex than other tandem cases, owing to the capability of using a rigid rotor hub system. For rotor disk sizes beyond 3 m, LS coaxial rotors could be an option, albeit with a higher K_{ov} trade-off. Moreover, this simplified calculation for K_{ov} of tandem rotorcraft is based on the same plane rotors overlapping, but in the practical designs, the rear rotor is placed at a greater height than the front rotor to minimize the interference effects of the front rotor wake. Thus, the K_{ov} would be further reduced and hence, also the required power.

3.9.2 Initial Sizing Application and Battery Considerations

Case 3 Tandem rotorcraft with a 3 m rotor disk size is selected for preliminary study as an example (Fig. 3.26). As mentioned in Section 3.7.2, the battery-specific energy (E_{sb}) used for Battery Mass Fraction (*BMF*) calculations for flight is 230 Wh/kg pack (including battery management system), based on a JPL technology forecast for next-generation Mars Science Helicopter. The usable energy is 70% of the nominal capacity (10% to 80% depth-of-discharge) with an average discharge efficiency of 90 % [5]. It is established from the results obtained that the power required at a vertical climb segment is 2400 Watts and at a cruise segment is 730 Watts, and the relative Battery Mass Fraction (*BMF*) is 0.019 and 0.008, respectively. The total *BMF* sums up to 0.027. As explained in Section 3.6, the nominal usage and discharge efficiency correction factors, totaling 1.4 (1.3 for 70% usable capacity and 1.1 for 90% averaged discharge efficiency deduced in [5]), are applied to adjust the total BMF. The adjusted BMF is now 0.038. It is predetermined, the total aerobot mass is set at 20 kg. Therefore, using Eq. (3.14) the battery mass (m_{b}) required for this 5-minute flight mission is calculated to be around 0.76 kg. Also, it is predetermined that the aerobot should potentially be capable of carrying a science payload of 2 kg. Using Eq. (3.15) in terms of Mass, the available aircraft's empty mass ($m_{\mathrm{e}} = m_{0} - m_{\mathrm{b}} -$

m_{payload}) is determined to be 17.24 kg, representing ~86% of the total aircraft mass, a feasible starting point for further analysis.

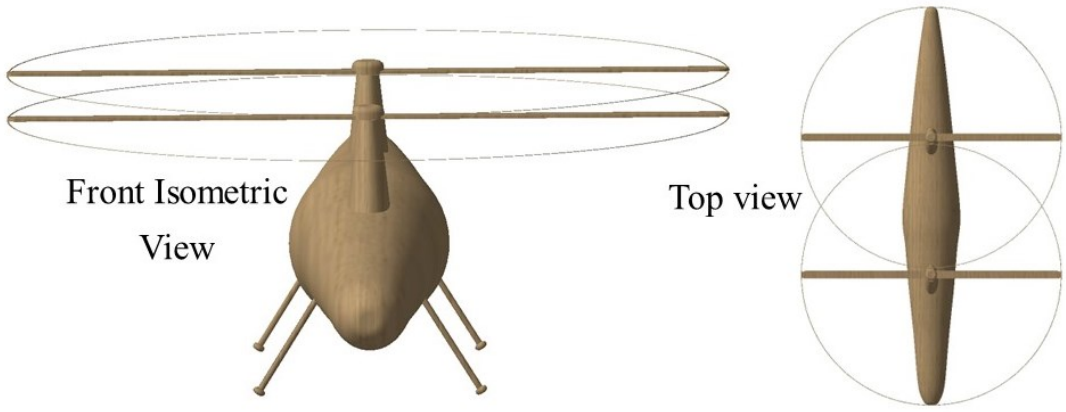


Fig. 3.27 Case 3 Tandem rotorcraft with a 3 m rotor disk size based on initial sizing (CAD model illustration: the left side is a front isometric view and the right side is a top view. Not to scale)

While the above calculations for battery mass provide a foundation, further review of available battery technologies is necessary to ensure the design meets the mission's power demands. The battery selection must consider not only energy capacity but also the maximum discharge current capability. The JPL forecast assumes a 10C discharge rate [5], allowing the battery to discharge at ten times its nominal capacity, fully depleting in just 1/10th of an hour. This high discharge capability is essential for intense power phases, such as vertical climb, where sustained delivery of 2400 W is required. To further evaluate the feasibility of the tandem rotorcraft design, the state-of-the-art INR-21700-P50B lithium-ion battery [44] is used as a reference for system configuration. This battery has a nominal voltage of 3.6 V, a capacity of 5 Ah (cell-specific energy 260 Wh/kg), a maximum continuous discharge current of 60 A (C-rate 12C), and a weight of 71 g per cell. By comparison, the Ingenuity helicopter used six Sony SE US18650 VTC4 cells with a nominal voltage of 3.6 V, a capacity of 2 Ah, an energy density of 144 Wh/kg, and a weight of 45 g per cell. The VTC4 cells have a higher C-rate (15C vs. 12C), but the INR-21700-P50B offers over twice the capacity and significantly higher energy density, enabling greater flight durations and improved efficiency.

Two battery configurations are examined: a 6-cell system (21.6 V) and a 14-cell system (50.4 V). The 6-cell system, with its lower voltage, results in a higher current demand during vertical climb. Using the relationship, $current = power/(voltage \times efficiency)$, at 2400 W and an efficiency of 90%, the current demand is approximately 123.5 A. This exceeds the 60 A discharge limit of a single cell, necessitating three parallel connections. The total number of cells required for this configuration is 18, with a corresponding battery mass of 1.278 kg. In contrast, the 14-cell system's higher voltage reduces the current demand to 52.9 A, which is within the discharge limit of a single cell. This eliminates the need for parallel connections, reducing complexity and total cell count. With 14 cells in series, the battery mass is 0.99 kg, significantly lighter than the 6-cell configuration and closer to 0.76 kg battery mass calculated earlier using the *BMF* method. The simplified design of the 14-cell system also reduces the need for a complex battery management system, improving reliability and operational efficiency.

Despite the clear advantages of the 14-cell system, the reliance on a 12C discharge rate presents significant challenges. High discharge rates generate substantial heat, requiring advanced thermal management systems to prevent overheating. Sustained high-current operations accelerate chemical degradation, reducing the battery's operational life and limiting mission longevity [5]. Additionally, the energy density of 230 Wh/kg, while high for current lithium-ion technology, restricts mission durations and payload capacity. The harsh Martian environment further complicates performance; low temperatures increase internal resistance, degrading battery efficiency and requiring additional heating systems, which consume energy and add mass.

Addressing these challenges will require advancements in battery technology. Selecting appropriate battery technology is crucial for Mars missions due to the planet's extreme conditions. Lithium-ion (Li-ion) batteries are widely used in space missions for their high energy density and reliability; for instance, NASA's Mars Exploration Rovers, Spirit and Opportunity, utilized rechargeable lithium-ion batteries to store energy generated from their solar panels, enabling operations

during periods without sunlight. Lithium polymer (LiPo) batteries offer high discharge rates and flexible form factors but generally have lower energy densities and are more susceptible to swelling and thermal runaway under extreme conditions, making them less suitable for the harsh Martian environment. Lithium iron phosphate ($LiFePO_4$) batteries are known for excellent thermal and chemical stability, enhancing safety and longevity; however, their lower energy density can be a disadvantage in weight-sensitive space applications. Emerging technologies like solid-state batteries, which utilize solid electrolytes, offer higher energy densities and improved safety profiles due to resistance to leakage and thermal runaway. They are being developed to operate effectively in extreme environments, including the temperature fluctuations on Mars. Furthermore, optimising the aerobot's mission profile to reduce power demand during critical phases, such as vertical climb, could help lower current requirements, simplifying the overall battery configuration.

In Section 3.6 the contents included in empty mass are described, and calculating the total mass of such components is a detailed process based on further design requirements (step 10, Fig. 3.1). For initial estimation, the mass of commercially available off-the-shelf (COTS) materials and components can be used. Alternatively, aircraft mass buildup can be evaluated by referencing the mass specifications of similar aircraft, for instance the weight estimation model used for second-generation Mars Science Helicopters in Ref. [5], which is based on the first Mars Helicopter.

3.9.3 Discussion

The primary aim of this parametric study is to provide a theoretical baseline using existing helicopter momentum theory to estimate power consumption for different rotorcraft configurations in Martian conditions. Given the early stage of this research, this fundamental approach focuses on understanding performance requirements for rotorcraft flight on Mars, similar to the use of blade element momentum theory in the conceptual design process of NASA's Mars helicopters [5]. However, the derivative method introduced here includes flight performance analysis of both overlapping and non-overlapping rotors, allowing effective

exploration of a wide range of configurations and parameters, establishing baseline estimates and comparative analyses. The results obtained from the parametric performance study conducted on rotorcraft with single and dual rotors, are reasonable within the framework of the momentum theory and include refinements based on insights from previous publications by the authors. Adjustments have been made to parameters such as the figure of merit, fuselage downwash interference factor, and Oswald's efficiency factor to suit Martian conditions. This methodology can be extended to include multirotor configurations, including quadrotors and hexarotors [45].

The initial sizing method applied in the preceding subsection assumed fixed values for payload mass and total rotorcraft mass to initiate the sizing process. However, while payload mass serves as a criterion for setting requirements, it can alternatively be integrated into the empty mass of the rotorcraft such that the total mass equals battery mass and empty mass ($m_0 = m_\mathrm{b} + m_\mathrm{e}$). This approach allows flexibility in adjusting payload mass because different rotorcraft configurations necessitate varying airframe and motor masses. Consequently, a heavier structure can accommodate a lighter payload, and vice versa, ensuring that the total rotorcraft mass remains constant. If the payload mass is predefined and fixed, adjustments in the total mass are essential depending on the calculated empty mass. Nevertheless, the next critical step in the preliminary design framework is the detailed mass buildup process (step 10, Fig. 3.1), as it accounts for factors such as rotor, propulsion and energy system mass adjustments based on rotor efficiency and changes in airframe mass according to configuration.

The tandem rotor configuration was selected for its power efficiency and mechanical simplicity, particularly in scenarios requiring higher payload capacities and extended endurance. This design offers advantages over single and coaxial rotors by distributing the aerodynamic load across two rotor disks with partial or no overlapping, thereby reducing individual disk loading and optimising power requirements. However, tandem configurations introduce significant aerodynamic challenges, including wake interactions between the

front and rear rotors. These wake effects can impact the overall aerodynamic efficiency, increase vibration levels, and complicate flight stability and control. Managing the aerodynamic interactions in a tandem rotor system requires sophisticated control strategies to maintain desired flight characteristics [46], especially in the thin Martian atmosphere where aerodynamic behaviours differ significantly from Earth's.

Given the unique challenges and high costs associated with Martian rotorcraft experimentation, the framework proposed in this research for the preliminary rotorcraft design, coupled with theoretical analytical methodology, serves as a crucial first step in a broader validation process. Future work involves refining the performance estimates of shortlisted rotorcraft configuration/s using advanced methodologies like blade element theory, vortex wake models or Computational Fluid Dynamics (CFD), alongside considerations of fuselage wake interaction and drag, to provide more precise estimates of battery mass and overall aerodynamic performance. Moreover, detailed assessments of rotor efficiency in forward flight become essential at high advance ratios where advancing blade tip speeds reach near-Mach numbers. These conditions introduce compressibility effects and altered aerodynamics, influencing rotor performance significantly. Thus, addressing these factors will be key to advancing the reliability and applicability of rotorcraft designs for Martian exploration.

3.10 Conclusion

The systematic methodology for the preliminary design of future rotary VTOL Martian aerobots was proposed and applied within a structured framework in this research using an example case study. The detailed analysis reveals the critical importance of an aerobot in exploring Mars' Southwestern Melas Basin in Valles Marineris, showcasing the complex mission planning required for successful Martian exploration. To pave the way for future Mars rotorcraft, this study addressed critical research gaps by defining essential parameters and conducting a comprehensive parametric analysis of various 20 kg rotorcraft configurations with single and dual rotors. Using simplified helicopter momentum theory equations, the power requirements for hover, vertical climb, and forward

flight concerning varying rotor disk diameter for diverse rotorcraft types were illustrated through graphical representations, revealing that conventional helicopters consume more power than other configurations under given parameters. Rotorcraft with two isolated rotors stand out due to the non-overlapping aerodynamic interference. Notably, as rotor disk diameter approaches the upper size limit, differences in power requirements among configurations become negligible. The paper outlines methodologies for sizing battery-electric aircraft and calculating Battery Mass Fractions for different flight segments to determine the required battery mass. The analysis of rotorcraft configurations led to the prioritisation of the Case 3 Tandem rotorcraft as an example for further feasibility assessments, due to its higher power efficiency and mechanical simplicity. Initial sizing calculations confirm its feasibility, presenting an available empty mass of 17.24 kg, marking a plausible starting point for subsequent design evaluations and developments. The proposed framework for preliminary rotorcraft design, combined with a theoretical and analytical methodology extendable to other multirotor configurations, serves as a crucial first step in a broader validation process for Martian rotorcraft given the unique challenges and high costs of experimentation. Future studies should address data limitations and explore environmental influences on rotorcraft performance for continued progress in Martian exploration.

Acknowledgements

The authors would like to express their sincere gratitude to Dr Wayne Johnson (NASA Ames Research Center), for the invaluable feedback and constructive comments, which have contributed to the improvement of the analysis in this paper.

Data availability statement

Data supporting this study are included within the article and/or supporting materials.

Declaration of interests

The authors declare that they have no known competing financial interests or personal relationships that could have appeared to influence the work reported in this paper.

References

[1] Hassanalian, M., Rice, D., & Abdelkefi, A. (2018). Evolution of space drones for planetary exploration: A review. Progress in Aerospace Sciences, 97, 2018. 61–105. https://doi.org/10.1016/J.PAEROSCI.2018.01.003

[2] NASA. Mars Helicopter - NASA Mars. Retrieved July 20, 2024, from https://mars.nasa.gov/technology/helicopter/#Flight-Log

[3] NASA. Overview | Mars – NASA Solar System Exploration. Retrieved November July 20, 2024, from https://solarsystem.nasa.gov/planets/mars/overview/

[4] Radotich, M., Withrow-Maser, S., deSouza, Z., Gelhar, S., & Gallagher, H. (2021). A study of past, present, and future mars rotorcraft. In 9th Biennial Autonomous VTOL Technical Meeting.

[5] Johnson, W., Withrow-Maser, S., Young, L., Malpica, C., Koning, W. J. F., Kuang, W., Fehler, M., Tuano, A., Chan, A., Datta, A., Chi, C., Lumba, R., Escobar, D., Balaram, J., Tzanetos, T., & Fjaer Grip, H. (2020). Mars Science Helicopter Conceptual Design. http://www.sti.nasa.gov

[6] Young, L. A., Chen, R. T. N., Aiken, E. W., Briggs, G. A., "Design Opportunities and Challenges in the Development of Vertical Lift Planetary Aerial Vehicles," Proceedings of the American Helicopter Society International Vertical Lift Aircraft Design Specialist's Meeting, January 2000.

[7] Underwood, C., & Collins, N. (2017). Design and Control of a Y-4 Tilt-Rotor VTOL Aerobot for Flight on Mars. Proceedings of the 68th International Astronautical Congress (IAC), 25–29. https://openresearch.surrey.ac.uk/esploro/outputs/conferencePresentation/Design-and-Control-of-a-Y-4-Tilt-Rotor-VTOL-Aerobot-for-Flight-on-Mars/99511131102346

[8] Aguirre, J., Casado, V., Chamie, N., & Zha, G. (2007). Mars Intelligent Reconnaissance Aerial and Ground Explorer (MIRAGE) AIAA 2007-244. https://doi.org/10.2514/6.2007-244

[9] Forshaw, J., & Lappas, V. (2012). Architecture and Systems Design of a Reusable Martian Twin Rotor Tailsitter. Acta Astronautica, 80(0), 166–180. https://doi.org/10.1016/J.ACTAASTRO.2012.05.008

[10] NASA. NASA TechPort - Mars Electric Reusable Flyer - Project Data (2018). Retrieved July 20, 2024, from https://techport.nasa.gov/view/93850

[11] Boelhouwer, R.N.J., Bunschoten, E.C., Debusscher, C.M.J., Frijters, W., van Goeverden, R.J., Legrand, E.B., Matton, J., Paliusis, K., and Verheyen, J.K.N. (2018). “Design Report, Martian Advanced Reconnaissance System.” Delft University of Technology, June 2018.

[12] RM Zubrin. (2012). The mars gashopper - Concepts and Approaches for Mars 2012. https://ui.adsabs.harvard.edu/abs/2012LPICo1679.4069Z/abstract

[13] Denys, K. Ukrainian invention to feel the ground for Mars colonization (GRAPHICS) - Jun. 06, 2016 | KyivPost. Retrieved July 20, 2024, from https://www.kyivpost.com/article/content/ukraines-it-edge/ukrainian-invention-to-feel-the-ground-for-mars-colonization-graphics-415570.html

[14] Fathepure, M., Booker, A. L., Abouzahr, O., Wang, N., & Tikalsy, D. (2021). Design and Construction of an Inflatable-Winged VTOL Mars Electric Flyer. In AIAA AVIATION 2021 FORUM (p. 2578) https://doi.org/10.2514/6.2021-2578

[15] Schatzman, N., Dominguez, M., Lee, P., & Young, L. (2022). LILI (Long-term Ice-field Levitating Investigator): Mars aerial and ground explorer for Martian polar regions. Aeromechanics for Advanced Vertical Flight Technical Meeting, Transformative Vertical Flight 2022. NASA Technical Reports Server. Retrieved December 15, 2024, from https://ntrs.nasa.gov/citations/20210026216

[16] S. Withrow, W. Johnson, L. A. Young, H. Cummings, J. Balaram, and T. Tzanetos, “An Advanced Mars Helicopter Design,” in ASCEND 2020, American Institute of Aeronautics and Astronautics.

[17] Sopegno, L., Martini, S., Pedone, S., Fagiolini, A., Rutherford, M. J., Stefanovic, M., Rizzo, A., Livreri, P., & Valavanis, K. P. (2024). An Advanced Hexacopter for Mars Exploration: Attitude Control and Autonomous Navigation. IEEE Transactions on Aerospace and Electronic Systems. https://doi.org/10.1109/TAES.2024.3365667

[18] Zappek, V., Rinker, M., Daxer, L., Hajek, M. (2023). Evaluation of aerial vehicle configurations for high-range Mars missions. CEAS Space J 15, 761–775. https://doi.org/10.1007/s12567-022-00479-4

[19] Lou, B., Yan, X., Zhao, P., Xie, A., Zhang, D., & Zhu, S. (2021). Preliminary design of several new kinds of Martian aircrafts. Proceedings of the Vertical Flight Society’s 77th Annual Forum & Technology Display. https://doi.org/10.4050/F-0077-2021-16736

[20] Hazarika, M. B., Santangelo, G., Gamba, M., & Wang, W. (2023, October 17). Development of a Preliminary Design Methodology for Rotorcraft in Martian Atmospheric Conditions and Experimental Validation of the Method. https://doi.org/10.2514/6.2023-4802

[21] Youhanna V, Felicetti L, Ignatyev D. (2024) Parametric analysis of rotary VTOL aerobot design configurations to fly on Titan. In: 75th International Astronautical Congress IAC-2024, 14-18 October 2024, Milan, Italy Retrieved December 22, 2024, from https://dspace.lib.cranfield.ac.uk/handle/1826/23153

[22] Grant, J. A., Golombek, M. P., Wilson, S. A., Farley, K. A., Williford, K. H., & Chen, A. (2018). The science process for selecting the landing site for the 2020 Mars rover. Planetary and Space Science, 164, 106–126. https://doi.org/10.1016/J.PSS.2018.07.001

[23] Cockell, C., Bridges, J., Dannatt, L., Burchell, M., Patel, M., & Danson, M. (2009). Where to land on Mars. Astronomy & Geophysics, 50(6), 6.18-6.26. https://doi.org/10.1111/J.1468-4004.2009.50618.X

[24] Banfield Et Al. Mars Science Goals, Objectives, Investigations, and Priorities: 2020 Version Mars Exploration Program Analysis Group (MEPAG) Prepared by the MEPAG Goals Committee. Retrieved July 20, 2024, from https://mepag.jpl.nasa.gov/reports/MEPAGGoals_2020_MainText_Final.pdf

[25] Farley, K. A., Williford, K. H., Stack, K. M., Bhartia, R., Chen, A., de la Torre, M., Hand, K., Goreva, Y., Herd, C. D., Hueso, R., Liu, Y., Maki, J. N., Martinez, G., Moeller, R. C., Nelessen, A., Newman, C. E., Nunes, D., Ponce, A., Spanovich, N., … Liu, Y. (2020). Mars 2020 Mission Overview. Space Sci Rev. https://doi.org/10.1007/s11214-020-00762-y

[26] NASA. Location Map for Perseverance Rover - NASA Mars. Retrieved July 20, 2024, from https://mars.nasa.gov/mars2020/mission/where-is-the-rover/

[27] NASA.Vallis Marineris. Retrieved July 20, 2024, from https://web.archive.org/web/20070711145413/http:/education.gsfc.nasa.gov/experimental/all98invProject.Site/Pages/Vallis.Marineris.html

[28] Christensen, P.R.; Engle, E.; Anwar, S.; Dickenshied, S.; Noss, D.; Gorelick, N.; Weiss-Malik, M.; JMARS – A Planetary GIS, http://adsabs.harvard.edu/abs/2009AGUFMIN22A..06C

[29] JOUAV. (2023) Top 10 Drones with the Longest Flight Time in 2023 - JOUAV. Retrieved July 20, 2024, from https://www.jouav.com/blog/drone-with-longest-flight-time.html

[30] Balaram, J., Aung, M., & Golombek, M. P. (2021). The ingenuity helicopter on the perseverance rover. Space Science Reviews, 217(4), 56. https://doi.org/10.1007/s11214-021-00815-w

[31] NASA. (2024) Hazard: Distance From Earth - NASA. Retrieved July 20, 2024, from https://www.nasa.gov/hrp/hazard-distance-from-earth/

[32] NASA. Mars Fact Sheet. Retrieved July 20, 2024, from https://nssdc.gsfc.nasa.gov/planetary/factsheet/marsfact.html

[33] NASA. (2021) Mars Atmosphere Model - Metric Units. Retrieved July 20, 2024, from https://www.grc.nasa.gov/www/k-12/airplane/atmosmrm.html

[34] NASA. (2021) Flying on Mars Is Getting Harder and Harder - NASA Mars. Retrieved July 20, 2024, from https://mars.nasa.gov/technology/helicopter/status/334/flying-on-mars-is-getting-harder-and-harder/

[35] Millour, E., Forget, F., Spiga, A., Pierron, T., Bierjon, A., Montabone, L., Vals, M., Lefèvre, F., Chaufray, J.-Y., Lopez-Valverde, M., Gonzalez-Galindo, F., Lewis, S., Read, P., Desjean, M.-C., and Cipriani, F. and the MCD Team: The Mars Climate Database (Version 6.1), Europlanet Science Congress 2022, Granada, Spain, 18–23 Sep 2022, EPSC2022-786, https://doi.org/10.5194/epsc2022-786

[36] D. Raymer. Aircraft design: A conceptual approach, 6. Ed., AIAA education series, Reston, Va., 2018, Chaps. 20.11, 21.3.

[37] Youhanna, V., Ignatyev, D., Felicetti, L., (2022). Futuristic Martian Aerobot Design. UKRAS22 Conference “Robotics for Unconstrained Environments” Proceedings, 64-65. doi:http://doi.org/10.31256/Ec2Na5W

[38] Leishman, J. Gordon. Principles of Helicopter Aerodynamics, 2. Ed., United Kingdom, Cambridge University Press, 2006. Chaps. 2.15, 5.5.11.

[39] Johnson, W. Rotorcraft Aeromechanics. Cambridge University Press. 2013. Chaps. 4.6, 5.3. https://doi.org/10.1017/CBO9781139235655

[40] Monolithic Power Systems. (Web Editor). (2024). Introduction to battery technology: Battery parameters. Monolithic Power Systems. Retrieved December 18, 2024, from https://www.monolithicpower.com/en/learning/mpscholar/battery-management-systems/introduction-to-battery-technology/battery-parameters

[41] Muelaner, Jody. (2022). Battery Power Tips. What to consider when evaluating battery performance. Battery Power Tips. Retrieved December 18,

2024, from https://www.batterypowertips.com/what-to-consider-when-evaluating-battery-performance-faq/

[42] Youhanna V, Felicetti L & Ignatyev D (2024) Conceptual Design Study based on Defined Parameters for Next Generation Martian Rotorcrafts. In: IEEE Aeroconf 2024, Montana, US, 2-9 March 2024, pp. 1-13, doi: 10.1109/AERO58975.2024.10521441

[43] Youhanna V, Felicetti L & Ignatyev D (2023) Parametric analysis of battery-electric rotorcraft configurations to fly on Mars. In: Aerospace Europe Conference Joint 10th EUCASS - 9th CEAS Conference 2023, Lausanne, 9-13 July 2023. DOI: 10.13009/EUCASS2023-319

[44] E-One Moli Energy Corp. (2024). Product data sheet of INR-21700-P50B. Retrieved December 20, 2024, from https://www.molicel.com/wp-content/uploads/Product-Data-Sheet-of-INR-21700-P50B-80122.pdf

[45] Youhanna V, Felicetti L & Ignatyev D (2024). Preliminary Investigation into Future Martian Multicopter Configurations. In: Vertical Flight Society's 80th Annual Forum & Technology Display, Montréal, Québec, Canada, May 7-9, 2024. https://doi.org/10.4050/F-0080-2024-1266

[46] Ferguson, K.M., Thomson, D.G., Anderson, D., Ireland, M.L., Tu, Z., Manso, S., Chandran, A.B., & Ibal, G. (2015). Comparing the flight dynamics characteristics of tandem and conventional helicopters for the purposes of automatic control. Presented at the 41th European Rotorcraft Forum, Munich, Germany, September 1-4th, 2015. Retrieved December 22, 2024, from https://dspace-erf.nlr.nl/server/api/core/bitstreams/a0eb3b54-7891-480a-b222-74360df252ac/content

4 Parametric Analysis of Multirotor Aerobot Configurations for Mars[4]

Vishal Youhanna, Leonard Felicetti, Dmitry Ignatyev

Faculty of Engineering and Applied Sciences, Cranfield University, UK

Abstract

The groundbreaking success of NASA's Ingenuity Helicopter has spurred immense potential for Martian exploration, emphasizing the pivotal role of aerobots alongside rovers and landers. However, the helicopter's limitations, stemming from its compact and simplistic design, are apparent in its restricted long-range endurance and payload capacity. This paper suggests a feasible optimisation approach for Martian rotorcraft concepts while addressing constraints and progressing Martian drone technology. The key focus lies in improving performance to meet the evolving demands of forthcoming Martian aerobot missions. Based on a comprehensive parametric analysis rooted in simplified rotorcraft momentum theory, this study focuses on power requirements of rotorcrafts with single, coaxial, tandem, quad and hexa rotors for hover, vertical climb, and forward flight segments. Modified to meet more demanding mission criteria, these designs are limited by the spacecraft aeroshell's maximum size for safe transport to Mars. Additionally, a 3D Mars Science Helicopter (MSH) blade mass scaling model was developed to provide improved mass estimation by incorporating material distribution, thickness-to-chord scaling, and structural reinforcement trends, ensuring a more accurate prediction of rotor mass growth across different rotor sizes. Among the considered configurations, the hexacopter emerged as the most efficient choice, offering a balance between performance, endurance, and payload capacity, while a conventional single main rotor configuration fell short within the specified parameters.

[4] This is an adapted version of the article targeted at MDPI Aerospace journal for publication: Youhanna, V., Felicetti, L., & Ignatyev, D. (2024). Systematic methodology for the preliminary design of future rotary VTOL Martian aerobots.

Keywords: Martian Aerial Drones, Planetary UAV, Rotorcraft Conceptual Design

4.1 Introduction

4.1.1 Planet Mars

The increasing interest in Mars exploration has catalysed the development of specialised aerial robots, known as aerobots, to support the sustainability of future missions in Mars' thin atmosphere. Prior to 2021, Mars missions primarily utilised spacecraft, landers, and rovers. However, unmanned aerial vehicles have gained attention for their advantages over surface rovers, including greater speed, wider range, superior obstacle avoidance, and enhanced visibility [1]. Historically, planetary exploration preferred lighter-than-air airships or fixed-wing planes due to the technical complexities of rotor-based aerobots. Nevertheless, recent advancements in drone technology have renewed interest in rotorcraft for Mars exploration.

Mars' unique atmospheric conditions present significant challenges for rotorcraft design. Although Mars has lower gravity, its atmospheric density is approximately 100 times lower than Earth's [2], resulting in very low Reynolds numbers for rotor operations, particularly for small-scale helicopters. However, the Mach number on Mars would be significantly higher due to two main factors: the necessity for higher tip speeds to compensate for the lower atmospheric density, and the reduced speed of sound on the Martian surface, which is only about 72% of that on Earth. These conditions impose substantial design constraints on rotorcraft [3]. A crucial challenge in sustaining flight for Martian drones is managing the heat generated by the propulsion system while generating the necessary lifting thrust, especially given the low Reynolds numbers. Furthermore, the use of an aeroshell, heat shield container, with a maximum diameter of 4.5 m for aerobot transport to Mars introduces additional complexities [4]. Historically, these elements have raised questions about the practicality of using rotorcraft on Mars. However, NASA's accomplishment in April 2021 with the deployment of the Ingenuity Mars Helicopter has discredited such scepticism.

4.1.2 Literature

Ingenuity, before retiring in February 2024, completed 72 short autonomous pre-commanded flights [2]. These flight tests transitioned Ingenuity from the Technology Demonstration phase to the Operations Demonstration phase, highlighting the potential for collaboration between future rovers and aerial surveyors. The knowledge gained from designing and operating the Mars Helicopter provides valuable insights for developing advanced aerobots for Mars exploration. Despite Ingenuity's success, its small size and basic configuration limit its endurance, range, and payload capacity, hindering its ability to conduct comprehensive scientific missions requiring long-distance flights, larger scientific payloads, advanced communication systems, or robust propulsion systems for high-altitude missions.

To address these limitations, this paper proposes enhancing the design of aerobots by setting more ambitious requirements for Martian aerobot missions. This involves developing a new rotorcraft design while considering practical operational and design constraints, including adhering to a maximum aeroshell diameter of 4.5 m, assuming that launch and re-entry technologies will remain relatively stable in the coming decades. The South-West (SW) Melas Basin of Melas Chasma within the Valles Marineris canyon system on Mars is selected as the mission location. Despite its rugged terrain presenting challenges, advancements in navigational planetary landing technology and the obstacle avoidance capabilities of aerobots make this site a promising candidate for in-situ exploration [3]. An aerobot deployed in this region could produce high-resolution aerial maps and identify potential locations for experimental sample collection for future rover missions. The primary mission objective is to capture high-quality images of the surveyed areas and effectively transmit this visual data to a rover from the same mission or a ground control station on Earth.

Increasing the size or adding fixed wings to the Ingenuity Helicopter is one way to enhance its capabilities. Vertical takeoff and landing (VTOL) fixed-wing aircraft with both rigid and retractable body configurations have been investigated in several Mars mission plans [6]-[11]. Young et al. (2000) introduced the pioneering

concept of rotary VTOL planetary aerial vehicles, exemplified by the Mars tiltrotor, which balances hover performance and cruise range, crucial for Mars exploration [6]. Various innovative designs, such as the Y-4 Tilt-Rotor VTOL Aerobot [7] and MIRAGE [8], utilise different propulsion configurations, including tiltrotors, coaxial rotors, and embedded fans. Concepts like tailsitters [9] and hopper [10] designs offer alternative approaches for Mars exploration, with projects like VALKERIE merging inflatable wing technology for transport efficiency [11]. NASA's second-generation Mars helicopters [4], including the Mars Science Helicopter (MSH) and Advanced Mars Helicopter (AMH), feature foldable designs with varying rotor sizes and payloads.

4.1.3 Proposed Study

Meeting more demanding specifications requires the development of new rotorcraft designs that adhere to practical limitations, particularly the maximum aeroshell diameter. It may be necessary to package a large rotorcraft with a smaller ground spacecraft, transport it separately, or use an innovative folding mechanism within the aeroshell to accommodate it. A comprehensive parametric analysis of rotorcraft designs is necessary to determine the overall benefits of larger or winged Martian rotorcraft and propose suitable configurations for further research. In a recent study by the authors, performance analysis of various battery-electric rotorcraft configurations with single, dual (Chap 3), quad [12] and hexa [13] rotors was conducted within defined parameters, including initial sizing estimation. This paper extends the analysis by incorporating additional cases of quadcopter and hexacopter configurations and improved adjustments to the parameters used, broadening the scope of the investigation to encompass a wider range of design possibilities and performance outcomes. In addition to power requirements, a 3D MSH blade mass scaling model is introduced to refine rotor blade mass predictions by integrating material distribution and thickness-to-chord scaling laws, addressing key structural considerations beyond conventional geometric scaling approaches. This enhancement provides a more physics-informed method for estimating blade mass across different rotor sizes, ensuring a more realistic evaluation of Martian rotorcraft feasibility.

The research article outlines a generalised methodology (section 4.2) based on simplified momentum theory for calculating the flight power of various Martian rotorcraft configurations, including those with overlapping rotors. The study further introduces methods for initial sizing of battery-electric aircraft (section 4.3), estimating battery mass based on flight power demands. Additionally, an initial rotor blade mass estimation approach (section 4.4) is developed, incorporating material distribution and thickness-to-chord scaling, contributing to a more accurate determination of total rotorcraft mass. Study cases for parametric analysis are established (section 4.5), involving single conventional helicopters, coaxial rotorcraft, three tandem rotorcraft configurations, quadcopter and hexacopter configurations. Then all the parameters are defined and summarised (section 4.6). Results and analysis (section 4.7) focus on power demands for hover, vertical climb, and forward flight across these configurations, informing the identification of the most power-efficient designs. However, theoretical optima may introduce complexities due to design constraints, necessitating careful configuration selection and refinement, as discussed in the penultimate section 4.8.

4.2 Power Requirement Analysis Methodology For Rotorcraft

4.2.1 Rotorcraft Types

Fig. 4.1 Rotorcraft Configurations Illustration depicts six rotorcraft configurations, including single, dual, quad, and hexarotor. Traditional rotary-wing aircraft usually have a single main rotor on top of the fuselage that provides both lift and thrust, along with a tail rotor to counteract torque. Coaxial rotorcraft, which have two rotors on the same axis rotating in opposite directions, do not require a tail rotor and are inherently more stable. Tandem rotor designs feature two main rotors placed one behind the other along the fuselage, which increases lift capacity and payload potential. Side-by-side rotorcraft include configurations, with multiple rotors positioned closely together, allowing for flexible operation in both hovering and forward flight. Quadcopters, a subtype of multicopters, have a four-rotor arrangement known for their simplicity, stability, and ease of control, making them a popular choice for UAVs and drones used on Earth. Hexacopters, with six

rotors, offer enhanced stability and payload capacity compared to quadcopters, making them suitable for more demanding applications requiring greater lift and redundancy.

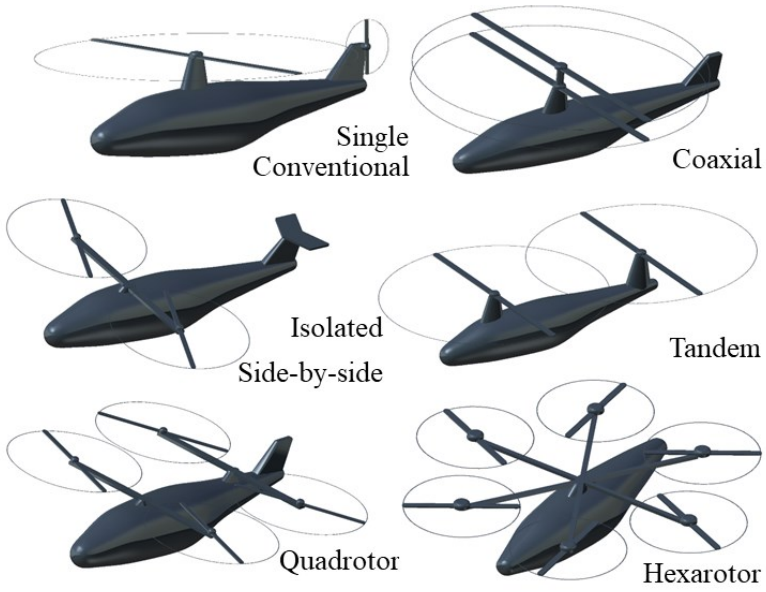


Fig. 4.1 Rotorcraft Configurations Illustration

4.2.2 Conventional Rotorcraft

The key factor determining the success of a reusable Martian aerobot is its ability to perform vertical takeoff and landing (VTOL), given that Mars lacks conventional runways. This VTOL capability is entirely dependent on the efficiency of its rotor propulsion system. To estimate the power consumption of the rotor during different flight phases such as hovering, vertical climb, and forward flight, momentum theory is applied. In this model, the rotor blades are treated as actuator disks with negligible thickness and a specific disk area (S). The model assumes uniform airflow distribution across the rotor disk and immediate energy transfer to the airflow while disregarding factors like airfoil profile drag losses, tip losses, and residual rotational velocities. To address these omissions, the figure of merit concept is introduced. This figure of merit (M) is the ratio of ideal power to actual power ($M = P_{ideal} / P_{actual}$) and indicates rotor efficiency. Equation (4.1) provides the calculation for the power required for a vertical climb or hover (when climb velocity is zero), specifically for a conventional helicopter [14]. The total power required also factors in the energy needed for the tail rotor. Typically, the

power ratio of the tail rotor to the main rotor ($\mathrm{P_{tail\ rotor}/P_{main\ rotor}}$) ranges from 0.14 to 0.22, as tail rotors generally have a diameter that is about 15-20% of the main rotor's diameter [14].

$$P_{(\text{Vert Climb or Hover})} = \left[\left(\frac{fW}{M}\sqrt{\frac{fW/S}{2\rho}}\right) + \frac{WV_{\text{Climb}}}{2}\right]\left[\frac{(1+P_{\text{tail rotor}}/P_{\text{main rotor}})}{\eta_{\text{mechanical}}}\right], \tag{4.1}$$

where P (Watt) is the power required; W (N) is the rotorcraft weight (=mg, where m (kg) is the mass of the rotorcraft and g ($\mathrm{m/s^2}$) is the surface gravity acceleration on Mars for the sake of this paper); S (m) is the rotor disk area; M is the figure of merit; V_{Climb} (m/s) is vertical climb velocity (=0 for hover); f is the adjustment for downwash on the fuselage (=1.06 typically); ρ ($\mathrm{kg/m^3}$) is the local air density on Mars; $\eta_{\text{mechanical}}$ is mechanical losses adjustment due to driving of the tail rotor (=0.97 typically)

During forward flight, the rotor acts like a circular wing with an aspect ratio of $4/\pi$. Empirical data indicates an Oswald efficiency factor for such wings between 0.5 and 0.8 [14]. This factor, determined at a given lift coefficient, is the ratio of the induced drag coefficient of the wing to that of an elliptical wing with the same aspect ratio at the same lift coefficient. Parasitic drag is expressed in terms of drag area (D/q), where 'q' is the dynamic pressure. The following equation integrates these elements and helps estimate the power needed for forward climb or level flight [14].

$$P_{(\text{Fwd}_{\text{climb}}\text{ or Fwd}_{\text{level}})} = \left[\frac{V}{\eta_{\text{p}}}\left\{q(D/q) + \frac{W^2}{4eqS} + W\sin(\gamma)\right\}\right]\left[\frac{(1+P_{\text{tail rotor}}/P_{\text{main rotor}})}{\eta_{\text{mechanical}}}\right], \tag{4.2}$$

where V (m/s) is the forward flight speed; γ (Deg) is the climb path angle (=0, when levelled); q (Pa) is the dynamic pressure; e is the equivalent Oswald's

efficiency factor (=0.5 to 0.8 typically); D/q (m^2) is the component drag area; η_p is the propeller efficiency (=0.6 to 0.85 typically).

In the equation, $W\sin(\gamma)$ represents the climb component, which depends on the climb path angle γ (equal to 0 for level flight). The rotor not only provides the necessary lift but also generates forward propulsion, functioning similarly to a propeller. Therefore, the propeller efficiency factor η_p is included in the calculation to provide a more accurate estimate of the rotor's forward thrust performance.

4.2.3 Coaxial Rotorcraft

In the traditional helicopter setup, the tail rotor serves to counteract the torque created by the main rotor's rotation by generating an opposing thrust. Another method to manage this torque involves substituting the tail rotor with an additional rotor of the same size but rotating in the opposite direction, thus providing extra lift. This method is exemplified in coaxial rotorcraft, where two rotors are mounted on the same shaft within a complex hub structure. However, the proximity of these rotors results in some loss of lift due to interference from the airflow wake. Theoretically, when the two rotors perfectly overlap, with zero vertical gap, the overlapping interference factor (K_ov) increases power consumption by approximately $\sqrt{2}$ or around 41% compared to two isolated rotors unaffected by the wake of each other [15]. When there is no vertical separation between the rotors in a coaxial setup, it is termed an equivalent single-rotor system. This equivalent single rotor resembles a system of smaller twin rotors with the same total thrust and projected area (disk loading), sharing similar rotor solidity [16]. Disk loading is the ratio of the helicopter's total weight to the rotor disk area (*W/S*), while rotor solidity is the ratio of total blade area to total disk area.

In practical scenarios, coaxial rotor configurations typically have some vertical separation between the two rotors. As this separation increases, the upper rotor's wake affects a smaller portion of the lower rotor, leading to a reduction in the overlapping interference factor (K_ov). For example, with a large separation (LS), typically around 10% of the rotor diameter, the K_ov becomes 1.281, assuming uniform disk loading [15] [16]. Consequently, Eq. (4.1), used to compute the

power required for vertical climb and hover for a coaxial rotor system with two equally sized rotors sharing the total rotorcraft weight (thrust), is adjusted by multiplying it by the overlapping interference factor to form Eq. (4.3). Similarly, Eq. (4.2), used for the forward flight of a conventional helicopter, is adapted to form Eq. (4.4) for a coaxial helicopter [15].

$$P_{(\text{Vert Climb or Hover})} = \left[\left(\frac{fW}{(2\sqrt{2})M}\sqrt{\frac{fW/S}{2\rho}}\right) + \frac{WV_{\text{Climb}}}{4}\right]\left[\frac{2}{\eta_{\text{mechanical}}}\right][K_{\text{ov}}] \quad (4.3)$$

$$P_{(\text{Fwd}_{\text{climb}} \text{ or } \text{Fwd}_{\text{level}})} = \left[\frac{V}{\eta_{\text{p}}}\left\{q(D/q) + \frac{W^2}{16eqS} + \frac{W\sin(\gamma)}{2}\right\}\right]\left[\frac{2}{\eta_{\text{mechanical}}}\right][K_{\text{ov}}] \quad (4.4)$$

In this setup, there is no tail rotor; instead, a second rotor is utilised to counteract the torque produced from the first rotor. As a result, the power ratio between the two equal-sized rotors ($P_{\text{second rotor}}/P_{\text{main rotor}}$) becomes equal to 1.

4.2.4 Isolated Rotors: rotorcraft having non-overlapping rotors

The K_{ov} factor, representing the degree of overlapping interference between equally sized rotors, transitions from $\sqrt{2}$ to 1 as their shared area moves from complete overlap to complete absence within the same plane. When there is no overlap, these rotors essentially operate independently. However, residual interference, whether advantageous or detrimental, might still be present in cases of vertical rotor separation without overlap, although it can be disregarded in preliminary investigations [15] [16]. One variant of side-by-side rotor configurations is transverse rotorcraft, where smaller rotors are horizontally mounted on the tips of side wings or an extended support frame of the fuselage. These smaller rotors are usually positioned to avoid overlap and function more like separate rotors. During cruise flight, they serve as forward propellers. In situations involving configurations of multiple rotors without overlap, like quad or hexa rotors, equations (4.1) and (4.2) can be adapted to accommodate a multirotor system with ' N ' equally sized rotors. In such arrangements, the total

thrust needed for the rotorcraft is assumed to be evenly distributed among all the rotors, as outlined in equations (4.5) and (4.6).

$$P_{(\text{Vert Climb or Hover})} = \left[\left(\frac{fW}{\left(N\sqrt{N}\right)M}\sqrt{\frac{fW/S}{2\rho}}\right) + \frac{WV_{\text{Climb}}}{2N}\right]\left[\frac{N}{\eta_{\text{mechanical}}}\right] \tag{4.5}$$

$$P_{(\text{Fwd}_{\text{climb}} \text{ or } \text{Fwd}_{\text{level}})} = \left[\frac{V}{\eta_{\text{p}}}\left\{q(D/q) + \frac{W^2}{(N^2)4eqS} + \frac{W\sin(\gamma)}{N}\right\}\right]\left[\frac{N}{\eta_{\text{mechanical}}}\right] \tag{4.6}$$

In configurations where rotors are aligned front-to-rear, an additional downwash effect is generated by the front rotor onto the rear one(s) in the forward flight. To ensure accurate power estimation, this downwash influence must be factored into the calculations for the rear rotor(s) [15], as detailed in the subsequent section on tandem configurations. The revised equation substitutes $[N]$ with $[1 + (P_{\text{tail rotor}}/P_{\text{main rotor}})]$ to indicate the number of rotors involved. This adjustment recognizes that in such configuration, there is no tail rotor; instead, all rotors are of equal size.

4.2.5 Rotorcraft with Partial Overlapping Rotors (e.g., Tandem Rotorcraft)

In tandem rotorcraft setups, two equal-sized rotors are arranged longitudinally on the fuselage, with one rotor positioned ahead of the other. The analysis of this configuration mirrors that of coaxial rotors, with overlapping disk areas determined by the horizontal gap between the rotors. Maximum tandem overlap occurs when one rotor's blade tip touches the hub center of the other rotor. Therefore, the initial power analysis of vertical climb or hover for tandem rotors

follows the same formula as that used for coaxial rotors, as described in Eq. (4.3). However, in a tandem configuration, the calculation of the overlapping

interference factor (K_{ov}) is affected by the ratio (d/D), representing the horizontal distance (d) between the two rotor axes to the rotor diameter (D). When the rotors are in the same plane (i.e., no vertical gap between rotors), K_{ov} can be approximated using Eq. (4.7) [15].

$$K_{\mathrm{ov}} = \left[\sqrt{2} - \frac{\sqrt{2}}{2}\left(\frac{d}{D}\right) + \left(1 - \frac{\sqrt{2}}{2}\right)\left(\frac{d}{D}\right)^2\right] \tag{4.7}$$

When rotors are positioned in separate planes and the lower rotor operates within the contracting wake of the upper rotor, determining the overlapping area for K_{ov} the calculation requires numerical integration. Moreover, side-by-side rotor configurations with overlapping rotors can adopt a similar approach to assess overall power requirements.

In estimating the power needed for forward flight in tandem rotorcraft, it is crucial to consider the downwash effect on the rear rotor caused by the presence of the front rotor. This downwash must be quantified and integrated into the calculation to accurately determine power loss. For initial theoretical analysis, this downwash (dw) is assumed to be the maximum value of the overlapping interference factor (max K_{ov} = K_{dw}) [15], which is 1.134 when calculated using Eq. (4.7) at maximum tandem overlap. Hence, the total power (P) required for forward flight is expressed by Eq. (4.8) [15]. In this preliminary analysis, it is assumed that the two equal-sized rotors generate equal thrust, thus requiring equal power consumption. Therefore, this expression is represented in Eq. (4.9), where the total power for forward flight of two isolated rotors (calculated using Eq. (4.6)) is divided by two and then multiplied by the downwash factor. Additionally, if there is an overlap between the two rotors, the overlapping interference factor (K_{ov}) is incorporated into the expression to calculate the total forward power.

$$P_{(\mathrm{Forward})} = P_{\mathrm{Front\ Rotor}} + P_{\mathrm{Rear\ Rotor}}(K_{\mathrm{dw}})\,, \tag{4.8}$$

$$P_{(\mathrm{Forward})} = (1 + K_{\mathrm{dw}})\frac{1}{2}P_{2\ \mathrm{Iso}}K_{\mathrm{ov}}\,, \tag{4.9}$$

where $P_{2\,\mathrm{Iso}}$ (Watt) is the required forward flight power of rotorcraft with 2 isolated rotors; K_{dw} is the downwash factor (=1.134); K_{ov} is the overlapping interference factor (=1, when no overlapping).

In scenarios without rotor overlap, such as non-overlapping same-plane tandem rotor configurations, the inclusion of K_{ov} is either omitted or its value is set to 1 in equations (4.3) and (4.9). This adjustment is crucial since the use of Eq. (4.7) for estimating K_{ov} becomes inaccurate when there is no rotor overlap.

4.3 Initial Sizing Methods for Battery-Electric Aircraft

Initial sizing of battery-electric aircraft involves accounting for the total mass of the aircraft at maximum take-off, including the empty mass, payload, and fuel components. In fuel-powered aircraft, mass decreases during flight due to fuel consumption across various flight stages: taxiing, take-off, ascent, cruising, and descent. This mass reduction affects aircraft performance and drag characteristics, necessitating detailed calculations for each flight phase during initial sizing evaluations. In contrast, electric aircraft do not experience variations in battery mass during flight, eliminating the need for integration across flight segments. Instead, the fuel component of the total aircraft mass is replaced with the mass of the battery (m_{b}). The required battery mass for each mission segment is determined using Eq. (4.10), which expresses it as a ratio of the battery mass to the total aircraft mass (m_{b}/m_0), known as the Battery Mass Fraction (*BMF*) [14].

$$BMF = \frac{m_{\mathrm{b}}}{m_0} = \frac{W_{\mathrm{b}}}{W_0} = \frac{EP_{\mathrm{used}}}{E_{\mathrm{sb}}\eta_{\mathrm{b2s}}m_0}, \tag{4.10}$$

where m_0 (kg) is the total take-off mass of the aerobot; m_{b} (kg) is the battery mass; W_0 (N) is the total take-off weight of the aerobot [=mg, where g $(\mathrm{m/s^2})$ is the surface gravity acceleration on Mars for this paper]; W_{b} (N) is the battery weight; P_{used} $(\mathrm{Watt\ or\ W})$ is the power required; E $(\mathrm{hour\ or\ h})$ is the known run time; E_{sb} $(\mathrm{Wh/kg})$ is the battery-specific energy; η_{b2s} is the total system efficiency from the battery to the motor output shaft (=0.9 typically).

The equation above considers parameters such as the known run-time endurance (E) and the power consumption during various flight phases, including vertical climb, hover, and forward flight for rotorcraft. The cumulative Battery Mass Fraction of the aircraft is then calculated by summing the *BMF*s corresponding to each flight phase [14]. This methodology enables a comprehensive assessment of the battery mass required for different stages of the aircraft's mission.

When estimating the Battery Mass Fraction (BMF) for electric aircraft, accounting for nominal usage and discharge efficiency is critical to refine battery mass calculations. Nominal usage refers to the operational capacity range of a battery, as fully discharging it (0–100%) is avoided to minimize degradation and prolong its lifespan. For example, restricting usage to 10–80% state of charge (SOC) limits usable capacity to 70%, balancing performance with longevity [17]. Discharge efficiency, the proportion of energy delivered during discharge compared to the energy stored during charging, also impacts sizing. A 95% efficiency implies a 5% energy loss (e.g., as heat), necessitating larger battery capacity to compensate [18]. By integrating these factors into BMF calculations, designers ensure the aircraft meets operational demands while maintaining battery health and system reliability.

Equation (4.11) is utilised to determine the total aircraft take-off mass (m_0), which is defined as the sum of the empty mass (m_e), battery mass (m_b), and payload mass (m_payload) [14].

$$m_0 = m_\mathrm{e} + m_\mathrm{b} + m_\mathrm{payload} \tag{4.11}$$

Eq. (4.11) undergoes modification to formulate Eq. (4.12) for battery electric aircraft sizing [14].

$$m_0 = \frac{m_\mathrm{payload}}{1 - BMF_\mathrm{total} - \frac{m_\mathrm{e}}{m_0}} \tag{4.12}$$

This adjustment involves considering both the total Battery Mass Fraction and the ratio of empty mass (m_e) to total mass (m_0) [14]. In this context, the payload may

consist of instruments or items for delivery, particularly for unmanned aircraft. Conversely, m_{e} encompasses all components except the payload or operational batteries, including the propulsion system, aircraft structure, avionics, navigation equipment, and other essential systems.

The initial sizing equation provides a starting point for preliminary estimations, taking into account factors such as the empty mass ratio, payload mass, and the calculated *BMF* requirement. These parameters allow for the determination of the total mass. Alternatively, known parameters can be utilised to infer unknown variables, such as estimating total mass and empty mass, and subsequently calculating the required BMF to assess the payload capacity of the aircraft. This sizing procedure involves iteration and may require multiple computations and adjustments until a reasonable estimate aligns with the desired objectives, facilitating preliminary design investigations.

4.4 Initial Sizing Methods and Analysis for Estimating Rotor Blade Mass

The variation in rotor diameter and number of blades directly impacts the mass of rotors, airframe, and motors, as well as the power requirements for flight, particularly in Martian rotorcraft designs. Blade mass is a critical factor in the total weight of a Mars rotorcraft, significantly more so than in terrestrial designs. Larger rotors are necessary to produce sufficient lift in the thin atmosphere, but this increases centrifugal forces, which are directly proportional to both the blade mass and rotor radius. For smaller to medium rotors, blade mass typically constitutes 10–30% of the Martian rotorcraft's weight [19]. However, as the rotor radius exceeds 12 m, the centrifugal forces and material stresses grow disproportionately, posing challenges for maintaining structural integrity without excessive weight. Despite this, Mars rotor blades are estimated to weigh only 10–14% of their terrestrial counterparts of the same size [19]. Such weight reduction is achieved through ultra-lightweight construction techniques, essential for ensuring sufficient lift and structural efficiency in Mars' challenging environment, regardless of rotorcraft size.

4.4.1 Existing Rotor Blade Mass Scaling Methods

Several methods have been proposed for estimating Martian rotor blade mass in the literature. A study [20] on Mars quadcopter design used a simple scaling law to estimate blade mass based on rotor diameter, assuming a uniform quadratic relationship. The blade mass (m_{blade}) is proportional to the square of the rotor diameter, expressed as:

$$m_{\mathrm{blade}} = k(D_{\mathrm{rot}}/D_{\mathrm{ref}})^2, \tag{4.13}$$

where k (kg) is the reference blade mass at a diameter D_{ref} (m). The baseline for this method is a rotor with a diameter of 0.8 m and a mass of 0.019 kg, achieved using lightweight composite blades constructed with a carbon fibre skin and foam core. This approach presupposes that airfoil thickness variations have a negligible effect on mass, making the blade's surface area the primary driver.

A similar geometric scaling approach appears in the report on Mars Science Helicopter (MSH) preliminary design [4], which takes the flight-proven Mars Helicopter (MH) blades as a baseline, with a diameter of 1.21 m and a single blade mass of about 0.035 kg. For the MSH, the initial blade weight was scaled with blade area using the formula:

$$m_{\mathrm{blade}} = iS_{\mathrm{blade}}, \tag{4.14}$$

where S_{blade} (m^2) represents blade area and i (=1.1) is a 110% MH's scaling factor [5]. This allowed for scaling to larger designs, with the MSH blade diameters reaching 2.5–2.7 m (coaxial) or 1.0–1.4 m (hexacopter). These geometric scaling methods simplify early-stage design evaluations due to their ease of use and scalability but are most accurate within a moderate range of rotor diameters around the baseline. Precision declines for significantly larger or smaller diameters as they fail to account for material redistributions, structural adaptations, and dynamic effects.

A more robust parametric method for first-order blade mass estimation was developed in an earlier study by Young et al. [19] at NASA, incorporating detailed geometric and material properties. This method was calibrated against a 2.44 m prototype blade and included a 25% knockdown factor to account for material

and structural optimisation. The blade design featured a graphite epoxy composite framework with a Mylar skin, optimised for low Reynolds numbers using cambered, circular-arc flat-plate airfoils with trailing edge cutouts to reduce weight while maintaining aerodynamic and structural efficiency. The total blade mass is estimated as [19]:

$$m_{\text{blade}}(X) \approx AF(m_{\text{struct}}(X) + m_{\text{skin}}), \tag{4.15}$$

where AF is an adjustment factor accounting for the blade's configuration (e.g., 1.1 for non-folded blades or 1.3 for folded/telescopic blades); X is dimensional chordwise station; m_{struct} (kg) is the structural mass; m_{skin} (kg) represent the skin mass. The structural mass is calculated as [19]:

$$m_{\text{struct}}(X) = \rho_{\text{material}} t_{\text{material}}(A + B), \tag{4.16}$$

where ρ_{material} (kg/m^3) is the density of the material used; t_{material} (m) is the thickness of the material used; A (m^2), the blade geometry contribution term, captures the primary blade geometry, including span and chord distribution, and incorporates terms such as chord length, radial positions, and spar contributions; B (m^2) is a structural reinforcement contribution term, representing the mass of structural reinforcements, such as spar caps and webs, depending on the number of webs and their spanwise extent. The skin mass is calculated using the skin material's density, thickness and the blade surface area [19]. Together, these components ensure the blade mass accurately reflects both the aerodynamic surface, and the structural reinforcements needed for strength, providing a precise and scalable solution for estimating blade mass in Martian rotorcraft design. While reasonable for rotor radius sizes up to 12 m, additional considerations for centrifugal forces and material stresses become necessary for massive configurations [19].

4.4.2 Proposed Rotor Blade Mass Scaling Model – 3D MSH Scale

This subsection presents a 3D scaling methodology, building upon the principles used in Young et al. [78] while introducing the novelty of incorporating modern Martian blade designs. The model predicts blade mass by integrating power-law scaling laws for chord, thickness, and material distribution, enabling a systematic adaptation of rotor blades across different sizes, from smaller hexacopters to

larger coaxial configurations. The subsequent analysis validates the scaling relationships against empirical data from prototype blades, establishes component-specific mass trends, and demonstrates how strategic material allocation (e.g., carbon-fiber spar, foam core) mitigates the risks of low aerodynamic damping and oscillatory instability inherent to Martian flight.

The next-generation Mars Science Helicopter (MSH) features advanced blade designs optimised for low-density atmospheric conditions and low Reynolds numbers [4]. Thin, sharp-edged airfoils induce early flow separation and vortex shedding, enhancing lift generation while minimising drag. A key challenge in Martian rotorcraft is the significantly lower aerodynamic damping, approximately ten times lower than on Earth, which affects blade flapping control and increases the risk of oscillatory mode coupling with vehicle dynamics. To mitigate this, the blades are stiffened well beyond structural stress requirements, raising the natural flap frequency above the critical control bandwidth [4], reducing resonance risks and improving stability.

The MSH's final optimised hybrid airfoil geometry incorporates diamond-shaped inboard sections with minimal thickness ratio, addressing structural and flap frequency constraints, while the outboard sections utilise thin, double-edged plate airfoils with sharp leading edges to enhance lift-to-drag ratio and delay stall onset. The MSH blade planform, includes a square tip, ensuring the tip vortex forms at the outermost span for improved hover efficiency, and a 9% of radius (R) root cutout to reduce inboard chord and minimise weight where lift contribution is negligible. The chord distribution transitions from negative taper in the root region, where the chord reduces from the root up to approximately $0.25R$, to a moderate linear taper at mid-span, followed by additional tip taper beyond $0.75R$. The blade planforms, shown in Fig. 4.2, were developed for two rotor sizes [4]: a 1.25 m radius rotor for the coaxial Mars Science Helicopter (MSH) and a 0.64 m radius rotor for the hexacopter configuration. From these figures the relative chord values are deduced for each rotor size, shown in Table 4.1, providing a basis for further analysis in this study.

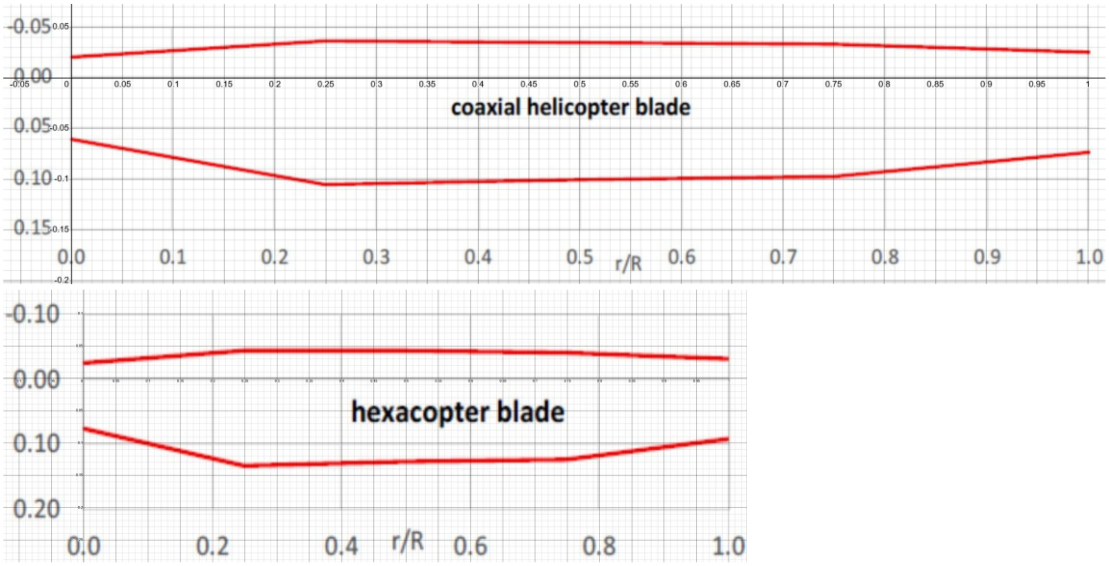


Fig. 4.2 Planform of the Mars Science Helicopter blade for a coaxial helicopter (R = 1.25 m) and a hexacopter (R = 0.64 m), with a typical 9%R root cutout (not shown). Adapted from [4], with graph plot images overlaid on a blank graph with minor axes for clarity. Not to scale.

Table 4.1 Relative chord (c/R) values at key radial positions (r/R) for the blades of rotor radius (R) 1.25 m and 0.64 m.

Radial Position (r/R)		0.09	0.25	0.5	0.75	1
Relative Chord (c/R)	R 1.25 m	0.1	0.14	0.135	0.13	0.1
	R 0.64 m	0.13	0.148	0.17	0.16	0.12
Averaged Relative Chord (c/R)	R 1.25 m	0.1307			0.1238	
	R 0.64 m	0.1512			0.1525	

4.4.2.1 Scaling Law for Relative Chord and Planform Area

The blade structure shown in Fig. 4.3, features a multi-layer composite design with a spar extending upto 50% span for primary load-bearing, an enclosed foam core for added support, outer skin layers optimised for mass efficiency and stiffness, and a metal root insert for secure rotor hub attachment. For analysis, the blade is divided into two segments (illustrated in Fig. 4.4): an inner segment extending from radial positions (r/R) of 0.09 to 0.50, containing spar and foam, and an outer segment ($0.5 \leq r/R \leq 1.0$) consisting only of skin. The average chord within each segment was calculated using the trapezoidal integration method. In this approach, the chord distribution was segmented into four trapezoid sections defined by the radial stations: 0.09 to 0.25, 0.25 to 0.50, 0.50

to 0.75, and 0.75 to 1.00 r/R. The area under the chord distribution curve was computed for each of these sections and then summed and divided by the total radial span of the respective segment to obtain an average chord value. For the 1.25 m rotor, the average chord-to-radius ratio for the inner segment ($0.09 \leq r/R \leq 0.5$) is approximately 0.1307, while for the outer segment ($0.5 \leq r/R \leq 1.0$) it is about 0.1238. For the 0.64 m rotor, these average ratios are higher, at approximately 0.1512 for the inner segment and 0.1525 for the outer segment. These results (shown in Table 4.1) indicate that as the rotor radius decreases, the relative chord length increases, an expected adaptation to maintain aerodynamic performance at a smaller scale.

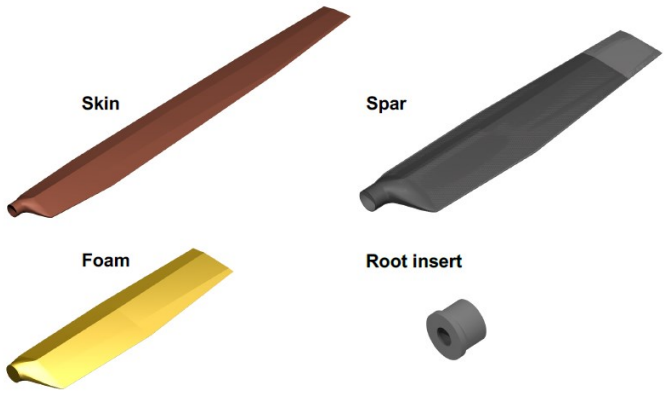


Fig. 4.3 MSH components: (top left) skin, (top right) spar, (bottom left) foam, (bottom right) root insert. Image Source [4].

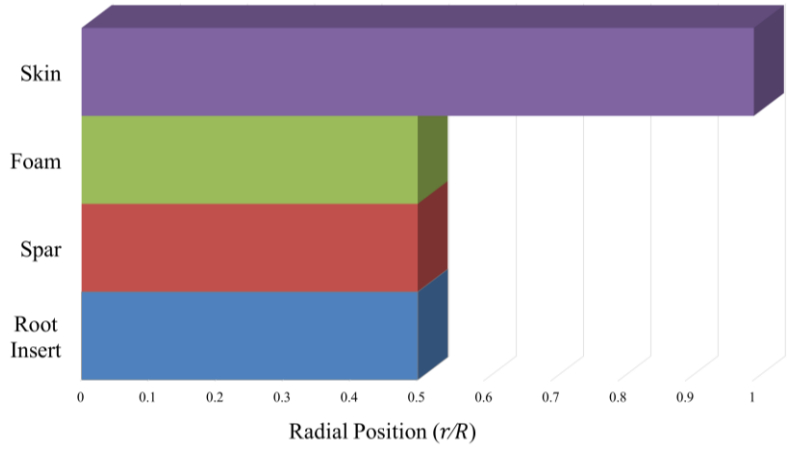


Fig. 4.4 Simplified representation of segmented blade components along the radial span. The inner region ($0.09 \leq r/R \leq 0.5$) contains the root insert, spar, and

foam, while the outer region ($0.5 \leq r/R \leq 1.0$) consists only of the skin. (Bars are not representation of the thickness)

To establish a continuous scaling relationship, a power-law method is used to generalise the chord-to-radius ratios across different rotor sizes relative to the 1.25 m rotor design. The scaling exponent is determined by comparing the relative chord-to-radius ratio $\left(\frac{c}{R}\right)$ values between the two baseline rotors for each segment (short formed to seg) and solving for the relative scaling exponent (n_{seg}) in a power-law function of the form:

$$\left(\frac{c}{R}\right)_{\text{seg}} = \left(\frac{c}{R}\right)_{\text{seg, 1.25}} \left(\frac{R}{1.25}\right)^{n_{\text{seg}}}, \tag{4.17}$$

By taking the natural logarithm of both sides, the exponent (n_{seg}) is calculated separately for each segment by solving:

$$n_{\text{seg}} = \frac{\ln\left(\frac{(c/R)_{0.64}}{(c/R)_{1.25}}\right)}{\ln\left(\frac{0.64}{1.25}\right)}, \tag{4.18}$$

Applying this method, the power-law scaling relationships for the average chord-to-radius ratios for the inner and outer segments are obtained:

$$\left(\frac{c}{R}\right)_{\text{inner}} = 0.1307 \left(\frac{R}{1.25}\right)^{-0.217}, \tag{4.19}$$

$$\left(\frac{c}{R}\right)_{\text{outer}} = 0.1238 \left(\frac{R}{1.25}\right)^{-0.311}, \tag{4.20}$$

The chord length then can be found using the relation:

$$c_{\text{seg}} = R \left(\frac{c}{R}\right)_{\text{seg}}, \tag{4.21}$$

These equations provide a simplified and efficient means to generalise the chord distribution for different rotor sizes while ensuring aerodynamic and structural consistency. With these scaling relationships in place, the planform area of each segment is computed based on the assumption that the average chord distribution in each segment could be approximated by its average value. The general formula for the planform area of a segment is:

$$S_{\text{seg}} = \Delta R_{\text{seg}} R^2 \left(\frac{c}{R}\right)_{\text{seg}}, \tag{4.22}$$

where ΔR_{seg} represents the normalised radial span of the segment. In this study, the inner segment extends from 0.09 to 0.50 r/R, resulting in a span of $0.41R$, while the outer segment spans 0.50 to 1.00 r/R, covering $0.50R$.

These planform area estimates are critical in evaluating the mass properties of the rotor and ensuring the structural integrity of the blade while maintaining aerodynamic efficiency. The integration of a power-law scaling approach provides a robust framework for extrapolating blade designs across different rotor sizes, ensuring that aerodynamic, structural, and inertial properties scale consistently for various configurations of the Mars Science Helicopter.

4.4.2.2 Scaling Law for Material Fraction and Thickness-to-Chord ratio

For a flap frequency requirement of approximately 1.5/rev, the hexacopter blade and the coaxial helicopter blade were designed with increased thickness to achieve the desired frequency [4]. The materials in the blade include a spar made of MTM45-1 M46J 12K unidirectional carbon fiber tape for stiffness and fatigue resistance, outer skin of 60 gsm HR40 spread-tow bi-directional carbon fiber cloth with knockdown E factors, a Rohacell 31F foam core for a high stiffness-to-weight ratio, and a 7075 aluminium root insert for efficient load transfer and minimised weight. The resulting blade weight was 78.1 g for the hexacopter and 341.4 g for the coaxial helicopter. Table 4.2 presents the material component composition of each blade; which includes skin, spar, foam, and root insert. For both blades, the skin consisted of 7 layers of cloth at the inner segment and 12 layers at the outer segment (outboard of $50\%R$). While both designs followed the same structural layout, the distribution of material mass varied between the two configurations, reflecting the influence of rotor radius on structural requirements.

Table 4.2 Comparison of blade components mass composition

Blade Components	Mass Composition (g)		Percentage Composition		Variation (%)
	R 0.64m	R 1.25m	R 0.64m	R 1.25m	R 0.64 to 1.25m
Skin	22.6	87.4	29%	26%	-3.3%
Spar	45.2	187.7	58%	55%	-2.9%
Foam	2.1	16.5	3%	5%	2.1%
Root Insert	8.2	49.8	10%	15%	4.1%
Total	78.1	341.4	100%	100%	Nil

A comparison of the mass percentage for each material component reveals important scaling trends. In the hexacopter blade, the skin accounted for ~29% of the total mass, while in the coaxial blade, it contributed only ~26%. This decrease in relative mass share suggests that while the absolute skin mass increases with rotor size, it constitutes a smaller proportion of the total blade mass at larger scales. A similar trend is observed in the spar, which is decreased by ~3% in the coaxial blade mass. The decreasing fraction of both the skin and spar indicates that the primary load-bearing structure does not scale proportionally with the total blade mass. Conversely, the foam core and root insert show the opposite behavior, increasing in their relative contribution as the rotor size grows. The foam fraction increased from ~3% in the hexacopter blade to ~5% in the coaxial blade, highlighting a greater role in maintaining structural stability via lighter material as the blade size increases. Similarly, the root insert by ~4% in the coaxial blade, reflecting the need for a stronger hub attachment in larger blades.

The composition of the material volume can be calculated through material densities, which is then used to estimate the thickness of each component. This approach is utilised for a more detailed understanding of the scaling behavior and structural performance, due to the limited information on the thickness variation of the blade components across the radius. The densities of Rohacell 31F foam core [21]and 7075 aluminium [22] are 32 kg/m³ and 2810 kg/m³, respectively, whereas the blade composite materials include both the dry constituents and their cured composite forms. For example, the MTM45-1 epoxy resin has a density of 1180 kg/m³ [23], while the carbon fibers used in the spar (M46J) [24] and in the skin (HR40) [25] have densities of 1840 kg/m³ and 1820 kg/m³, respectively. However, these fibers are not used in their dry form; instead, they are included

as prepregs. The prepreg process involves impregnating dry carbon fiber fabrics with epoxy resin to achieve a controlled fiber volume fraction (Vol_{f}), which significantly influences the mechanical properties and overall mass distribution. The effective density of each prepreg material is determined using the rule of mixtures [26], given by:

$$\rho_{\mathrm{prepreg}} = \rho_{\mathrm{f}} Vol_{\mathrm{f}} + \rho_r(1 - Vol_{\mathrm{f}}) , \tag{4.23}$$

where ρ_{prepreg} $(\mathrm{kg/m^3})$ is the density of the cured prepreg laminate; ρ_{f} is the density of the fiber; ρ_r is the density of the resin; Vol_{f} is the fiber volume fraction.

For both the spar and skin prepregs, the fiber volume fraction is taken as 0.6 (60%), a value within the typical range [27] for aerospace-grade composites optimised for high stiffness-to-weight ratios. For spare M46J carbon fiber prepreg using the resin MTM45-1, the density is calculated to be 1576kg/m³ and for skin HR40 carbon fiber prepreg density is 1564 kg/m³ (with an assumption of using the same resin).

Using these densities, the volume occupied by each material component can be determined, based on the relationship: $volume = mass/density$. The Table 4.3 presents the material volume component composition and relative percentage of each blade.

Table 4.3 Comparison of blade material components volume composition

Blade Components Material		Density (kg/m³)	Mass Composition (g)		Volume Composition (m³)		Percentage Composition (%)		Volume Variation (%)
			R 0.64m	R	R 0.64m	R 1.25m	R 0.64m	R 1.25m	R 0.64 to 1.25m
Skin	MTM45-1 HR40	1580	22.6	87.4	1.43E-05	5.53E-05	13%	7.8%	-5.0%
Spar	MTM45-1 M46J	1592	45.2	187.7	2.84E-05	1.18E-04	26%	16.7%	-8.8%
Foam	Rohacell 31F	32	2.1	16.5	6.56E-05	5.16E-04	59%	73.0%	14.0%
Root Insert	7075 Al	2801	8.2	49.8	2.93E-06	1.78E-05	3%	2.5%	-0.1%
Total			78.1	341.4	1.11E-04	7.07E-04	100%	100%	Nil

The differences in volume distribution further confirm the scaling effect observed in the mass fraction analysis. As the blade size increases, the foam core becomes a larger proportion of the total volume, while the spar and skin, despite increasing

in absolute mass, contribute proportionally less to the total volume. This demonstrates the effectiveness of weight reduction strategies in larger rotor designs while maintaining structural integrity.

Building on the material composition and volume estimates, the next step is to determine the average thickness of each material component in the rotor blades. This is accomplished by dividing the volume of each component by its corresponding planform area ($thickness = volume/area$). The spar, foam core, and root insert are confined to the inner segment region of the blade ($0.09 \leq r/R \leq 0.5$); whereas, the skin spans both the inner segment and the outer segment regions ($0.5 \leq r/R \leq 1.0$). Therefore, separate average thickness measurements are obtained for the skin in each segment. The skin volume in each segment is determined by considering both the number of carbon fibre layers (plies) present and the relative planform area, which is particularly important when the blade exhibits sharp edges and non-uniform shapes. Thus, weighting distribution factor is introduce in the volume distribution for each segment, and is given by:

$$Vol_{\text{skin, seg}} = Vol_{\text{skin, total}}\left[f_{\text{skin, seg}}\right] \tag{4.24}$$

$$f_{\text{skin, seg}} = \frac{N_{\text{layer, seg}} S_{\text{blade, seg}}}{(N_{\text{layer, inner}} S_{\text{blade, inner}}) + (N_{\text{layer, outer}} S_{\text{blade, outer}})}, \tag{4.25}$$

where $Vol_{\text{skin, seg}}$ (m^3) is the volume of the skin material for the segment (inner or outer) in this study; $f_{\text{skin, seg}}$ is the weighting distribution factor for the segment; $N_{layer,\ seg}$ is the number of carbon fibre plies/layers for the segment; $S_{\text{blade, seg}}$ is the planform area of the blade for the segment (inner or outer).

The HR40 carbon fiber cloth plies are distributed as 7 layers in the inner segment and 12 layers in the outer. Based on the equation (4.22), planform area (S_{blade}) is calculated for the inner and outer segments of the blades. $S_{\text{blade, inner}}$ is 0.0254 m^2 and 0.0838 m^2, while $S_{\text{blade, outer}}$ is 0.0312 m^2 and 0.0968 m^2 for blade radii 0.64 m and 1.25 m, respectively. The weighting distribution factor, calculated using Eq. (4.25), for inner segment skin ($f_{\text{skin, inner}}$) is ~ 0.37 (37%) and ~ 0.34 (34%), while $f_{\text{skin, outer}}$ is ~ 0.63 (63%) and ~ 0.66 (66%) for blade radii 0.64 m

and 1.25 m, respectively. Then using Eq. (4.24), the skin volume in each segment is computed.

Table 4.4 informs the thickness of each component in its relative planform. The foam thickness increases significantly in the larger (coaxial) blade, supporting the scaling effect that foam contributes more to weight reduction in larger rotors. The spar thickness increases slightly, but not proportionally to rotor size, confirming that stiffness constraints govern spar sizing rather than just scale effects indicating that stiffness constraints, rather than geometric scaling, govern its sizing. The skin thickness decreases marginally, with inner and outer regions reducing by ~2% and ~3%, respectively, reflecting improved material efficiency in the larger blade. The root insert thickness scales proportionally, ensuring consistent load transfer and hub attachment across both designs.

Table 4.4 Comparison of blade material components thickncss composition

Blade Components	Segment Region	Relative Planform Area		Volume Composition (m³)		Relative Average Thickness (m)		Percentage Composition (%)		Thickness Variation (%)
		R 0.64m	R 1.25m	R 0.64m	R 1.25m	R 0.64m	R 1.25m	R 0.64m	R 1.25m	R 0.64 to 1.25m
Skin	Inner	0.02548	0.0837	4.65E-06	1.88E-05	1.82E-04	2.24E-04	4.2%	2.7%	-1.6%
	Outer	0.03134	0.09666	9.80E-06	3.71E-05	3.13E-04	3.84E-04	7.3%	4.6%	-2.7%
Spar	Inner	0.02548	0.0837	2.87E-05	1.19E-04	1.13E-03	1.42E-03	26.1%	16.9%	-9.2%
Foam	Inner	0.02548	0.0837	6.56E-05	5.16E-04	2.58E-03	6.16E-03	59.7%	73.3%	13.6%
Root Insert	Inner	0.02548	0.0837	2.93E-06	1.78E-05	1.15E-04	2.12E-04	2.7%	2.5%	0.2%
Total				1.12E-04	7.08E-04	4.31E-03	8.40E-03	100%	100%	

With the thickness variation across rotor sizes quantified, a scaling relationship is established to generalise the thickness distribution for different rotor radii. The thickness-to-chord ratio of each blade component (short formed to cmpt) in a segment, $(t/c)_{\text{compt}}$, follows a power-law function of the form:

$$\left(\frac{t}{c}\right)_{\text{cmpt, seg}} = \left(\frac{t}{c}\right)_{\text{cmpt, seg, 1.25}} \left(\frac{R}{1.25}\right)^{e_{\text{cmpt, seg}}}, \tag{4.26}$$

where $(t/c)_{\text{cmpt, seg, 1.25}}$, is the reference thickness-to-chord ratio of a blade component in a segment at radius (R) =1.25 m. $e_{\text{cmpt, seg}}$ is the relative scaling exponent for thickness-to-chord ratio of a blade component in a segment. The $e_{\text{cmpt, seg}}$ is determined empirically using measured thickness values at two known rotor sizes (R =1.25 m and R = 0.64 m), based on the power-law relationship where the blade thickness scales as: $thickness(R) \propto R^e$.

By taking the natural logarithm of both sides, $e_{\text{cmpt, seg}}$ is solved:

$$e_{\text{cmpt, seg}} = \frac{\ln\left(\frac{t_{\text{cmpt, seg, 0.64}}}{t_{\text{cmpt, seg, 1.25}}}\right)}{\ln\left(\frac{0.64}{1.25}\right)}, \tag{4.27}$$

Substituting the measured thickness values from Table 4.4, the scaling exponent ($e_{\text{cmpt, seg}}$) is calculated for each blade component. The results are summarised in Table 4.5. The foam core exhibits the highest scaling exponent ($e_{\text{foam, inner}} = 1.583$), indicating a significant increase in thickness with rotor size, reinforcing its role in weight reduction for larger blades; whereas, the spar and skin scales at a low rate.

Table 4.5 Thickness-to-chord scaling exponents ($e_{\text{cmpt, seg}}$) for blade components in a segment

$e_{\text{skin, inner}}$	$e_{\text{skin, outer}}$	$e_{\text{spar, inner}}$	$e_{\text{foam, inner}}$	$e_{\text{root, inner}}$
0.577	0.577	0.630	1.583	1.198

The graph Fig. 4.5 illustrates the variation in average thickness of different blade components as a function of rotor blade radius, plotted on a logarithmic scale (base 2) for better visualisation of scaling effects. Foam thickness in the inner segment increases significantly, reflecting its role in weight optimisation at larger scales. Spar thickness grows moderately, driven by structural stiffness needs, while skin thickness in both segments remains nearly constant, improving material efficiency. The averaged root insert thickness scales slightly to maintain load-bearing integrity. This confirms foam as the primary contributor to thickness growth, while other components follow constrained scaling trends.

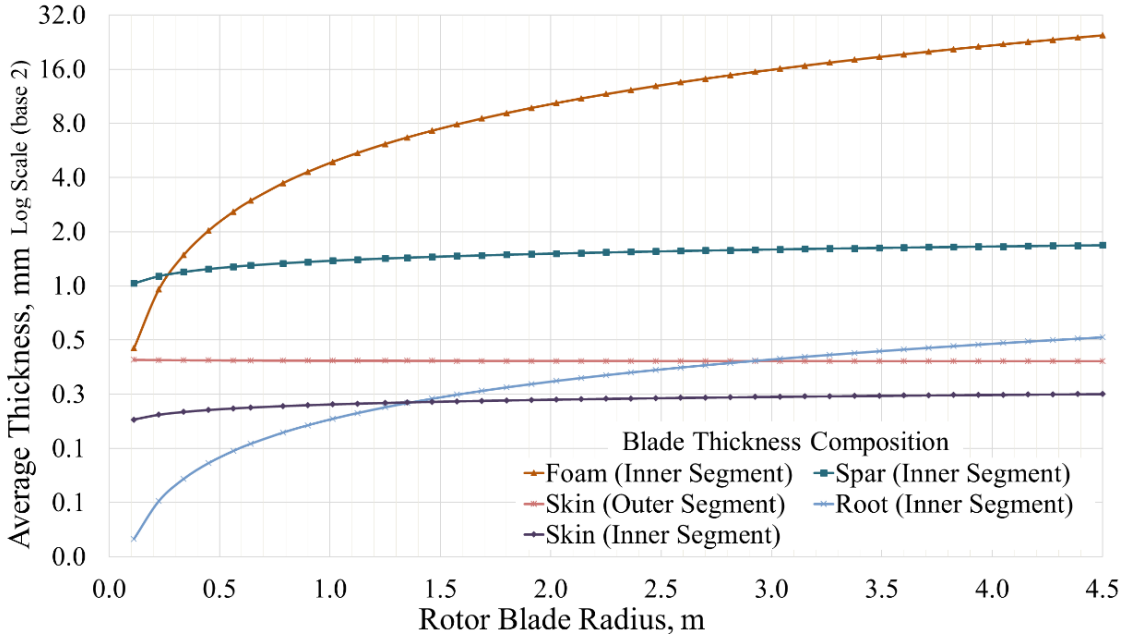


Fig. 4.5 Scaling trends of blade component thickness with rotor radius, plotted on a logarithmic scale (base 2).

4.4.2.3 Using Scaled Parameteric Relationships to Compute Blade Mass

With the thickness-to-chord ratio scaling relationship established, the total mass of each blade component, $m_{\text{cmpt, seg}}(R)$, can now be determined using the fundamental mass equation:

$$m_{\text{cmpt, seg}}(R) = \rho_{\text{cmpt}} Vol_{\text{cmpt, seg}}(R)\,, \tag{4.28}$$

$$Vol_{\text{cmpt, seg}}(R) = t_{\text{cmpt, seg}}(R) S_{\text{seg}}(R)\,, \tag{4.29}$$

where ρ_{cmpt} is the density of a component material; $Vol_{\text{cmpt, seg}}(R)$ is the volume of a component in a segment; $t_{\text{cmpt, seg}}(R)$ is the component thickness for a segment, derived from thickness-to-chord scaling; $S_{\text{seg}}(R)$ is the planform area of a blade segment.

Since thickness scales with (t/c) and chord scales with rotor radius (R), $t_{\text{cmpt, seg}}$ is substituted with the following equation:

$$t_{\text{cmpt, seg}} = c_{\text{seg}} \left(\frac{t}{c}\right)_{\text{cmpt, seg}}, \tag{4.30}$$

where the chord length (c_{seg}) follows the scaling law established earlier in Eq. (4.17) for chord-to-radius ratio, such that:

$$c_{\text{seg}} = c_{\text{seg, 1.25}} \left(\frac{R}{1.25}\right)^{n_{\text{seg}}}, \tag{4.31}$$

Hence, once subtituted with Eq. (4.26) and (4.31), the Eq. (4.30) is expanded to:

$$t_{\text{cmpt, seg}} = c_{\text{seg, 1.25}} \left(\frac{t}{c}\right)_{\text{cmpt, seg, 1.25}} \left(\frac{R}{1.25}\right)^{n_{\text{seg}}+e_{\text{cmpt, seg}}}, \tag{4.32}$$

Alternatively, if the component thickness for the segment of the reference blade radius (in this case i.e, 1.25 m) is known, then:

$$t_{\text{cmpt, seg}} = t_{\text{cmpt, seg, 1.25}} \left(\frac{R}{1.25}\right)^{n_{\text{seg}}+e_{\text{cmpt, seg}}}, \tag{4.33}$$

Similarly, the S_{segment} established in Eq. (4.22) is expanded to:

$$S_{\text{seg}} = \Delta R_{\text{seg}} R^2 \left(\frac{c}{R}\right)_{\text{seg, 1.25}} \left(\frac{R}{1.25}\right)^{n_{\text{seg}}}, \tag{4.34}$$

Substituting the planform area and thickness expressions into Eq. (4.29):

$$\begin{aligned} &Vol_{\text{cmpt, seg}}(R) \\ &= c_{\text{seg, 1.25}} \left(\frac{t}{c}\right)_{\text{cmpt, seg, 1.25}} \left(\frac{R}{1.25}\right)^{n_{\text{seg}}+e_{\text{cmpt, seg}}} \Delta R_{\text{seg}} R^2 \left(\frac{c}{R}\right)_{\text{seg, 1.25}} \left(\frac{R}{1.25}\right)^{n_{\text{seg}}}, \end{aligned} \tag{4.35}$$

The above equation simplifies to:

$$\begin{aligned} &Vol_{\text{cmpt, seg}}(R) \\ &= \Delta R_{\text{seg}} R^2 \left(\frac{c}{R}\right)_{\text{segment, 1.25}} c_{\text{seg, 1.25}} \left(\frac{t}{c}\right)_{\text{cmpt, seg, 1.25}} \left(\frac{R}{1.25}\right)^{2n_{\text{seg}}+e_{\text{cmpt, seg}}}, \end{aligned} \tag{36}$$

To accurately capture the role of individual blade components in particular section, the total mass is separated into contributions from the inner segment and the outer segment. The inner segment contains the spar, foam core, root insert, and inner skin, while the outer segment consists solely of the outer skin. Accordingly, the total blade mass is determined as:

$$m_{\text{blade}}(R) = AF[m_{\text{inner}}(R) + m_{\text{outer}}(R)], \tag{4.37}$$

where AF is an adjustment factor accounting for the blade's configuration, similar to the Eq. (4.17) based on Young et al. [17] method. However, in this model this adjustment factor is only incorporated if the blades include folded mechanism [$AF = 1.1$ for $(1.5m \leq R)$and $AF = 1.2$ for $(R \geq 1.5m)$] or more complex telescopic mechanism (AF=1.3). For non-folded blades, the adjustment factor due to balde's configuration is not required ($AF = 1$) to avoid over estimation of the mass, as this model is based on the state-of-the-art blade construction.

The inner segment of the blade mass is given by:

$$m_{\text{inner}}(R) = R^2 \sum_{\text{Inner Cmpts}} \rho_{\text{cmpt}} \Delta R_{\text{inner}} \left(\frac{c}{R}\right)_{\text{inner, 1.25}} c_{\text{inner, 1.25}} \left(\frac{t}{c}\right)_{\text{cmpt, 1.25}} \left(\frac{R}{1.25}\right)^{2n_{\text{seg}}+e_{\text{cmpt, seg}}}, \quad (4.38)$$

The outer segment of the blade mass, which essentially skin, is given by:

$$m_{\text{outer}}(R) = R^2 \rho_{\text{skin}} \Delta R_{\text{outer}} \left(\frac{c}{R}\right)_{\text{outer, 1.25}} c_{\text{outer, 1.25}} \left(\frac{t}{c}\right)_{\text{cmpt, 1.25}} \left(\frac{R}{1.25}\right)^{2n_{\text{seg}}+e_{\text{cmpt, seg}}}, \quad (4.39)$$

This segmentation provides a structured approach to mass scaling, ensuring that individual materials are scaled appropriately based on their function and location within the blade structure. These results demonstrate that mass scaling in rotorcraft blades is influenced not only by geometric expansion but also by material efficiency optimisations, particularly for lightweight materials such as foam and composite skins.

4.4.2.4 Results of Blade Mass Estimation Models

The graph in Fig. 4.6 presents the variation in blade mass as a function of rotor blade radius for different mass estimation models. The 3D Mars Science Helicopter (MSH) Scale provides a segment-wise breakdown, distinguishing between the inner segment and outer segment (dotted lines), with the total mass summing both contributions. The D² scale and the MH Blade Area Scale offer alternative mass scaling approaches based on simpler geometric relationships. The 3D MSH Scale - Total follows an exponent greater than 2, reflecting the contributions of thickness scaling and material composition differences. The inner segment mass grows at a higher rate than the outer segment, emphasising the

increasing structural reinforcement requirements in the root region. The D² scale, which assumes mass proportional to the square of the rotor radius, underestimates the mass relative to the more detailed MSH scaling model. The MH Blade Area Scale falls even lower, as it considers only planform area without thickness adjustments.

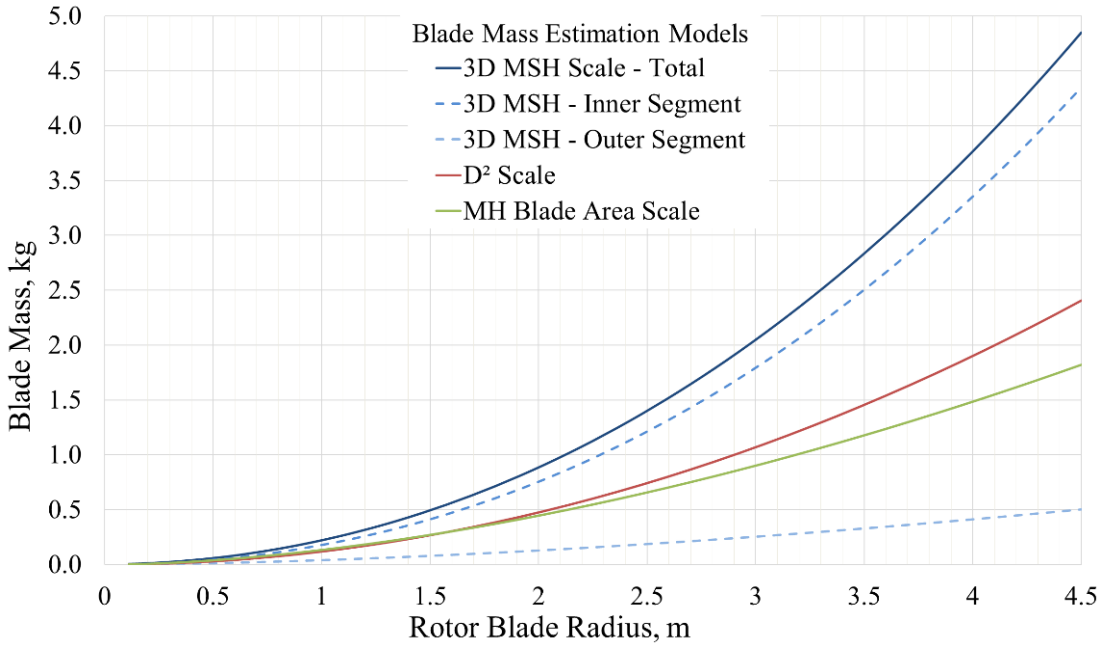


Fig. 4.6 Blade Mass vs. Rotor Blade Radius – Comparison between scaling models for blade mass estimation

The close-up view of the Blade Mass vs. Rotor Blade Radius graph in Fig. 4.7 focuses on the range 0.25 m to 2.25 m, providing a detailed comparison between various blade mass estimation models and empirical rotor blade data points. The plotted data includes the MarBird-VII rotor (radius 0.45 m, mass 0.024 kg), Ingenuity MH (0.61 m, 0.043 kg), Hexa MSH (0.64 m, 0.079 kg), and Coaxial MSH (1.25 m, 0.341 kg). The D² scale, derived from the MarBird-VII study, closely follows the empirical mass trends of MarBird-VII and Ingenuity MH, suggesting that these rotor blades adhere to a simpler quadratic scaling law. The MH Blade Area Scale, based on a 110% scaled initial estimate of MSH, also provides reasonable agreement with smaller rotor sizes but begins to deviate at larger scales. In contrast, the 3D MSH scaling models, which are developed based on the optimized blade designs of Hexa MSH and Coaxial MSH, provide a more

accurate prediction for larger rotor sizes. The Hexa MSH (0.64 m) and Coaxial MSH (1.25 m) data points align closely with the 3D MSH inner and outer segment models, highlighting the importance of incorporating structural reinforcement, material distribution, and optimised blade geometry into mass prediction at increasing scales. This comparison underscores the limitations of purely geometric scaling approaches and demonstrates how 3D MSH scaling more accurately accounts for structural and aerodynamic optimisation effects in rotor blade design.

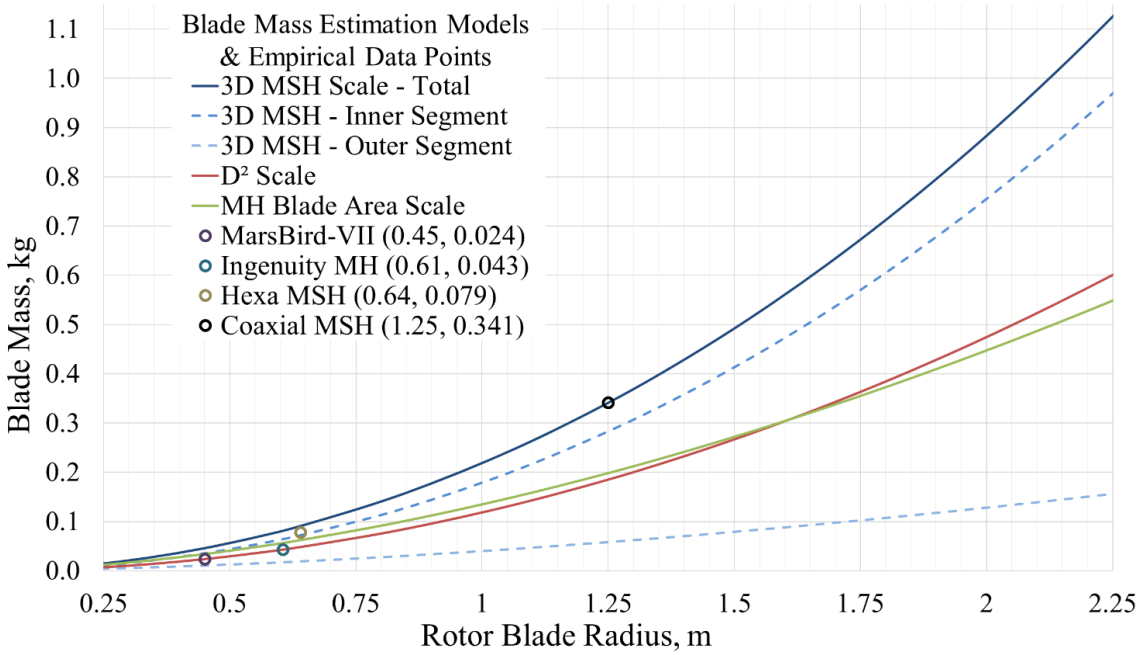


Fig. 4.7 Close-up view of the graph plot - Blade Mass vs. Rotor Blade Radius (Rotor Radius Limits – 0.25 m to 2.25 m). Showing comparison of scaling models for blade mass estimation and empirical rotor blades data points, including the Ingenuity MH rotor (radius 0.61 m, mass 0.043 kg).

Fig. 4.8 illustrates the variation in blade mass composition as a function of rotor blade radius, highlighting the contribution of individual components to the total blade mass; such as spar, root insert, skin, and foam. The 3D MSH Scale - Total increases as expected with rotor size, driven by the combined contributions of individual components. Among these, the spar exhibits the most significant mass increase, reflecting the need for greater structural reinforcement in larger rotors, while the foam and skin contribute more gradually.

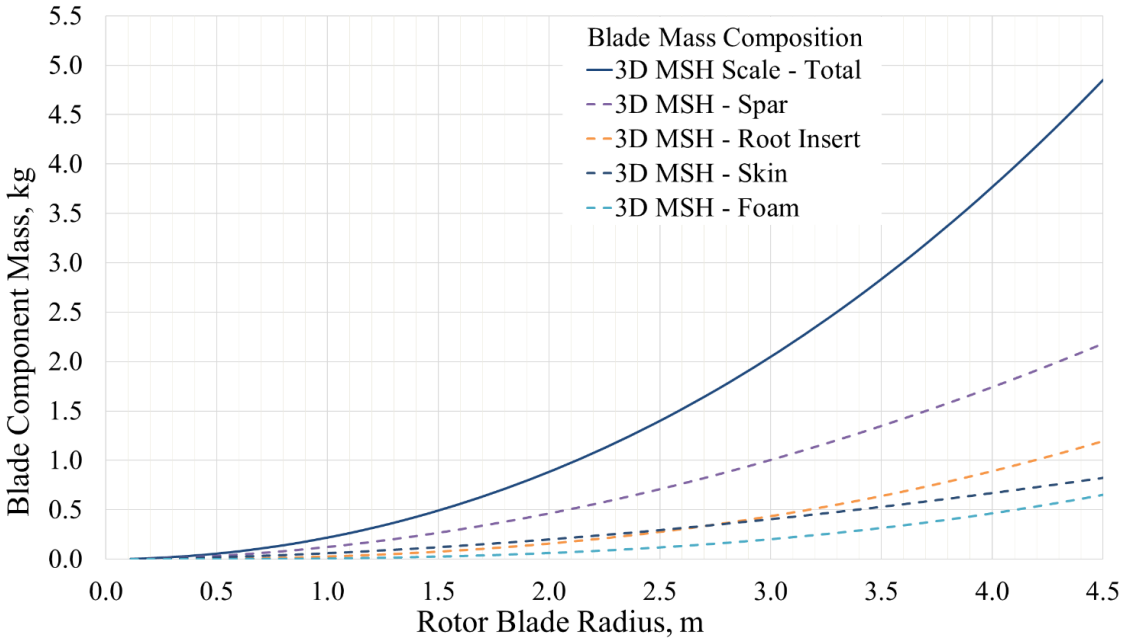


Fig. 4.8 Blade mass composition as a function of rotor blade radius, illustrating the contributions of individual components (spar, root insert, skin, and foam) to total blade mass using 3D MSH blade mass scale.

4.4.2.5 Effects of Rotor with Multiple Blades on its Mass and Solidity

The graph in Fig. 4.9 presents rotor mass estimations based on the 3D MSH Scale Model for varying rotor blade configurations, ranging from two-bladed to five-bladed rotors. As expected, rotor mass increases with blade radius and the number of blades, with the five-bladed rotor exhibiting the highest mass growth. The relationship follows a non-linear trend, reflecting the combined effects of increasing blade volume, material distribution, and thickness scaling. The two-bladed rotor has the lowest mass growth rate, as fewer blades result in reduced structural reinforcement requirements. Conversely, the five-bladed rotor grows significantly faster, indicating that higher blade counts contribute substantially to overall rotor mass. This trend underscores the importance of balancing blade count and structural efficiency in rotorcraft design, particularly for Mars rotorcraft applications, where minimizing mass is critical for mission feasibility.

The number of blades directly affects rotor solidity, defined as the ratio of total blade area to the disk area. Higher blade counts lead to increased solidity, which enhances lift generation and aerodynamic performance, particularly in low-

density Martian atmospheres where higher disk loading is required. However, this comes with a trade-off: higher rotor mass, as seen in the steeper curves for four- and five-bladed rotors. From a design perspective, selecting the optimal number of blades involves a balance between, aerodynamic efficiency, structural mass, and power and efficiency trade-offs. More blades improve thrust and reduce the per-blade loading, mitigating stall effects. However, additional blades significantly increase mass, impacting vehicle payload capacity and energy efficiency. While higher solidity improves lift, increased drag and inertia require greater power input, impacting endurance and operational feasibility. For Mars rotorcraft, minimising weight is crucial for energy efficiency and flight feasibility. While a higher blade count improves aerodynamic performance in thin atmospheres, the added structural mass must be carefully managed to maintain an efficient thrust-to-weight ratio. This trade-off is evident in the graph, where increasing the number of blades significantly increases total rotor mass, potentially affecting overall system performance.

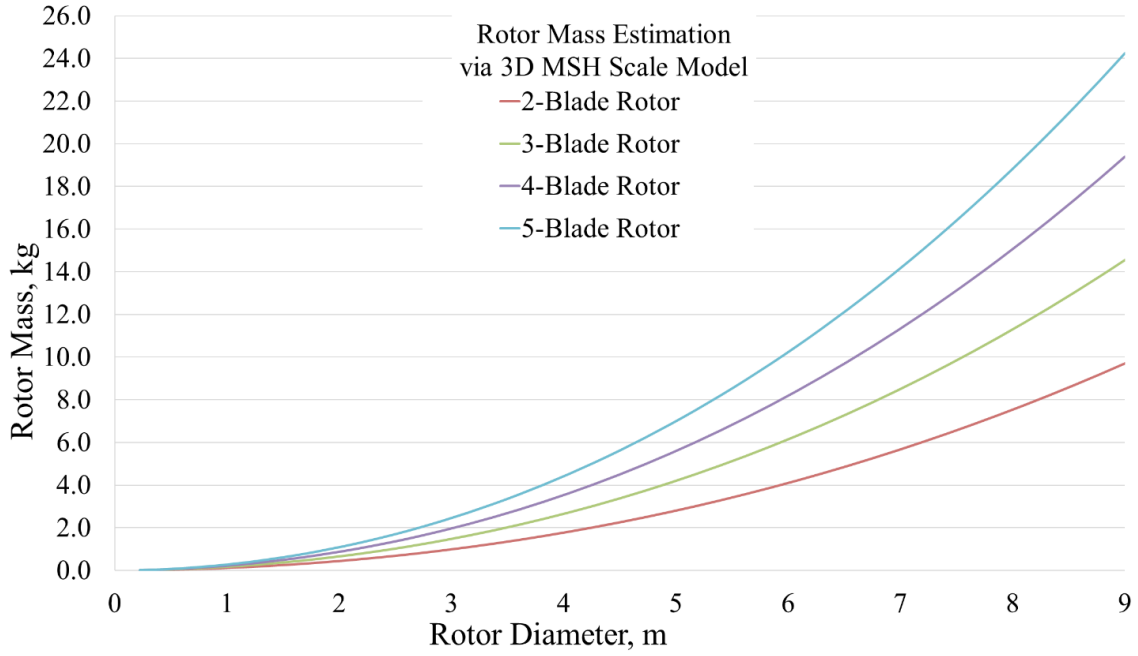


Fig. 4.9 Rotor Mass vs Rotor Diameter - Comparison between rotors with varying number of blades (2 to 5)

4.4.2.6 Adaptability and Limitations of 3D MSH Blade Mass Scaling Model

The 3D MSH Scale model offers a flexible approach for estimating rotor blade mass across varying rotor sizes by incorporating material distribution, thickness-to-chord scaling, and structural reinforcement trends. A key strength of this model lies in its adaptability, allowing modifications to material density, blade planform, and segment definitions to accommodate different rotorcraft designs. By adjusting input parameters such as material densities (e.g., alternative composites or metallic reinforcements), the model can predict mass variations due to different structural configurations. Similarly, modifications to the planform shape, such as varying taper ratios or different chord distributions, enable the model to account for design optimisations adapted to specific aerodynamic and structural requirements. Mathematically, the model can be generalised to different rotor types through segment-wise integration, where each material component is assigned a specific density and thickness function.

Despite its adaptability, the model has inherent limitations. The mass scaling is primarily based on two reference rotor sizes (Hexa MSH at 0.64 m and Coaxial MSH at 1.25 m), restricting accuracy for significantly different rotor sizes. Moreover, the assumption that blade flap frequency remains constant across scales ensures stability but does not fully capture the increasing stiffness demands for larger rotors. In reality, maintaining a fixed flap frequency at larger scales necessitates additional structural reinforcement, which could result in an even greater mass increase than predicted by the current model. To enhance accuracy, future refinements should include expanded empirical datasets for validation at different rotor sizes, higher-order stiffness adjustments to account for nonlinear mass growth, and better representation of material and manufacturing variations. Further refinements could also introduce adaptive scaling factors that integrate rotor solidity scaling and blade count effects while using computational validation through finite element analysis for structural verification.

4.5 Definition of Rotorcraft Configurations

4.5.1 Tandem Rotorcraft Cases

The arrangement of tandem rotorcraft can vary depending on how the rotors are longitudinally positioned on top of the fuselage. The same fuselage is used for all the configurations for consistency during parametric analysis. Considering the structural constraints of the aeroshell, three scenarios are examined for the analysis of power consumption (also specified in Chapter 3 and [28]). In these scenarios, the two equal-sized rotors are placed at equidistant points from the midpoint, resulting in displacements of 2.25 m, 1.125 m, and 0.75 m for Cases 1, 2, and 3, respectively. This assumes that the fuselage length matches the maximum size of the aeroshell, which is 4.5 m. Fig. 4.10 illustrates these rotor positions on the aerobot fuselage within an aeroshell dome. These configurations represent extreme scenarios for parametric analysis (Fig. 4.11): Case 1 positions foldable rotors at the fuselage ends, allowing for a maximum diameter of 9 m; Case 3 situates the rotors to fit within the aeroshell boundary, with a maximum diameter of 3 m; and Case 2 falls in between, enabling rotors with a maximum diameter of 4.5 m. It is important to note that, in practical applications, rotor blades must be spaced from the inner walls of the aeroshell and rotor hubs. However, this theoretical study does not consider such clearances.

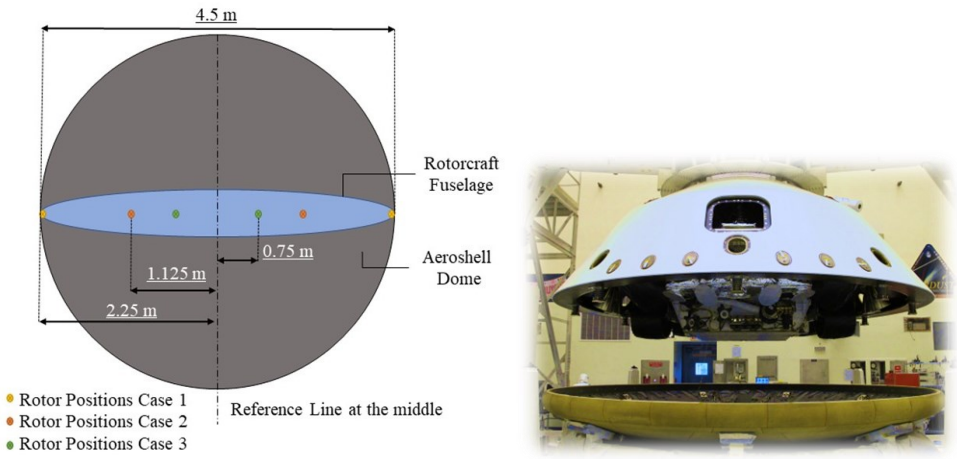


Fig. 4.10 Schema of the positioning of rotor hubs of tandem rotorcraft Cases 1, 2, and 3, on the fuselage placed inside an aeroshell [28]. (Not to scale). On the right is the aeroshell of NASA's Mars Science Laboratory mission, which was sent to Mars in 2011. Image Credit: NASA/JPL-Caltech

In Case 1, a folding mechanism, potentially with an articulated rotor hub system, is needed to fit within the aeroshell for stowage if the rotor diameter exceeds 2.25 m. Similarly, Case 2 would require identical folding mechanisms and possibly an articulated rotor hub system if the rotor diameter surpasses 2.25 m. In contrast, Case 3 permits the use of a rigid rotor hub system without the need for linkages. An outline of the defined parameters for each of the three tandem rotorcraft is provided in Table 4.6, along with quadcopter and hexacopter study cases (discussed in the subsequent sections).

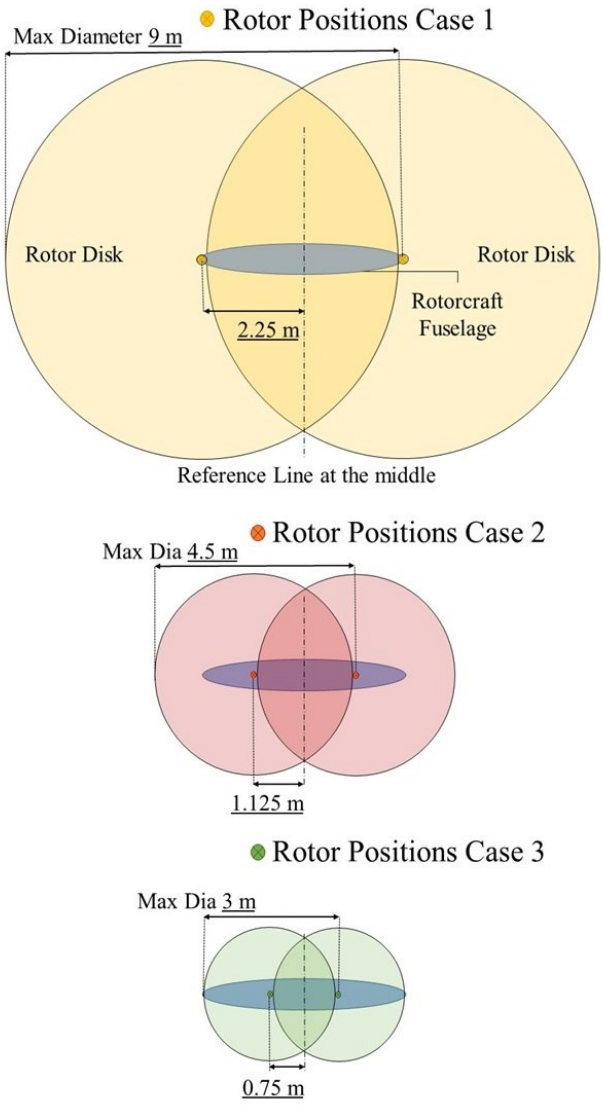


Fig. 4.11 Diagrammatic illustration of the rotor positioning of tandem rotorcraft Cases 1, 2, and 3 in operational mode [28]. (Not to scale)

4.5.2 Quadcopter and Hexacopter Cases

Both quadcopter and hexacopter configurations can vary based on the longitudinal placement of the rotor hub support frames atop the fuselage, similar to the cases mentioned earlier with tandem rotorcraft configurations. However, in this study, only configurations with non-overlapping rotors are considered, as this is typical of such multicopters.

For quadcopter configurations, parametric analysis is conducted with two non-overlapping, equal-sized rotors positioned at distances of 2.25 m and 1.125 m from the midpoint on each side, corresponding to Case 1 and Case 2, respectively. Case 1 requires a folding mechanism, both for rotor blades and support frames, for stowage inside the aeroshell, whereas Case 2 (first detailed in [12]) does not. Fig. 4.12 visually depicts the defined parameters for these quadcopter cases. Similarly, hexacopter configurations are established for parametric analysis, with six non-overlapping, equal-sized rotors positioned at radial distances of 2.25 m and 1.5 m from the center, spaced 60° apart, corresponding to Case 1 and Case 2, respectively. Like the quadcopter, Case 1 hexacopter requires a folding mechanism for stowage inside the aeroshell, whereas Case 2 (first detailed in [12]) does not. Fig. 4.13 schematically shows the defined parameters for these hexacopter cases.

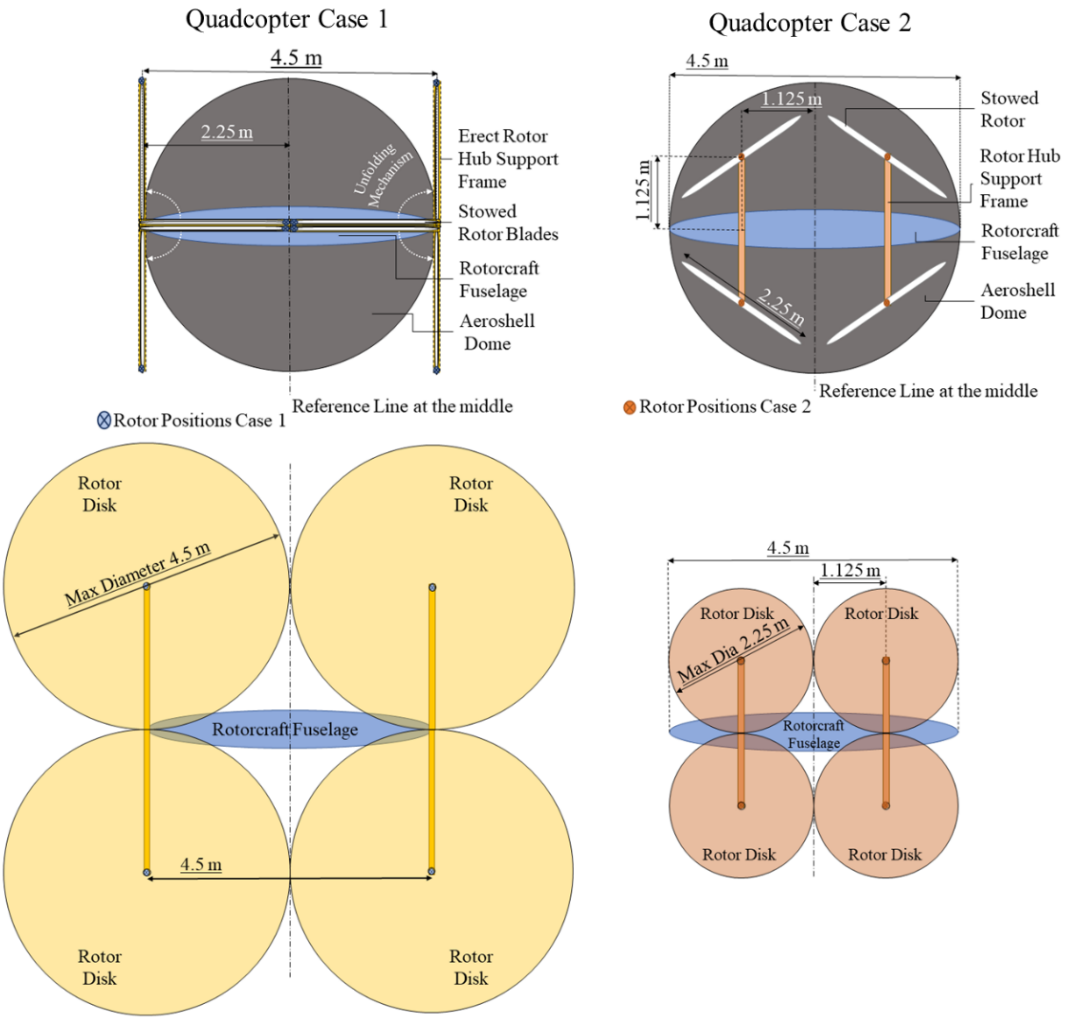


Fig. 4.12 Diagram (not to scale) of the rotor hub positioning of quadrotor configuration with nonoverlapping equal-sized rotors. Top: stowed inside aeroshell. Bottom: operational mode

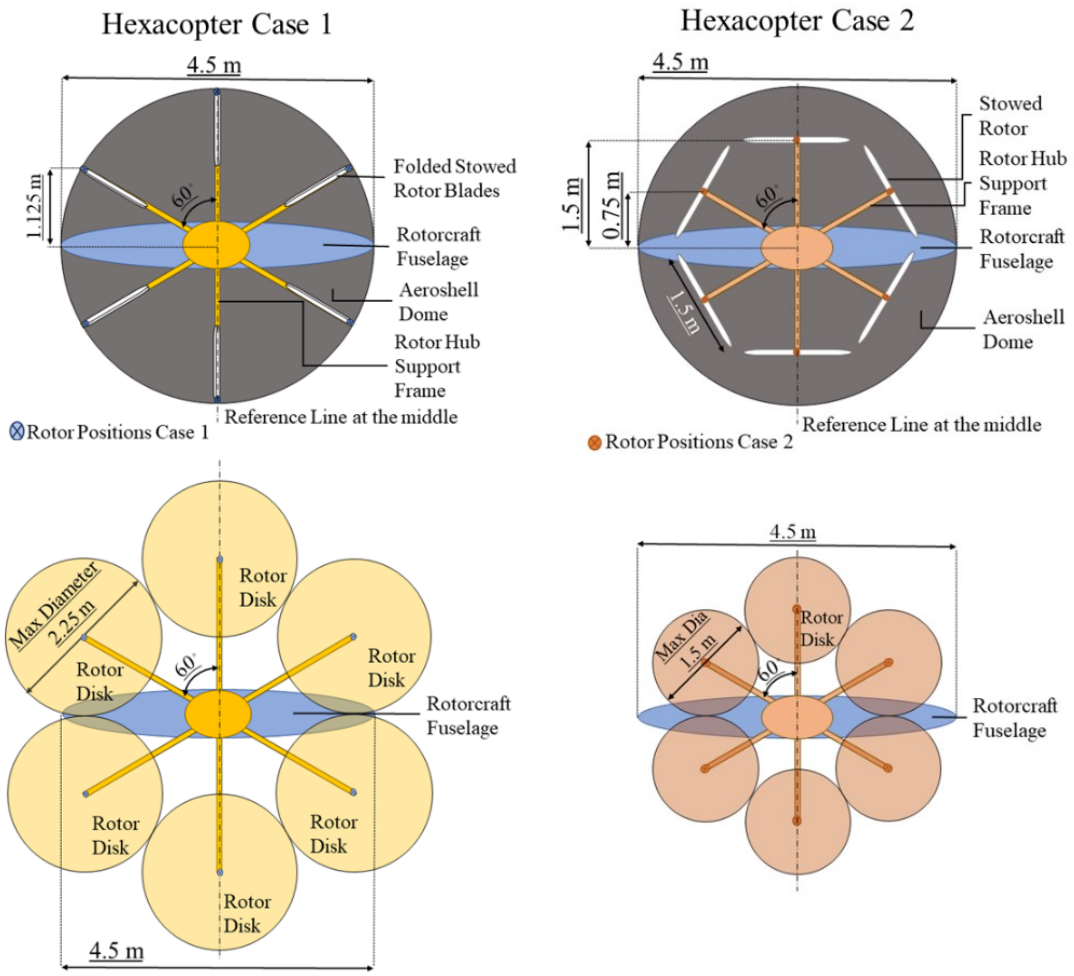


Fig. 4.13 Schematic illustration (not to scale) of the rotor hub positioning of hexarotor configuration with nonoverlapping equal-sized rotors. Top: stowed inside aeroshell. Bottom: operational mode

The established quadcopter and hexacopter configurations ensure a maximum allowable rotor diameter without overlap during operation or stowage inside the aeroshell dome. For quadrotor cases 1 and 2, the rotor diameter is limited to 4.5 m and 2.25 m to prevent overlapping, respectively. For hexacopter cases 1 and 2, the rotor diameter is limited to 2.25 m and 1.5 m to avoid overlapping, respectively. Similar to tandem rotors Case 3, quadrotor and hexacopter configurations can utilise a rigid or semi-rigid rotor hub system. Detailed information is summarised is provided in Table 4.6.

Table 4.6 Configuration Summary of Tandem, Quad & Hexa Rotorcraft Cases

Case No.	Rotor System Type	Folding Mechanism	Maximum Diameter	Rotor Position	Isolated Rotor behaviour
Tandem 1	Articulated	Yes	9 m	2.25 m*	D ≤ 4.5 m
Tandem 2	Articulated∴	Yes∴	4.5 m	1.125 m*	D ≤ 2.25 m
Tandem 3	Rigid	No	3 m	0.75 m*	D ≤ 1.5 m
Quad 1	Rigid	Yes	4.5	2.25 m†	D ≤ 4.5 m
Quad 2	Rigid	No	2.25	1.125 m†	D ≤ 2.25 m
Hexa 1	Rigid	Yes	2.25	2.25 m‡	D ≤ 2.25 m
Hexa 2	Rigid	No	1.5	1.5 m‡	D ≤ 1.5 m

* Rotor hub position atop fuselage from its center in longitudinal direction

∴ When rotor D is > 2.25 m

† Rotor hub position atop fuselage equidistant from its center

‡ Radial position atop fuselage from its centre

4.6 Definition of Parameters for Performance Analysis

During rotorcraft flight, the encountered air density is a crucial factor for initial power sizing considerations. Mars' average surface air density is approximately 0.02 kg/m³ [29], although it varies based on location, altitude relative to sea level, and changes with seasons and time of day. For the primary mission in SW Melas Chasma, approximately 2 km below the datum, the Mars Climate Database (Version 6.1) [30] is utilised to estimate regional air density values during a flight time corresponding to the 11th hour of local solar time [31]. This investigation, as detailed in Chapter 3, yielded a mean air density estimate of 0.016 kg/m³. The maximum allowable size of the aerobot is limited by the diameter and height of the protective aeroshell, set at 4.5 m and approximately 2.2 m, respectively, constraining the design and evaluation of Martian aerobot configurations. The rotor disk size range considered for the parametric performance study of design configurations spans from 5% to 100% (i.e., 0.23m to 4.5m) of the aeroshell diameter, apart from tandem rotorcraft case 1 which goes up to 9m diameter.

On Mars, operational restrictions are imposed on rotor tip speed and forward velocity to prevent the formation of transonic compression waves, given the sound speed of approximately 240 m/s [3]. Typically, the rotor advancing blade tip speed is limited to about 0.75 Mach (180 m/s), ensuring adequate lift sustenance on the retreating blade during forward flight, requiring the advancing blade's speed to be nearly three times that of a helicopter [14]. Consequently, a

maximum forward speed of 60 m/s is advised, equivalent to one-third of the maximum rotor tip speed and one-quarter of Mars' average sound speed. Rotorcraft sizing is based on range, cruising speed, takeoff, and ascent, and assumes continuous high-power operation. Descent and landing phases are omitted for simplicity [14]. The flight profile in this study (depicted in Fig. 4.14) entails a 2-minute ascent to 1 km (at an average vertical climb velocity of 8.33 m/s), followed by a 3-minute traverse of 10 km (with an average cruising velocity of 55.56 m/s), culminating in vertical descent. These values are derived from the mission specifications and expected aerobot performance constraints discussed in Chapter 3 Section 3.3, which consider power availability, achievable flight speeds, and energy efficiency. This theoretical method's outcomes align well with experimental data when the aircraft's advance ratio ranges from 0.1 to 0.3 [15]. The advance ratio of a rotorcraft denotes the ratio of its forward flight speed to its rotor tip speed.

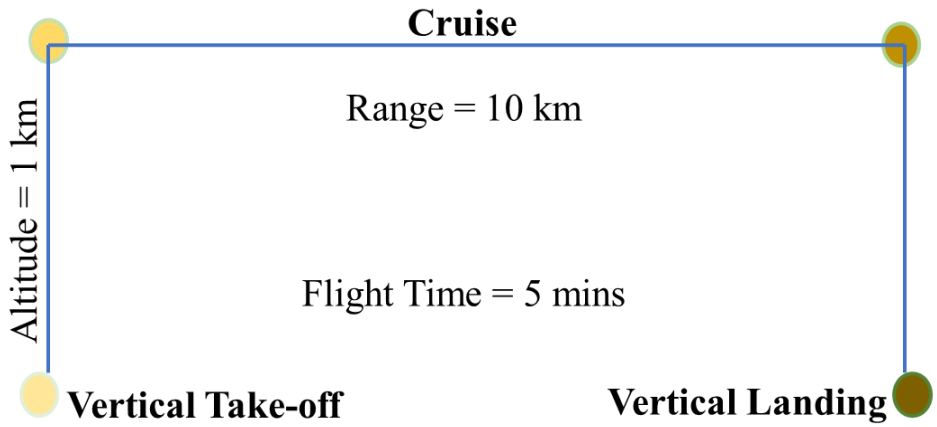


Fig. 4.14 Flight profile for the performance analysis

Table 2 summarises the parameters discussed in this subsection that are utilised in the power analysis for various rotorcraft configurations during forward flight, vertical climb, and hover phases. For the mission, the aerobot's Maximum Take-Off Gross (MTOG) mass is fixed at 20 kg. An average value of 0.6 for the figure of merit, *M*, is used, considering its typical range from 0.6 to 0.8 [14]. Additionally, based on a JPL technological projection, the battery's specific energy (E_{sb}), which is utilised to calculate the Battery Mass Fraction (*BMF*) for flights, is anticipated to be 230 Wh/kg [4].

Table 4.7 Parameters utilised in analysing power requirements for forward flight, vertical climb, and hover across various rotorcraft configurations.

Parameter	Values			Unit
Mars Mean Air Density at SW Melas Basin	0.016			kg/m^3
Speed of Sound	240			m/s
Surface Gravity Acceleration on Mars	3.73			m/s^2
Aircraft MTOG Mass	20			kg
Aircraft MTOG Weight, W	74.60			N
Allowable Max Rotor Advancing Tip Mach Number, M_{at}	0.75			Mach
Air Speed at Max M_{at} on Mars	180			m/s
Traverse Range as per Flight Mission	10			km
Cruise Flight Endurance, E	3.0			min
Cruise Flight Velocity, V	55.56			m/s
Dynamic Pressure at the Cruise Velocity, q	24.69			Pa
Flight Altitude as per Flight Mission	1			km
Vertical Climb Endurance, E	2.00			min
Average Vertical Climb Velocity, V_{climb}	8.33			m/s
Rotor Blade Diameter, Blade D	0.23	to	9.0	m
Rotor Disk Area, S	0.04	to	63.6	m^2
Battery Specific Energy, E_{sb}	230.00			Wh/kg
Figure of Merit, M	0.6			
Mechanical efficiency factor, $\eta_{mechanical}$	0.97			
Fuselage downwash adjustment, f	1.06			
Helicopter Power ratio ($P_{tail\ rotor}/P_{rotor}$)	0.18			
Coaxial Power ratio ($P_{second\ rotor}/P_{main\ rotor}$)	1			
System efficiency battery to motor (η_{b2s})	0.9			
Propeller Efficicency, η_p	0.8			
Oswald Efficiency, e	0.5			
Parasitic Drag Area, D/q (Front Area x Drag data)	**Front Area**	**Drag Data**	**D/q**	
D/q Fuselage (radius 0.15 m)	7.1E-02	0.09	6.0E-03	m^2
D/q Tubular Landing 4 legs (0.002m x 0.03m, each)	2.4E-04	1.01	2.4E-04	m^2
D/q Unfaired Single Rotor Hub (0.005m x 0.003m)	1.5E-05	1.20	1.8E-05	m^2
Downwash Interference Drag Fuselage	7.1E-02	0.02	1.4E-03	m^2
Leakage & Protuberance Drag (15% Total D/q)			1.2E-03	m^2

There are a few other parameters that are essential for forward flight analysis, including the frontal area of the aircraft body. The fuselage's frontal size, landing legs, and unfaired rotor hub remain consistent across all variants. Helicopter-specific drag statistics published by D. Raymer [14] provide the drag area (D/q) per unit frontal area, which can be multiplied by the helicopter's frontal area to derive specific values for each component's drag area. The calculated total parasitic drag is then integrated into the conventional helicopter's Eq. (4.2) and, correspondingly, into the forward flight equations for other types of rotorcraft. While drag data may not precisely determine parasitic drag, it serves adequately

for the initial sizing of rotorcraft until the design progresses sufficiently for further exploratory research.

4.7 Results and Analysis

4.7.1 Hover and Vertical Climb Analysis

In Fig. 4.15, the power required for a conventional Martian helicopter is plotted against the rotor disk diameter. As the rotor diameter increases, so does the rotor disk area, leading to a decrease in disk loading (*W/S*, total weight divided by disk area). Lower disk loading implies less battery power is needed for hovering or ascending, allowing for a higher power loading (*W/P*) - which represents the ratio of the helicopter's weight to its engine power. However, it is crucial to acknowledge that reduced disk loading results in larger rotor blades, contributing to increased weight, higher drag during forward flight, and a higher risk of encountering shocks on the advancing blade [14], aspects not covered in this study.

The graph indicates that smaller rotors consume significantly more power than larger ones, with power decreasing noticeably and dramatically as rotor disk diameter increases (also discussed in Chapter 3 and [13]). Additionally, as the aerobot's total mass increases, the power required for smaller rotor disks rises sharply, while the increase in power demand for larger rotor disk diameters is minimal. This disparity is evident in the 40 kg versus 20 kg Helicopter graph shown in Fig. 4.15. It is apparent from the power requirements that the helicopter requires slightly more power for vertical ascent than for hovering, which is expected due to the energy needed for vertical forward propulsion. However, over time, the difference between the two power requirements becomes more pronounced as the rotor disk size increases.

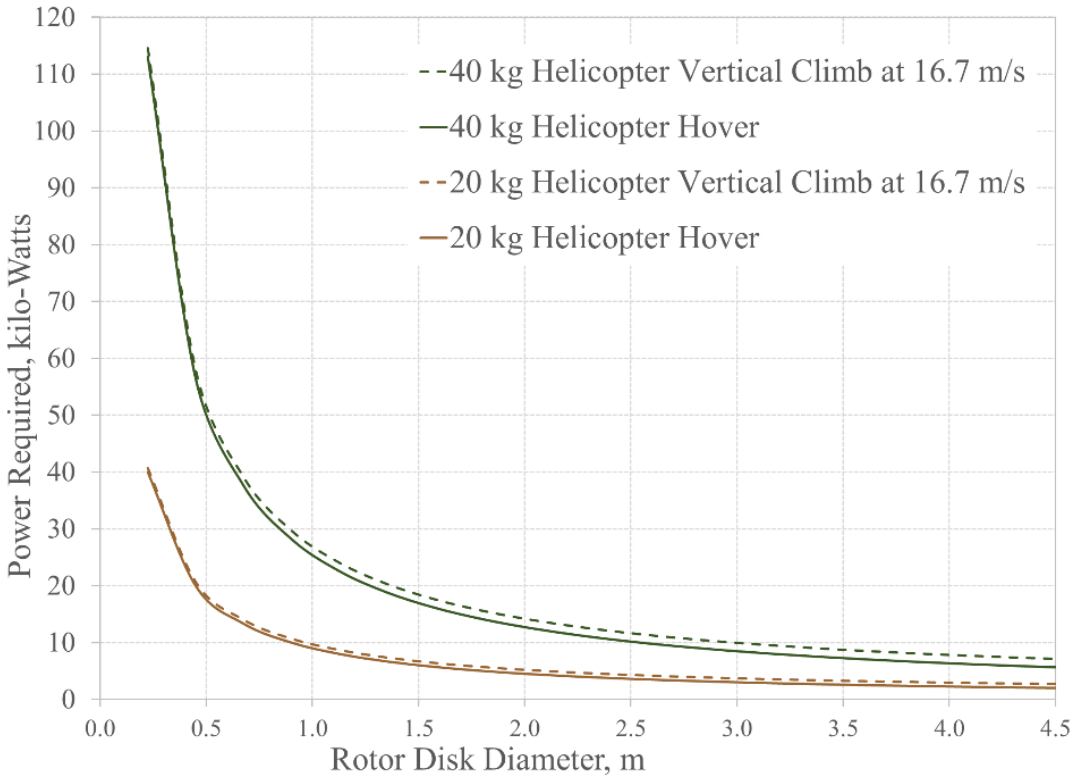


Fig. 4.15 Power Required (Hover & Vertical Climb) vs Rotor Disk Diameter - 20 kg & 40 kg Martian Conventional Helicopters

The graph plots in Fig. 4.16 and Fig. 4.17 illustrate the hover power and vertical climb power (at a velocity of 8.33 m/s) respectively, across various rotorcraft designs relative to the rotor disk diameter. These configurations encompass the conventional helicopter, LS (large separation) coaxial rotorcraft, rotorcraft with two isolated rotors, three tandem rotorcraft cases, two quadcopter and two hexacopter cases. While the inclusion of power data for two isolated rotors is primarily for analytical comparison with tandem rotor Case 1, it serves to highlight significant trends. Corresponding to the pattern observed in the helicopter power requirements graph, all configurations exhibit higher power demands for vertical climbing compared to hovering, with this disparity increasing as the rotor disk diameter grows. Among these, the conventional helicopter stands out for consuming the most power.

In contrast, the power consumption of two equal-sized coaxial rotors is notably lower, especially with smaller rotor sizes. For instance, at a rotor size of 0.23 m in diameter, the coaxial rotorcraft consumes roughly 9000 Watts less power, while

tandem rotorcraft configurations require about 16,000 Watts less power than the conventional helicopter for both hovering and vertical climbing. Similarly, the quadrotor requires approximately 23,000 Watts less power, whereas hexacopter require around 26000 Watts lesser power. At the maximum aeroshell size (corresponding to a rotor diameter of 4.5 m), hover and vertical climb power requirements remain below 2,500 Watts for all configurations.

Interestingly, across all three tandem rotorcraft scenarios, the power consumption of the tandem rotorcraft system aligns with that of the two isolated rotors before any overlap occurs between them. Furthermore, the power requirements for all variants decrease inversely and stabilize as the rotor diameter increases. As seen in tandem rotorcraft Case 1, this difference becomes negligible for rotor disk sizes between 4.5 and 9 m. Noteworthy is the significantly lower power consumption of quadcopter and hexacopter compared to all other rotorcraft types, particularly when installing smaller rotor diameters.

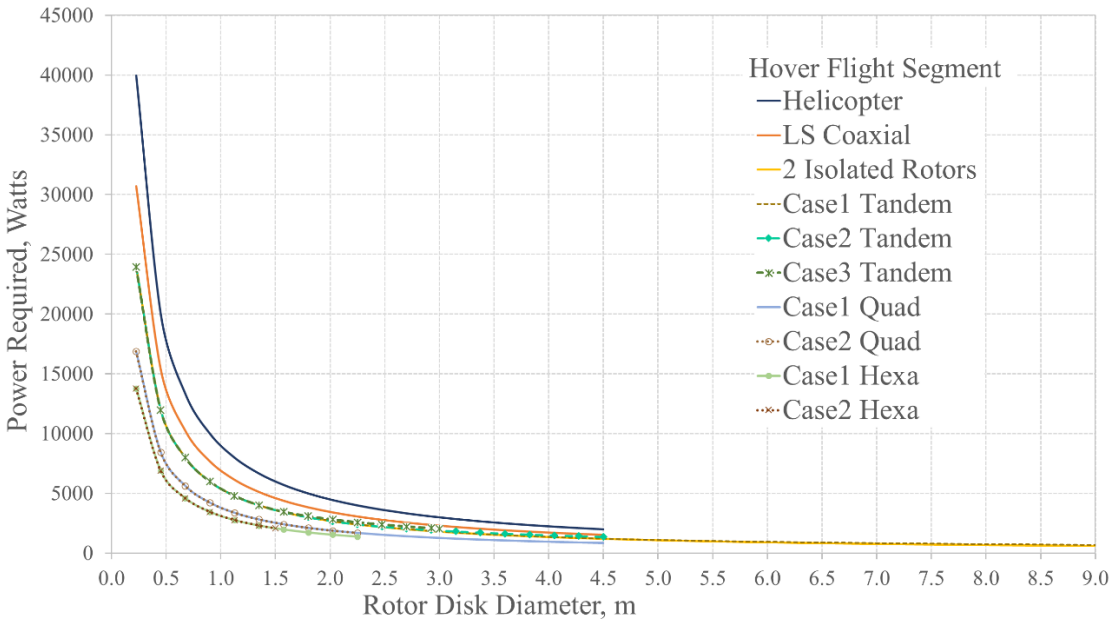


Fig. 4.16. Hover Power Required vs Rotor Disk Diameter – Comparison between various 20 kg rotorcraft configurations (Helicopter, Coaxial, 2 Isolated Rotors, and Cases of Tandem, Quadcopter, Hexacopter)

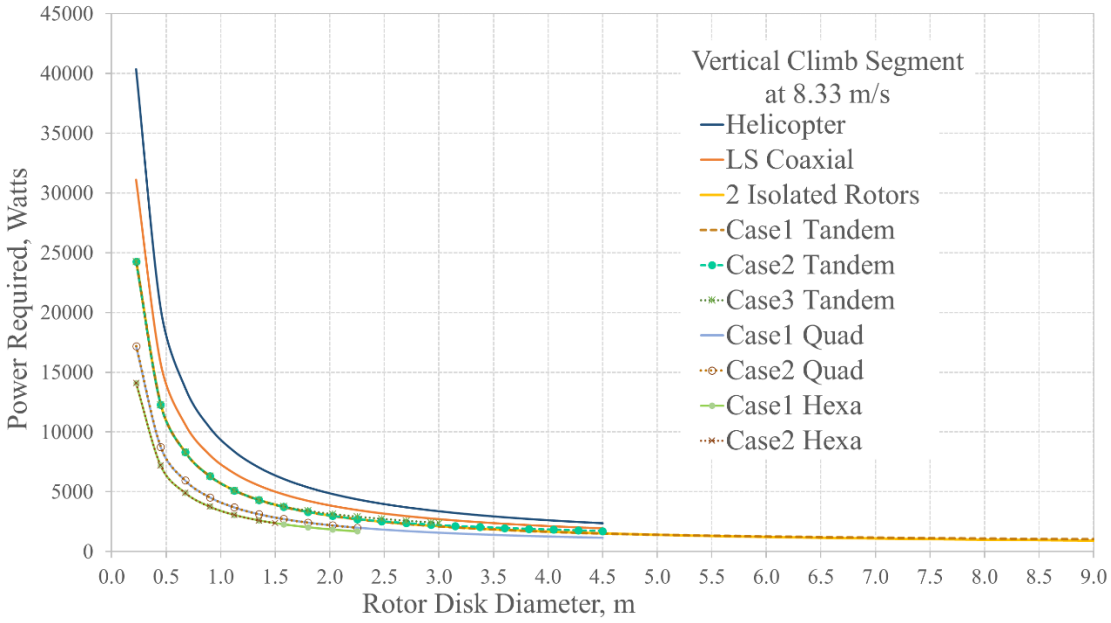


Fig. 4.17. Vertical Climb Power Required (at 8.33 m/s) vs Rotor Disk Diameter – Comparison between various 20 kg rotorcraft configurations (Helicopter, Coaxial, 2 Isolated Rotors, and Cases of Tandem, Quadcopter, Hexacopter)

4.7.2 Forward Flight Analysis

The power required for forward-level flight and forward climb flight at a 20-degree climb path angle is analysed for each of the specified rotorcraft configurations, considering a forward flying speed of 55.56 m/s. Fig. 4.18 illustrates the power required for a Martian conventional helicopter to fly forward as its rotor disk size increases.

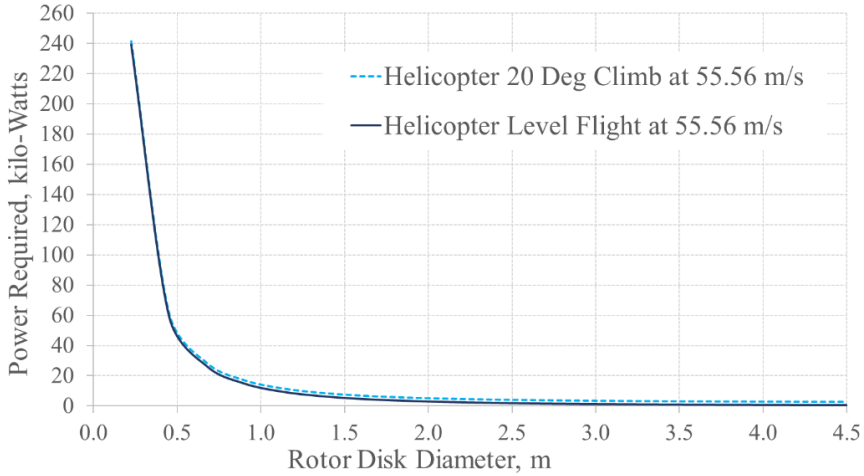


Fig. 4.18. Forward Flight Power Required (at 55.56 m/s) vs Rotor Disk Diameter - 20 kg Martian Conventional Helicopter

The graph depicts how ascending during forward flight requires more power compared to level flight. However, for smaller rotor disk diameters, the power consumption for both flight modes remains similar, with the disparity between the two requirements becoming noticeable only at rotor disk diameters exceeding 0.5 m approximately. As the rotor disk size increases, the reduction in power requirements for forward climb flight is less as compared to the level flight.

Fig. 4.19 provides an overview of the power demands for forward-level flight across all selected rotorcraft types, considering rotor disk diameters up to 9 m. Notably, at the smallest rotor disk size, conventional helicopters exhibit the highest and most excessive power requirement, followed by coaxial rotorcraft, two isolated rotors, tandem rotorcraft cases, quadcopter cases and finally hexacopter configurations. However, with a modest increase in rotor disk size, the power demand decreases rapidly, reaching a point where the difference in power becomes negligible beyond a rotor size of 2 m forward.

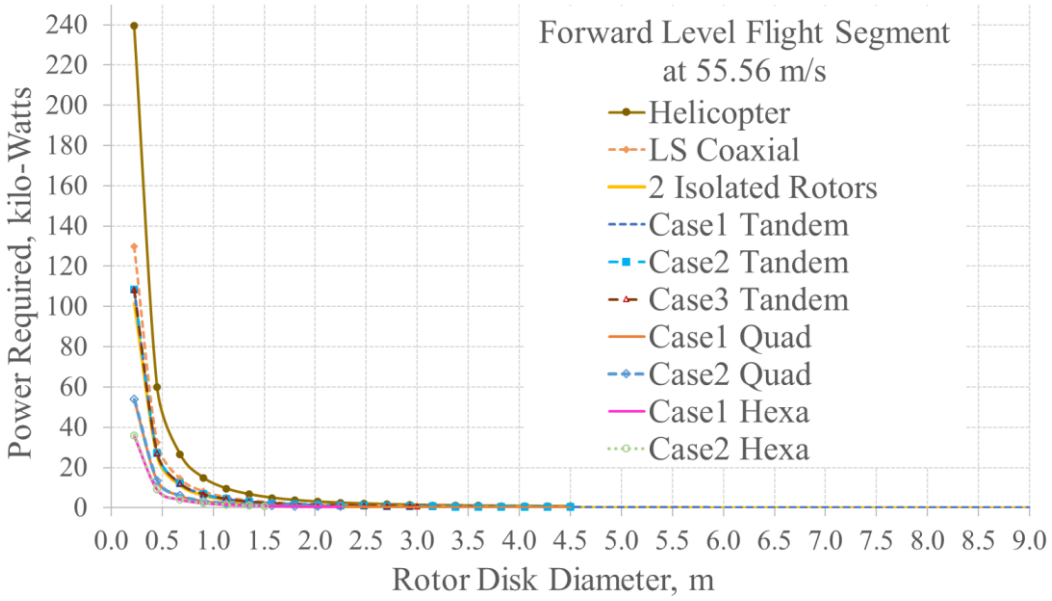


Fig. 4.19 Forward Level Flight Power Required (at 55.56 m/s) vs Rotor Disk Diameter (Area) - 20 kg Martian Various Rotorcraft Configurations

Fig. 4.20 zooms in on the power variations for forward level and climb flights across different rotorcraft configurations, with a rotor disk diameter starting from 1 m on the horizontal axis. A noteworthy observation is made in the forward climb of tandem rotorcraft Case 1, where power requirements start to increase after

reaching a minimum value across the rotor disk size range. This increase occurs when the tandem rotors overlap, apparent beyond a rotor diameter of 4.5 m for Case 1, due to the additional overlapping interference factor (K_{dw}) combined with the downwash factor (K_{dw}). Similarly, Case 2 of tandem rotorcraft exhibits a comparable pattern, albeit closer to the upper limit of the rotor diameter. Similar to what is observed in hover and vertical climb flight analysis, especially with smaller rotor diameters, quadcopters and hexacopters consume significantly less power than other types of rotorcrafts.

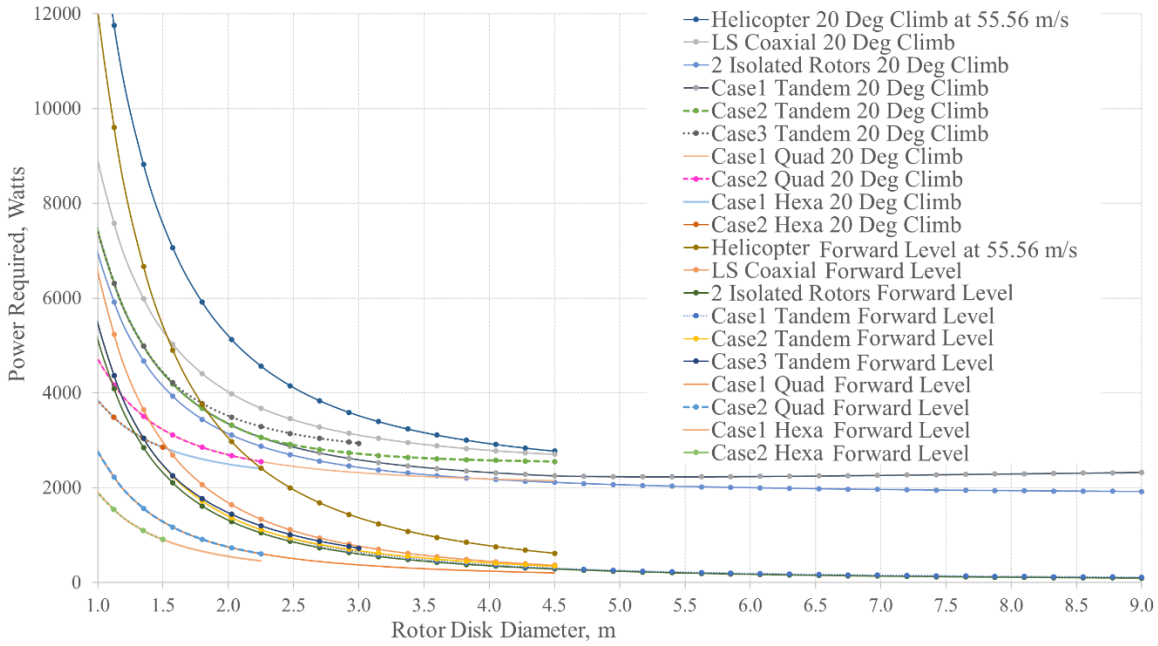


Fig. 4.20. Forward Flight Power Required (at 55.56 m/s) vs Rotor Disk Diameter (Rotor Diameter Limits – 1 m to 4.5m) – Comparison between various 20 kg rotorcraft configurations (Helicopter, Coaxial, Tandem Cases, 2 Isolated Rotors, Quadcopter, Hexacopter)

Climbing during forward flight necessitates more power than level flight, ascending while moving forward proves to be more energy efficient. Flying at a lower altitude reduces energy losses by creating an air cushion beneath the aircraft, known as ground effects, facilitating the attainment of optimal flying speed before ascent. To prevent the formation of air shocks at the rotor tip speed, this analysis is conducted at the maximum allowable forward flying speed. Experimenting with higher forward speeds could potentially reduce the required

power. Similarly, reducing the climb path angle would lead to a decrease in the power required for forward climb flight.

4.7.3 BMF Comparative Analysis of Rotor Configurations

The Battery Mass Fraction (BMF) is depicted in Fig. 4.21 by plotting the power required for vertical climb against the increasing rotor disk diameter for each designated rotorcraft configuration. In the calculation of BMF using Eq. (4.10), parameters such as a 2-minute run time (E), an 8.33 m/s climb speed, and a constant total mass of 20 kg are considered. The trend of the vertical climb BMF lines mirrors the dependency observed in Fig. 4.17, where increasing power demands result in higher BMF values, indicating the necessary battery weight for this flight segment. Similarly, Fig. 4.22 illustrates a comparable BMF trend for the forward-level flight segments, reflecting the power requirements of the forward-level flight shown in Fig. 4.19.

The battery mass can be obtained by multiplying the BMF by the overall mass of the aircraft. For instance, a BMF of 0.05 would yield a battery mass of 1 kg (0.05 x 20 kg). It is important to note that the BMF for each segment needs to be combined with the BMF of other flight segments, as discussed in the third section, to determine the total BMF and the overall battery mass required for a specific flight regime. Additionally, it should be remembered that the BMF calculated for the flying mission does not include the battery mass needed for avionics and electronic payload instrumentation, which would require separate computations unless they are powered by independent batteries.

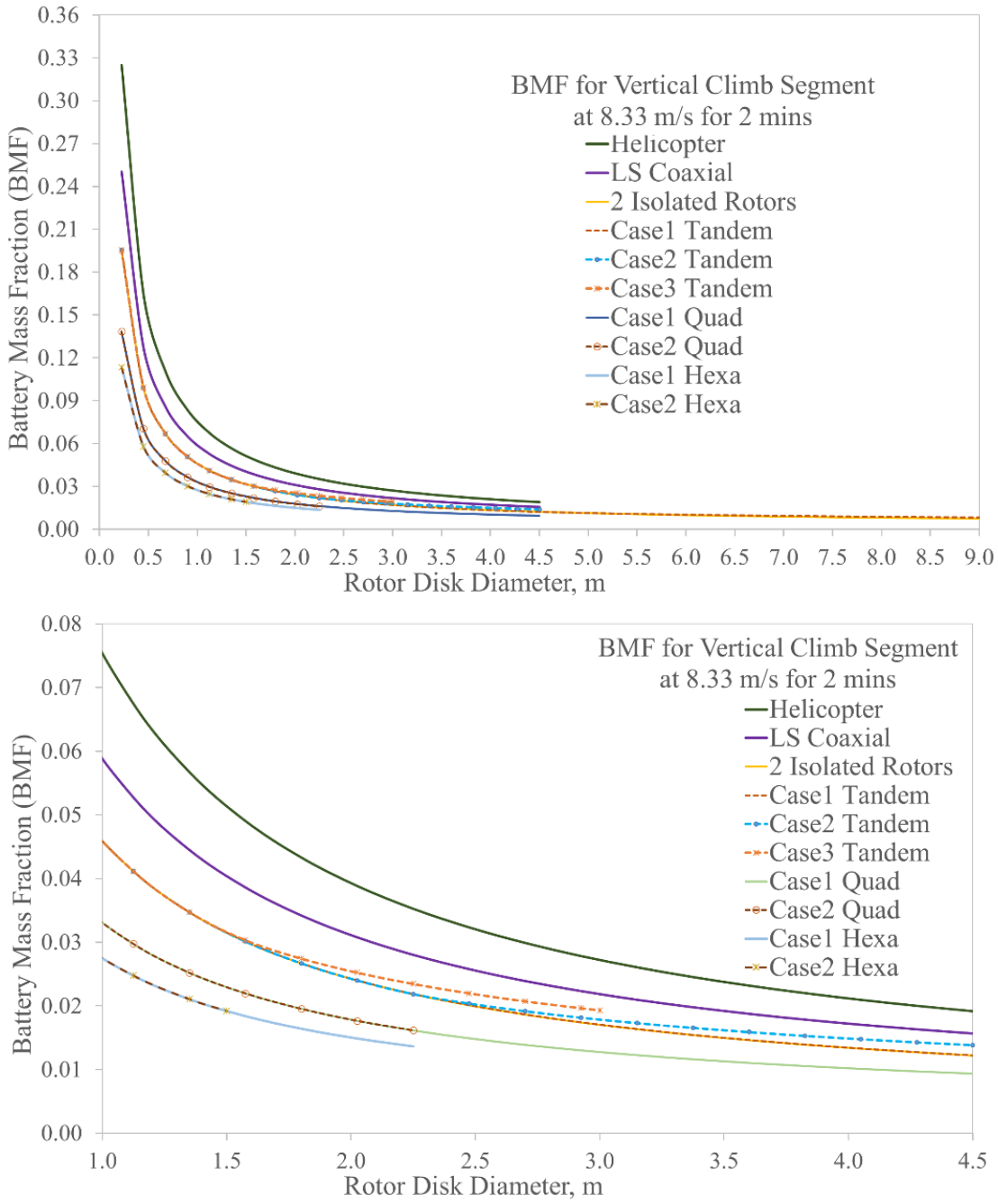


Fig. 4.21. Vertical Climb (at 8.33 m/s for 2 mins) BMF vs Rotor Disk Diameter - 20 kg Martian rotorcrafts. Top - BMF for rotor diameters from 0 to 9 m. Bottom – Close-up view, focusing on BMF for rotor diameters from 1 m to 4.5 m on the x-axis for clarity

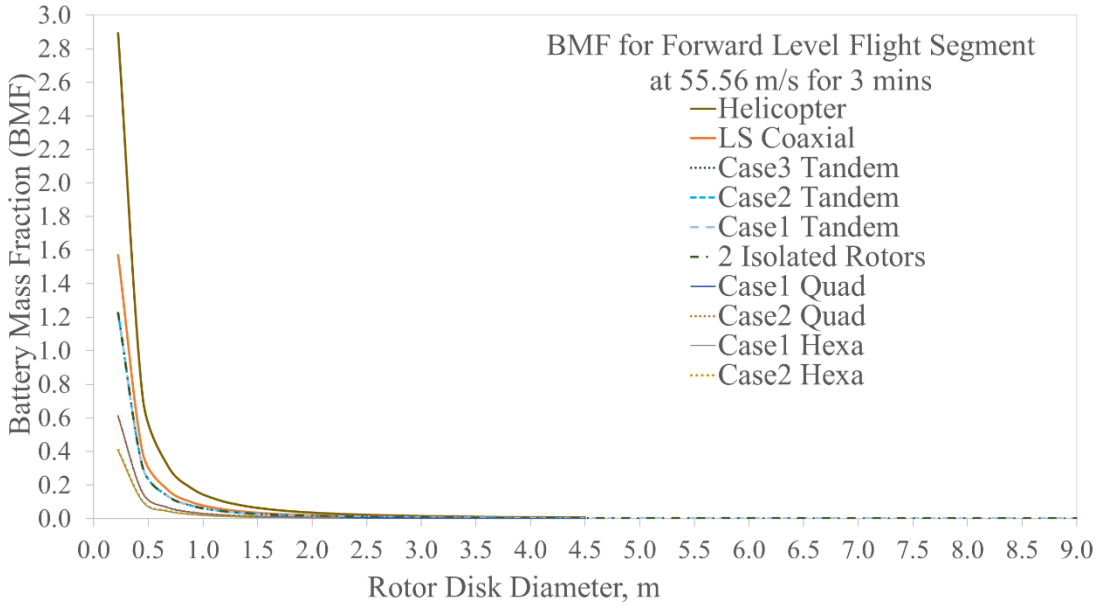


Fig. 4.22. Forward Level Flight (at 55.56 m/s for 3 mins) BMF vs Rotor Disk Diameter (Area) - 20 kg Martian rotorcrafts

4.7.4 Power Efficient Rotor Configuration

Fig. 4.23 and Fig. 4.24 depict analytical graphs illustrating the power required by various rotorcraft configurations, including the conventional helicopter, LS (Large Separation) coaxial rotorcraft, three tandem rotorcraft cases, two quadcopter, and two hexacopter for vertical climb and forward level flight, respectively, in relation to the rotor disk diameter. When comparing power requirements between single and dual rotors, tandem rotorcraft display the lowest power consumption. However, among the three tandem rotorcraft cases, Tandem Case 3 emerges as a priority, as outlined in [28] and Chapter 3, due to its comparatively simpler and lighter configuration, coupled with enhanced power efficiency. However, Tandem rotor configurations pose considerable aerodynamic challenges, primarily due to wake interactions between the front and rear rotors. These interactions can reduce overall aerodynamic efficiency, increase vibration, and complicate both flight stability and control.

The data presented in these graphs indicate that, within the given parameters, hexarotor configurations require the least power compared to single, dual, and quad rotors. It is evident from the graph plot that the lowest power consumption for the hexarotor configuration occurs in Case 1, primarily because its rotor disk

size can extend up to 2.25 m. Similarly, for the quadrotor configurations, Case 1 exhibits the lowest power requirement, which is attributable to its rotor disk size being allowed to reach 4.5 m. According to the formulas utilised in this simplified approach, unlike tandem rotorcraft, quadrotor and hexarotor operate as independent entities without overlapping interference, except for the downwash generated by frontal rotors during forward flight. This downwash effect can be minimized for a quad rotorcraft, thus enhancing power efficiency, by altering the quad setting from square to diamond [32].

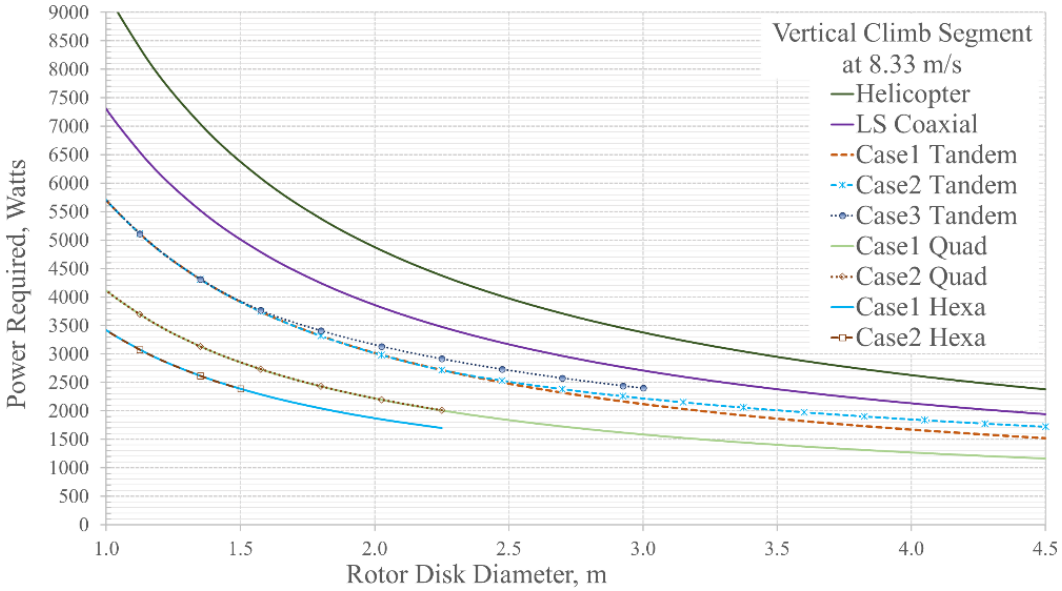


Fig. 4.23. Power Required (Vertical Climb at 8.33 m/s) vs Rotor Disk Diameter (Rotor Diameter Limits – 1 m to 4.5m) – Comparison between various 20 kg rotorcraft configurations

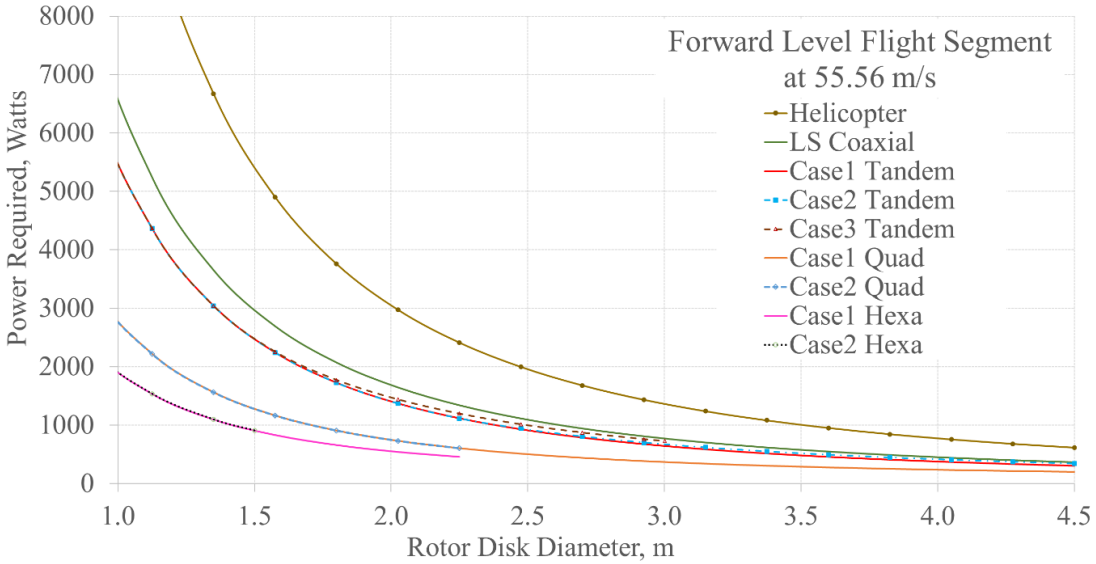


Fig. 4.24. Power Required (Forward Level at 55.56 m/s) vs Rotor Disk Diameter (Rotor Diameter Limits – 1 m to 4.5m) – Comparison between various 20 kg rotorcraft configurations

4.7.5 Implementing Initial Sizing on Selected Configuration

Hexacopters are particularly advantageous due to their inherent stability and redundancy; the additional rotors provide greater control and allow for continued operation even if one rotor fails, making them more reliable than quadrotors, especially in challenging environments like Mars. This added redundancy is a significant advantage over quadrotors, which would have significantly reduced stability if a single rotor failed. For both hexacopter and quadcopter configurations, Case 1 requires a folding mechanism, making it more complex and heavier compared to Case 2, which can be stowed inside the aeroshell without requiring a folding mechanism. Therefore, while Case 2 quadrotor may be more efficient in terms of simplicity and weight, the robustness and fail-safety of hexacopters make them a preferable choice for missions where stability and reliability are critical.

A hexacopter configuration with a 1.5 m rotor disk size is selected for the initial sizing process. As mentioned in section 4.6, the battery-specific energy (Esb) used for Battery Mass Fraction (BMF) calculations for flight is 230 Wh/kg, based on a JPL technology forecast [4]. The power required for the vertical climb segment is determined to be ~2390 Watts, while for the cruise segment, it is ~900

Watts. The corresponding Battery Mass Fraction (BMF) values are calculated to be 0.019 and 0.01, respectively. Summing up these BMF values yields a total BMF of 0.029. As explained in Section 4.3, the nominal usage and discharge efficiency correction factors, totalling 1.4 (1.3 for 70% usable capacity and 1.1 for 90% averaged discharge efficiency deduced in [4]), are applied to adjust the total BMF. The adjusted BMF is now 0.041. Given the predetermined total aerobot mass of 20 kg, Eq. (4.10) is utilised to calculate the required battery mass (m_{b}) for the 5-minute flight mission, resulting in 0.82 kg. Additionally, considering that the aerobot must accommodate a science payload weighing 2 kg, Eq. (4.11) is used in terms of Mass to determine the available aircraft's empty mass, resulting in 17.18 kg. This represents ~86% of the total aircraft mass, offering a feasible starting point for further analysis.

The blade mass estimated, using the method in Section 4.4.2 (graph in Fig. 4.9), for this configuration and rotor diameter is as follows: a 2-blade rotor weighs 0.25 kg, while a 4-blade rotor weighs 0.5 kg. For the entire hexarotorcraft (six rotors), this translates to a total blade mass of 1.5 kg for the 2-blade configuration and 3.0 kg for the 4-blade configuration. Relative to the total rotorcraft weight of 20 kg, the 2-blade rotor configuration accounts for 7.5% of the total mass, while the 4-blade configuration contributes 15%. This demonstrates the considerable impact of blade count on overall system mass, with the 4-blade configuration doubling the blade mass compared to the 2-blade setup. However, both relative percentages are well within the typical blade mass range (10–30%) [19] of the Martian rotorcraft's weight with smaller to medium rotors. While increasing the number of blades per rotor enhances lift capacity and aerodynamic performance, it also introduces higher structural loads, rotational inertia, and power demands, necessitating careful design trade-offs. These estimates account only for blade mass and do not include additional reinforcements or hub modifications required for mounting extra blades, which could further influence airframe weight and system dynamics. The higher-mass 4-blade configuration may offer advantages in rotor efficiency and stability, particularly in thin Martian atmosphere, but at the cost of increased structural reinforcements, power consumption, and overall vehicle weight. Therefore, the choice of blade configuration must align with

mission objectives, endurance constraints, and payload capacity to achieve an optimal balance between performance and efficiency.

Fig. 4.25 shows the CAD model illustration of the Case 2 Hexacopter configuration concept with a 1.5 m rotor disk size analysed and sized. Design assumptions included a carbon fiber body, landing gears and blades. The fuselage, like Ingenuity, is a Warm Electronics Box offering thermal protection for critical electronics and batteries, while also serving as a barrier against environmental contamination. It is assumed to be made from a polyamide film membrane, designed to absorb solar energy effectively and emit little heat. This membrane is wrapped around a lightweight composite frame, creating an insulating gas layer to reduce heat loss. The top of the fuselage is covered with highly efficient solar panels. The bottom of the fuselage has payload attachments such as a surveillance camera, along with navigation cameras. Alternatively, it could contain other scientific payload attachments. The fuselage contains computing processors, communication electronics, GNC systems and heaters. The rotor blade is based on the structure and design of the optimised blade of the Mars Science Helicopter proposed in [4].



Fig. 4.25 CAD Model illustration of a Case 2 Hexacopter configuration with a 1.5 m rotor disk size. Bottom left image shows the Hexacopter flying on Mars. (Not to scale)

The initial sizing assumed fixed values for payload and total rotorcraft mass, but adjustments can be made by integrating payload mass into the empty mass of the rotorcraft. This approach allows for flexibility in balancing airframe and motor mass with payload, ensuring the total mass remains constant. The iterative process of refining rotorcraft sizing will involve adjustments to mass components to achieve a more accurate preliminary design. The results of this study serve as a critical first step toward validating rotorcraft designs for Martian exploration. Future work will focus on refining performance estimates using advanced methodologies such as Computational Fluid Dynamics (CFD) and vortex wake models. These techniques will be essential for improving rotor efficiency at high advance ratios, where compressibility effects become significant. Addressing these factors will be key to advancing the reliability and applicability of rotorcraft designs, ensuring that they can meet the demanding requirements of Mars missions.

4.8 Discussion and Conclusion

4.8.1 Discussion

This parametric study establishes a theoretical baseline for estimating power consumption across a wide range of rotorcraft configurations under Martian conditions, using simplified helicopter momentum theory. The analysis encompasses both overlapping and non-overlapping rotor systems to identify the most power-efficient designs for aerobot missions, where simplicity is essential due to the impracticality of maintenance on Mars. In selecting efficient configurations, the study examines single, dual, tandem, quad, and hexacopter designs. For example, in a case study of a tandem rotorcraft with a 9 m rotor diameter, design constraints were imposed to avoid theoretical optima that would require excessively heavy materials and complex folding, stowing, and control mechanisms. Similarly, smaller rotors are advantageous for multicopters only when they remain light and mechanically simple; otherwise, the addition of multiple motors and hub systems increases empty weight and reduces payload capacity.

Rotor radius and positioning significantly influence the mass of rotors, airframe, and motors. Larger rotors, while enhancing lift efficiency and reducing power requirements per unit thrust, demand heavier blades due to increased length and the need for additional reinforcement against centrifugal forces. Conversely, rotor positioning affects weight distribution and aerodynamic interference. Tandem and coaxial configurations centralise loads and can simplify airframe design, yet introduce control complexity, while side-by-side or non-overlapping setups reduce interference but require larger, heavier airframes. Overlapping rotors, as in coaxial systems, experience wake interference that necessitates extra power, though their shared load distribution may reduce the overall footprint.

For Martian rotorcraft, these trade-offs are critical. Tandem configurations can optimise load distribution by reducing aerodynamic interference, while coaxial rotors offer a compact solution that, despite requiring reinforced hubs, can lower overall structural mass. Distributed configurations such as hexacopters spread loads across multiple axes, allowing for lighter blades and motors with built-in

redundancy; for instance, a hexacopter with a 1.5 m diameter 4-blade rotor achieved a feasible blade weight of 0.5 kg. Balancing rotor radius and positioning is key, as larger blades reduce power requirements but add weight through increased structural demands, whereas smaller blades demand higher power but enable lighter overall designs.

Given the unique challenges and costs associated with Martian rotorcraft experimentation, this framework represents a crucial first step in validating rotorcraft designs. Future work will refine performance estimates with advanced methods such as vortex wake modelling and CFD, focusing on rotor efficiency at high advance ratios where compressibility effects are significant.

4.8.2 Conclusion

Rotorcraft operations on Mars have been proven feasible through the successful flight of NASA's Mars Helicopter. To advance Mars rotorcraft technology, future missions will rely on advanced approaches built upon this foundation. Addressing a critical research gap, this study describes its objectives and establishes essential parameters for a comprehensive analysis of 20 kg rotorcraft configurations, encompassing both single and multiple rotor designs. Utilising simplified equations derived from helicopter momentum theory, the methodology is adapted and streamlined for each rotorcraft configuration under examination. Furthermore, the study introduces an initial methodology for sizing battery-electric aircraft, utilizing the Battery Mass Fraction to estimate battery mass for different flight segments. Graphical representations depict the power requirements for hover, vertical ascent, and forward flight, correlating with increasing rotor disk diameter across various rotorcraft types, including conventional helicopters, coaxial rotorcraft, tandem rotorcraft, quadcopter and hexacopter. Notably, conventional helicopters exhibit higher power consumption than alternative configurations under the specified parameters. Among multicopter configurations, hexacopters demonstrate superior performance followed by quadcopters, especially for rotor disk sizes up to 1.5 m. However, as rotor disk diameter approaches the upper limit, discrepancies in power requirements between configurations become marginal. Additionally, this study

introduces a 3D MSH blade mass scaling model to refine rotor blade mass estimation through material distribution and thickness-to-chord scaling laws, addressing key structural considerations beyond purely geometric approaches. The findings reinforce that while geometric scaling methods provide useful approximations, increasing structural reinforcement requirements at larger rotor sizes significantly impact mass growth. These results provide a crucial foundation for the development of next-generation rotorcraft capable of meeting the demanding conditions of Martian exploration, ensuring more efficient, structurally optimised, and reliable aerial missions in the future.

Declaration of interests

The authors declare that they have no known competing financial interests or personal relationships that could have appeared to influence the work reported in this paper.

References

[1] Hassanalian, M., Rice, D., & Abdelkefi, A. Evolution of space drones for planetary exploration: A review. Progress in Aerospace Sciences, 97, 2018. 61–105. https://doi.org/10.1016/J.PAEROSCI.2018.01.003

[2] NASA. Overview | Mars – NASA Solar System Exploration. Retrieved April 22, 2024, from https://solarsystem.nasa.gov/planets/mars/overview/

[3] Radotich, M., Withrow-Maser, S., deSouza, Z., Gelhar, S., & Gallagher, H. (2021, January). A study of past, present, and future Mars rotorcraft. In 9th Biennial Autonomous VTOL Technical Meeting.

[4] Johnson, W., Withrow-Maser, S., Young, L., Malpica, C., Koning, W. J. F., Kuang, W., Fehler, M., Tuano, A., Chan, A., Datta, A., Chi, C., Lumba, R., Escobar, D., Balaram, J., Tzanetos, T., & Fjaer Grip, H. (2020). Mars Science Helicopter Conceptual Design. http://www.sti.nasa.gov

[5] NASA. (2023) Mars Helicopter - NASA Mars. Retrieved April 22, 2024, from https://mars.nasa.gov/technology/helicopter/#Flight-Log

[6] Young, L. A., Chen, R. T. N., Aiken, E. W., Briggs, G. A., "Design Opportunities and Challenges in the Development of Vertical Lift Planetary

Aerial Vehicles," Proceedings of the American Helicopter Society International Vertical Lift Aircraft Design Specialist's Meeting, January 2000.

[7] Underwood, C., & Collins, N. (2017). Design and Control of a Y-4 Tilt-Rotor VTOL Aerobot for Flight on Mars. Proceedings of the 68th International Astronautical Congress (IAC), 25–29. https://openresearch.surrey.ac.uk/esploro/outputs/conferencePresentation/Design-and-Control-of-a-Y-4-Tilt-Rotor-VTOL-Aerobot-for-Flight-on-Mars/99511131102346

[8] Aguirre, J., Casado, V., Chamie, N., & Zha, G. (2007). Mars Intelligent Reconnaissance Aerial and Ground Explorer (MIRAGE) AIAA 2007-244, Reno, Nevada. https://doi.org/10.2514/6.2007-244

[9] Forshaw, J., & Lappas, V. (2012). Architecture and Systems Design of a Reusable Martian Twin Rotor Tailsitter. Acta Astronautica, 80(0), 166–180. https://doi.org/10.1016/J.ACTAASTRO.2012.05.008

[10] RM Zubrin. (2012). The Mars Gashopper. Concepts and Approaches for Mars 2012. June 12-14, 2012 in Houston, Texas. https://ui.adsabs.harvard.edu/abs/2012LPICo1679.4069Z/abstract

[11] Fathepure, M., Booker, A. L., Abouzahr, O., Wang, N., & Tikalsy, D. (2021). Design and Construction of an Inflatable-Winged VTOL Mars Electric Flyer. In AIAA AVIATION 2021 FORUM (p. 2578) https://doi.org/10.2514/6.2021-2578

[12] Youhanna V, Felicetti L & Ignatyev D (2024). Preliminary Investigation into Future Martian Multicopter Configurations. In: Vertical Flight Society’s 80th Annual Forum & Technology Display, Montréal, Québec, Canada, May 7-9, 2024. https://doi.org/10.4050/F-0080-2024-1266

[13] Youhanna V, Felicetti L & Ignatyev D (2024). Preliminary Design Exploration of Prospective Multirotor Aerobots for Mars. In: 34th Congress of the International Council of the Aeronautical Sciences (ICAS 2024), Florence, Italy, September 9-13, 2024.

[14] D. Raymer. Aircraft design: A conceptual approach, 6. Ed., AIAA education series, Reston, Va., 2018, Chaps. 20.11, 21.3.

[15] Leishman, J. Gordon. Principles of Helicopter Aerodynamics, 2. Ed., United Kingdom, Cambridge University Press, 2006. Chaps. 2.15, 5.5.11.

[16] Johnson, W. Rotorcraft Aeromechanics. Cambridge University Press. 2013. Chaps. 4.6, 5.3. https://doi.org/10.1017/CBO9781139235655

[17] Monolithic Power Systems. (Web Editor). (2024). Introduction to battery technology: Battery parameters. Monolithic Power Systems. Retrieved December 18, 2024, from https://www.monolithicpower.com/en/learning/mpscholar/battery-management-systems/introduction-to-battery-technology/battery-parameters

[18] Muelaner, Jody. (2022). Battery Power Tips. What to consider when evaluating battery performance. Battery Power Tips. Retrieved December 18, 2024, from https://www.batterypowertips.com/what-to-consider-when-evaluating-battery-performance-faq/

[19] Young, L. A., Aiken, E. W., Lee, P., & Briggs, G. A. (2004). Mars rotorcraft: Possibilities, limitations, and implications for human/robotic exploration. NASA Technical Reports Server. Retrieved January 21, 2025, from https://ntrs.nasa.gov/citations/20090028805

[20] Tang, B., Quan, Q., Pan, D., Wang, C., Zheng, H., Wang, K., Tang, D., & Deng, Z. (2024). Design and experimental verification of propulsion system for a Mars quadcopter. *Acta Astronautica, 225,* 992–1000. https://doi.org/10.1016/j.actaastro.2024.09.069

[21] Evonik Operations GmbH. (2022, April). ROHACELL® IG-F: Structural foam technical data sheet. Retrieved February 26, 2025, from https://products.evonik.com/assets/35/34/ROHACELL_IG_F_2022_April_EN_243534.pdf

[22] Gabrian International (H.K.) Ltd. (2020.). 7075 aluminum alloy: Properties. Retrieved February 26, 2025, from https://www.gabrian.com/7075-aluminum-properties/

[23] Cytec. (2012). MTM45-1 epoxy resin data sheet. Retrieved February 26, 2025, from https://cstjmateriauxcomposites.files.wordpress.com/2017/11/cytec_mtm45-1_resine_epoxyde.pdf

[24] Toray Composite Materials America, Inc. (2018). M46J carbon fiber technical data sheet. Retrieved February 26, 2025, from https://www.toraycma.com/wp-content/uploads/M46J-Technical-Data-Sheet-1.pdf

[25] Mitsubishi Rayon Co., Ltd. (n.d.). Pyrofil HR40 12K: High modulus carbon fiber. Retrieved February 26, 2025, from https://fileserver.mates.it/Prodotti/1_Rinforzi/TDS/Carbonio/Fibre/Pyrofil%20HR40%2012K.pdf

[26] Julias, A. A. (2021.). Rule of mixture for composites. Crescent Institute of Science and Technology. Retrieved February 26, 2025, from https://crescent.education/wp-content/uploads/2021/03/Rule-of-Mixture-of-composites.pdf

[27] Gurit. (2022). Guide to composites. Retrieved February 26, 2025, from https://www.gurit.com/wp-content/uploads/2022/12/guide-to-composites-1.pdf

[28] Youhanna V, Felicetti L & Ignatyev D (2023). Conceptual Design Study based on Defined Parameters for Next Generation Martian Rotorcrafts. In: IEEE Aeroconf 2024, Montana, US, 2-9 March 2024. DOI: https://doi.org/10.1109/AERO58975.2024.10521441

[29] NASA. (2023) Mars Fact Sheet. NASA Goddard Space Flight Center. Retrieved April 22, 2024, from https://nssdc.gsfc.nasa.gov/planetary/factsheet/marsfact.html

[30] Millour, E., Forget, F., Spiga, A., Pierron, T., Bierjon, A., Montabone, L., Vals, M., Lefèvre, F., Chaufray, J.-Y., Lopez-Valverde, M., Gonzalez-Galindo, F., Lewis, S., Read, P., Desjean, M.-C., and Cipriani, F. and the MCD Team: The Mars Climate Database (Version 6.1), Europlanet Science Congress 2022, Granada, Spain, 18–23 Sep 2022, EPSC2022-786, https://doi.org/10.5194/epsc2022-786

[31] Balaram, J., Aung, M. & Golombek, M.P. The Ingenuity Helicopter on the Perseverance Rover. Space Sci Rev 217, 56 (2021). https://doi.org/10.1007/s11214-021-00815-w

[32] Han, D., & Barakos, G. N. (2020). Aerodynamic interference model for multirotors in forward flight. Journal of Aircraft, 57(6), 1220–1223. https://doi.org/10.2514/1.C035978/ASSET/IMAGES/LARGE/FIGURE3.JPEG

5 Conclusion

This thesis has developed a structured framework for the conceptual design and optimisation of rotary VTOL aerobots for Mars exploration, addressing key challenges posed by the planet's thin atmosphere, low gravity, and extreme environmental conditions. The study systematically investigates rotorcraft configurations, power efficiency, and deployment constraints to establish a foundation for future aerial robotic missions.

The research begins with an analysis of the limitations of traditional Mars exploration methods, highlighting the need for aerobots to complement landers and rovers in accessing diverse and rugged terrains. To guide the design process, the Mars Aerobot Design Thinking Matrix is introduced, providing a systematic methodology for integrating planetary constraints and mission-specific requirements into aerobot development. This framework ensures that proposed rotorcraft configurations are optimised for the Martian environment.

A key achievement of this research is the adaptation of helicopter momentum theory for Martian rotorcraft, enabling accurate power consumption estimates across different flight phases. The parametric analysis conducted on multiple rotorcraft configurations such as single-rotor, coaxial, tandem, quadcopter, and hexacopter, demonstrated that hexacopters provide the most efficient balance between power consumption, stability, and redundancy. The findings indicate that for a 20 kg Martian hexacopter with a 1.5 m rotor disk size, the estimated hover power requirement is approximately 2390 W, while forward flight at 55.56 m/s requires about 900 W. Additionally, the battery mass fraction (BMF) is maintained around 0.041, ensuring a feasible energy-to-mass ratio. These findings confirm that multirotor designs can offer superior flight efficiency compared to traditional single-rotor or tandem configurations.

Additionally, this study introduces a 3D MSH blade mass scaling model to refine rotor blade mass estimation through material distribution and thickness-to-chord scaling laws, addressing key structural considerations beyond purely geometric approaches. The findings reinforce that while geometric scaling methods provide

useful approximations, increasing structural reinforcement requirements at larger rotor sizes significantly impact mass growth. Furthermore, this research addresses practical deployment challenges, proposing foldable rotor systems to accommodate aerobots within existing spacecraft aeroshells. These innovations ensure that aerial robots can be efficiently transported and deployed on Mars without compromising performance.

The findings of this study contribute significantly to the advancement of planetary aerial exploration, providing a validated design methodology and performance benchmarks for future Mars aerobot missions. By establishing rotorcraft configurations and assessing their feasibility, this research supports the development of aerial vehicles capable of broader scientific investigations of Mars and other planetary bodies with atmospheres.

5.1.1 Potential Impact

The findings of this research have significant implications for the future of Mars exploration and the broader field of planetary science. The conceptual frameworks developed for Martian aerobot design and missions, along with streamlined power estimations for different rotorcraft configurations, especially those with overlapping rotors, have practical implications. This advances decision-making, aiding researchers in selecting optimal designs and saving considerable time and effort in preliminary Martian aerobot design.

The Mars Aerobot Design Thinking Matrix provides a systematic approach because it integrates environmental constraints, mission-specific requirements, and engineering trade-offs into a structured decision-making framework, ensuring that aerobot designs are both feasible and optimised for sustained flight in Mars' challenging atmospheric conditions. This approach can be adapted to the design of aerial robots for other planetary bodies with similar environmental challenges, such as Titan or Venus. This adaptability enhances the utility of the framework beyond Mars, potentially influencing the design of future exploratory missions across the solar system.

The adaptation of helicopter momentum theory for Martian conditions represents preliminary estimation and optimisation of multirotor configurations. This modelling capability introduced as a step within the preliminary design phase will serve as a theoretical baseline, enabling engineers and researchers to design more efficient and reliable aerial vehicles for use in harsh extraterrestrial environments, increasing the likelihood of mission success.

Practically, the insights gained from this research will directly influence the design and implementation of next-generation aerobots for Mars exploration. These aerobots, capable of carrying larger payloads, covering more extensive areas, and operating in extreme conditions, will enable more comprehensive and effective scientific exploration of the Martian surface. This enhanced exploration capability could significantly advance our understanding of Mars' geology, climate, and potential for life, thereby contributing to the broader goals of planetary science and exploration. Moreover, this research underscores the importance of integrating advanced control systems and energy-efficient designs into autonomous exploration technologies. The methodologies and strategies developed here are not only relevant to Mars but also have broader applications in the design of aerial robotic systems for other challenging environments, potentially shaping the future of space exploration.

5.2 Future Work Recommendations

While this thesis has provided considerable advancements in selecting an optimal design of rotary VTOL aerobots for Mars exploration, several areas require further investigation to build upon the findings and address the identified following limitations:

- Future research should focus on refining the theoretical models presented in Chapters 3 and 4 through advanced Computational Fluid Dynamics (CFD) simulations and vortex wake models. These techniques would allow for a more detailed analysis of aerodynamic interactions, particularly in overlapping rotor configurations, addressing the limitations of the simplified models used in this thesis. Complementing these efforts, experimental validation is crucial.

Testing prototype aerobots in Mars-analogue environments, such as high-altitude deserts or vacuum thermal chambers, would provide empirical data to validate the theoretical models and refine the designs, ensuring their reliability and effectiveness for actual Mars missions.

- Developing advanced autonomous control systems is another critical area for future research. The operational challenges posed by Mars' thin atmosphere, highlighted in the thesis, underscore the need for stable, autonomous flight. Future work should explore the integration of machine learning algorithms to dynamically optimise flight paths, avoid obstacles, and adjust to environmental changes in real-time. Additionally, sensor fusion techniques should be utilised to enhance the comprehensive understanding of the environment, improving the resilience and operational efficiency of aerobots in the challenging Martian environment.

- Energy efficiency remains a critical area for future research. Investigating alternative energy sources, such as high-efficiency solar panels and compact nuclear power sources like radioisotope thermoelectric generators (RTGs), could significantly extend the operational life and range of Martian aerobots. Advancements in battery technology, including solid-state batteries and supercapacitors, should also be explored for their potential to increase energy density and reduce weight, thereby enabling more extended and complex exploration missions on Mars.

- Finally, the integration of aerobots with existing rover and lander systems presents a valuable opportunity for enhancing mission strategies. Future research should develop robust communication and operational protocols that enable seamless cooperation between aerobots and ground-based systems. Such integration would allow aerobots to perform aerial reconnaissance, map routes, and scout areas of interest, significantly improving the efficiency and scientific yield of Mars exploration missions by leveraging the strengths of both aerial and terrestrial platforms.

Global References/Bibliography

The references below are a collection of all the references used in the above chapters.

- Abd El-Hameed, A. M. (2022). Radiation effects on composite materials used in space systems: A review. NRIAG Journal of Astronomy and Geophysics, 11(1), 313-324. https://doi.org/10.1080/20909977.2022.2079902

- Ackerman, E. (2021). JPL's plan for the next Mars helicopter. *IEEE Spectrum*. Retrieved August 15, 2024, from https://spectrum-ieee-org.cdn.ampproject.org/c/s/spectrum.ieee.org/amp/the-next-mars-helicopter-2654506042

- Afshar-Mohajer, N., Wu, C.-Y., Curtis, J., & Gaier, J. (2015). Review of dust transport and mitigation technologies in lunar and Martian atmospheres. Advances in Space Research, 56(6), 1212-1229. https://doi.org/10.1016/j.asr.2015.06.007

- Aguirre, J., Casado, V., Chamie, N., & Zha, G. (2007). Mars Intelligent Reconnaissance Aerial and Ground Explorer (MIRAGE) AIAA 2007-244. 45th AIAA Aerospace Sciences Meeting and Exhibit, Reno, NV. https://doi.org/10.2514/6.2007-244

- Analog Devices, Inc. (2023). Mars Perseverance and hardened technology in extreme environments. Retrieved August 15, 2024, from https://www.analog.com/en/signals/articles/mars-perseverance-hardened-technology.html

- Balaram, J., Aung, M., & Golombek, M. P. (2021). The Ingenuity Helicopter on the Perseverance Rover. Space Science Reviews, 217(4), 56. https://doi.org/10.1007/s11214-021-00815-w

- Banfield, D., et al. (2020). Mars science goals, objectives, investigations, and priorities: 2020 version. Mars Exploration Program Analysis Group (MEPAG).

Retrieved September 3, 2024, from https://mepag.jpl.nasa.gov/reports.cfm?expand=science

- Calle, L. M. (2019). Corrosion on Mars: Effect of the Mars environment on spacecraft materials. NASA Technical Publication No. 2019–220238. Retrieved from https://ntrs.nasa.gov/citations/20190027256

- Christensen, P. R., Engle, E., Anwar, S., Dickenshied, S., Noss, D., Gorelick, N., & Weiss-Malik, M. (2009). JMARS – A planetary GIS. Retrieved from http://adsabs.harvard.edu/abs/2009AGUFMIN22A..06C

- Clavé, E., et al. (2024). Radiation-induced alteration of apatite on the surface of Mars: First in situ observations with SuperCam Raman onboard Perseverance. *Scientific Reports, 14*, 11284. https://doi.org/10.1038/s41598-024-61494-5

- Cockell, C., Bridges, J., Dannatt, L., Burchell, M., Patel, M., & Danson, M. (2009). Where to land on Mars. *Astronomy & Geophysics, 50*(6), 6.18-6.26. https://doi.org/10.1111/J.1468-4004.2009.50618.X

- Colozza, A. (1990). Preliminary design of a long-endurance Mars aircraft. *26th Joint Propulsion Conference, Orlando, FL*. https://doi.org/10.2514/6.1990-2000

- Colozza, A., Landis, G., & Lyons, V. (2003). Overview of innovative aircraft power and propulsion systems and their applications for planetary exploration. *International Air and Space Symposium and Exposition*. https://doi.org/10.2514/6.2003-631

- Cox, B. (Presenter). (2010). *Wonders of the Solar System, Dead or Alive, Olympus Mons on Mars* [Video]. BBC Two. Retrieved September 3, 2024, from https://www.bbc.co.uk/programmes/p0073lg1

- Cytec. (2012). MTM45-1 epoxy resin data sheet. Retrieved February 26, 2025, from https://cstjmateriauxcomposites.files.wordpress.com/2017/11/cytec_mtm45-1_resine_epoxyde.pdf

- D. Raymer. (2018). *Aircraft design: A conceptual approach* (6th ed.). AIAA Education Series, Reston, VA. Chaps. 20.11, 21.3.

- Datta, A., Roget, B., Griffiths, D., Pugliese, G., Sitaraman, J., Bao, J., Liu, L., & Gamard, O. (2003). Design of a Martian autonomous rotary-wing vehicle. *Journal of Aircraft, 40*(3), 461-472. https://doi.org/10.2514/2.3141

- Delaune, J., Izraelevitz, J., Sklyanskiy, E., Schutte, A., Fraeman, A., Scott, V., Leake, C., Ballesteros, E., Aaron, K., Young, L. A., Johnson, W., Withrow-Maser, S., Cummings, H., Bhagwat, R., Veismann, M., Wei, S., Lee, R., Madrid, L. P., Gharib, M., & Rapin, W. (2020). Motivations and preliminary design for mid-air deployment of a science rotorcraft on Mars. *Accelerating Space Commerce, Exploration, and New Discovery Conference, ASCEND 2020*. https://doi.org/10.2514/6.2020-4030

- Denys, K. (2016). Ukrainian invention to feel the ground for Mars colonization (GRAPHICS). *KyivPost*. Retrieved July 20, 2024, from https://www.kyivpost.com/article/content/ukraines-it-edge/ukrainian-invention-to-feel-the-ground-for-mars-colonization-graphics-415570.html

- Dorminey, B. (2020). NASA eyes wind turbines to power Martian weather stations. Forbes. Retrieved September 2, 2024, from https://www.forbes.com/sites/brucedorminey/2020/08/30/nasa-eyes-tiny-wind-turbines-to-power-martian-weather-stations/

- E-One Moli Energy Corp. (2024). Product data sheet of INR-21700-P50B. Retrieved December 20, 2024, from https://www.molicel.com/wp-content/uploads/Product-Data-Sheet-of-INR-21700-P50B-80122.pdf

- ESA Web Team. (2019). The hazards of landing on Mars. *European Space Agency*. Retrieved August 20, 2024, from https://exploration.esa.int/web/mars/-/58307-the-hazards-of-landing-on-mars

- Evonik Operations GmbH. (2022, April). ROHACELL® IG-F: Structural foam technical data sheet. Retrieved February 26, 2025, from

https://products.evonik.com/assets/35/34/ROHACELL_IG_F_2022_April_EN_243534.pdf

- Farley, K. A., Williford, K. H., Stack, K. M., Bhartia, R., Chen, A., de la Torre, M., Hand, K., Goreva, Y., Herd, C. D., Hueso, R., Liu, Y., Maki, J. N., Martinez, G., Moeller, R. C., Nelessen, A., Newman, C. E., Nunes, D., Ponce, A., Spanovich, N., & Liu, Y. (2020). Mars 2020 mission overview. *Space Science Reviews, 216*, 142. https://doi.org/10.1007/s11214-020-00762-y

- Fathepure, M., Booker, A. L., Abouzahr, O., Wang, N., & Tikalsy, D. (2021). Design and construction of an inflatable-winged VTOL Mars electric flyer. *AIAA AVIATION 2021 Forum*, 2578. https://doi.org/10.2514/6.2021-2578

- Ferguson, K.M., Thomson, D.G., Anderson, D., Ireland, M.L., Tu, Z., Manso, S., Chandran, A.B., & Ibal, G. (2015). Comparing the flight dynamics characteristics of tandem and conventional helicopters for the purposes of automatic control. Presented at the 41th European Rotorcraft Forum, Munich, Germany, September 1-4th, 2015. Retrieved December 22, 2024, from https://dspace-erf.nlr.nl/server/api/core/bitstreams/a0eb3b54-7891-480a-b222-74360df252ac/content

- Forshaw, J., & Lappas, V. (2012). Architecture and systems design of a reusable Martian twin rotor tailsitter. *Acta Astronautica, 80*, 166–180. https://doi.org/10.1016/J.ACTAASTRO.2012.05.008

- Fraser, C. (2005). Static electricity in space. *Universe Today*. Retrieved September 6, 2024, from https://www.universetoday.com/10830/static-electricity-in-space/

- Gabrian International (H.K.) Ltd. (2020.). 7075 aluminum alloy: Properties. Retrieved February 26, 2025, from https://www.gabrian.com/7075-aluminum-properties/

- Genova, A. (2017). Mars Gravity Field: GMM-3. PGDA. Retrieved September 6, 2024, from https://pgda.gsfc.nasa.gov/products/57

- Grant, J. A., Golombek, M. P., Wilson, S. A., Farley, K. A., Williford, K. H., & Chen, A. (2018). The science process for selecting the landing site for the

2020 Mars rover. *Planetary and Space Science, 164*, 106–126. https://doi.org/10.1016/J.PSS.2018.07.001

- Greeley, R., Christensen, P. R., Cantrell, J., Clark, B. C., Price, R. S., Zubrin, R. M., Cutts, J. A., Oberto, R. E., Haberle, R. M., & Malin, M. C. (1996). The Mars Aerial Platform (MAP) concept. *34th AIAA Aerospace Sciences Meeting and Exhibit, Reno, NV*. https://doi.org/10.2514/6.1996-335

- Gurit. (2022). Guide to composites. Retrieved February 26, 2025, from https://www.gurit.com/wp-content/uploads/2022/12/guide-to-composites-1.pdf

- Guzik, M. C., Jakupca, I. J., Gilligan, R. P., Bennett, W. R., Smith, P. J., & Fincannon, J. (2017). Regenerative fuel cell power systems for lunar and Martian surface exploration. *AIAA SPACE and Astronautics Forum and Exposition, AIAA 2017-5368*. https://doi.org/10.2514/6.2017-5368

- Han, D., & Barakos, G. N. (2020). Aerodynamic interference model for multirotors in forward flight. *Journal of Aircraft, 57*(6), 1220–1223. https://doi.org/10.2514/1.C035978

- Hanneke, W. (2016). US will send people to Mars by 2030s, Barack Obama says. *Space*. Retrieved September 3, 2024, from https://www.space.com/34351-obama-says-america-will-send-people-to-mars.html

- Hartmann, W. K., & Raper, O. (1974). *The new Mars: The discoveries of Mariner 9*. NASA. Retrieved September 3, 2024, from https://ntrs.nasa.gov/citations/19750005657

- Hassanalian, M., Rice, D., & Abdelkefi, A. (2018). Evolution of space drones for planetary exploration: A review. *Progress in Aerospace Sciences, 97*, 61–105. https://doi.org/10.1016/J.PAEROSCI.2018.01.003

- Hazarika, M. B., Santangelo, G., Gamba, M., & Wang, W. (2023, October 17). Development of a Preliminary Design Methodology for Rotorcraft in Martian

Atmospheric Conditions and Experimental Validation of the Method. https://doi.org/10.2514/6.2023-4802

- HiRISE Team. (2024). High resolution imaging science experiment – Catalog. *University of Arizona*. Retrieved September 3, 2024, from https://www.uahirise.org/catalog/

- Johnson, W. (2013). *Rotorcraft aeromechanics*. Cambridge University Press. https://doi.org/10.1017/CBO9781139235655

- Johnson, W., Withrow-Maser, S., Young, L., Malpica, C., Koning, W. J. F., Kuang, W., Fehler, M., Tuano, A., Chan, A., Datta, A., Chi, C., Lumba, R., Escobar, D., Balaram, J., Tzanetos, T., & Grip, H. F. (2020). Mars Science Helicopter conceptual design. *NASA STI*. https://doi.org/10.1007/s11214-021-00815-w

- JOUAV. (2023). Top 10 drones with the longest flight time in 2023. *JOUAV*. Retrieved July 20, 2024, from https://www.jouav.com/blog/drone-with-longest-flight-time.html

- Julias, A. A. (2021.). Rule of mixture for composites. Crescent Institute of Science and Technology. Retrieved February 26, 2025, from https://crescent.education/wp-content/uploads/2021/03/Rule-of-Mixture-of-composites.pdf

- Jun, I., Garrett, H., Kim, W., et al. (2024). A review on radiation environment pathways to impacts: Radiation effects, relevant empirical environment models, and future needs. *Advances in Space Research, 74*(2), 1-22. https://doi.org/10.1016/j.asr.2024.03.079

- Landis, G. A., Kerslake, T. W., Jenkins, P. P., & Scheiman, D. A. (2004). Mars solar power. *NASA/TM—2004-213367*. National Aeronautics and Space Administration, Glenn Research Center. Retrieved from https://ntrs.nasa.gov/citations/20040191326

- Landis, G. A., Oleson, S. J., & McGuire, M. (2012). Design study for a Mars Geyser Hopper. *50th AIAA Aerospace Sciences Conference*, Nashville, TN, January 9-12, 2012. https://doi.org/10.2514/6.2012-631

- Larson, K., & Fries, M. (2017). Ultraviolet testing of space suit materials for Mars. *47th International Conference on Environmental Systems, NASA Johnson Space Center*. Retrieved from https://ntrs.nasa.gov/api/citations/20170002050/downloads/20170002050.pdf

- Lavagna, M., Colagrossi, A., Pesce, V., Punzi, C., & Ciarambino, M. (2015). ARMONIA: Feasibility study on aerobots in Martian atmosphere to enhance science return. *66th International Astronautical Congress, Jerusalem, Israel*.

- Lee, M. (2024). NASA Artemis mission progresses with SpaceX Starship test flight. *NASA*. Retrieved August 20, 2024, from https://www.nasa.gov/directorates/esdmd/artemis-campaign-development-division/human-landing-system-program/nasa-artemis-mission-progresses-with-spacex-starship-test-flight/

- Leishman, J. G. (2006). *Principles of helicopter aerodynamics* (2nd ed.). Cambridge University Press. https://doi.org/10.1017/CBO9780511809933

- Lemmon, M. T., Lorenz, R. D., Rabinovitch, J., Newman, C. E., Williams, N. R., Sullivan, R., Golombek, M. P., Bell, J. F., Maki, J. N., & Vicente-Retortillo, A. (2022). Lifting and transport of Martian dust by the Ingenuity Helicopter rotor downwash as observed by high-speed imaging from the Perseverance Rover. *Journal of Geophysical Research: Planets, 127*(12). https://doi.org/10.1029/2022JE007605

- Li, J., Aierken, A., Liu, Y., Zhuang, Y., Yang, X., Mo, J., Fan, R., Chen, Q., Zhang, S., Huang, Y., & Zhang, Q. (2021). A brief review of high-efficiency III-V solar cells for space application. *Frontiers in Physics, 8*. https://doi.org/10.3389/fphy.2020.631925

- Li, Y. (2007). Information gathering strategies for a combined Martian system of aerobots and rovers (Master's thesis). *Luleå University of Technology & Cranfield University*. Retrieved September 2, 2024, from https://www.diva-portal.org/smash/get/diva2:1022648/FULLTEXT01.pdf

- Lou, B., Yan, X., Zhao, P., Xie, A., Zhang, D., & Zhu, S. (2021). Preliminary design of several new kinds of Martian aircrafts. Proceedings of the Vertical Flight Society's 77th Annual Forum & Technology Display. https://doi.org/10.4050/F-0077-2021-16736

- Lowry, A. (2018). NASA TechPort - Project data. NASA. Retrieved September 1, 2024, from https://techport.nasa.gov/view/93850

- Malla, R., Loo, S. H., Liew, L. Y., Wai, N. S., Edmonston, D., Dinh, T., & Mahathalagalage, N. (2000). Martian Airborne Exploration Vehicle (MAEV). *Wichita State University, Department of Aerospace Engineering, HEDS-UP Forum*.

- Mars Education Program (ASU) Team. (2024). Mars Education | Atmosphere. *Arizona State University*. Retrieved September 6, 2024, from https://marsed.asu.edu/mep/atmosphere

- Mars Education Program (ASU) Team. (2024). Mars Education | Dust. *Arizona State University*. Retrieved September 6, 2024, from https://marsed.asu.edu/mep/dust

- Mars Education Program (ASU) Team. (2024). Mars Education | Wind. *Arizona State University*. Retrieved September 6, 2024, from https://marsed.asu.edu/mep/wind

- MCD Team. (2024). Martian seasons and solar longitude Ls. *Laboratoire de Météorologie Dynamique*. Retrieved September 6, 2024, from https://www-mars.lmd.jussieu.fr/mars/time/solar_longitude.html

- McMillon-Brown, L., Peshek, T. J., Pal, A., & McNatt, J. (2020). A study of photovoltaic degradation modes due to dust interaction on Mars. *Solar Energy Materials & Solar Cells, 221*, 110880. https://doi.org/10.1016/j.solmat.2020.110880

- Messier, D. M. (1996). Soviet/Russian Mars program. *Instituto de Física da UFRGS*. Retrieved September 3, 2024, from http://astro.if.ufrgs.br/solar/sovmars.htm

- Michael McAuley (NASA/JPL). (2002). Catalog Page for PIA03480. *NASA Photojournal*. Retrieved August 15, 2024, from https://photojournal.jpl.nasa.gov/catalog/PIA03480

- Millour, E., Forget, F., Spiga, A., Pierron, T., Bierjon, A., Montabone, L., Vals, M., Lefèvre, F., Chaufray, J.-Y., Lopez-Valverde, M., Gonzalez-Galindo, F., Lewis, S., Read, P., Desjean, M.-C., & Cipriani, F., and the MCD Team. (2022). The Mars Climate Database (Version 6.1). *Europlanet Science Congress 2022*, Granada, Spain, 18–23 Sep 2022. https://doi.org/10.5194/epsc2022-786

- Mindy Weisberger. (2021). Meet Au-Spot, the AI robot dog that's training to explore caves on Mars. *Space*. Retrieved September 2, 2024, from https://www.space.com/ai-mars-robot-dogs-agu

- Mitsubishi Rayon Co., Ltd. (n.d.). Pyrofil HR40 12K: High modulus carbon fiber. Retrieved February 26, 2025, from https://fileserver.mates.it/Prodotti/1_Rinforzi/TDS/Carbonio/Fibre/Pyrofil%20HR40%2012K.pdf

- Monolithic Power Systems. (Web Editor). (2024). Introduction to battery technology: Battery parameters. Monolithic Power Systems. Retrieved December 18, 2024, from https://www.monolithicpower.com/en/learning/mpscholar/battery-management-systems/introduction-to-battery-technology/battery-parameters

- Muelaner, Jody. (2022). Battery Power Tips. What to consider when evaluating battery performance. Battery Power Tips. Retrieved December 18, 2024, from https://www.batterypowertips.com/what-to-consider-when-evaluating-battery-performance-faq/

- Nagai, H., & Oyama, A. (2016). Development of Japanese Mars airplane. *67th International Astronautical Congress (IAC)*, Guadalajara, Mexico, 26-30 September 2016.

- Nancy Atkinson. (2022). Martian dust is starting to darken Ingenuity's solar panels. *Universe Today*. Retrieved September 6, 2024, from https://www.universetoday.com/155864/martian-dust-is-starting-to-darken-ingenuitys-solar-panel/

- Nancy Atkinson. (2024). Glowing helicopters on Mars. *Universe Today*. Retrieved September 6, 2024, from https://www.universetoday.com/154356/glowing-helicopters-on-mars/

- NASA Langley Research Center. (2017). NASA Langley engineers propose Mars Flyer concept [YouTube]. Retrieved September 1, 2024, from https://www.youtube.com/watch?v=9xjHCHR5_50

- NASA SMD Content Editors. (2024). Curiosity Rover location map. *NASA Science*. Retrieved September 3, 2024, from https://science.nasa.gov/mission/msl-curiosity/location-map/

- NASA SMD Content Editors. (2024). Mars - NASA Science. *NASA Science*. Retrieved September 3, 2024, from https://science.nasa.gov/mars/

- NASA SMD Content Editors. (2024). Mars: Facts. *NASA Science*. Retrieved September 3, 2024, from https://science.nasa.gov/mars/facts/

- NASA SMD Content Editors. (2024). Perseverance Rover components. *NASA Science*. Retrieved September 3, 2024, from https://science.nasa.gov/mission/mars-2020-perseverance/rover-components/

- NASA SMD Content Editors. (2024). Perseverance Rover location map. *NASA Science*. Retrieved September 3, 2024, from https://science.nasa.gov/mission/mars-2020-perseverance/location-map/

- NASA SMD Content Editors. (2024). Spirit and Opportunity by the numbers. *NASA Science*. Retrieved September 3, 2024, from https://science.nasa.gov/resource/spirit-and-opportunity-by-the-numbers/

- NASA SMD Content Editors. (2024). *Venus: Facts*. NASA Science. Retrieved September 3, 2024, from https://science.nasa.gov/venus/venus-facts/

- NASA SMD Content Editors. (2024). *Viking Project*. NASA Science. Retrieved September 3, 2024, from https://science.nasa.gov/mission/viking/

- NASA. (2020). Mars 2020 Perseverance launch press kit | Mission overview. *NASA*. Retrieved August 20, 2024, from https://www.jpl.nasa.gov/news/press_kits/mars_2020/launch/mission/

- NASA. (2021). Flying on Mars is getting harder and harder. *NASA Mars*. Retrieved July 20, 2024, from https://mars.nasa.gov/technology/helicopter/status/334/flying-on-mars-is-getting-harder-and-harder/

- NASA. (2021). Mars atmosphere model - Metric units. *NASA*. Retrieved July 20, 2024, from https://www.grc.nasa.gov/www/k-12/airplane/atmosmrm.html

- NASA. (2021). Mars Global Reference Atmospheric Model (Mars-GRAM): User guide. *NASA Technical Reports Server*. Retrieved September 6, 2024, from https://ntrs.nasa.gov/api/citations/20210023957/downloads/Mars-GRAM%20User%20Guide.pdf

- NASA. (2023). Mars fact sheet. *NASA Goddard Space Flight Center*. Retrieved April 22, 2024, from https://nssdc.gsfc.nasa.gov/planetary/factsheet/marsfact.html

- NASA. (2023). Mars Helicopter. *NASA Mars*. Retrieved April 22, 2024, from https://mars.nasa.gov/technology/helicopter/#Flight-Log

- NASA. (2024). Hazard: Distance from Earth. *NASA*. Retrieved July 20, 2024, from https://www.nasa.gov/hrp/hazard-distance-from-earth/

- NASA. (2024). Location map for Perseverance Rover. *NASA Mars*. Retrieved July 20, 2024, from https://mars.nasa.gov/mars2020/mission/where-is-the-rover/

- NASA/JPL-Caltech Web Team. (2001). Airy-0: The Martian Prime Meridian Crater. *NASA Photojournal*. Retrieved September 3, 2024, from https://photojournal.jpl.nasa.gov/catalog/PIA03207

- NASA/JPL-Caltech Web Team. (2002). MGS MOC Mars Digital Map. *NASA Photojournal*. Retrieved September 3, 2024, from https://photojournal.jpl.nasa.gov/catalog/PIA03467

- National Aeronautics and Space Administration (NASA). (2010). *NASA's contributions to aeronautics: Flight environment, operations, flight testing and research* (Vol. 2). NASA Scientific and Technical Information Office.

- National Renewable Energy Laboratory. (2024). Best research-cell efficiency chart. *Photovoltaic Research | NREL*. Retrieved August 10, 2024, from https://www.nrel.gov/pv/cell-efficiency.html

- National Research Council. (2002). *Safe on Mars: Precursor measurements necessary to support human operations on the Martian surface*. Washington, DC: The National Academies Press. https://doi.org/10.17226/10360

- North, G. R., Pyle, J., & Zhang, F. (2015). *Encyclopedia of atmospheric sciences* (2nd ed.). Elsevier. https://doi.org/10.1016/B978-0-12-382225-3.00034-2

- Novaković, Z., Vasić, Z., Ilić, I., Medar, N., & Stevanović, C. (2016). Integration of tactical-medium range UAV and catapult launch system. *Scientific Technical Review, 66*(4), 22-28. https://doi.org/10.5937/STR1604022N

- O'Brien, P. C. (2012). Using a robotic helicopter to fuel interest in and augment the human exploration of the planet Mars. *American Institute of Aeronautics and Astronautics*. https://doi.org/10.2514/6.2003-6275

- Ojha, L., Lewis, K., Karunatillake, S., & Schmidt, M. (n.d.). The Medusae Fossae Formation as the single largest source of dust on Mars. *Nature Communications*, 9, Article 2867. https://doi.org/10.1038/s41467-018-05291-5

- Osnat Katz. (2021). Landing on Mars is difficult, often fails, and will never be risk-free. *Phys.org*. Retrieved September 3, 2024, from https://phys.org/news/2021-05-mars-difficult-risk-free.html

- Perez Lebbink, L. (2006). UAV mission design for the exploration of Mars. *ESA/EUROAVIA Design Workshop 2006*. Retrieved September 2, 2024, from http://hdl.handle.net/1853/26454

- Petrosyan, A., et al. (2011). The Martian atmospheric boundary layer. *Reviews of Geophysics, 49*, RG3005. https://doi.org/10.1029/2010RG000351

- Piqueux, S., Byrne, S., Kieffer, H. H., Titus, T. N., & Hansen, C. J. (2015). Enumeration of Mars years and seasons since the beginning of telescopic exploration. *Icarus, 251*, 332-338. https://doi.org/10.1016/j.icarus.2014.12.014

- Radotich, M., Withrow-Maser, S., deSouza, Z., Gelhar, S., & Gallagher, H. (2021). A study of past, present, and future Mars rotorcraft. *9th Biennial Autonomous VTOL Technical Meeting*. Retrieved September 3, 2024, from https://ntrs.nasa.gov/api/citations/20210000448/downloads/1459_Radotich_011321.pdf

- Ramos, R. L., Carante, M. P., Ferrari, A., Sala, P., Vercesi, V., & Ballarini, F. (2023). A mission to Mars: Prediction of GCR doses and comparison with astronaut dose limits. *International Journal of Molecular Sciences, 24*(3), 2328. https://doi.org/10.3390/ijms24032328

- Rodrigue, C. M. (2024). Areography: A regional geography of Mars. *California State University, Department of Geography*. Retrieved July 10, 2024, from https://home.csulb.edu/~rodrigue/mars/finallect.html

- S. Withrow, W. Johnson, L. A. Young, H. Cummings, J. Balaram, & T. Tzanetos. (2020). An advanced Mars helicopter design. *ASCEND 2020, American Institute of Aeronautics and Astronautics*.

- Samuelson, A. (2019). How an atomic clock will get humans to Mars on time. *NASA JPL Caltech*. Retrieved September 3, 2024, from https://www.jpl.nasa.gov/news/how-an-atomic-clock-will-get-humans-to-mars-on-time

- Schorbach, V., & Weiland, T. (2022). Wind as a back-up energy source for Mars missions. *Acta Astronautica, 191*, 472–478. https://doi.org/10.1016/J.ACTAASTRO.2021.11.013

- Sercel, J. C., Blandino, J. J., & Wood, K. L. (1987). The ballistic Mars Hopper: An alternative Mars mobility concept. *23rd Joint Propulsion Conference, San Diego, CA*. https://doi.org/10.2514/6.1987-1901

- Sharp, R. P. (1973). Mars: Fretted and chaotic terrains. *Journal of Geophysical Research, 78*(20), 4073–4083. https://doi.org/10.1029/JB078i020p04073

- Shea, G. (2023). Why go to space? *NASA*. Retrieved September 3, 2024, from https://www.nasa.gov/humans-in-space/why-go-to-space/

- Shubbak, M. (2019). Advances in solar photovoltaics: Technology review and patent trends. *Renewable and Sustainable Energy Reviews, 115*, 109383. https://doi.org/10.1016/j.rser.2019.109383

- Smith, D. E., Zuber, M. T., Frey, H. V., Garvin, J. B., Head, J. W., Muhleman, D. O., Pettengill, G. H., Phillips, R. J., Solomon, S. C., Zwally, H. J., Banerdt, Ø. B., Duxbury, T. C., Golombek, M. P., Lemoine, F. G., Neumann, G. A., Rowlands, D. D., Aharonson, O., Ford, P. G., & Sun, X. (2001). Mars Orbiter Laser Altimeter: Experiment summary after the first year of global mapping of Mars. *Journal of Geophysical Research: Planets, 106*, 689–712. https://doi.org/10.1029/2000JE001364

- Smith, S. W., LeBeau, R. P., Seigler, T. M., Reasor, D. A., Jacob, J. D., Gleeson, D., & Scarborough, S. (2008). Testing of compact inflatable wings for small autonomous aircraft. *49th AIAA/ASME/ASCE/AHS/ASC Structures, Structural Dynamics, and Materials Conference*, Schaumburg, IL. https://doi.org/10.2514/6.2008-2216

- Solaero Technologies Corp. (2021). SolAero Technologies' solar panel powers NASA's Mars Helicopter - Ingenuity. *PR Newswire*. Retrieved August 11, 2024, from https://www.prnewswire.com/news-releases/solaero-technologies-solar-panel-powers-nasas-mars-helicopter---ingenuity-301271650.html

- Solomon, S. C., & Head, J. W. (1982). Evolution of the Tharsis province of Mars: The importance of heterogeneous lithospheric thickness and volcanic construction. *Journal of Geophysical Research, 87*(B12), 9755–9774. https://doi.org/10.1029/JB087iB12p09755

- Sopegno, L., Martini, S., Pedone, S., Fagiolini, A., Rutherford, M. J., Stefanovic, M., Rizzo, A., Livreri, P., & Valavanis, K. P. (2024). An advanced hexacopter for Mars exploration: Attitude control and autonomous navigation. *IEEE Transactions on Aerospace and Electronic Systems*. https://doi.org/10.1109/TAES.2024.3365667

- SpaceX Media Team. (2024). SpaceX - Missions: Mars. *SpaceX*. Retrieved August 20, 2024, from https://www.spacex.com/humanspaceflight/mars/

- SpaceX Team. (2020). Starship users guide. *SpaceX*. Retrieved August 20, 2024, from https://www.spacex.com/media/starship_users_guide_v1.pdf

- SpaceX Web Team. (2024). SpaceX - Starship. *SpaceX*. Retrieved August 20, 2024, from https://www.spacex.com/vehicles/starship/

- Stocking, P., & Summer, L. (2005). M-4 Minerva Mars atmospheric flight vehicle and CRATER drop test vehicle project executive summary. *Cranfield University, Department of Power, Propulsion, and Aerospace Engineering*.

- Svedhem, H., Titov, D., Taylor, F., & Mueller-Wodarg, I. (2007). Venus as a more Earth-like planet. *Nature, 450*(7170), 629–632. https://doi.org/10.1038/nature06432

- Tamir Eshel. (2017). Lockheed Martin UK developed a submarine-launched UAV. *Defense Update*. Retrieved September 1, 2024, from http://defense-update.com/20170912_outrider.html

- Tamsyn Brann. (2020). MAVEN maps electric currents around Mars that are fundamental to atmospheric loss. *NASA*. Retrieved September 3, 2024, from https://www.nasa.gov/news-release/maven-maps-electric-currents-around-mars-that-are-fundamental-to-atmospheric-loss/

- Tang, B., Quan, Q., Pan, D., Wang, C., Zheng, H., Wang, K., Tang, D., & Deng, Z. (2024). Design and experimental verification of propulsion system for a Mars quadcopter. Acta Astronautica, 225, 992–1000. https://doi.org/10.1016/j.actaastro.2024.09.069

- The Planetary Society Team. (2024). Cost of Perseverance. *The Planetary Society*. Retrieved August 22, 2024, from https://www.planetary.org/space-policy/cost-of-perseverance

- The Planetary Society Team. (2024). The cost of NASA's Phoenix mission to Mars. *The Planetary Society*. Retrieved August 22, 2024, from https://www.planetary.org/space-policy/phoenix-cost

- Toray Composite Materials America, Inc. (2018). M46J carbon fiber technical data sheet. Retrieved February 26, 2025, from https://www.toraycma.com/wp-content/uploads/M46J-Technical-Data-Sheet-1.pdf

- U.S. Geological Survey. (1998). *Topographic map of Mars* (USGS I Map 2782). U.S. Department of the Interior. Retrieved January 7, 2022, from https://pubs.usgs.gov/imap/i2782/

- U.S. Geological Survey. (n.d.). *Mars 1:5,000,000 THEMIS quadrangles*. USGS Astrogeology Science Center. Retrieved September 3, 2024, from https://planetarynames.wr.usgs.gov/Page/mars1to5mTHEMIS

- Underwood, C., & Collins, N. (2017). Design and control of a Y-4 tilt-rotor VTOL aerobot for flight on Mars. *Proceedings of the 68th International Astronautical Congress (IAC)*. https://openresearch.surrey.ac.uk/esploro/outputs/conferencePresentation/Design-and-Control-of-a-Y-4-Tilt-Rotor-VTOL-Aerobot-for-Flight-on-Mars/99511131102346

- University of Oregon. (2024). Experiments find that electrical sparks are possible on Mars. *SciTechDaily*. Retrieved July 27, 2024, from https://scitechdaily.com/experiments-find-that-electrical-sparks-are-possible-on-mars/

- Veismann, M., Dougherty, C., Rabinovitch, J., Quon, A., & Gharib, M. (2021). Low-density multi-fan wind tunnel design and testing for the Ingenuity Mars Helicopter. *Experiments in Fluids, 62*(9). https://doi.org/10.1007/s00348-021-03278-5

- Vernikos, J. (2008). Human exploration of space: Why, where, what for? *Hippokratia, 12*(Suppl 1), 6-9.

- Wang, J., Rosenbaum, J., Prasad, A., Raad, R., Putman, E., Aintablian, H., & Hynek, B. (2024). Geological health hazards from Martian dust and appropriate countermeasures for the human exploration of Mars. *55th Lunar and Planetary Science Conference*, Texas.

- Web Team (Aerospace Testing International). (2020). How engineers test the radiation shielding of electronics in space vehicles. *Aerospace Testing International*. Retrieved September 6, 2024, from https://www.aerospacetestinginternational.com/features/requirements-are-changing-for-the-testing-of-electronics-used-on-board-space-vehicles.html

- Williams, D. R. (NASA Web Editor). (2022). *ExoMars Rover - NASA NSSDCA - Spacecraft details*. NASA. Retrieved September 3, 2024, from https://nssdc.gsfc.nasa.gov/nmc/spacecraft/display.action?id=EXOMARS22

- Williams, D. R. (NASA Web Editor). (2022). *Mariner 2 - NASA NSSDCA - Spacecraft details*. NASA. Retrieved September 3, 2024, from https://nssdc.gsfc.nasa.gov/nmc/spacecraft/display.action?id=1962-041A

- Williams, D. R. (NASA Web Editor). (2022). *Mariner 4 - NASA NSSDCA - Spacecraft details*. NASA. Retrieved September 3, 2024, from https://nssdc.gsfc.nasa.gov/nmc/spacecraft/display.action?id=1964-077A

- Williams, D. R. (NASA Web Editor). (2022). *Mariner 9 - NASA NSSDCA - Spacecraft details*. NASA. Retrieved September 3, 2024, from https://nssdc.gsfc.nasa.gov/nmc/spacecraft/display.action?id=1971-051A

- Williams, D. R. (NASA Web Editor). (2022). *Vega 1 Balloon - NASA NSSDCA - Spacecraft details*. NASA. Retrieved September 3, 2024, from https://nssdc.gsfc.nasa.gov/nmc/spacecraft/display.action?id=1984-125F

- Williams, D. R. (NASA Web Editor). (2022). *Venera 13 Descent Craft - NASA NSSDCA - Spacecraft details*. NASA. Retrieved September 3, 2024, from https://nssdc.gsfc.nasa.gov/nmc/spacecraft/display.action?id=1981-106D

- Williams, D. R. (NASA Web Editor). (2024). *Mars exploration timeline*. NASA. Retrieved September 3, 2024, from https://nssdc.gsfc.nasa.gov/planetary/chronology_mars.html

- Williams, D. R. (NASA Web Editor). (2024). *Planetary fact sheet*. NASA. Retrieved September 3, 2024, from https://nssdc.gsfc.nasa.gov/planetary/factsheet/

- Williams, D. R. (NASA Web Editor). (2024). *Venus exploration timeline*. NASA. Retrieved September 3, 2024, from https://nssdc.gsfc.nasa.gov/planetary/chronology_venus.html

- Wörner, L., Root, B., Bouyer, P., Braxmaier, C., Dirkx, D., Encarnarcao, J., Hauber, E., Hussmann, H., Karatekin, O., Koch, A., Kumanchik, L., Migliaccio, F., Reguzzoni, M., Ritter, B., Schilling, M., Schubert, C., Thieulot, C., Klitzing, W., & Witasse, O. (2023). MaQuIs - Mars Quantum Gravity Mission. *ESSOAr*. https://doi.org/10.22541/essoar.167397424.46877056/v1

- Wu, H., Liu, M., Mi, Y., Wang, J., & Guo, M. (2022). Key parameters of a design for a novel reflux subsonic low-density dust wind tunnel. *Aerospace, 9*(662). https://doi.org/10.3390/aerospace9110662

- Youhanna V, Felicetti L, Ignatyev D. (2024) Parametric analysis of rotary VTOL aerobot design configurations to fly on Titan. In: 75th International Astronautical Congress IAC-2024, 14-18 October 2024, Milan, Italy Retrieved December 22, 2024, from https://dspace.lib.cranfield.ac.uk/handle/1826/23153

- Youhanna, V., Felicetti, L., & Ignatyev, D. (2023). Conceptual design study based on defined parameters for next generation Martian rotorcrafts. *IEEE Aeroconf 2024*, Montana, US, 2-9 March 2024. https://doi.org/10.1109/AERO58975.2024.10521441

- Youhanna, V., Felicetti, L., & Ignatyev, D. (2023). Parametric analysis of battery-electric rotorcraft configurations to fly on Mars. *Aerospace Europe Conference Joint 10th EUCASS - 9th CEAS Conference 2023*, Lausanne, 9-13 July 2023. https://doi.org/10.13009/EUCASS2023-319

- Youhanna, V., Felicetti, L., & Ignatyev, D. (2024). Preliminary design exploration of prospective multirotor aerobots for Mars. *34th Congress of the International Council of the Aeronautical Sciences (ICAS 2024)*, Florence, Italy, September 9-13, 2024.

- Youhanna, V., Felicetti, L., & Ignatyev, D. (2024). Preliminary investigation into future Martian multicopter configurations. *Vertical Flight Society's 80th Annual Forum & Technology Display*, Montréal, Québec, Canada, May 7-9, 2024. https://doi.org/10.4050/F-0080-2024-1266

- Youhanna, V., Ignatyev, D., & Felicetti, L. (2022). Futuristic Martian Aerobot Design. *UKRAS22 Conference "Robotics for Unconstrained Environments" Proceedings*, 64-65. https://doi.org/10.31256/Ec2Na5W

- Young, L. A., Aiken, E. W., Lee, P., & Briggs, G. A. (2004). Mars rotorcraft: Possibilities, limitations, and implications for human/robotic exploration.

NASA Technical Reports Server. Retrieved January 21, 2025, from https://ntrs.nasa.gov/citations/20090028805

- Young, L. A., Chen, R. T. N., Aiken, E. W., & Briggs, G. A. (2000). Design opportunities and challenges in the development of vertical lift planetary aerial vehicles. *American Helicopter Society International Vertical Lift Aircraft Design Specialist's Meeting*. https://rotorcraft.arc.nasa.gov/Publications/files/Young_AHS_Design2000.pdf

- Yu-Yan, S. Z., Zhou, D., Li, X., Liu, J., Wang, S., & Ouyang, Z. (2020). The evolution of scientific goals for Mars exploration and future prospects. National Science Review, 65(7). https://doi.org/10.1360/TB-2019-0638

- Zappek, V., Rinker, M., Daxer, L., Hajek, M. (2023). Evaluation of aerial vehicle configurations for high-range Mars missions. CEAS Space J 15, 761–775. https://doi.org/10.1007/s12567-022-00479-4

- Zubrin, R. M. (2012). The Mars Gashopper. Concepts and Approaches for Mars 2012 Conference, Houston, TX. Retrieved from https://ui.adsabs.harvard.edu/abs/2012LPICo1679.4069Z/abstract
Schuerger, A. C., & Borrell, A. V. (2023). Shock-impacts and vibrational g-forces can dislodge Bacillus spp. spores from spacecraft surfaces. Microorganisms, 11(10), 2421. https://doi.org/10.3390/microorganisms11102421

Appendices

Appendix A Appendix A. Ethical approval letter

12 September 2024

Dear Mr Youhanna ,

Reference: CURES/23672/2024
Project ID: 26960
Title: Conceptual Design of Martian Aerial Robots

We are pleased to inform you that you have successfully declared that your research project is a **Literature Review – based solely on openly available literature which is in the public domain, and you are undertaking desk-based research not involving any other form of data or information.**

You have also confirmed that your project **does not meet** any of the literature review specified exceptions, listed both within the relevant section of the CURES form and below:

1) Your supervisor has requested that you apply for approval through CURES because:

- The journals or data are in a sensitive area (please discuss this with your supervisor)
- The project will be embargoed **i.e. will not be publicly available via the Cranfield library immediately or longer term**

2) Approval is/will be specifically required by another external body e.g. journal publishers

Therefore, **you do not require ethical approval** and your CURES application will be automatically closed.

Please keep a copy of this letter safe, if this exception is in relation to your thesis project, you will need to include a copy with your final thesis submission.

If you have any queries, please contact CURES Support.

We wish you every success with your project.

Regards,

CURES Team